Coarsening of bubbly suspensions and foams: the interplay of capillarity and yield stress

Nicolò Galvani

▶ **To cite this version:**

Nicolò Galvani. Coarsening of bubbly suspensions and foams: the interplay of capillarity and yield stress. Soft Condensed Matter [cond-mat.soft]. Université Gustave Eiffeil, 2024. English. NNT : . tel-04881842

HAL Id: tel-04881842
https://hal.science/tel-04881842v1

Submitted on 12 Jan 2025

HAL is a multi-disciplinary open access archive for the deposit and dissemination of scientific research documents, whether they are published or not. The documents may come from teaching and research institutions in France or abroad, or from public or private research centers.

L'archive ouverte pluridisciplinaire **HAL**, est destinée au dépôt et à la diffusion de documents scientifiques de niveau recherche, publiés ou non, émanant des établissements d'enseignement et de recherche français ou étrangers, des laboratoires publics ou privés.

Distributed under a Creative Commons Attribution 4.0 International License

Université Gustave Eiffel

Coarsening of bubbly suspensions and foams: the interplay of capillarity and yield stress

Thèse de doctorat de l'Université Gustave Eiffel

Ecole doctorale Sciences, Ingénierie et Environnement EDSIE
Spécialité de doctorat: Sciences des Matériaux
Unité de recherche : Laboratoire Navier

Nicolò Galvani

Composition du Jury

Frédéric Restagno Directeur de recherche, Université Paris-Saclay	Président du jury
Christophe Raufaste Professeur, Université Côte d'Azur	Examinateur
Marie Le Merrer Chargée de recherche, Université Claude Bernard Lyon 1	Rapportrice
Guillaume Ovarlez Directeur de recherche, Université de Bordeaux	Rapporteur

Encadrement de la thèse

Olivier Pitois Directeur de recherche, Université Gustave Eiffel	Directeur de thèse
Sylvie Cohen-Addad Professeure, Université Gustave Eiffel	Co-Directrice de thèse

Acknowledgment

My first acknowledgment goes to the members of the Jury, who have accepted to dedicate their time to the evaluation of my work. It results from three wonderful years which taught me how much I love doing research, and I hope to have transferred you a bit of the wonder I felt while preparing it.

I need also to express my gratitude to my supervisors, Sylvie and Olivier. Sylvie, for guiding me step by step in this journey, always with a smile and words of encouragement; I learnt from you to be rigorous in my work, to care for the details and never to take something for granted. Olivier, always calm and collected, for inspiring me with never ending ideas; I learnt from you not to stop at the first obstacle, to remain focused on the priorities, and to always search for an innovative approach to reach the goal.

I owe so much to both of you.

I want to thank the people who let me start this unexpected journey: Vittorio Morandi, who first gave me the idea; Daniela Cavalcoli and Massimiliano Marangolo, who built a bridge from Bologna to Paris. I want to thank my comrades, which helped me exit from my comfort zone, with whom I discovered Paris, and share with me the struggles of the lockdowns: Caterina, Eugenio, Francesco, Claudia, Giacomo.

I thank Jean Sulem, who welcomed me in Laboratoire Navier, and Geoffroy Prevot, who welcomed me in his team. Thanks to the fellow PhD students, who welcomed me from the very beginning: Jordan, Elisa, Antoine, Anatole, Nabil, Margaux, Mark, Ahmad, Ali, Paul.

Thanks to the scientists who provided help and insight for my work: Brice, Xavier, Reinhard, Olivier.

Thanks to the technical team, who gave life to all my projects: Mathieu, Michel, Boumedien, Laurent, Cédric, Julien.

Thanks to the Orsay team, with whom I shared a very fruitful collaboration, central to my research: Dominique, Anniina, Emmanuelle, Alice, Shailesh. Thank you for your precious help and the friendly environment you created.

I apologise to the international readers for the following language switch, but I feel it necessary to give the appropriate acknowledgement.

Sono molto grato a coloro che mi hanno accolto e fatto sentire a casa in questi anni francesi, offrendomi continuamente calore a allegria: Laura, Uddin, Elena, Pier, Kim. Grazie per esserci stati, e per avermi fatto sentire parte della 'famiglia' dal primo momento.

Grazie ai miei affetti, che non hanno mai smesso di farmi sentire il loro supporto e la loro vicinanza qualunque fosse il numero di kilometri a separarci. Mi sarei sentito perso e solitario senza questo filo a collegarci; se questa certezza fosse vacillata non ne sarebbe valsa la pena. Più nello specifico, senza un ordine preferenziale:

Grazie ai miei genitori, a Tommaso, Eleonora, e Claudia, sempre capaci di donarmi

un sorriso e leggerezza. Grazie a mio nonno, che ha sempre un consiglio saggio da darmi.

Grazie a Natascia, Paolo, Ilaria e Giacomo, per avermi preso in questi anni dentro la loro famiglia, facendomi sentire come se ne fossi sempre stato parte.

Grazie ai miei amici, per la assidua e certa frequentazione: Lorenzo, Federico, Eugenia, Diego, Simone, Matteo.

Grazie Giulia. Amica, compagna, moglie. Grazie, per non aver mai smesso mai di illuminarmi e riscaldarmi con la tua fiamma creativa, a di avermi sopportato nei momenti complicati.

"The most important step a man can take. It's not the first one, is it? It's the next one. Always the next step." - Brandon Sanderson, Oathbringer

Abstract

This dissertation explores the coarsening dynamics of bubble dispersions in both simple surfactant solutions and concentrated emulsions, which serve as model yield stress fluids. Liquid foams, prevalent in diverse industries, are key in applications from food to building construction, where their low density, high surface area, and insulation properties are valued. However, controlling their microstructure during solidification remains a challenge, especially due to foam aging mechanisms such as drainage, coalescence, and coarsening. Coarsening, driven by gas transfer from smaller to larger bubbles, is particularly difficult to arrest. The aim of this thesis is to investigate how yield stress fluids affect coarsening of wet foams and bubbly liquids, with the hypothesis that a sufficiently high yield stress could counteract bubble growth.

The research is based on experiments conducted both on Earth and in microgravity aboard the International Space Station (ISS), which allows to investigate bubble coarsening across a wide range of liquid fractions—from dry foams to dilute bubbly liquids. On ground, the evolution of the foam structure is observed by videomicroscopy at the surface of two ageing cells mounted on a clinostat, a classical one at fixed volume and one at controlled osmotic pressure, specially constructed for this study, whereas in microgravity the experiments were conducted during the first mission of the Soft Matter Dynamics instrument. We measure the size and morphology of individual bubbles on images acquired along the coarsening using image treatment and analysis with machine learning tools. We show that the natural bubble size distribution of a simple wet foam coarsening in the scaling state is hierarchical with a network of bubbles in contact and a population of small bubbles roaming through its interstices. A key finding is the abrupt change at the jamming transition between the coarsening behavior of wet foams, which follows a parabolic growth law for the average bubble size, and that of bubbly liquids, which follows a cubic growth law. Moreover we study the average bubble coarsening rate as a function of the liquid fraction and show how it is modified by the effect of the small adhesive forces observed between bubbles. A major consequence of these forces is that the change in coarsening regime is observed at a liquid fraction higher than that characterizing the Random Close Packing of spherical bubbles.

We study the coarsening of foamed emulsions as a function of the emulsion yield stress and foam liquid fraction. Our results show how the coarsening rate is damped by the plasticity of the emulsion and allow to assess the conditions for coarsening arrest. Our analysis presents a comprehensive coarsening diagram based on the Bingham number and liquid volume fraction, identifying five distinct coarsening regimes according to three features: the average growth law, the individual bubble ripening, and the bubble morphology. This thesis contributes significantly to understanding the transition between capillary and plastic regimes in bubble dispersions and proposes models that could describe coarsening behaviour in various yield stress fluids.

Résumé

Cette thèse explore la dynamique de murissement des dispersions de bulles dans des solutions aqueuses de tensioactifs et des émulsions concentrées, qui servent ici de modèles pour les fluides à seuil. Les mousses liquides, courantes dans diverses industries, jouent un rôle clé dans des applications allant de l'alimentation à la construction, où leurs faibles densités, grandes surfaces spécifiques et propriétés isolantes sont valorisées. Cependant, contrôler leur microstructure lors de la solidification reste un défi, en particulier en raison des mécanismes de vieillissement des mousses tels que le drainage, la coalescence et le murissement. Le murissement, qui se définit par le transfert de gaz des petites bulles vers les plus grosses, est particulièrement difficile à arrêter. L'objectif de cette thèse est d'étudier comment les fluides à seuil d'écoulement influencent le murissement des mousses humides et des liquides bulleux, en anticipant qu'un seuil de mise en écoulement suffisamment élevé pourrait contrer la croissance des bulles.

Les travaux se basent sur des expériences menées à la fois sur Terre et en microgravité, à bord de la Station Spatiale Internationale (ISS), ce qui permet d'étudier le murissement des bulles sur une large gamme de fractions liquides, allant des mousses sèches aux liquides bulleux dilués. Au sol, l'évolution de la structure de la mousse est observée par vidéo-microscopie à la surface de deux cellules de vieillissement montées sur un clinostat : l'une classique, à volume fixe, et l'autre à pression osmotique contrôlée, spécialement construite pour cette étude. En microgravité, les expériences ont été réalisées lors de la première mission de l'instrument Soft Matter Dynamics. Nous mesurons la taille et la morphologie des bulles individuelles sur des images acquises au cours du murissement, en utilisant des outils de traitement d'image et d'analyse avec des méthodes d'apprentissage automatique. Nous montrons que la distribution naturelle des tailles de bulles d'une mousse humide simple au cours de son murissement dans l'état stationnaire est hiérarchique, avec un réseau de bulles en contact et une population de petites bulles se déplaçant dans les interstices que font apparaître les premières. Une découverte clé est la transition abrupte au point de jamming entre le comportement de murissement des mousses humides, qui suit une loi de croissance parabolique de la taille moyenne des bulles, et celui des liquides bulleux, qui suit une loi de croissance cubique. De plus, nous étudions le taux de murissement moyen des bulles en fonction de la fraction liquide et montrons comment celui-ci est modifié par l'effet des petites forces adhésives observées entre les bulles. Une conséquence majeure de ces forces est que le changement de régime de murissement est observé pour une fraction liquide plus grande que celle qui caractérise le Random Close Packing des bulles sphériques.

Nous étudions le murissement des émulsions moussées en fonction de la contrainte seuil de l'émulsion et de la fraction liquide de la mousse. Nos résultats montrent comment le taux de murissement est amorti par la plasticité de l'émulsion et permettent d'évaluer les conditions d'arrêt du murissement. Notre analyse présente un diagramme complet du murissement, basé sur le nombre de Bingham et la fraction volumique de liquide, identifiant cinq régimes de murissement distincts selon trois caractéristiques : la loi de croissance moyenne, le murissement des bulles individuelles et la morphologie des bulles. Cette thèse contribue de manière significative à la compréhension de la transition entre les régimes capillaire et plastique dans les dispersions de bulles et propose des modèles pouvant décrire le comportement de murissement dans divers fluides à seuil d'écoulement.

Contents

List of Tables

List of Symbols

Symbol	Description	Units
	Physical-chemistry	
γ	Surface tension	$N\ m^{-1}$
$\mathcal{C}$	Surfactant concentration	g/L
$\mathcal{G}$	Glycerol weight percentage	1
D	Diffusivity	m^2/s
H_e	Solubility	$mol/Pa/m^3$
v_m	Molar volume	m^3/mol
	Foam description	
ϕ	Liquid volume fraction	1
R	Air bubble radius	m
φ	Oil volume fraction	1
φ_l	Aqueous volume fraction	1
r_d	Oil droplet radius	m
$\bar{p}$	Bubble gas pressure	Pa
P_w	Pressure in the liquid	Pa
Π	Osmotic pressure	Pa
Π_c	Capillary pressure	Pa
p_0	Liquid pressure at infinite distance (dilute limit)	Pa
K	Permeability	m^2
	Coarsening	
Ω_p	Coarsening rate in the parabolic regime	$m^2\ s^{-1}$
Ω_0	Coarsening rate in the dry limit	$m^2\ s^{-1}$
Ω_c	Coarsening rate in the cubic regime	$m^3\ s^{-1}$
K_0	Coarsening rate in the dilute limit	$m^3\ s^{-1}$
h	Film thickness	m
θ_c	Contact angle	$^\circ$

Symbol	Description	Units
	Rheometry	
$\dot{\varepsilon}$	Strain rate	s^{-1}
τ	Stress	Pa
G'	Storage modulus	Pa
G''	Loss modulus	Pa
η	Dynamic viscosity	$Pa\ s$
κ	Consistency	$Pa\ s^{1-n}$
n	Power index	1
τ_y	Yield stress	Pa
G	Static shear modulus	Pa
τ_{vf}	Viscous component of the stress	Pa
	Bubble analysis	
$\overline{R}$	Mean radius	m
R_{32}	Sauter average radius	m
p_{32}	Polydispersity	1
R_b	Bump radius	m
S	Yielded medium shell radius	m
	Foamability	
Γ_∞	Surface concentration of adsorbed surfactant at the saturation	mol/m^2
R_s	Saturation radius	m
v_g	Gas volume fraction in the foam	1
v_o	Oil volume fraction in the foam	1
v_w	Water volume fraction in the foam	1
	Adimensional numbers	
N_Y	Plasto-elastic ratio	1
Y	Yield parameter	1
Y_g	Bingham gravitational number	1
Bi	Bingham capillary number	1
Bi_{eff}	Bingham capillary number of the effective medium	1
Ca_{el}	Elastocapillary number	1

Publications

Journals

1. Pasquet, M., N. Galvani, O. Pitois, S. Cohen-Addad, R. Höhler, A. T. Chieco, S. Dillavou, J. M. Hanlan, D. J. Durian, E. Rio, A. Salonen and D. Langevin "Aqueous foams in microgravity, measuring bubble sizes", Comptes Rendus. Mécanique, 2023, 351(S2): 139-161.

2. Pasquet, M., N. Galvani, A. Requier, S. Cohen-Addad, R. Hohler, O. Pitois, E. Rio, A. Salonen and D. Langevin, "Coarsening transitions of wet liquid foams under microgravity conditions", Soft Matter, 2023, 19(33): 6267-6279.

3. Galvani, N., M. Pasquet, A. Mukherjee, A. Requier, S. Cohen-Addad, O. Pitois, R. Hohler, E. Rio, A. Salonen, D. J. Durian and D. Langevin, "Hierarchical bubble size distributions in coarsening wet liquid foams", Proc Natl Acad Sci U S A, 2023, 120(38): e2306551120.

International Conferences

1. Nicolò Galvani, Sylvie Cohen-Addad, Olivier Pitois, "Bumpy bubbles in a coarsening foamed emulsions" 15th Eufoam Conference, Dresden, Germany, 2024, Tome, Pages.

2. Nicolò Galvani, Sylvie Cohen-Addad, Olivier Pitois, Brice Saint-Michel, "How does a foamed yield-stress fluid coarsen?" CMD31-General Conference of the Condensed Matter Division, Braga, Portugal, 2024, Tome, Pages.

National Conferences

1. Nicolò Galvani, Sylvie Cohen-Addad, Olivier Pitois, "Aging of liquid foams: bubble abnormal growth", Le GDR Micropesanteur fondamentale et appliquée, 04/11/2022, Hyères, France.

2. Nicolo Galvani, Sylvie Cohen-Addad, Douglas Durian, Reinhard Höhler, Dominique Langevin, Marina Pasquet, Olivier Pitois, Alice Requier, Emmanuelle Rio, Anniina Salonen, "The natural coarsening of drainage-free wet foams", 26ème Congrès Général de la SFP, 05/07/2023, Paris, France

3. Nicolò Galvani, Sylvie Cohen-Addad, Olivier Pitois, "Coarsening in complex wet foams", Journées CNES des Jeunes Chercheurs, 12/10/2023, Toulouse, France.

4. Nicolò Galvani, Sylvie Cohen-Addad, Olivier Pitois, "Hierarchical structure of coarsening liquid foams", Le GDR Micropesanteur fondamentale et appliquée, 26/10/2023, Hyères, France.

5. Nicolò Galvani, Sylvie Cohen-Addad, Olivier Pitois, "Coarsening bubbly assemblies: from dry to dilute", Le GDR Micropesanteur fondamentale et appliquée, 14/10/2024, Hyères, France.

Introduction

Liquid foams are ubiquitous in everyday life and industrial processes, in applications ranging from food and cosmetics to materials science, or separation processes. Moreover liquid foams play a major role as precursors of solid foams. Such aerated materials are looked for their light weight density, their high specific surface area, their thermal and acoustic insulation properties, and their mechanical strength. The field of housing construction is a good example of the use of these porous materials, such as polymer foams used for their excellent insulation properties. Cement and plaster foams aim to eventually replace them, at least partially, if we manage to produce them with good control over their microstructure. However, controlling the morphology and the functional properties of foamed materials can be challenging due to the intrinsic aging of liquid foams.

Three processes can be at play during the solidification process: drainage is caused by density difference between air bubbles and the material, (ii) coarsening is a gas transfer from smaller bubbles to bigger bubbles, and (iii) coalescence refers to thin film breakage between two neighboring bubbles. The magnitude of these processes depends on various parameters, such as bubble size, liquid content, surfactant type and concentration. In principle, the use of appropriate surfactants allows for the coalescence process to be counteracted. Drainage is expected to be counteracted if a complex fluid exhibiting yield stress behavior, such as a paste or a dense particulate suspension, is used as foaming liquid, with a yield stress sufficient to balance hydrostatic pressure. Up to now, coarsening remains challenging to be counteracted and this is detrimental to the production of solid well controlled foamed materials, whatever the field of application.

We conjecture that coarsening could be slowed down or even arrested by the use of a yield stress fluid with a yield stress large enough to overcome bubble Laplace pressure.Even if one can imagine that the yield stress of the medium surrounding the bubble is sufficient to prevent changes in its size, what happens when there are more bubbles and less yield-stress fluid? When the foam has a liquid fraction of 10%, it is these 10% of yield-stress fluid that must now prevent the bubbles, representing 90% of the volume, from changing size! It is difficult to anticipate how much the yield stress will need to be increased to continue preventing size changes. Actually, the fundamental knowledge about yield stress fluid coarsening is scarce. The dynamics, the bubble size growth laws, the bubble size distributions or the bubble morphology in coarsening yield stress fluids raise many open questions.

Another crucial element is to tackle the problem of foams with large amount of liquid (in the perspective applications). This comes back to study the ageing of bubble dispersions as a function of their liquid volume fraction, from the bubbly regime to the "wet" foam regime close to the jammed transition where the bubbles are closely packed. This has been the objective of a research project proposed by an international consortium (in which Laboratoire Navier and Institut des Nanosciences de Paris take part) who developed a dedicated instrument to be operated on board the International Space Station. Microgravity conditions allow to delineate capillary effects from gravity effects which is propitious to the investigation of coarsening of wet foams. Successive missions between 2020 and 2024 provide an extensive corpus of data.some of which has been processed and

analyzed as part of this thesis.

In this thesis, we study the coarsening of bubble dispersions, made of either simple surfactant solutions or concentrated emulsions, which constitute model yield stress fluids. We propose an experimental approach based on dedicated experiments on ground and on the analysis of data acquired with the Soft Matter Dynamics instrument in the ISS.

In Chapter 1, we review the state of the art in foam and emulsion research. We begin by exploring the production methods for aqueous foams, discussing the structure and dynamics governed by the Laplace law, and analyzing the drainage behavior of liquid from the foam structure. The chapter then delves into the theoretical foundations of coarsening, covering Ostwald ripening in dilute systems, with key developments based on LSW theory, and contrasting it with jammed systems described by Lemlich theory. Additionally, the rheological properties of foams and emulsions are discussed, with a particular focus on how these properties affect foam stability and drainage. Finally, we examine the production of foamed emulsions, their modified rheology compared to simple foams or emulsions, and their enhanced resistance to drainage due to their unique flow properties.

In Chapter 2, we study the coarsening behavior of aqueous wet foams, particularly in microgravity environments where the effects of gravity are minimized. This allows us to focus on the intrinsic growth laws of wet foams and bubbly liquids, examining the role of adhesion which, even if it is small, eventually plays an important role in coarsening as the transition between foams and bubbly liquids approaches. We also analyze scaling state bubble size distributions and reveal, for the first time, the presence of a population of small bubbles roaming in the liquid interstices, a phenomenon that determines a hierarchical size distribution.

Chapter 3 investigates the coarsening behavior in bubble dispersions from the foam regime to the dilute bubbly regime. We present the clinostat setup, which allows to counteract the gravitational drainage in the samples. In addition, in the bubbly regime, the samples are stabilized against drainage thanks to a continuous phase made of a small yield stress emulsion. Thus, we detail the preparation, rheological characterization and foamability of the emulsions. We study coarsening growth laws over a range of liquid fractions, from dry foams to dilute bubbly liquids, which had never been considered until now. Furthermore, we propose a model to account for the effect of adhesion forces between bubbles on the foam coarsening rate.

In Chapter 4, we explore the morphological and kinetic modifications that occur in a foamed emulsion undergoing coarsening. This chapter begins with the development of an automatic recognition system for analyzing bubble morphology, which includes machine learning training, image processing, and data post-processing. We then investigate how the yield stress of the medium in bubbly emulsions modifies the coarsening growth law, leading to damped growth behavior. We also discuss the phenomenon of arrested coarsening, observed in both the foamy and bubbly regimes, and the appearance of surface bumps on bubbles, providing a theoretical support to explain their formation. The chapter concludes with a extensive coarsening diagram that provides an overview of the coarsening characteristics as a function of liquid fraction and the Bingham capillary number.

This dissertation aims to provide new insights into bubble coarsening over the full range of bubble volume fraction. Moreover, we study how the presence of a yield stress in the interstitial liquid alters the characteristics of coarsening, in terms of the rate at which this phenomenon occurs, of the bubble shape and size distribution, and even of the arrest of coarsening.

Context

The Ph.D. work presented in this dissertation was funded by Centre National d'Études Spatiales and European Space Agency. It it was developed at the Laboratoire Navier, at Université Gustave Eiffel, and at the Institut des Nanosciences de Paris, at Sorbonne Université.

Chapter 1

State of the art

Contents

1.1 Aqueous foams

A foam is a dense packing of gas bubbles dispersed in a continuous phase, which can be either a liquid phase [1] or a solid phase [1]. Be it sea froth, firefighting foam, a meringue or aerated cement, all of these materials are created by trapping a gas volume inside a liquid, they presente reduced thermal and acoustic transport properties with respect to the continuous phase itself, and after their formation in the liquid state they undergo aging processes that alter their structure.

This section delves into the properties common to liquid foams: it starts describing the ways of foam production, then it focuses on their physical equilibrium properties, and finally it details the mechanisms of foam aging.

It is important to highlight that emulsions — as dispersions of oil droplets in a continuous aqueous phase — exhibit properties similar to those of foams. Therefore, much of the reasoning presented here for foams is equally applicable to emulsions.

1.1.1 Foaming techniques

Liquid foams are characterized by large liquid-gas surface area per unit volume. Thus foaming consists in the creation of such interfaces. Cohesive forces act to minimize surfaces in the liquid, and mechanical work is needed to provide the amount of energy necessary to create an interface.

The free energy required to increase the interfacial area by an amount dS, at constant temperature and pressure, is

$$dG = \gamma dS \tag{1.1}$$

where γ is the liquid-gas surface free energy which can be also viewed as its surface tension. The generation of interfaces can be eased by dissolving in the liquid molecules called surfactants, often constituted with a polar head and a long non polar tail. Thanks to their amphiphilic nature, they spontaneously adsorb at the interfaces and reduce their surface tension.

Many methods exist to create a foam, but they can be classified into two categories: techniques where freely floating bubbles are created in a liquid, and techniques involving topological changes to divide a gas volume into bubbles [2]. Structural properties such as the liquid volume fraction ϕ, defined as the ratio of the volume of liquid to the total volume of foam, or the average bubble size are in many instances desired to be controlled.

1.1.1.1 Nucleation

The first category includes all the mechanisms of chemical and biological nature: the gaseous phase is the product of a chemical reaction involving species dissolved in the liquid. It can be either externally stimulated (as in *electrolysis*) or it can be due to the activity of microorganisms (*yeasting*). Alternatively, it can be induced by a liquid-gas phase transition. In a 1-phase system, the transition can be achieved if the liquid's vapor pressure overcomes its static pressure, by imposing a temperature increase which raises the former (*boiling*) or a pressure drop which decreases the latter (*cavitation*). In a 2-phases system, like a gas dissolved inside a supersaturated liquid, or like an emulsion with a volatile dispersed phase, a sudden depressurization can induce the fast nucleation of the dissolved phase. This technique is employed in aerosol foams [3]: the foaming solution is kept pressurized in a can together with a propellant vapor; when the nozzle of the spray head opens, the propellant pushes the fluid through a tube and inside the external air, which has a pressure lower than the can and induces the phase transition in the fluid.

1.1.1.2 Creation of interfaces

The second category includes only physical methods: either or both the gaseous and liquid phases are active and provide the mechanical work necessary to form the liquid/gas interfaces. Here is a non-exhaustive list of methods:

- *Bubbling* [4]: gas is injected at a constant flow rate through one or several nozzles immersed in the liquid phase. Initially, the gas accumulates pressure to overcome the capillary forces at the nozzle opening. Once this threshold is surpassed, the bubble begins to expand into the liquid. The bubble detaches from the nozzle when the capillary pressure anchoring it equals the upward force due to buoyancy or any external flow forces. For instance, if the nozzle is vertically aligned, bubbles rise to the liquid surface due to buoyancy. Another common configuration, widely encountered in microfluidic techniques, is co-flow, where the liquid flows in the same direction as the gas, and the viscous drag of the liquid aids bubble detachment. In both cases, the ratio of gas to liquid flow rates governs the final foam's liquid content and bubble size.

- *Turbulent mixing* [5]: Here, both the gas and liquid phases are injected simultaneously at high speeds through a nozzle. The turbulence generated by the collision of the two jets creates intense mixing, resulting in foam formation. As with bubbling, the gas-to-liquid flow rate ratio controls the liquid fraction and bubble size in the resulting foam.

- *Shear mixing*: This method includes techniques like whipping, shaking, or using kitchen blenders. The process involves first gas entrainment into the liquid, followed by bubble breakup due to the high shear forces generated by rapid mixing [6]. The resulting bubble size and liquid fraction depends on the speed of mixing and the viscosity of the continuous phase.

- *Double syringe method* [7]: liquid and gas are mixed by alternately pushing them between two connected syringes. Each passage from one syringe to the other generates new liquid/gas interfaces, leading to foam formation. The liquid fraction is controlled by the respective amounts of gas and liquid introduced in each syringe. The bubble size is controlled by the size of the smallest constriction which the flow encounters. The simplicity and control of this method make it useful for small-scale applications (like in varicose veins sclerotherapy for instance) or model lab experiments.

Now, let us present the equilibrium properties of foam structure.

1.1.2 Foam equilibrium properties

Foams are complex systems with characteristic length spanning a wide range of scales, as illustrated in Fig. 1.1. At the macroscopic scale, Fig. 1.1(a) shows the entire foam, which can range from millimeters to meters in size. A so-called wet foam appears at the bottom, with a large liquid content, while the upper part of the foam is dry, characterized by thin liquid films separating the gas bubbles. Moving down to smaller scales, Fig. 1.1(b) reveals individual bubbles in a dry section of the foam, typically ranging from 10^{-4} to 10^{-2} m in diameter. The packing of the bubbles and their interaction with the surrounding liquid governs the physical properties of the foam, such as its stability and its mechanical rigidity.

At even smaller scales, Fig. 1.1(c) highlights an edge i.e. a liquid-filled channel where films meet. In dry foams, they are called Plateau borders. These edges, usually between 10^{-6} and 10^{-4} m in length, play a crucial role in foam drainage and stability. The liquid content in the Plateau borders governs the overall wetness of the foam and contributes to the capillary forces that sustain the structure.

Finally, at the molecular level, Fig. 1.1(d) shows the gas/liquid interface, where surfactant molecules are adsorbed. These molecules, with length typically on the order of a few nm have hydrophilic heads in the liquid phase and hydrophobic tails extending into the gas phase. Surfactant adsorption at the interfaces reduces the surface tension, and create interfacial stresses that stabilize the foam.

The hierarchical structure of foams, spanning from molecular size to the bubble packing, confers them macroscopic properties arising from the coupling between processes at these different length-scales.

1.1.2.1 Foam structure

Foam structure depends on three key parameters: the characteristic bubble size and polydispersity of the bubble packing, the liquid fraction ϕ and the structural order, as illustrated in Fig. 1.2. To quantify the bubble size variability in polydisperse dispersions,

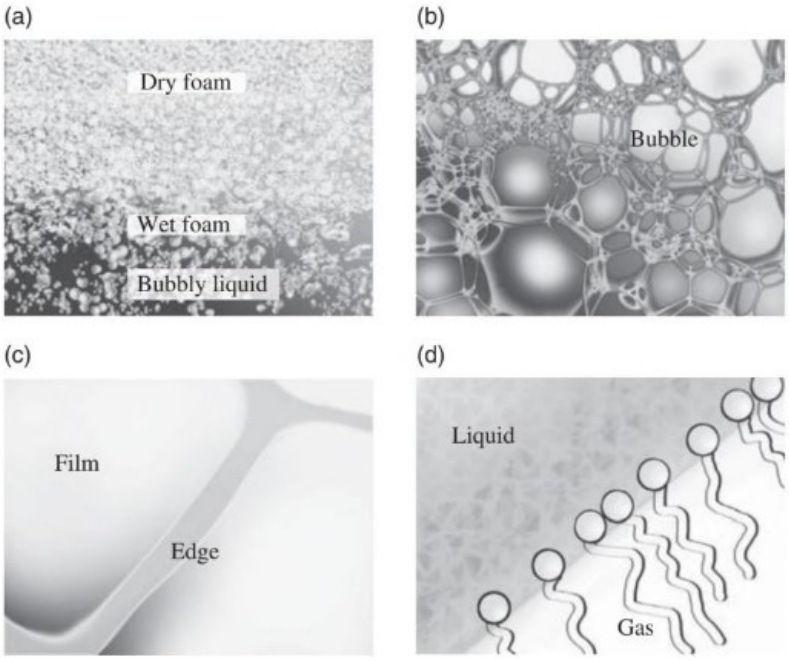

Figure 1.1: Foam structure at different length scales. (a) foam at the macroscopic scale, appearing wet at the bottom and dry at the top, typical scale $\sim$ 1cm $-$1 m. (b) Bubbles, $\sim$ 1μm - 1 cm. (c) Edge (liquid channel at the junction between films) length, $\sim$ 1μ m - 1 mm. (d) Gas/liquid interface with adsorbed surfactant molecules with hydrophobic tails (in the gas phase) and hydrophilic heads (in the liquid phase) $\sim$ 1nm. Image from [1].

different moments of the bubble size distributions are often used. For instance, the mean bubble radius can be characterized by the number (arythmetic) average radius $\overline{R}$ or the Sauter mean radius R_{32}, defined as:

$$R_{32} = \frac{\langle R^3 \rangle}{\langle R^2 \rangle} \tag{1.2}$$

where the brackets denote average over the ensemble of bubbles. This radius is particularly useful as it captures the average volume-to-surface ratio of the foam, a critical factor in understanding foam stability and gas exchange processes. The Sauter radius is sensitive to the presence of larger bubbles,and for bubble size distribution typically encountered in foams, we have $R_{32} > \overline{R}$.

The packing polydispersity can be characterized by the parameter p introduced by Kraynik [8]:

$$p_{32} = \frac{R_{32}}{\langle R^3 \rangle^{1/3}} - 1. \tag{1.3}$$

High polydispersity indicates a foam where bubbles span a broad range of sizes, while low polydispersity characterizes foams where the bubbles are more uniform in size. When all bubbles are nearly the same size ($p = 0$), the foam is referred to as *monodisperse*.

Based on their liquid volume fraction ϕ, bubble dispersions can be classified into three distinct regimes, each with unique structural and dynamic characteristics [1]:

- **Dry foam** ($0 \leq \phi \lesssim 0.05$): bubbles have a polyhedral shape. The liquid is confined to thin slender channels, so-called Plateau borders, located at the edges where polyhedral faces meet 3 by 3, with 120 degrees between them, according to Plateau's

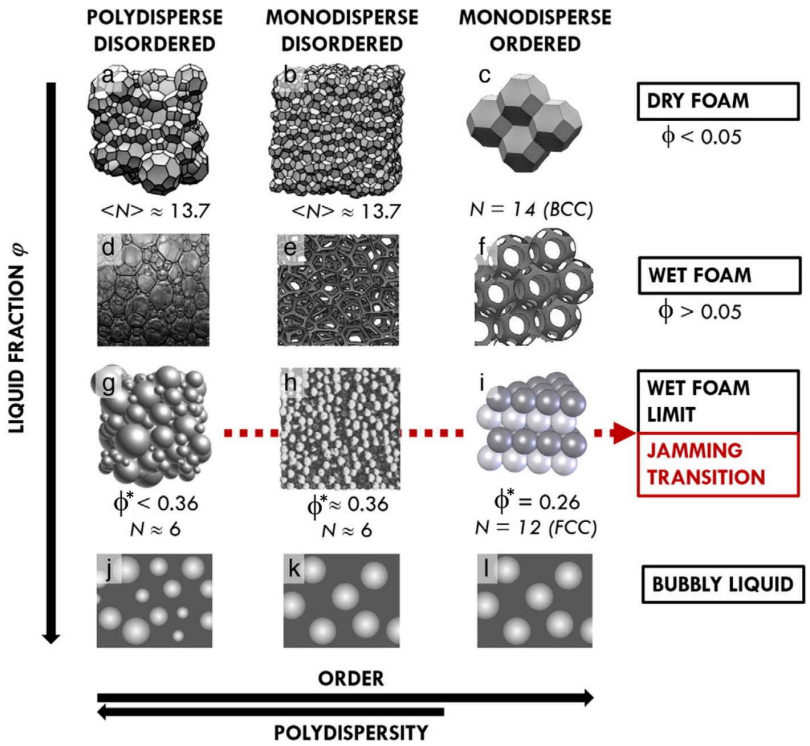

Figure 1.2: Different foam structures as a function of the structural parameters: liquid fraction ϕ, polydispersity and order/disorder. N denotes the number of neighbours of a bubble. Image adapted from [9].

laws [1]. The radius of curvature of a Plateau border scales with bubble radius and liquid fraction [1];

$$r_{PB} \approx \frac{R}{\sqrt{3\phi}}. \tag{1.4}$$

Most of the bubble surface is occupied by the films shared with its neighbours.

- **Wet foam** ($0.05 \lesssim \phi \lesssim \phi^*$): as the liquid fraction increases, the bubbles shape progressively evolves from polyhedral to spherical. The area of the contact films decreases. At the jamming transition $\phi = \phi^*$, the bubbles are spherical, and the contacts between them are point-like, and the film surface area vanishes.

- **Bubbly liquid** ($\phi^* \lesssim \phi \leq 1$): the bubbles are spherical and form a suspension dispersed in the continuous liquid phase. They do not share contacts with each other, unless the surfactant determines an adhesive force between the bubbles. As the liquid fraction increases, the average distance between bubbles grows.

Both structural order and polydispersity play a role in determining the jamming transition, ϕ^*, which sets the limit below which the packing exhibits solid-like behaviour. ϕ^* corresponds to the close packing fraction of hard spheres with characteristics similar to those of the bubbles in the foam. In ordered foams, with a face-centered cubic (FCC) structure, the jamming transition occurs at $\phi^* = \phi_{FCC} \approx 0.26$. In disordered, monodisperse foams, the random close packing fraction $\phi^* = \phi_{rcp} \approx 0.36$ is larger. In disordered polydisperse foams, small bubbles can occupy the interstitial spaces between large ones, reducing the value of the packing fraction ϕ_{rcp} compared to monodisperse disordered foams [10].

In the following, we present the characteristic pressures of foams at equilibrium.

1.1.2.2 Pressure in foams

The Young-Laplace law relates the pressure difference ΔP across a curved liquid/gas interface to its mean curvature and its surface tension:

$$\Delta P = \gamma \left(\frac{1}{R_i} + \frac{1}{R_j} \right) \tag{1.5}$$

where R_i and R_j are the principal radii of curvature.

The equilibrium structure of a foam results from the minimization of its surface free energy density, which can be achieved by minimizing the surface area density. Since a dry foam has a higher surface energy density than a wet foam, it will tend to suck the liquid from a connected reservoir [1]. The corresponding foam *osmotic pressure* is defined as the difference between the average pressure within the foam, P, and the pressure of the continuous liquid phase, P_w: $\Pi \equiv P - P_w$. This pressure can be seen as a confinement pressure applied to the entire set of bubbles (using a membrane permeable only to the liquid) to extract the liquid and thus impose the liquid fraction phi within the foam. As it accounts for the repulsive forces at contacts between the bubbles, it is a decreasing function of the liquid fraction ϕ, and it vanishes at ϕ^*. The dependency of the osmotic pressure Π with the liquid fraction is predicted by a semi-empirical relation [11, 12]. For a polydisperse disordered foam, the dimensionless osmotic pressure $\tilde{\Pi}$ writes*:

$$\tilde{\Pi} \equiv \Pi/(\gamma/R) = \frac{k(\phi - \phi_{\mathrm{rcp}})^2}{\sqrt{\phi}} \tag{1.6}$$

where the coefficient k, like ϕ_{rcp}, is a function of the polydispersity of the foam [13]:

$$k(\phi_{rcp}) = \frac{0.3}{(3 - \phi_{rcp})\sqrt{\phi_{rcp}} + (\phi_{rcp} - 1)(3 + \phi_{rcp}) arctanh(\sqrt{\phi_{rcp}})} \tag{1.7}$$

For a disordered assembly of monodisperse bubbles $k = 3.2$.

The pressure difference between the gas $\bar{p}$ and the liquid P_w is called *capillary pressure* $\Pi_c = \bar{p} - P_w$. It is related to the osmotic pressure [14]:

$$\tilde{\Pi_c} \equiv \Pi_c/(\gamma/R) = 2 + \frac{\tilde{\Pi}}{1 - \phi}. \tag{1.8}$$

As ϕ decreases towards the dry foam regime, the Plateau borders become narrower, leading to higher capillary pressures. Conversely, in bubbly liquids ($\phi > \phi_{rcp}$), one gets the capillary pressure corresponding to spherical bubbles, i.e. $2\gamma/R$.

In the films, the opposite interfaces stabilized by adsorbed surfactants interact with each other, generating a *disjoining pressure*, Π_d, which resists the collapse of the film and is a function of the film thickness h. According to DLVO theory, Π_d results from three contributions: van der Waals attraction; electrostatic repulsion for charged surfactant molecules; steric repulsion. A film can assume only the values of h corresponding to negative $d\Pi_d/dh$, allowing stable films only in certain ranges of h: $h \gtrsim 20\ nm$ for the so-called *Common black films*; $h \sim 4\ nm$ for the so-called *Newton black films*, where the film does not contain any liquid. This is illustrated in Fig. 1.3(left). The disjoining pressure can be measured on a film hold on a porous ring with with imposed liquid depression, as shown in Fig. 1.3(right) for different surfactants. In a foam, while the disjoining pressure works against film thinning, the capillary pressure acts to suck the liquid from the films towards the Plateau borders. Since the balance between disjoining pressure and capillary pressure sets the equilibrium film thickness, we may expect variations of the equilibrium film thickness with the liquid fraction and the bubble size.

*for a monodisperse ordered foam, $R_{32} = R$, and ϕ_{rcp} becomes ϕ_{FCC}, $k = 7.3$

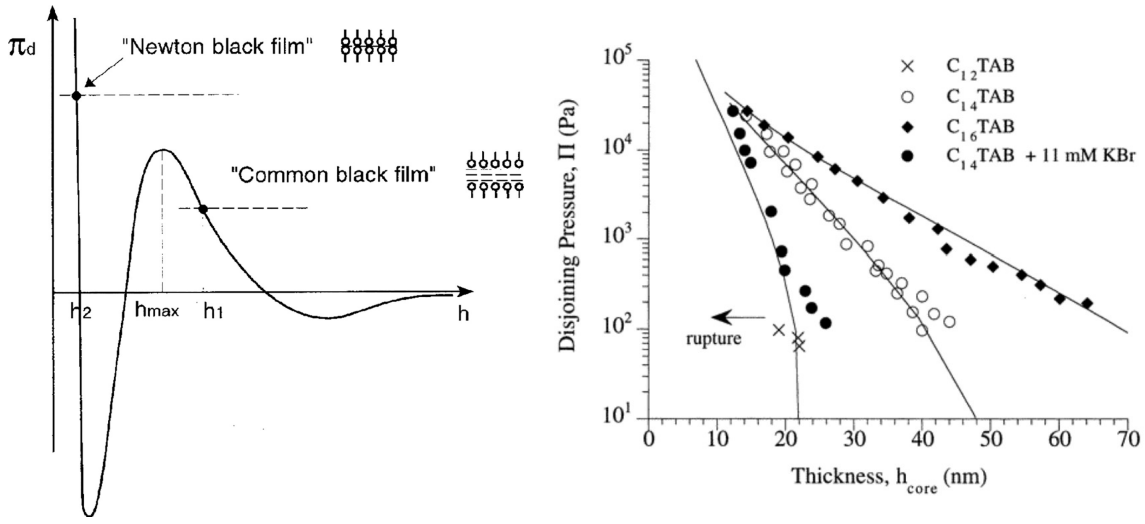

Figure 1.3: (left) Schematic representation of the variation of the disjoining pressure Π_d with film thickness h, including contributions of van der Waals attraction and electrostatic and short-range repulsions. The horizontal dashed lines correspond to different applied pressures ΔP and the intersections with the curve give the equilibrium thicknesses. Image from [15]. (right) Disjoining pressure measured for alkyltrimethylammonium bromide common black films. The surfactant concentration is equal to the salt-free cmc, and the continuous line represents DLVO prediction. Image from [16].

1.1.3 Foam drainage

Drainage usually refers to the gravitational flow of liquid, which is denser than the air in the bubbles, toward the bottom of the foam. This process progressively reduces the liquid fraction ϕ, inducing an inhomogeneous transition from wet to dry foam, and significantly affecting both the foam's stability and lifespan. As the liquid fraction decreases, the foam becomes increasingly fragile, with its mechanical properties changing accordingly.

In a foam at hydrostatic equilibrium, the pressure in the liquid phase follows the relation $P_w(z) = P_w(0) - \rho_w g z$, where ρ_w is the liquid density and z represents the vertical height, with $z = 0$ defined at the bottom of the foam. At this point, the bubbles are spherical, and the air fraction corresponds to the random close packing fraction, ϕ_{rcp}. However, when the foam is not in hydrostatic equilibrium, liquid flows between the bubbles in a manner analogous to fluid flow in a porous medium with porosity ϕ. The average liquid velocity through a foam column can be modeled using Darcy's law, which describes the fluid flow through porous media:

$$u = \frac{K\rho g}{\eta} \tag{1.9}$$

where η represents the dynamic viscosity of the liquid, and K denotes the foam permeability. The foam permeability is a critical parameter, as it captures the ease with which liquid can flow through the foam and depends strongly on the properties of the interfaces.

For foams and emulsions with rigid interfaces, where the dispersed phase behaves similarly to hard spheres, the system's permeability is constrained, and the Carman–Kozeny law holds for K for the complete range of liquid fractions ϕ [17]:

$$K = \frac{R_{32}^2 \phi^2}{312(1 - 2.15\phi + 1.37\phi^2)^2}. \tag{1.10}$$

In this case, R_{32} is the Sauter mean radius, and ϕ represents the liquid fraction. The expression reflects how the permeability diminishes as the foam becomes more concentrated. Conversely, in systems with mobile interfaces, the permeability is enhanced due

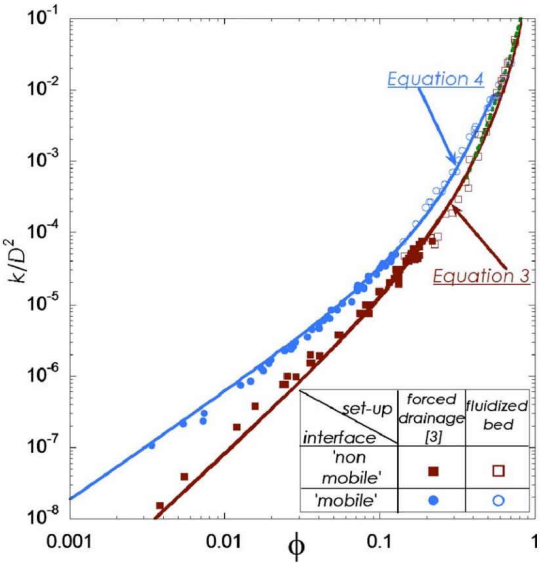

Figure 1.4: Permeability of monodisperse bubble dispersions as a function of liquid fraction. Experimental data are compared with the permeability calculated from Carman–Kozeny law, Eq. 1.10, and to Eq. 1.11. Image from [17].

to the greater fluidity at the boundaries between the liquid and gas phases. This is typical in foams with less rigid films or highly dynamic interfaces, where the permeability follows [17]:

$$K = \frac{R_{32}^2 \phi^{3/2}}{425(1 - 2.7\phi + 2.2\phi^2)^2}. \tag{1.11}$$

1.2 Coarsening theory

Two-phase separation is a ubiquitous phenomenon in material processing and aging, whenever a system tends to minimize its interfacial energy. This mechanism is driven by the difference in the Laplace pressure of the dispersed domains (cf. Eq. 1.5): larger ones are under a smaller pressure than the small ones, and absorb gas at their expense.Thus, larger and larger entities form thanks to the dissolution of the smaller ones, a process known as coarsening or Ostwald ripening. The kinetics of coarsening are crucial because they determine the evolving microstructure of the material, their average domain size and size distribution. As such, coarsening has been extensively studied across various fields.

For example, the coarsening of metallic alloys has been a classic topic of investigation [18], but the phenomenon also plays a pivotal role in processes like protein crystallization, chiral separations, and even protein compartmentalization within cells [19]. The seminal theoretical model due to Lifshitz, Slyozov [20], and Wagner [21] (LSW model) provides the foundation for predicting domain growth in the limit of their infinite dilution. While LSW theory is most accurate for systems where the continuous phase dominates, many real-world applications deviate from this limit, making the study of coarsening in a wider range of volume fractions critical for applications across materials science, colloidal systems, and biology.

We first present a summary of the original theory for the dilute limit [22, 23]. Then, we show how the model has been extended by Ardell[24] to the bubbly regime with finite liquid volume fraction ϕ, in order to take into account the finite spatial extension of the concentration of the dissolved species in the medium surrounding the bubbles. Finally, we discuss the case of a jammed system, like a foam or a concentrated emulsion, where gas exchanges happen directly across the contact films with a given thickness.

1.2.1 Ostwald ripening

Let us consider a dilute ensemble of gas bubbles dispersed in a liquid medium at rest, with an average inter-bubble distance d much larger than the average bubble size $\overline{R}$: $R/d \to 0$. The bubbles are assumed to be suspended without gravitational effects, in absence of chemical reactions and in isothermal conditions. In this system the bubbles exchange gas with the liquid phase around them, with a characteristic time $t_{dissolution}$, and this gas diffuses around each bubble with a characteristic time $t_{diffusion}$. If we focus on a bubble of radius R, the gas concentration field $c(r,t)$ around it has spherical symmetry, and depends only on the radial distance r from the bubble center and the time t. It is solution of Fick's second law of diffusion: $\partial c/\partial t = D\Delta c$, where D is the diffusion coefficient of the gas in the medium. In the limit of fast dissolution $t_{dissolution} \ll t_{diffusion}$, and assuming thatconvective transport of the dissolved gas is negligible, the bubble evolution can be considered as a steady diffusion problem : $\partial c/\partial t = 0$. The gas concentration is at each instant equal to that around a bubble of fixed radius. This assumption will be valid for the gas we consider here (air) which has a relatively solubility in water [23]. The steady radial profile of the gas concentration around the bubble then writes:

$$c(r) = c_\infty + (c(R) - c_\infty)\,\frac{R}{r} \tag{1.12}$$

where c_∞ is the concentration of gas at infinite distance from the bubble surface. The concentration at the bubble surface sets a time-dependent boundary condition. Fick's first law of diffusion sets the inward gas volume flux across the bubble surface:

$$J \equiv \frac{1}{4\pi R^2}\frac{1}{v_m}\frac{dV}{dt} = D\nabla c|_{r=R} \tag{1.13}$$

where v_m is the ideal gas molar volume, and $V \equiv 4/3\pi R^3$ is the bubble volume. Using Eqs. 1.12 and 1.13 we deduce the rate of radius variation:

$$\frac{dR}{dt} = D v_m \frac{c_\infty - c(R)}{R}. \tag{1.14}$$

The concentration at the bubble surface $c(R)$ is in equilibrium with the gas pressure $\bar{p}$ inside the bubble:

$$c(R) = H_e \bar{p} \tag{1.15}$$

where H_e is the Henry's law constant. We rewrite Eq. 1.14 using Eq. 1.15:

$$\frac{dR}{dt} = \frac{D H_e v_m}{R}\left(\frac{c_\infty}{H_e} - \bar{p}(R)\right). \tag{1.16}$$

The bubble gas pressure is itself set by Laplace law (cf. Eq. 1.5):

$$\bar{p}(R) = P_0 + \frac{2\gamma}{R} \tag{1.17}$$

where P_0 is the reference hydrostatic pressure, and γ the surface tension. We substitute it in Eq. 1.16 and collect the constant terms:

$$\frac{dR}{dt} = \frac{2\gamma D H_e v_m}{R}\left(\frac{sP_0}{2\gamma} - \frac{1}{R}\right). \tag{1.18}$$

where $s = \frac{c_\infty - c_0}{c_0}$ is the saturation parameter, with $c_0 = H\ P_0$. For $s < 0$ (understuration) the bubble can only loose gas and collapse; if instead $s > 0$ (oversaturation), there is an unique critical radius

$$R_c = \frac{2\gamma}{sP_0} \tag{1.19}$$

which characterizes a bubble in equilibrium with the surrounding liquid. As a consequence, bubbles with $R > R_c$ can only grow, and bubbles with $R < R_c$ can only shrink.

The dependency of dR/dt with the rescaled radius R/R_c can be treated in the mean-field approximation, imposing two requirements: the total volume of gas in the medium is conserved; the system satisfies a continuity equation of the form:

$$\frac{\partial g}{\partial t} + \frac{\partial (g\dot{R})}{\partial R} = 0 \tag{1.20}$$

where $g(R,t)$ is the bubble size distribution. The asymptotic solution given in LSW yields three predictions:

- the presence of a scaling state, where all the moments of distribution follow the same scaling with time $g(R,t) = \overline{R}(t)\ g(R/\overline{R})$;
- a critical radius for ripening equal to the average radius $R_c = \overline{R}$;
- a maximum radius size admitted by the distribution $g(R/\overline{R})$: $R_m/\overline{R} = 1.5$.

It follows that Eq. 1.18 becomes:

$$\frac{dR}{dt} = \frac{2\gamma D H_e v_m}{R^2}\left(\frac{R}{\overline{R}} - 1\right). \tag{1.21}$$

In the scaling state, the average growth rate of the bubble dispersion is set by the ripening rate of the maximum radius size R_m. For $R = R_m = 1.5\overline{R}$, Eq. 1.21 gives:

$$3\overline{R}^2 \frac{d\overline{R}}{dt} = \frac{8}{9}\gamma D H_e v_m. \tag{1.22}$$

By integration, we determine the growth law of the average radius in the scaling state:

$$\overline{R}^3 - \overline{R_0}^3 = K_0(t - t_0) \tag{1.23}$$

where K_0 is the coarsening rate in the dilute limit:

$$K_0 = \frac{8}{9}\gamma D H_e v_m. \tag{1.24}$$

1.2.2 Beyond the dilute limit

Over the years, following the Lifshitz-Slyozov-Wagner (LSW) model, which addresses bubble ripening in the dilute limit, a series of models have emerged to account for the effects of a finite liquid fraction ϕ [25]. Each of these models builds upon the foundational principles established by LSW, yet they diverge in how they incorporate the influence of the finite distance between bubbles, on the solute concentration gradients surrounding each bubble, and the method of resolution for the diffusion problem. In the LSW model, the infinite dilution assumption simplifies the treatment of bubble interactions, as bubbles are assumed to be sufficiently far apart to neglect any overlap in concentration fields (cf. Eq. 1.12). However, as ϕ increases, this assumption no longer holds, and the concentration gradient near one bubble can be significantly perturbed by the presence of nearby bubbles. Thus, the need arises for more sophisticated models that account for a gradient developing over some finite distance R':

$$\left.\frac{dc}{dr}\right|_{r=R} = \frac{c(R') - c(R)}{R(1 - R/R')} \tag{1.25}$$

We present here the mean field model proposed by Ardell, which has been a reference for successive mean-field theories, and it is instructive to observe the differences with the LSW theory.

In the modified LSW (MLSW) model [24], the average solute concentration in the continuous phase is set on the surface of an 'influence sphere', centered around each bubble, with a radius R' dependent on the inter-bubble distance l':

$$\overline{R'} \equiv 2\overline{R} + l' = 2\overline{R}(1 + \frac{1}{\beta(\phi)}) \tag{1.26}$$

where the second term represents the average distance between neighboring bubbles, by assuming that the bubbles are monodisperse and randomly distributed throughout the continuous phase. $\beta(\phi)$ is an decreasing function of the liquid fraction, and it vanishes for dilute systems $\beta(1) = 0$. It writes:

$$\beta = \frac{6(1-\Phi)^{1/3}}{e^{8(1-\Phi)}\Gamma(\phi)} \tag{1.27}$$

where $\Gamma(\phi)$ is a modification of the Gamma function $\Gamma(\frac{1}{3})$:

$$\Gamma(\phi) = \int_{8(1-\Phi)}^{\infty} x^{-2/3} e^{-x} dx. \tag{1.28}$$

By combining Eqs. 1.14, 1.25 and 1.26 and following the passages described in LSW model, we get an expression for the individual ripening equivalent to Eq. 1.18:

$$\frac{dR}{dt} = \frac{2\gamma D H_e v_m}{R} \left(\frac{1}{R_c} - \frac{1}{R}\right) \left(1 + \beta \frac{R}{R_c}\right) \tag{1.29}$$

where R_c is the critical radius for equilibrium with the surrounding medium (cf. Eq. 1.19). The new factor is a direct consequence of the screening over shorted distances of the gradient of the solute concentration.

This diffusion problem is again solved through mean-field approximation, requiring the solute volume conservation and the continuity of the bubble size distribution $g(R,t)$ (cf. Eq. 1.20). Like in LSW model, a scaling state is predicted, but the bubble size distribution $g(R/\overline{R}, \phi)$ exhibits a shape dependent on ϕ, as shown in Fig. 1.5(left). As ϕ decreases, the distribution spreads up to larger values of $R_m/\overline{R}$, flattening its peak. The critical radius R_c is no more equal to the average radius, but it becomes itself a function of $1-\phi$. Finally, the model predicts that the coarsening rate increases from the dilute value K_0, determined from the LSW model with Eq. 1.24, for decreasing liquid fractions ϕ:

$$\Omega_c(\phi) = C_3 K_0 f_3(\phi) \tag{1.30}$$

where C_3 is a constant depending on the type of the average performed for the radius ($C_3 = (\langle R \rangle / \overline{R})^3$), and $f_3(\phi)$ is a *coarsening enhancement factor*, which describes the relative variation of the coarsening rate with ϕ. We show the MLSW prediction of $f_3(\phi)$ as a function of the gas fraction $1-\phi$ in Fig. 1.5(right). The coarsening rate doubles for a 1% increase in the gas fraction, and then it varies almost linearly as the gas volume fraction increases.

Like MLSW, the other models for coarsening in bubbly liquids predict an evolution of the bubble size distribution and the coarsening rate with the gas fraction. Each model has its expression for β, $g(R/\overline{R}, \phi)$, $f_3(\phi)$; with differences dependent on the initial physical assumptions. There are comparisons between models and experiments [26], but they are limited to alloys; the gravity-induced instability of bubbly liquids has impeded the experimental study of coarsening, over times long enough to properly characterize the scaling state.

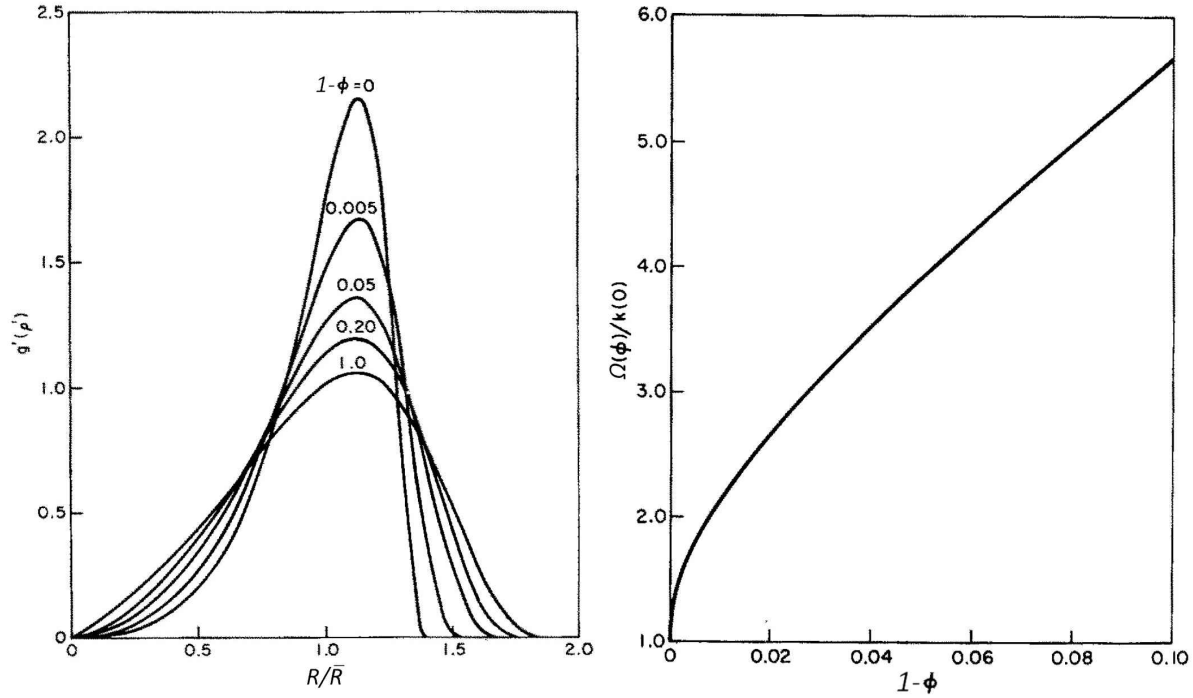

Figure 1.5: (left) Theoretical distribution of particle sizes as a function of the relative radius $R/\overline{R}$, for multiple gas volume fraction $1-\phi$, as predicted by MLSW theory [24]. The distribution in the dilute limit corresponds to the one predicted by the LSW model [20]. (right) Coarsening rate $\Omega_c(1-\phi)$ normalized by the rate predicted by LSW model (cf. Eq. 1.24), as a function of the gas volume fraction $1-\phi$. Figures from [24].

1.2.3 Jammed systems

We present here the Lemlich mean-field model [27] for foam coarsening ($\phi < \phi^*$), clearly inspired by LSW model. The average gas concentration $\bar{c}$ in the liquid phase can be related to an equivalent Laplace pressure via Henry's law (cf.Eq. 1.15):

$$\frac{2\gamma}{\rho} = \frac{\bar{c}}{H_e} \tag{1.31}$$

where ρ is the radius of a *fictitious* spherical bubble. Thus, the pressure difference between any bubble of radius R and the liquid can be written as:

$$\Delta P = 2\gamma \left(\frac{1}{\rho} - \frac{1}{R}\right) \tag{1.32}$$

This pressure difference ΔP can be either positive or negative, depending on the relative sizes of ρ and R. The molar gas transfer rate from the liquid to a bubble writes:

$$\dot{m} \equiv 4\pi R^2 f_2(\phi)\kappa\Delta P \tag{1.33}$$

where m is the number of moles of gas in a bubble, κ represents the effective permeability for gas transfer, and where $f_2(\phi)$ is the fraction of bubble surface covered by films. Combining Eqs. 1.32 and 1.33 leads to:

$$\dot{m} = 8\pi\kappa\gamma f_2(\phi)\left(\frac{R^2}{\rho} - R\right). \tag{1.34}$$

Conservation of the total number of moles of gas in the foam along time implies $\sum \dot{m} = 0$, where the summation is over all n bubbles in the foam, and it leads to: (n is not so clear.

Could you introduce $n(R)$ the number of bubbles with radius R, and change accordingly in both equations below ?)

$$\sum n \left(\frac{R^2}{\rho} - R \right) = 0 \tag{1.35}$$

If ρ is an average value, common to all the bubbles at a given time, it follows that this radius is a moment of the distribution

$$\rho = \frac{\sum nR^2}{\sum nR} \equiv R_{21}. \tag{1.36}$$

Like in LSW theory (cf. Eq. 1.18), bubbles can grow if they present a radius larger than a critical radius, here identified by R_{21}, and shrink otherwise. By writing the number of gas moles in a bubble as $m = \frac{4\pi R^3}{3v_m}$ in Eq. 1.34, the individual ripening rate writes:

$$\frac{dR}{dt} = 2\gamma\kappa v_m f_2(\phi) \left(\frac{1}{R_{21}} - \frac{1}{R} \right). \tag{1.37}$$

In the asymptotic limit, Lemlich theory predicts a scaling state, with an average growth law described by:

$$\overline{R}^2 - \overline{R_0}^2 = \Omega_p (t - t_0) \tag{1.38}$$

where Ω_p is the growth rate in the *parabolic regime*:

$$\Omega_p = C_2 \, \Omega_0 \, f_2(\phi). \tag{1.39}$$

Here $C_2 = (R_{21}/\langle R \rangle)^2$ is a geometrical prefactor, and $\Omega_0 = \gamma\kappa v_m$ represents the coarsening rate of the average bubble size in the dry limit ($\phi \to 1$). We can express the effective permeability for diffusion across a film as $\kappa = DH_e/h_{eff}$, where H_e is the gas solubility, D the diffusivity in the liquid, and h_{eff} the effective thickness of the film; for thick films $h_{eff} = h$, for thinner ones the permeability of the monolayer may become a limiting factor to gas transfer, and $h_{eff} > h$ [28]. Thus, the explicit definition of the coarsening rate becomes:

$$\Omega_0 = \frac{\gamma D H_e v_m}{h_{eff}}. \tag{1.40}$$

This expression is expected to hold across the entire range of liquid fractions within the foam regime. Recent theoretical work derived $f_2(\phi)$ for arbitrary polydispersity and for liquid fractions up to the jamming point [14]:

$$f_2(\phi) = \frac{\tilde{\Pi}}{\tilde{\Pi} + 2(1 - \phi)}. \tag{1.41}$$

$\tilde{\Pi}$ is the normalized osmotic pressure, described by Eq. 1.6. In the dry limit $f_2(0) = 1$; it decreases for increasing liquid fractions up to the jamming transition, where it vanishes $f_2(\phi_{rcp}) = 0$.

1.3 Rheology

Foams and emulsions, are complex materials that exhibit a combination of elastic, plastic and viscous responses [29, 30]. In this discussion of the rheological properties, we will focus on the case of emulsions. Their properties will be expressed in terms of the *oil volume fraction* $\varphi = \frac{V_{oil}}{V_{liquid}}$.

1.3.1 Rheology of unjammed suspensions

Let's consider the case of emulsions below the jamming transition. The rheological behaviour of non-colloidal suspensions and emulsions can be well described by Newtonian constitutive law [31]:

$$\tau = \eta\dot{\varepsilon} \tag{1.42}$$

where τ is the shear stress, $\dot{\varepsilon}$ is the shear rate, and η is the shear viscosity. The viscosity of these suspensions is neither that of the continuous phase η_c, nor that of the dispersed phase η_d, but an intermediate value.

The viscosity of suspensions of solid particles is well captured by the Krieger-Dougherty model [32]. It predicts that the relative viscosity η_r, defined as the ratio between the viscosity of the suspension η to that of the continuous phase η_c, is given by the following empirical relation:

$$\eta_r = \left(1 - \frac{\varphi}{\varphi^*}\right)^{-2.5\varphi^*} \tag{1.43}$$

where φ is the volume fraction of the dispersed phase, and $\varphi^* = 0.634$ is the maximum packing fraction at which jamming occurs. At first order, this model reduces to Einsten model in the dilute limit $\eta_r = 1 + 2.5\varphi$, and it captures the rapid increase in viscosity as the system approaches the jamming transition, with the viscosity diverging as the volume fraction nears φ^*. In the case of emulsions, the finite value of the ratio $\lambda = \eta_d/\eta_c$ plays a role in the expression of the relative viscosity [33]:

$$\eta_r \left(\frac{2\eta_r + 5\lambda}{2 + 5\lambda}\right)^{1.5} = \left(1 - \frac{\varphi}{\varphi^*}\right)^{-2.5\varphi^*}. \tag{1.44}$$

It is straightforward to demonstrate that, in the limit of infinite λ, this equation reduces to Eq. 1.43, recovering the form for solid particle suspensions.

1.3.2 Rheology of jammed suspensions

In the following, we present the rheological behaviour of concentrated emulsions and foams. In this section, φ denotes the volume fraction of the dispersed phase: φ for emulsions, or $1 - \phi$ for foams. When emulsions are subjected to a small stress, they exhibit a solid-like elastic response with an elastic modulus G. For stresses larger than the yield stress τ_y, they start flowing with a shear-thinning response, well described by the Herschel-Bulkley law [34]:

$$\tau = G\varepsilon \qquad \tau < \tau_y \tag{1.45}$$

$$\tau = \tau_y + \kappa\dot{\varepsilon}^n \quad \tau \geq \tau_y \tag{1.46}$$

where κ is the material's consistency, and n is the power index, which for emulsions is $n = 1/2$ [34]. Fig. 1.6 shows experimental measurements of the real and imaginary parts of the shear modulus $G^*(\varepsilon)$ in the static and flowing regimes, in both foams and emulsions.

Both the elastic modulus G and the yield stress τ_y scale as the Laplace pressure γ/r_d of the oil droplets, and depend on the oil fraction. Experimentally, they are well described by the semi-empirical relations [1]:

$$G = \alpha\frac{\gamma}{r_d}\varphi(\varphi - \varphi^*) \tag{1.47}$$

$$\tau_y = \beta\frac{\gamma}{r_d}(\varphi - \varphi^*)^2. \tag{1.48}$$

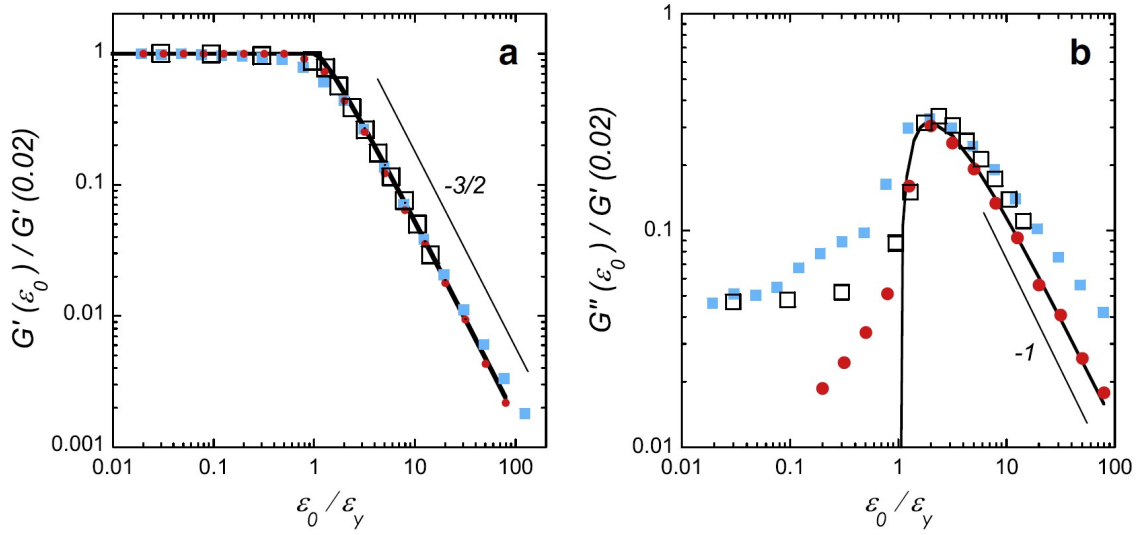

Figure 1.6: The real (a) and imaginary (b) parts of the strain amplitude dependent complex shear modulus $G^*(\varepsilon) = G'(\varepsilon) + i\ G"(\varepsilon)$, both normalized by $G'(0.02)$, are plotted versus the strain amplitude ε, normalized by the yield strain ε_y. The latter is determined as the intercept between the two asymptotic power laws that characterize the experimental $G'(\varepsilon)$ data at low and high strain amplitudes. $G^*(\varepsilon)$ is measured for: (blue square) an emulsion ($\varphi = 0.83$, $R = 2.4\mu m$, frequency 1 Hz); (red disk) an emulsion with smaller droplets ($\varphi = 0.80$, $R = 0.53\mu m$, frequency 0.16 Hz); (empty square) an aqueous foam ($\phi = 0.03$, $R = 25\mu m$, frequency 1 Hz). The full line is the prediction for the generic elastoplastic response described in the text, while the straight thin lines are guides to the eye, representing power laws with the indicated exponents. Figures from [30].

Experiments and simulations in highly concentrated emulsions $\varphi \sim 0.90$ have probed the flowing regime, and found a relation between the dimensionless viscous stress $\tilde{\tau_{vf}} \equiv (\tau - \tau_y)/(\gamma/r_d)$, the oil fraction, and the capillary number of the emulsion $Ca = \eta_c r_d \dot{\varepsilon}/\gamma$ [35]:

$$\tilde{\tau_{vf}} \approx 1.162 Ca^{0.47} \frac{\varphi^{5/6}(\varphi - \varphi^*)^{1/10}}{(1-\varphi)^{1/2}} \tag{1.49}$$

1.4 Foamed emulsions

Aerated materials play a crucial role in numerous industrial sectors due to their unique properties. In the construction industry, cement foam offers an illustrative case of how meticulous optimization is required to balance lightness with mechanical strength. Plaster foams, as another example, have found widespread application in various fields thanks to their excellent thermal and acoustic insulation capabilities. This duality of properties has generated growing interest in studying the characteristics of the precursory aerated yield stress-fluids.

In this context, we refer to a broader class of materials as *foamed emulsions*, defined as emulsions containing gas bubbles. To characterise the ratio of the volume of the phases, we will continue to use the oil volume fraction $\varphi = \frac{V_{oil}}{V_{liquid}}$ and the liquid volume fraction $\phi = \frac{V_{liquid}}{V_{tot}}$, where the liquid volume is the sum of the aqueous and oil volumes. When the liquid fraction is below the jamming transition $\phi < \phi^*$, the system is termed a *foamy emulsion*,whereas for liquid fractions greater than the jamming transition $\phi > \phi^*$, the material is called a *bubbly emulsion*.

In this section, we begin by exploring different methods to produce foamed emulsions.

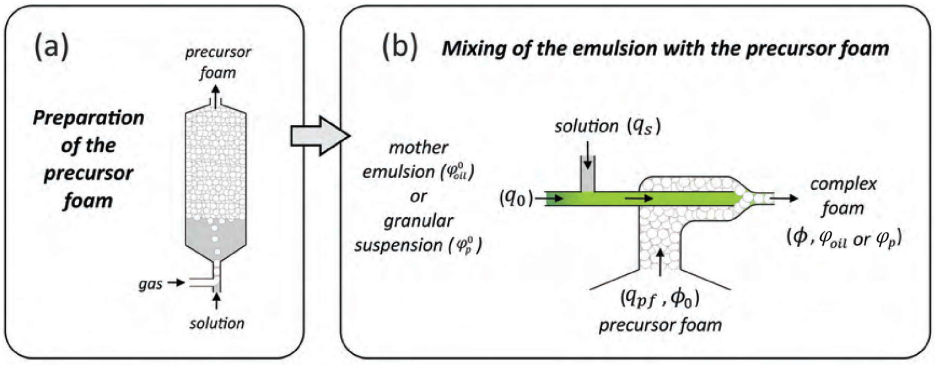

Figure 1.7: Elaboration of complex liquid foams. (a) Precursor aqueous foam is generated and stabilized in a glass column. (b) Then foam is pushed toward a device where it is mixed with concentrated emulsion or granular suspension. Note that the mixed emulsion results from the dilution of a mother emulsion with (foaming) solution. Controlling the entry flow rates allows tuning the volume fractions of constituents in the produced foam. Figure from [36].

Next, we examine how the rheological properties of these systems differ from those of simple emulsions and traditional foams. Specifically, we highlight how the inclusion of gas bubbles modifies the plasticity of the emulsion, and how the inclusion of oil droplets modifies the plasticity of the foam. We then address the enhanced stability of foamed emulsions, considering how the interaction between the dispersed gas and liquid phases contributes to prolonged lifespans compared to standard foams and bubbly liquids. Finally, as a reference for understanding the coarsening processes in these systems, we present a model that describes the ripening of an individual gas bubble within a yield stress fluid, outlining the key mechanisms that govern bubble growth and stability over time.

1.4.1 Production methods

The production of foamed emulsions requires the formation of stable interfaces for both the oil droplets and the gas bubbles. To ensure their compatibility, they must share the same continuous aqueous phase. In this process, it is required the control of the following parameters: the radius of the gas bubbles R, the radius of the oil droplets r_d, the liquid volume fraction ϕ, the oil volume fraction φ. The production methods can be divided into three groups:

- Mixing of foam and emulsion independently prepared [36]. As shown in Fig. 1.7, the foaming and the emulsification processes can be separately performed with the preferred methods, to obtain a dry precursor foam and a concentrated mother emulsion with set R and r_d. The two fluids can be mixed in coaxial flow, to obtain a foamed emulsion with a liquid fraction ϕ and oil fraction φ tuned according to the flow rates of the precursory fluids.

- Emulsion foaming [37]. An emulsion with set r_d and φ can be foamed using the techniques presented in Section 3.2. Turbulent mixing has been successfully employed for this scope, but the rheological properties of the emulsion restricts the range of ϕ which can be obtained.

- One-step preparation of foamed emulsions [38]. The three phases (gas, oil, aqueous) are mixed together with set volume fractions using the double syringe method,

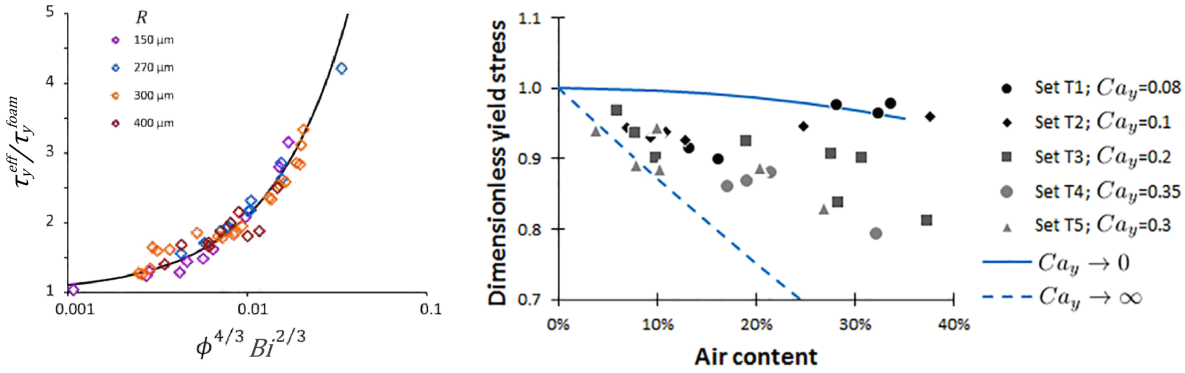

Figure 1.8: (left) Yield stress of foamy emulsions divided by the yield stress of the corresponding aqueous foam (i.e., same bubble size and same gas volume fraction, estimated by Eq. 1.48, as a function of the liquid fraction ϕ and the Bingham capillary number $Bi = \tau_y^{emulsion} R/\gamma$. Figure from [36]. (right) Yield stress of bubbly emulsions divided by the yield stress of the emulsion, for samples made with TTAB. Theoretical curves, which have been observed experimentally on model yield stress fluid by Ducloué [39], are indicated for non-deformable bubbles (full line) and fully deformable bubbles (dotted line). Figure from [40].

producing at the same time the gas bubbles and the oil droplets. It is a fast technique of simple execution, but it is limited in the range of R, r_d which can produce: for whatever combination of ϕ, φ the size ratio $R/r_d \approx 8$ is constant, with a minimum $r_d \gtrsim 2.5\mu m$, and a large polydispersity of the oil droplet sizes.

1.4.2 Rheological properties

Foams exhibit an intrinsic yield stress, as detailed in Section 1.3.2. By employing a yield stress fluid as the continuous phase, the overall stress response of the material can be significantly enhanced, as evidenced by detailed physical insights from Gorlier [36]. For foamy emulsions, an empirical law effectively captures the yield stress behavior of the medium:

$$\tau_y^{eff} = \tau_y^{foam}(1 + cBi^{2/3}\phi^{4/3}), \tag{1.50}$$

where τ_y^{foam} is given by Eq. 1.48, $c \approx 110$ is a fitted parameter, and $Bi = \tau_y^{emulsion} R/\gamma$ the Bingham capillary number. The model shows excellent agreement with experimental data in the liquid fraction range of $\phi \lesssim 0.25$ [36], as shown in Fig. 1.8(left).

In contrast, in bubbly emulsions, the yield stress of the continuous phase is reduced due to the inclusion of gas bubbles. The interfacial tension at the gas-liquid boundary results in the bubbles resisting deformation, thereby acting as soft elastic inclusions within the unyielded suspending emulsion. The overall elasticity of the suspension is influenced by the ratio of the emulsion's elastic modulus to the effective elasticity of the bubbles, governed by an elasto-capillary number, defined as the ratio between the emulsion's elastic modulus and the capillary stress scale associated with the bubbles' Laplace pressure:

$$Ca_{el} = \frac{G^{emulsion} R}{\gamma}. \tag{1.51}$$

For a suspension of bubbles with known radius in a given emulsion, Ca_{el} is fully determined, and the effective medium's elastic modulus, G^{eff}, becomes an increasing function of the liquid volume fraction ϕ, reaching $G^{eff}(1) = G^{emulsion}$ at $\phi = 1$. Micro-mechanical calculations provide an estimate in the semi-dilute limit ($\phi \gtrsim 0.50$) of the elastic modulus

ratio [41]:

$$\frac{G^{eff}}{G^{emulsion}} = 1 - \frac{5(1-\phi)(2Ca_{el}-1)}{5+6Ca_{el}+2(1-\phi)(2Ca_{el}-1)}. \tag{1.52}$$

This is derived using the Mori-Tanaka homogenization scheme. Furthermore, both experiments and simulations demonstrate that the yield stress of the effective medium correlates with its linear response function $g(\phi)$, representing the evolution of any linear property with ϕ. Identifying this linear response as $g(\phi) = G^{eff}(\phi)/G^{emulsion}$, the yield stress can be expressed as [39]:

$$\frac{\tau_y^{eff}(\phi)}{\tau_y} = \sqrt{\phi \frac{G^{eff}}{G^{emulsion}}(\phi, Ca_{el})}. \tag{1.53}$$

1.4.3 Arrested drainage

It is known by a long time that yield stress fluids are able to entrap air bubbles inside, opposing the bubble buoyancy with the plasticity of the surrounding medium. The interplay between the two stresses is measured by the Bingham gravitational number Y_g [42]:

$$Y_g = \frac{3}{2}\frac{\tau_y}{R\Delta\rho g} \tag{1.54}$$

where R is the bubble radius, $\Delta\rho$ is the density difference between the bubble and the surrounding medium, g is the gravitational acceleration. Recent simulations [43] compare well with previous experiments, and predicts that a bubble should be entrapped in a yield-stress fluid if its $Y_{gc} \geq 0.2 \pm 0.02$. This critical value sets the maximum radius for bubble entrapment in bubbly emulsions:

$$R_M^{bubble}(\tau_y) = \frac{3}{2}\frac{\tau_y}{Y_{gc}\Delta\rho g}. \tag{1.55}$$

In foamy emulsions, the stop of drainage has been experimentally observed [44]. It has been explained as the effect of a yield stress τ_y larger than the hydrostatic pressure in the Plateau borders:

$$\tau_d \sim \rho g r_{PB} \tag{1.56}$$

where ρ is the density of the continuous phase, g the gravitational acceleration and r_{PB} the radius of curvature of a Plateau border, which scales with the Sauter radius R_{32} and the liquid fraction ϕ (cf. Eq. 1.4). Thus, the arrest of drainage in foamy emulsions is expected for $\tau_y \geq \tau_d$ [45].

1.4.4 Model of a bubble ripening in a yield-stress fluid

In this section, we focus on the coupling involved when a bubble is caused to grow or shrink in a yield-stress fluid, as proposed by the model of Venerus [46, 47].

We consider an isolated gas bubble of initial radius R_0 surrounded by an infinite incompressible medium at rest. The bubble is assumed to be suspended without gravitational effects, in absence of chemical reactions and in isothermal conditions. We use the spherical coordinates (r, θ, ϕ), with the origin at the center of the bubble, to benefit of the spherical symmetry of the problem. The bubble changes its size with a radial velocity $\frac{dR}{dt} \ll v_{sound}$, and generates a purely radial velocity field in view of the spherical symmetry. From the mass conservation of the elastic medium we write the continuity equation:

$$\frac{\partial \rho}{\partial t} + \overline{\nabla}(\rho \overline{v}) = 0 \tag{1.57}$$

where ρ is the density of the medium and v its velocity. From the incompressibility of the medium we can neglect its spatial and temporal dependency. As discussed, the velocity field of the the medium is purely radial, and we can write:

$$\frac{\partial}{\partial r}(r^2 v_r) = 0 \rightarrow v_r = \frac{f(t)}{r^2} \tag{1.58}$$

where $f(t)$ is a function dependent only on time. To determine its value we impose at the bubble interface $v_r(R) = \frac{f(t)}{R^2} = \frac{dR}{dt}$, to finally determine:

$$v_r = \frac{dr}{dt} = \frac{R^2}{r^2}\frac{dR}{dt}. \tag{1.59}$$

We consider finite deformations and express the deformation gradient tensor $\underline{\underline{F}} = \frac{\partial \boldsymbol{r}}{\partial \boldsymbol{r_0}}$, which relates changes between material point positions at present $\boldsymbol{r}$ and past $\boldsymbol{r_0}$ times[†]. We now consider a material element at initial position $\boldsymbol{r_0}$, around a bubble of initial radius R_0. By separating variables in Eq. 1.59 and by integrating over time, we can write the new position of the element $\mathbf{r}$ when the bubble radius has changed to R:

$$r^3 = r_0^3 + R^3 - R_0^3 \tag{1.60}$$

which gives, by derivation, the radial deformation gradient:

$$F_{rr}(r) = \frac{\partial r}{\partial r_0} = \left(1 - \frac{R^3 - R_0^3}{r^3}\right)^{2/3}. \tag{1.61}$$

By symmetry, the deformation field is purely extensional and $\underline{\underline{F}}$ has only diagonal components:

$$\underline{\underline{F}} = \begin{pmatrix} F_{rr} & 0 & 0 \\ 0 & F_{rr}^{-1/2} & 0 \\ 0 & 0 & F_{rr}^{-1/2} \end{pmatrix}. \tag{1.62}$$

As proposed by Venerus [46], we describe the rheological behavior of the yield stress material using Oldroyd constitutive law[‡]:

$$\underline{\underline{\tau}} = \begin{cases} G[\underline{\underline{F}} \cdot \underline{\underline{F}}^T - \underline{\underline{I}}] & \text{for} \quad \sqrt{tr(\underline{\underline{\tau}} \cdot \underline{\underline{\tau}})} < \sqrt{2}\tau_y \\ \left[\eta \pm \tau_y / \sqrt{tr(\dot{\underline{\underline{\varepsilon}}} \cdot \dot{\underline{\underline{\varepsilon}}})/2}\right] \dot{\underline{\underline{\varepsilon}}} & \text{for} \quad \sqrt{tr(\underline{\underline{\tau}} \cdot \underline{\underline{\tau}})} \geq \sqrt{2}\tau_y \end{cases} \tag{1.63}$$

[†] we use here the notations from Macosko [48]

[‡] we have corrected a typo present in ref. [46] Eq. 16.

where G is the shear modulus of the material, τ_y its yield stress and η its viscosity. $\dot{\underline{\underline{\varepsilon}}} = (\nabla\overline{v} + \nabla\overline{v}^T)/2$ is the rate of strain tensor. When the medium flows, the positive (resp. negative) sign refers to the case of a growing (resp. shrinking) bubble. This law is a first approximation for the behaviour of Bingham plastics: it describes the linear elastic response of a neo-Hookean solid for small stresses up to the yield stress, and the viscoplastic shear-thinning liquid behaviour above. The separation between the two behaviours is set by *von Mises yielding criterion* [48]:

$$\sqrt{tr(\underline{\underline{\tau}} \cdot \underline{\underline{\tau}})} = \sqrt{2}\tau_y. \tag{1.64}$$

Later in the discussion we'll consider models which describes more accurately emulsions.

As illustrated in Fig. 1.9, there is a shell of yielded material in the vicinity of the bubble, which extends up to the distance S where von Mises criterion is satisfied. Beyond S, the material responds elastically. Using Eq. 1.63, we express the stress components in the yielded shell as:

$$\tau_{rr}(r) = -2\tau_{\theta\theta}(r) = \mp\frac{2}{\sqrt{3}}\tau_y - 4\eta\frac{R^2}{r^3}\frac{dR}{dt} \quad \text{for } R \leq r < S \tag{1.65}$$

and in the unyielded region as:

$$\begin{aligned}\tau_{rr}(r) &= G\left[\left(1 - \frac{R^3 - R_0^3}{r^3}\right)^{4/3} - 1\right] \\ \tau_{\theta\theta}(r) &= G\left[\left(1 - \frac{R^3 - R_0^3}{r^3}\right)^{-2/3} - 1\right] \quad \text{for } S \leq r \leq \infty\end{aligned} \tag{1.66}$$

where, in both cases, a negative (resp. positive) stress refers to the case of a growing (shrinking) bubble.

The external radius of the shell is determined by solving von Mises criterion (Eq. 1.64) with the stress given by Eq. 1.66, which gives:

$$\left[\left(1 - \frac{R^3 - R_0^3}{S^3}\right)^{4/3} - 1\right]^2 + 2\left[\left(1 - \frac{R^3 - R_0^3}{S^3}\right)^{-2/3} - 1\right]^2 = 2(\tau_y/G)^2. \tag{1.67}$$

Here we have taken into account the spherical symmetry of the system, which sets $\tau_{\theta\theta} = \tau_{\phi\phi}$. By rewriting it in terms of the *yield factor* defined as $Y = \frac{R^3 - R_0^3}{S^3}$ we obtain a single variable equation of the parameter $N_Y = \tau_y/G$:

$$[(1-Y)^{4/3} - 1]^2 + 2[(1-Y)^{-2/3} - 1]^2 = 2N_Y^2 \tag{1.68}$$

whose solutions are plotted in Figure 1.9(b). In the limit $N_Y \leq 0.2$ (in our emulsions $N_Y \leq 0.05$) the two branches corresponding to positive (resp. negative) Y for a growing (resp. shrinking) bubble superimpose in absolute value, and we find the linear scaling $|Y| = \frac{\sqrt{3}}{2}N_Y$. In this limit, the shell boundary S is simply determined by the relation:

$$S = \sqrt[3]{\frac{2}{\sqrt{3}}\frac{|R^3 - R_0^3|}{N_Y}}. \tag{1.69}$$

which predicts a large shell, extending for a distance $2-5$ times larger than $\sqrt[3]{|R^3 - R_0^3|}$ (as shown in Fig. 1.9(a)). This is true for the majority of bubble evolution, but at the very beginning the medium is all unyielded, and the shell radius coincides with the bubble

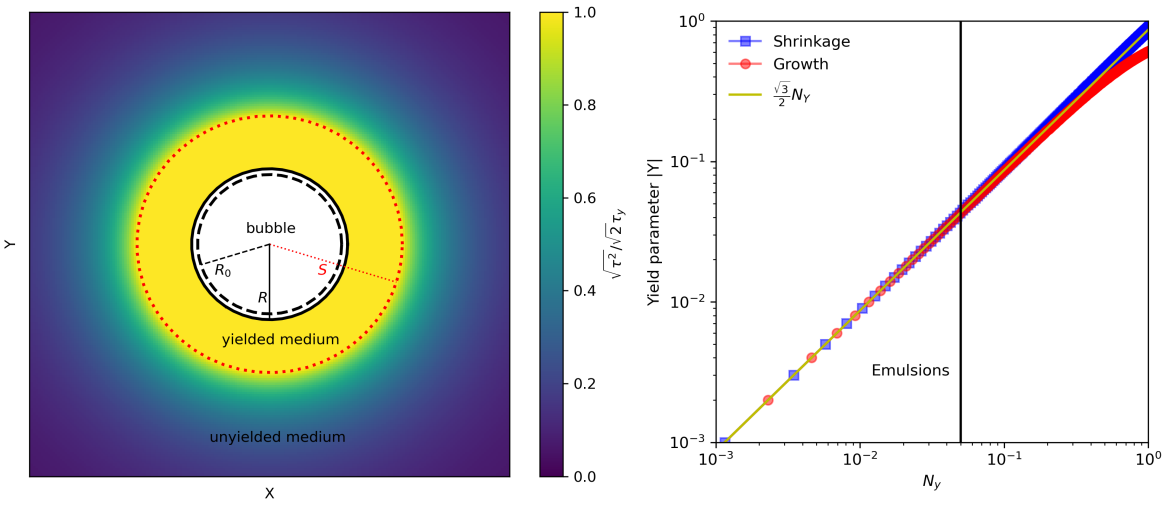

Figure 1.9: Medium yielding for an isolated bubble. (left) Normalized second invariant of the stress tensor (cf. Eq. 1.64) created around an inflating bubble in a yielding medium. The medium yields when it reaches unity, or responds elastically otherwise. The relevant radial distances R_0, R, S are labelled. (right) Solutions to Von Mises criterion for Y in function of N_Y, for the case of a shrinking (blue squares) or growing (red disks) bubble. In the range of N_Y compatible with emulsions the two branches superimpose, and follow the scaling $|Y| = \frac{\sqrt{3}}{2} N_Y$.

radius $S = R$. The transition between unyielded and yielded happens when the bubble reaches the threshold radius R_y, defined again by Von Mises criterion:

$$\left[\left(\frac{R_0}{R_y}\right)^4 - 1\right]^2 + 2\left[\left(\frac{R_0}{R_y}\right)^{-2} - 1\right]^2 = 2N_Y^2. \tag{1.70}$$

By comparing it to Eq. 1.68, we can equate $\frac{R_0}{R_y} = \sqrt[3]{1-Y}$ and recover the solution for the emulsion limit:

$$\frac{R_y}{R_0} = \left(1 \mp \frac{\sqrt{3}}{2} N_Y\right)^{-1/3} \rightarrow \left|\frac{R_y - R_0}{R_0}\right| \lesssim 1.5\% \tag{1.71}$$

With such a small difference between R_y and R_0 we can assume the bubbles to be surrounded by a shell of yielded medium. Elasticity is the sole contribution of the medium only in the limit of small deformations, otherwise the contribution of plasticity will be dominant.

We consider slow rate of bubble inflation or deflation (compared to the speed of sound) such that inertial forces can be neglected. In the absence of bulk forces, the equation of motion reduces to the stress balance of the total Cauchy stress tensor $\underline{\underline{T}} = \underline{\underline{\tau}} - p\underline{\underline{I}}$ as: $\boldsymbol{\nabla} \cdot \underline{\underline{T}} = 0$. The radial component yields:

$$\frac{\partial p}{\partial r} = \left[\frac{\partial \tau_{rr}}{\partial r} + 2\frac{\tau_{rr} - \tau_{\theta\theta}}{r}\right] \tag{1.72}$$

where p is the pressure in the incompressible medium. By integrating it over the domain $R \leq r < \infty$ we get:

$$p_0 - p(R) = 2\int_R^\infty \frac{\tau_{rr} - \tau_{\theta\theta}}{r} dr - \tau_{rr}(R) \tag{1.73}$$

where p_0 is the pressure at infinite distance from the bubble. At the bubble interface, the stress balance writes:

$$T_{rr}(R) \equiv \tau_{rr}(R) - p(R) = \frac{2\gamma}{R} - \overline{p} \tag{1.74}$$

where $\overline{p}$ is the pressure inside the bubble, and γ the surface tension.

By combining Eqs. 1.65, 1.66, 1.73 and 1.74 we get the pressure difference between the bubble and the liquid at infinity $\Delta p = \bar{p} - p_0$:

$$\Delta p = \frac{2\gamma}{R} \pm 2\sqrt{3}\tau_y \ln\left(\frac{S}{R}\right) + 4\frac{\eta}{R}\frac{dR}{dt}\left[1 - \left(\frac{R}{S}\right)^3\right] + \frac{G}{2}\left[5 - \left(1 - \frac{R^3 - R_0^3}{S^3}\right)^{1/3}\left(5 - \frac{R^3 - R_0^3}{S^3}\right)\right]. \tag{1.75}$$

At equilibrium conditions, an isolated bubble stops ripening if $\Delta p = 0$. Simulations predict this to happen for a shrinking bubble, if the medium offers a strong plastic response ($\gamma/R \ll \tau_y$) [46]. In this simple picture, the plasticity of the surrounding medium is able to win against capillarity, and eventually hinder coarsening. A more realistic description of the problem would need to account also for the presence of the neighbours, each growing or shrinking and straining the medium.

1.5 Open issues

Coarsening is a mechanism common to a wide variety of two-phase systems undergoing phase separation : solid precipitation in supersaturated solutions, alloys annealing, foams or emulsions for instance. In the 1960s, the seminal LSW meanfield theory [20, 21] predicted the particle growth in dilute dispersions in the limit of infinite dilution: After a transient time, the dispersion reaches a Scaling State where its normalized particle size distribution becomes time invariant and where the average particle radius grows with time following a cubic law. Since then many theoretical, numerical and experimental work has been devoted to predict and study the regime of finite dilution [25, 26].

For bubble dispersions, most of the experimental and numerical research has focused on foam coarsening well below the jamming transition ϕ^*. In the limit of dry or moderately wet foams, a scaling state where the average bubble radius increases following a parabolic growth is predicted [27, 49]. However studies of wet foam coarsening on ground are impeded by gravitational drainage [50]. Investigations are restricted to $\phi \lesssim 0.20$ and allow growth laws to be studied only on short coarsening duration [51]. For larger liquid fractions close to the jamming transition, the timescale of coarsening is too large with respect to that of drainage, and experiments require stabilizing the samples against drainage. Using stabilization by diamagnetic levitation, the growth laws for liquid fractions on both sides of the jamming transition was studied [52]; a progressive decrease of the growth law exponent from the parabolic to the cubic regime was reported as the foam becomes wet, but the liquid fraction was not well controlled. Moreover, none of these experiments were able to determine the bubble size distributions, and the existence of scaling state was not proved.

In so called adhesive emulsions, attractive forces between droplets tend to stick them to each other promoting contact areas larger than expected if the packing cohesion were solely due to capillary interactions [53]. It is known that the rheological properties of emulsions are strongly impacted by the adhesion, if only the jamming transition (at the onset of elastic behavior) is shifted to liquid fractions that can be significantly larger than ϕ_{rcp} [30, 54]. If adhesive forces were at play in foams, they should have an impact on their structure and their coarsening dynamics, but this effect is expected to become dominant only close to the jamming transition where osmotic pressure tend to vanish.

Thus, open questions remain about coarsening on both sides of the jamming transition: what are the bubble size growth laws of wet foams and of bubbly liquids? What are the bubble size distributions of these systems? Do they evolve toward a time-invariant characteristic shape? Do these systems reach a scaling state, after a transient time? How does the coarsening rate depend on the liquid fraction? Can inter-bubble adhesive forces shift the jamming transition like in emulsions and have an impact on the coarsening rate?

To tackle these issues, we perform coarsening experiments on foams stabilized against gravitational drainage, using two approaches: a clinostat cell with slow rotation speed, and eventually for the bubbly liquids we used an emulsion with a small yield stress to compensate the hydrostatic pressure. The results of these experiments are combined with the analysis of data from experiments in microgravity, using the Soft Matter Dynamic instrument in the ISS.

Foamed emulsions are innately stabilized against gravitational drainage provided that the yield stress of the the continuous phase is able to compensate the hydrostatic pressure, for both the foamy[45] and the bubbly [42] regime. When the continuous phase of a bubble dispersion is made of a yield stress fluid such as a concentrated emulsion, its coarsening is expected to be affected by the plastic stresses that can build up as bubbles grow or shrink and counteract the Laplace pressure which drives the coarsening. The natural dimensionless number that measures the relative contribution of plastic stress and capillary pressure exerted on bubbles is the Bingham number $Bi \equiv \tau_y R/\gamma$. A theoretical model of an isolated ripening bubble predicts that the plasticity of the surrounding material can arrest the bubble dissolution [46]. A recent experiment showed that coarsening of a dry foamy emulsion ($\phi \approx 0.10$) can be slowed down [55]: the growth law exhibits an effective exponent smaller than that predicted for simple foams 1/2, and the foam dynamics presents an increase in the characteristic timescale of bubble rearrangements. No modelization of the modified growth law is provided. Qualitatively, one can expect coarsening arrest to be reached when $Bi \sim 1$[45]. We found only one experimental observation of it [56], for a bubbly gelled system with a single liquid fraction ϕ.

Thus, open issues arise about the coarsening dynamics of bubbly emulsions ($\phi > \phi^*$) as well as foamy emulsions ($\phi < \phi^*$). How does the damping of the average bubble growth laws depend on the Bingham number and on the liquid fraction? Can the coarsening foamed emulsions reach a scaling state? Can coarsening be arrested? If so, how would the bubble size distributions be affected? Moreover, at the scale of the individual bubbles, what is the effect of plastic stresses on their ripening? Can their morphology be affected, as their shape may exhibit some remanence of the surrounding plastic stresses?

To address these questions, we propose an experimental approach, based on videomicroscopy observations of the structure of coarsening foamed emulsions, with controlled parameters Bi, ϕ. To analyse large quantities of images, we implemented an automatic object segmentation model based on machine learning. In the meantime, we establish the foamability diagram of emulsions, depending on the parameters ϕ, φ. Along with the clinostat cell we use an original setup that we call an osmotic cell, to reach large emulsion yield stress while circumventing the problem of foaming such high yield stress materials.

Chapter 2

Coarsening in aqueous wet foams

Contents

Many studies have described the interplay between coarsening and drainage [50, 57], others have tried to remove drainage by magnetic levitation [52]. In this chapter we describe a series of experiments performed in microgravity, on the International Space Station (ISS), to study the coarsening of wet foams in drainage-free conditions [13, 19, 58, 59]. Specifically, we present the analysis that we conducted on data of Mission 1, to elucidate the coarsening behaviour across the *jamming transition*, where bubbles in a foam loose the reciprocal contact and become bubbly liquids. We study the average bubble growth laws, the evolution of the coarsening rate with the liquid fraction. We unveil the natural bubble size distributions exhibited by coarsening wet foams and bubbly liquids, in the scaling state, and reveal their hierarchical structure.

2.1 Experimental details

Experiments conducted in microgravity, particularly aboard the International Space Station, are subject to stringent constraints. The samples must be hermetically sealed for the entire mission duration, which can range from several months to a year. During this time, the foaming solutions must remain chemically stable and must not interact with the sample holder. Additionally, all sample characterizations must be carried out without

removing the sample from its container, while allowing for the simultaneous execution of experiments across different research groups.

In the following, we provide detailed descriptions of the Soft Matter Dynamics container, which houses the experiments; the analysis methods and sample preparation protocols; and the tests that confirm surface observations via videomicroscopy are indeed representative of the foam's bulk state.

2.1.1 Soft Matter Dynamics experiment container

The experiment container is a sophisticated module designed for conducting scientific experiments aboard the International Space Station (ISS) within the Fluid Science Laboratory (FSL). It is integrated into a drawer, which is securely attached to the FSL rack using anti-vibration rubber interfaces. This design minimizes the impact of vibrations on the sensitive experiments, a critical factor in the microgravity environment of the ISS. Additionally, accelerometers are mounted on the drawer to monitor the microgravity levels, ensuring that the experiments are conducted under the required conditions. The container is also connected to the FSL through the Video Management Unit (VMU-2), which manages data and video communications, allowing for remote control and monitoring of the experiments.

Temperature control within the experiment container is achieved through a two-stage system. The entire sample cell carrier is housed inside an isothermal enclosure, which is connected to a water cooling loop provided by the FSL. This system maintains the sample cells at a temperature slightly below the target temperature. A variable heat source is then used to fine-tune the temperature of the sample cells, compensating for any fluctuations in the cooling water temperature and for the heat generated during certain experimental processes, such as foam generation. The temperature within the sample cells is closely monitored using three sensors located between the cells, and it is typically maintained at around 25°C, with deviations kept within $\pm 0.5K$.

One of the novel features of the experiment container is its separation of diagnostics and sample processing, which enhances its versatility. The container was developed by the FOAM-C collaboration, and its flexible sample cell carrier, combined with advanced optical diagnostics like light scattering and microscopy, makes it adaptable for use by various scientific communities. The container also allows for remote control of the samples in the measurement position and facilitates on-orbit exchange of the Sample Cell Units (SCUs), shown in Fig. 2.1. Up to five SCUs can be mounted on a rotating tray within the container, allowing any of the sample cells to be positioned for measurement and optical diagnostics. This tray also includes a reference stop for precise positioning and barcodes on the SCUs for unambiguous sample identification. The design permits manual exchange of the SCUs by astronauts through a hatch when the container is removed from the drawer in the FSL. Communication with the SCUs is maintained through connectors at each position, allowing for temperature readings and selective power supply to each sample cell.

2.1.2 Methods of analysis

Foams inside the sample cells are probed using a combination of optical diagnostics and specialized equipment designed to assess the structural and dynamic properties of the foam. In Fig. 2.1 we show a drawing of a sample cell.

Light scattering

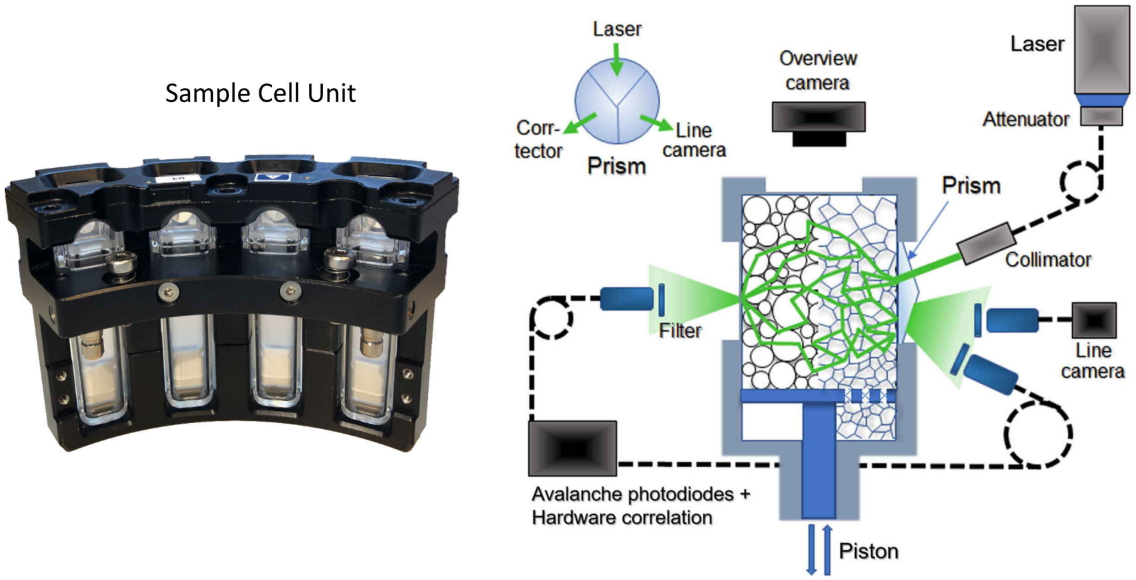

Figure 2.1: Schematic representation of the optical diagnostics of the soft matter dynamics experiment container. Central to the scheme is a sample cell as used in the experiments described in Sec. III. Up to four of such sample cells form a sample cell unit located on the carousel. One sample cell at a time can be made accessible to the diagnostics by moving it with the carousel to a measurement position. The intensity of the laser light is set by a motorized attenuator before being guided and collimated onto the sample cell. The sample cell body is made out of a transparent polycarbonate (PC) or a cyclic olefin copolymer (COC) and comprises a three-faceted prismatic interface for the illuminating light and the light being backscattered from the sample. In the upper left, a front view of this interface is given. Two collimators oriented normal to their respective facets collect the light for the line camera and the avalanche photodiodes in the backscattering direction. In the transmission direction, the collimator collects light transmitted through the flat cell wall and feeds it into the photodiodes. Polarizers and bandpass filters ensure that only multiple scattered laser light is fed into the fiber optics. The overview camera with a microscope objective images the sample through the top surface of the sample cell. The sample is illuminated by three light emitting diodes (LEDs) mounted in the SMD experiment container for imaging (LEDs not shown). A piston mechanism can be used for foaming or compressing the samples, respectively. Figure adapted from [58].

Light scattering diagnostics are employed to examine the inner dynamics and structure of the foam samples. A diode-pumped laser with a wavelength of $532nm$ and a power output of $200mW$ is used to illuminate the foam. The light scattering setup includes a three-faced prismatic structure engraved on the front of the transparent sample cell. This structure allows the laser light to enter the foam at specific angles, and the scattered light is then detected using avalanche photodiodes and a high-speed line camera. The backscattered and transmitted light are collected through fiber optics, and the signals are analyzed with Diffusing Wave Spectroscopy (DWS) and Time-Resolved Correlation (TRC) spectroscopy.

Videomicroscopy

In addition to light scattering, video microscopy is used to visually inspect the foam samples. Blue LEDs illuminate the foam through the transparent cell walls, and a camera records images of the foam structure. This technique allows for the observation of bubble sizes and distribution, particularly near the surface of the foam, where light scattering is less effective due to the strong scattering properties of the bubbles.

The images are analyzed "by hand" using the software ImageJ. The contour of each bubble taken at the middle of the dark ring outlining the bubble is manually fitted by an ellipse (with small ellipticity, *i.e.* between 1 and 1.15), and its area A is measured. Then, the equivalent radius of a circular bubble of the same area is calculated as $R = \sqrt{A/\pi}$. The systematic error that affects the measure of R from the ISS images is estimated to be of the order of one pixel, *i.e.* about 6 μm. This image analysis allows the determination of the bubble radius distribution, since the earliest age just after the end of the foaming process until the end of the coarsening duration where there remains about 50 bubbles at the sample surface, for all investigated liquid fractions. From these effective radius distributions, we determine the mean radius $\overline{R}$ and the Sauter mean radius $R_{32} = \overline{R^3}/\overline{R^2}$.

2.1.3 Sample preparation

The foams were made by mixing air with aqueous solutions of an ionic surfactant, tetradecyltrimethyl - ammonium bromide (TTAB), with concentration $\mathcal{C} = 5g/l$. This surfactant does not evolve chemically in water, hence it was chosen because of the long storage periods imposed by experiments in the ISS. The water was ultrapure water from a Millipore device (resistivity 18 MΩ).

In ISS experiments, the foam is produced in place in the upper part of each cell. Bubbles are formed as the liquid and the gas are forced by the piston motion to mix through the thin gap between the lateral sides of the piston and the walls of the chamber. The piston is actuated periodically for a few minutes by a magnetic field, producing foam with average bubble radius of about $R = 50$ μm. When the study of a sample cell is terminated, the carousel rotates to move a new cell in front of the laser and the various cameras. After the piston is stopped, the overview camera begins recording images of the foam at the top window of the cell. Ten different liquid fractions were studied: 15.2, 20.3, 25.4, 30.6, 32.5, 35.1, 37.9, 40.2, 45.3 and 50.2%. The weights and volumes of all the cells were measured and the foaming liquids were weighed using a precision balance during filling. This results in the high precision in the value of the liquid fraction. In the text, the liquid fraction values are rounded to the nearest integer to facilitate the reading.

In ground experiments, the double syringe method is used [7]. A syringe is filled with the liquid, while a second identical syringe is filled with air saturated with perfluorohexane vapor, which is used here to strongly slow down coarsening [10], in proportion to achieve the desired liquid fraction in the final foam. Then the two syringes are connected with

a rigid connector (Combifix Adapter Luer–Luer) and put on a support which fixes the piston positions. To produce foam the jointed bodies of the syringes are then moved back and forth, at 1 Hz for 2 minutes. A syringe is filled with the liquid phase, while a second identical syringe is filled with air saturated with perfluorohexane vapor, which is used here to strongly slow down coarsening [60], in proportion to achieve to the desired liquid fraction in the final foam. Then the two syringes are connected with a rigid connector (Combifix Adapter Luer-Luer) and put on a support which fixes the piston positions. The jointed bodies of the syringes are then moved back and forth to mix the two fluids, doing 60 cycles/minute for 2 minutes.

2.1.4 Measuring bubble size from the foam surface

Due to successive reflections and refractions at the liquid-gas interfaces, foams strongly scatter visible light preventing direct visualization of bubbles deep inside a bulk 3D sample. This effect becomes more and more pronounced as the liquid fraction increases. In our ISS experiments, where the investigated range of liquid fraction is comprised between 15% and 50%, the observations made with the overview camera in the Soft Matter Dynamics experiment container (cf. Fig. 2.1) are limited to the first layer of bubbles in contact with the top window. This would also be the case with standard microscopy observation on ground. Thus the question arises whether the bubble size distribution measured at the surface of a 3D foam sample is representative of the real bubble size distribution characteristic of the bulk foam within the full range of investigated liquid fractions. There could be also a difference in the coarsening between surface and bulk, which would increase over time the gap between what we can measure and the average behaviour of the foam.

To address the first problem, we have done a ground experiment in the purpose of measuring the bubble size distribution at the surface of 3D foam sample together with the bubble size distribution of a monolayer of bubbles obtained by diluting the exact same foam sample with the foaming solution. To clarify whether surface and bulk bubbles follow the same average growth law, we measure the average bubble radius in the bulk of the foam, in parallel with the surface observations, for all the investigated liquid fractions.

2.1.4.1 Comparison of the bubble size distributions

To study foams on the ground similar to those used in the ISS experiments, we employed an equivalent liquid solution composed of TTAB surfactant ($\mathcal{C} = 5\ g/L$) dissolved in ultrapure MilliQ water and generated foams using the double syringe method [7].

Within less than 60 s after foaming, we filled a large slab (2 mm thick) with transparent glass windows with the foam, while simultaneously injecting 1 μL of foam into a cell pre-filled with the foaming liquid (also equipped with transparent glass windows). The bubbles in the foam disperse in the liquid, forming a dilute monolayer of bubbles at the upper window. Both the surface of the foam sample and the bubble monolayer were observed in videomicroscopy, with the sample illuminated by transmitted light. The first images were captured within two minutes of the foaming process's conclusion.

The bubbles in the monolayer appear as dark disks with a sharp contour. Given that the average bubble size is within the range of 10 μm $-$ 20 μm, their Bond numbers range from 2.10^{-5} to $1.2 \cdot 10^{-4}$, implying that the bubbles maintain a spherical shape. Since the slab's thickness is more than 50 times the average bubble diameter, light is strongly scattered by the underlying bubbles, resulting in surface bubbles with dark contours similar to those observed in ISS images. For each sample, several pictures were taken in different regions to check for homogeneity, and two images were taken in the same region one minute apart to confirm that bubble size remained unchanged at both the foam surface and in the monolayer. We concluded that, over this short time, neither

drainage, coalescence, nor coarsening altered the structures, making the monolayer images representative of the bubble population in the foam sample. The images were analyzed with ImageJ, where ellipses were manually fitted to each bubble. Between 1000 and 1200 bubbles per image were counted.

These experiments were conducted with three different liquid fractions: $\phi = 15\%$, 30%, and 50%. For each fraction, we measured the bubble radius distributions at the foam surface and for the bubble monolayer. We then deduced the mean bubble radius at the foam surface $\overline{R}$, the mean radius of the monolayer bubbles $\overline{R_m}$ (representing the "true" mean radius of the bubbles in the foam), and the polydispersity index p, evaluated at the foam surface and in the monolayer. The polydispersity index is defined as $p = (R_3^{2/3}/R_2) - 1$. As shown in Table 2.1, for the 15% and 30% liquid fractions, the mean radius at the foam surface $\overline{R}$ is smaller than that of the monolayer $\overline{R_m}$, indicating that surface measurements underestimate the true bubble size. This can be attributed to the fact that the dark contour outlining the bubbles is smaller than the actual bubble circumference. This is due to light refraction, where the contact between two adjacent bubbles, as in the 15% and 30% liquid fraction cases, is not visible. Based on geometrical optics, the relationship between the contour radius R and the real radius R_m of a spherical bubble illuminated under diffuse transmission conditions has been predicted to be [61]: $R = R_m \cos(\theta_c/2)$, where θ_c is the critical angle for total internal reflection between the gas and liquid phases. For the air-water interface, $\theta_c = 48.8°$, yielding $R \approx 0.91 R_m$.

For our sample with a 50% liquid fraction, which is well above the jamming transition for our disordered samples, the bubbles remain spherical. As expected, $\overline{R} \approx 0.91\overline{R_m}$, consistent with our findings (see Table 2.1), within the limits of measurement uncertainty. Further ray-tracing studies should be conducted to explore the origin of the proportionality factor between the average radii $\overline{R}$ and $\overline{R_m}$ as a function of liquid fraction.

Figure 2.2 shows the probability density functions of the bubble radius normalized by its mean value measured either at the surface of the foam sample or for the bubble monolayer. For a given liquid fraction, both bubble size distributions are similar. The cumulative distributions superpose remarkably to each other. The application of the Kolmogorov-Smirnov statistical test on each couple of observations (monolayer and foam observed at surface) strengthen the assumption of similarity for the 15%, with a p-value=0.54, and 30%, with a p-value=0.34; the same test applied to the 50% data yields a p-value=0.005, which reveals a statistical difference. This is correlated to the observed difference in the polydispersity index at this liquid fraction (cf. Table 2.1). Deeper statistical analysis would require further investigations with an increase in the experimental precision.

These results show that the bubble size distribution, deduced from the outline contour of the bubbles at the surface of a 3D foam illuminated by diffuse transmitted light, are representative of the real bubble size distribution in the bulk of the sample, in the range of

Liquid fraction (%)	$\overline{R_m}$ (μm)	$\overline{R}$ (μm)	p_m	p
15	21.3 ± 0.7	16.2 ± 0.9	0.13	0.12
30	17.6 ± 0.7	13.0 ± 0.9	0.15	0.17
50	9.1 ± 0.7	9.9 ± 0.9	0.13	0.17

Table 2.1: Mean apparent bubble radius $\overline{R}$ measured at the surface of the foam, mean bubble radius measured for the monolayer made of the same foam $\overline{R_m}$, and corresponding polydispersity indices p and p_m (defined in the text), for samples with different liquid fractions. The uncertainty on the mean radii is evaluated as a systematic error of 1 pixel size.

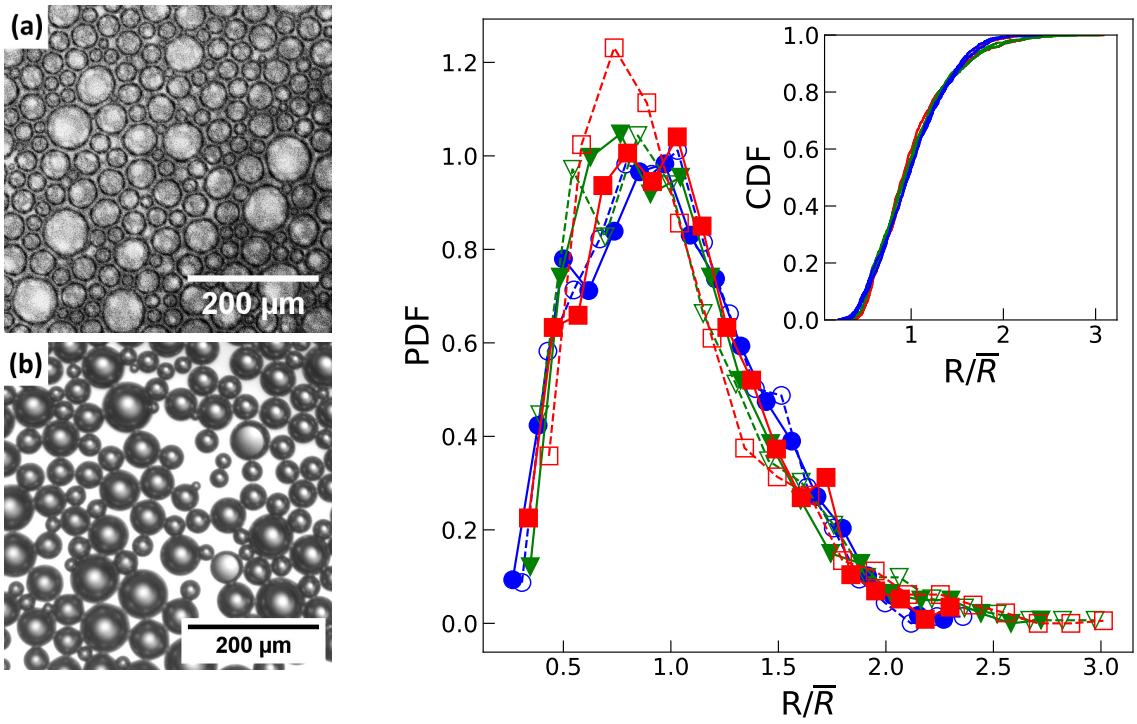

Figure 2.2: (left) Pictures of a foam with $\varepsilon = 15\%$ studied on ground: (top) surface of a 3D foam, (bottom) bubbles in a monolayer. (right) Probability density functions of the radius distribution normalized by the average radius $\overline{R}$, for three liquid fractions: (●, ○) 15% , (▼, ▽) 30% , (■, □) 50% . Filled markers refer to observations of bubbles in a monolayer, while empty markers correspond to bubbles at the surface of a 3D foam sample. Lines are guides for the eye. The inset shows the cumulative density functions of the same distributions.

liquid fraction comprised between 15% and 50%. This corresponds to the domain of foams and illumination conditions of our experiment in the ISS. In addition, the distributions observed here are similar to the initial distributions of the foams produced in the ISS at the same liquid fractions. According to these findings, we can infer that the bubble growth laws measured at the surface of the samples are representative of the bulk growth laws.

2.1.4.2 Comparison of the growth laws

Using the ISS set-up, the diffuse intensity transmitted through the foam sample is monitored during the coarsening process (cf. Section 2.1.1). This measurement allows us to determine the evolution of the photon transport mean free path ℓ^*, the average distance a photon travels between successive scattering events. It quantifies the extent of multiple scattering and is directly related to the foam's microstructure: by knowing it, we can deduce the average bulk bubble radius over time for any given liquid fraction.

In this experimental configuration, the foam sample is contained in a rectangular cuboid cell with thickness $L = 11.3$ mm, and lateral dimensions $a = 14.1$mm and $b = 9.0$mm. The sample is enclosed by transparent walls on three sides, with the bottom surface acting as an opaque, diffusing wall due to the presence of a piston used for generating the foam. Illumination is focused at the center of one face of the cell, and the multiply scattered light is collected via an optical fiber positioned at the center of the

opposite face. A specific model for this "point-in point-out" configuration was developed, which accounts for the unique geometry and lateral reflectivity conditions of the cuboid cell [59].

The ISS set-up does not permit absolute measurements of the transmitted intensity F_T^{cuboid}. Consequently, for each experiment, a calibration must be performed using a reference pair: a known transport mean free path ℓ^o and the corresponding transmitted intensity $F_{T,o}^{cuboid}$. The reference ℓ^o is derived from the surface-averaged radius R_2 at a specific coarsening time t_o, once the foam has reached the scaling state. In this regime, the bubble size distribution becomes self-similar, characterized by a single independent length scale, and the n-th moment R_n of the radius distribution is related to the mean radius $\overline{R}$ by [49, 62]: $R_n \propto \overline{R}^n$. The proportionality between ℓ^* and R_2 remains constant for a given bubble size distribution, ensuring that the surface calibration introduces no bias into the determination of ℓ^*.

For a given coarsening sample, we numerically interpolate ℓ^* as a function of the measured normalized intensity $F_T^{cuboid}/F_{T,o}^{cuboid}$ using the *point-in point-out cuboid model* [59]. This method enables the determination of ℓ^* throughout the coarsening process. However, towards the latter stages of coarsening, the measured transmission signal exhibits significant fluctuations due to the presence of larger-than-average bubbles encountered along the light path. As a result, transmission data is only considered reliable when $L/\ell^* \gtrsim 10$. Thus, for consistency with the model, we limit our analysis to conditions where $b/\ell^* \gtrsim 10$ and $a/\ell^* \gtrsim 10$.

Once ℓ^* is determined, we calculate the Sauter mean radius R_{32} assuming $R_{32} \propto \ell^*$. This assumption holds in the scaling state, where the foam structure is self-similar. The temporal evolution of R_{32} for various liquid fractions is shown in Fig. 2.3. The strong agreement between the bulk R_{32} values and those measured at the surface indicates that surface measurements provide an accurate representation of bulk bubble evolution. For foams with higher liquid fractions, we observe small fluctuations in bulk R_{32} at later stages of coarsening. These fluctuations likely arise from larger bubbles near the optical axis, which transmit light more efficiently, leading to locally elevated ℓ^* values. Alternatively, regions with lower packing density might contribute to these variations. At early stages of coarsening, when the bubble size distribution has not yet reached the scaling regime, both the geometrical factors ℓ^*/R_2 and R_{32}/R_2 may deviate slightly from their asymptotic values. These deviations may introduce a weak dependency on polydispersity, affecting the calculated bulk radius. Nevertheless, these variations do not significantly impact the analysis of the average bubble growth in the scaling state.

In conclusion, for wet foams, both the bubble growth laws and the size distributions measured at the surface are representative of the foam's bulk behavior. In the following sections, we will explore how these foam characteristics depend on the liquid fraction ϕ.

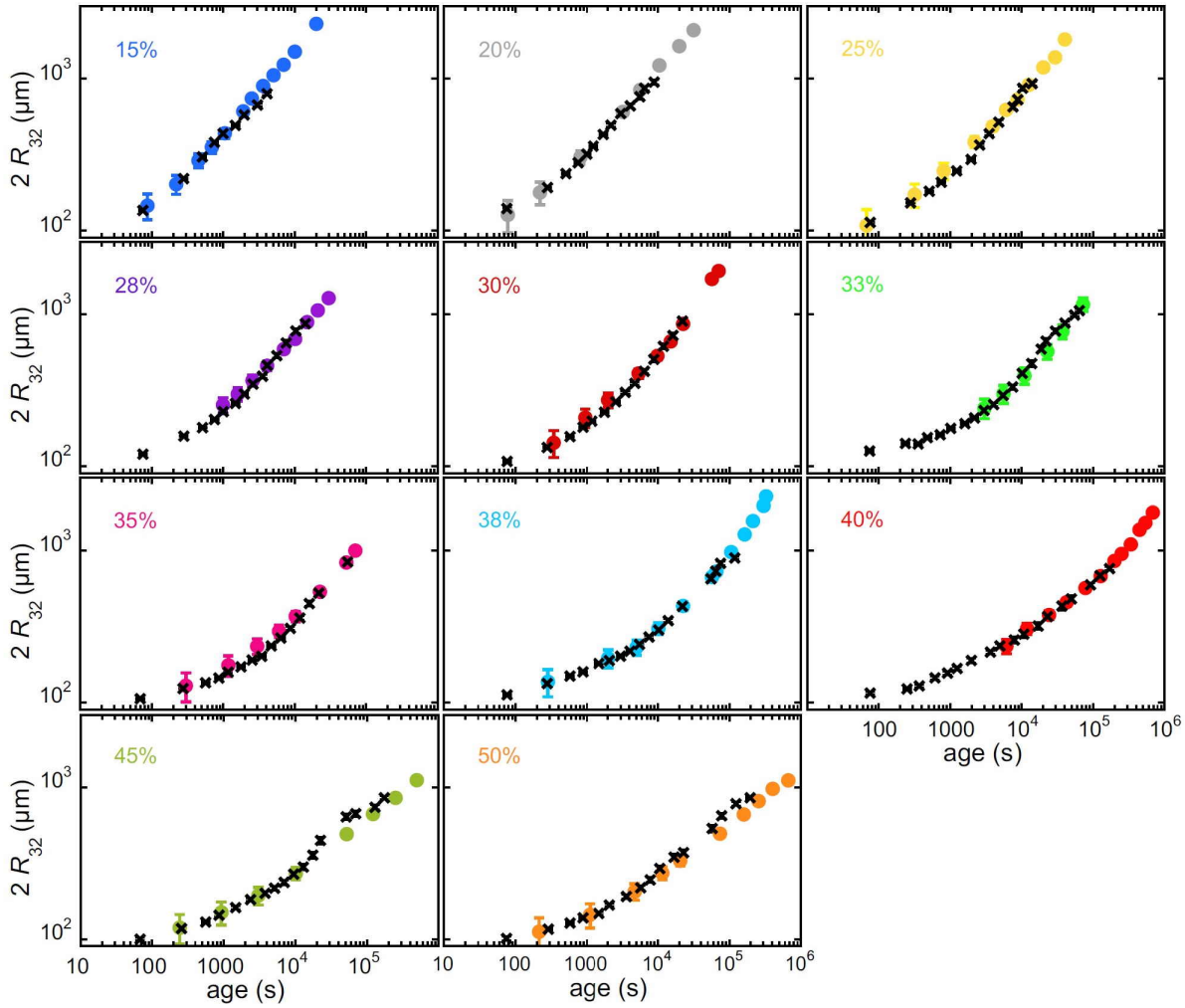

Figure 2.3: Sauter mean diameter R_{32} as a function of foam age, measured either in the bulk of foam using Diffuse Transmission Spectroscopy (crosses) or at the foam surface using videomicroscopy (disks). The Sauter mean radii measured at the foam surface are deduced from the distributions of the radii of the contour of the bubbles, as explained in section 2.1.2. The ages t_o chosen for the calibration reference of the DTS measurements are: $t_o = 1050$ s for $\phi = 15\%$, $t_o = 3230$ s for $\phi = 20\%$, $t_o = 3940$ s for $\phi = 25\%$, $t_o = 4110$ s for $\phi = 28\%$, $t_o = 9860$ s for $\phi = 30\%$, $t_o = 10960$ s for $\phi = 33\%$, $t_o = 22500$ s for $\phi = 35\%$, $t_o = 22520$ s for $\phi = 38\%$, $t_o = 24300$ s for $\phi = 40\%$, $t_o = 10150$ s for $\phi = 45\%$, $t_o = 4730$ s for $\phi = 50\%$. The error bars over the surface data, shown unless of the size of the symbols, represent measurement uncertainties. Statistical uncertainty on DTS measurements are smaller than the size of the symbols. The liquid volume fraction is labelled inside each graph. Figure from [59].

ϕ(%)	15	20	25	27	30	32	35	37.5	40	45	50
R_{32}/R_{21}	1.3	1.3	1.3	1.3	1.3	1.2	1.2	1.2	1.1	1.1	1.1
R_{32}/R_{10}	2.0	2.2	2.0	2.0	1.9	1.7	1.6	1.6	1.2	1.2	1.1
Polydispersity	0.38	0.41	0.37	0.37	0.34	0.27	0.25	0.24	0.09	0.09	0.06
t_o (s)	87	78	68	68	68	68	68	284	243	243	214
Fitted exponent α	0.55	0.55	0.55	0.52	0.59	0.55	0.52	0.51	0.36	0.35	0.35
Prefactor (μm/s$^\alpha$)	5.00	3.48	2.60	3.17	1.20	1.18	1.51	1.36	4.90	5.79	4.90
Exponent	1/2	1/2	1/2	1/2	1/2	1/2	1/2	1/2	1/3	1/3	1/3
$\Omega_{p,R_{32}}(\mu\text{m}^2/\text{s})$	55	31	16	13	7.9	4.3	3.2	2.1	-	-	-
$\Omega_{c,R_{32}}(\mu\text{m}^3/\text{s})$	-	-	-	-	-	-	-	-	288	281	219

Table 2.2: Relations between average radii, coarsening rates and exponents evaluated in the scaling state. The polydispersity index is $p = {R_{32}/R_{30}}^{1/3} - 1$[8], with R_{30} the third moment of radius distribution. The time t_o is the reference time at which $R_{32} = 60$ μm. The measurement uncertainty on the coarsening rate is about 10%.

2.2 Transition in coarsening growth laws

The goal of our study is to investigate how coarsening is impacted by the structural changes occurring near the jamming transition. In dry foams, gas is transferred between neighboring bubbles primarily through diffusion across the thin liquid films separating them. There is a strong correlation between the topology of the packing and the concentration gradients driving gas exchange between adjacent bubbles. In the opposite limit of large liquid fractions, bubbles form a dilute dispersion and exchange gas with the surrounding continuous phase, which acts as a reservoir for dissolved gas. This process is commonly referred to as Ostwald ripening. While bubble growth in both regimes follows asymptotic power laws, the exponents governing these laws differ.

The transition between these two limiting cases, and its connection to the structural changes at the jamming transition, remains poorly understood. Existing experimental studies with foams and emulsions have yet to provide a comprehensive global picture of coarsening in this context. It is worth noting that grain growth in solid dispersions exhibits similarities to foam coarsening, though it is further complicated by the anisotropy of the crystal lattice. To explore these phenomena, we conducted coarsening experiments on samples with liquid fractions in the range $15\% \leq \phi \leq 50\%$, spanning both sides of the jamming transitions [13]. The studied liquid fractions are reported in Table 2.2.

2.2.1 Growth laws

As discussed in Section 2.1.4.1, the moments of the bubble size distributions are determined from videomicroscopy measurements applied at the sample surface, and they are consistent with the evolution in the bulk determined from DTS scattering data. Among the multiple averages $\langle R \rangle$ that we recover from the distribution, three are of special interest for coarsening:

- In the Lemlich model for foam coarsening [27] (cf. Section 1.2.3), the critical radius for foam coarsening is predicted to be R_{21}.

- In the LSW model for Ostwald ripening [20, 21] (cf. Section 1.2.1), valid in the dilute limit, the critical radius for foam coarsening is predicted to be the mean radius $\overline{R} = R_{10}$.

- The characteristic foam pressures Π, Π_c, scale with the surface/volume ratio of the bubbles in the foam $1/R_{32}$ (cf. Section 1.1.2.2), where R_{32} is the mean Sauter radius (cf. Eq. 1.2).

Where we have used the convention $R_{ij} = \langle R^i \rangle / \langle R^j \rangle$. We will pursue the analysis in terms of R_{32}. For the maximal clarity, we will specify the radius average considered in the evaluation of the coarsening rate, as in $\Omega_{p,\langle R \rangle}$. The relations between the moments of the bubble size distributions are reported in Table 2.2.

We show the evolution of the mean Sauter radius R_{32} as a function of foam age, in Fig. 2.4. We observe for any liquid fraction ϕ that, for bubble sizes $R_{32} \geq 200\mu m$, the increase of R_{32} with time is compatible with a power law:

$$\langle R \rangle = \Omega_\alpha \, t^\alpha. \tag{2.1}$$

We fit Eq. 2.1 to the data in that regime, and report the fitted parameters Ω_α, α in Table 2.2. We plot the effective exponent α as a function of the liquid fraction ϕ in Fig. 2.5. We observe that the experiments are well separated into two groups: for $\phi < 0.39$ the effective exponent $\alpha \approx 1/2$ is consistent with the coarsening of a foam (cf. Eq. 1.38); for $\phi > 0.39$ the effective exponent $\alpha \approx 1/3$ is consistent with the coarsening of a bubbly liquid (cf. Eq. 1.23). We deduce that for the chosen surfactant (TTAB $\mathcal{C} = 5g/L$) the jamming transition is located at $\phi^* = 0.39$. This value is higher than the expected $\phi_{rcp} = 0.36$, with a sharp transition of the effective exponent in a range of liquid fractions $\Delta\phi \approx 2\%$. We will discuss more in detail this result in the next Section.

With a criterion to distinguish samples into foams and bubbly liquids, we fit Eq. 1.38 to the temporal evolution of the Sauter radius R_{32} of experiments in the first group, and Eq. 1.23 to experiments of the second group. For all the experiments we fix the initial radius $R_0 = 60\mu m$ and the initial time t_0, indicated in Table 2.2; the free parameters Ω_p and Ω_c are reported as well in Table 2.2. We see that the growth laws describes really well the data, for the complete range of liquid fractions ϕ. In the following, we discuss separately the two regimes.

2.2.2 Coarsening rates in the bubbly regime

To compare the coarsening rates $\Omega_{c,R_{32}}$ with those predicted for $\overline{R}$ concentrated particle dispersions, we must take into account the polydispersity of the samples. For each ϕ, we determine the ratio R_{32}/R_{10} (cf. Table 2.2), which gives the geometrical coefficient $C = (R_{32}/R_{10})^3$. We show the coarsening rate $\Omega_{c,R_{10}} = \Omega_{c,R_{32}}/C$ as a function of the liquid fraction ϕ, in Fig. 2.6. We observe that the coarsening rate decreases with the liquid fraction ϕ. This is in agreement with the predictions offered by coarsening theories for bubbly liquids beyond the dilute limit, detailed in Section 1.2.2. In the dilute limit $\phi = 1$ studied by LSW theory, the average inter-bubble distance is large with respect to bubble size ($d/R \to \infty$), and the concentration gradients of the gas dissolved in the continuous phase is assumed to extend independently up to an infinite distance around each bubble. For smaller ϕ, the average distance between bubbles decreases, and the concentration gradients extend only up to a finite distance. As a consequence, the coarsening rate is expected to increase as the ϕ decreases.

The evolution of Ω_c with the liquid fraction is captured, according to Eq. 1.30, by the *coarsening enhancement factor* $f_3(\phi)$. Different predictions of $f_3(\phi)$ have been proposed, mainly in order to describe the coarsening of grains in annealing alloys. Measurements in alloys with continuous phase volume fractions between $0.40 \leq \phi \leq 0.80$ showed that $f_3(\phi)$ varies by a factor of about 3 [25]. In these systems, each phase is anisotropic and sometimes heterogeneous, and the grain boundaries do not have a unique energy, in contrast to the

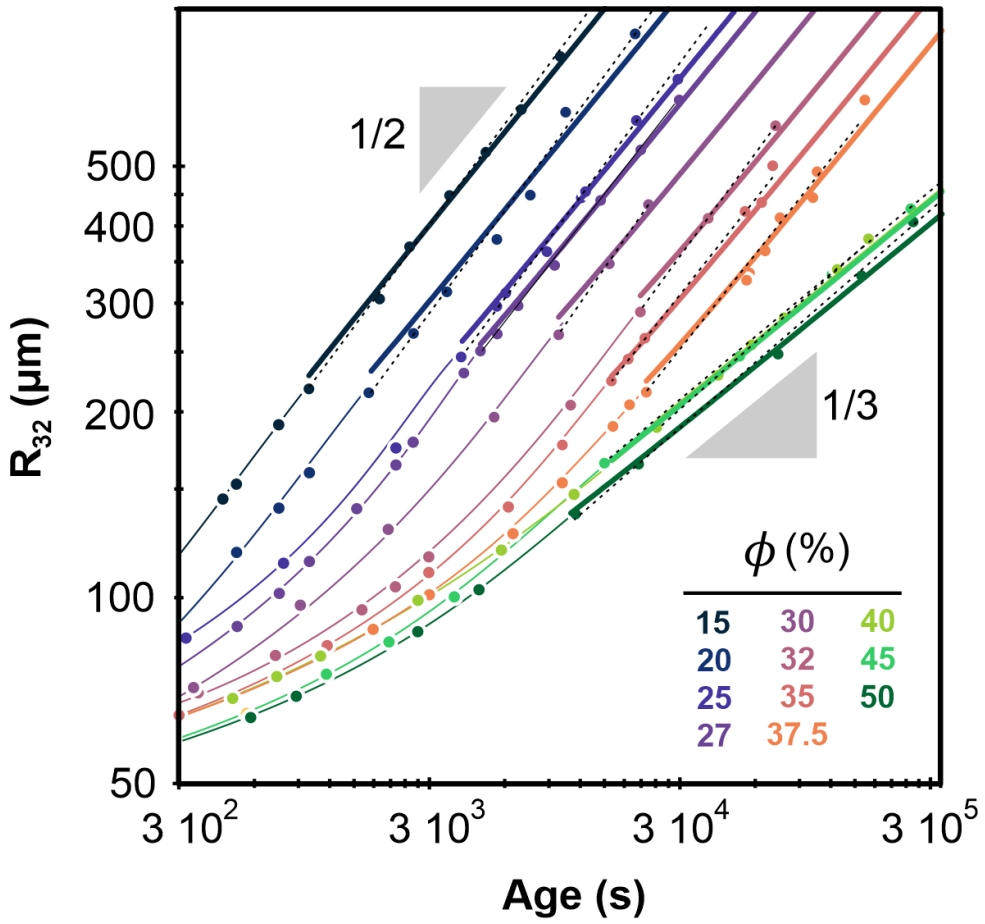

Figure 2.4: Average bubble Sauter radius versus foam age for the different liquid fractions. The radii are measured with an accuracy of 15 μm. Dotted lines represent power laws $R_{32} \propto t^{\alpha}$ obtained by fits within the scaling state. Corresponding prefactors and exponents α are reported in table 2.2. The thick continuous lines represent growth laws within the scaling state, obtained by fitting Eq. 1.38 to the data for $\phi \leq 37.5\%$ and Eq. 1.23 to the data for $\phi \geq 40\%$, as explained in the text. The fixed parameters $R_o = 60$ μm, and corresponding t_o are indicated in table 2.2 for ϕ values increasing from 15% to 50% as labelled in the graph. The thin curves are extrapolations of the thick ones using equations Eq. 1.38 and Eq. 1.23 curves.

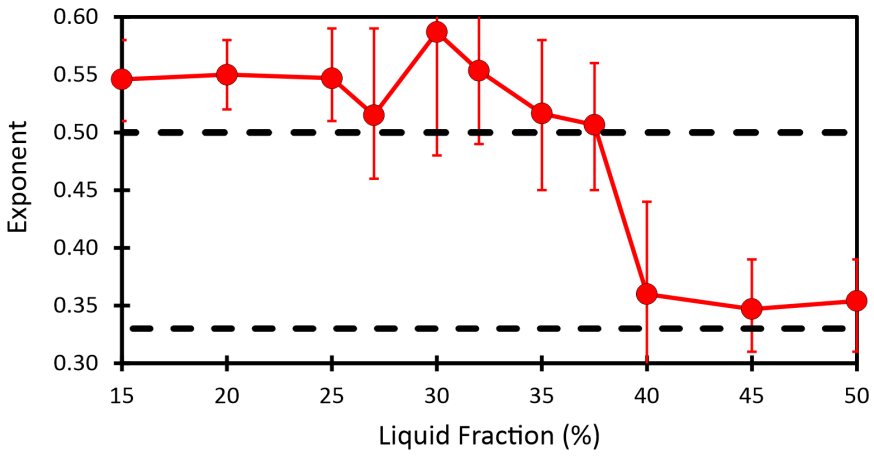

Figure 2.5: Effective exponent α, obtained by fitting Eq. 2.1 on the data presented in Fig. 2.4, as a function of the liquid fraction ϕ. The horizontal dashed lines correspond to the exponents: 1/2, expected for coarsening foams (cf. Eq. 1.38); 1/3, expected for coarsening bubbly liquids (cf. Eq. 1.23).

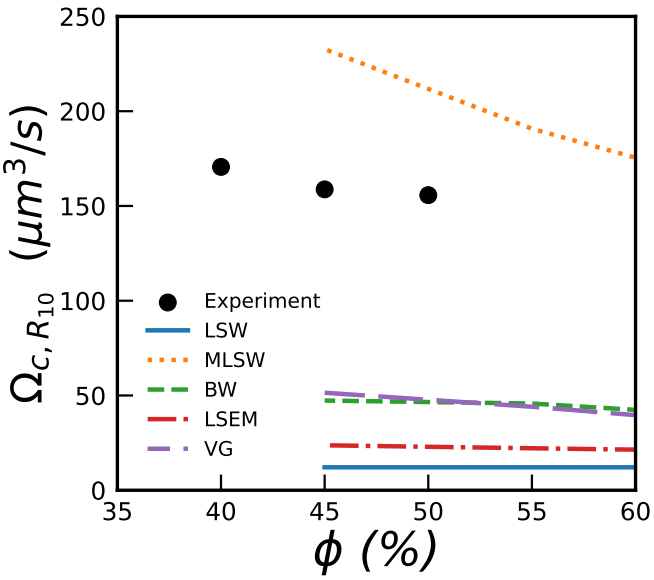

Figure 2.6: Coarsening rate $\Omega_{c,R_{10}}$ for bubbly liquids as a function of the liquid fraction ϕ. The continuous blue line shows the coarsening rate estimated by LSW in the dilute limit $K_0 = 12.1\mu m^3/s$ (cf. Eq. 1.24). The other lines are and estimations of Eq. 1.30, with fixed K_0, and the $f_3(\phi)$ function numerically predicted by 4 theories: MLSW [24], BW [66], LSEM [67], VG [68]. The corresponding values of $f_3(\phi)$ are collected and reported in two reviews [25, 26], only down to $\phi = 45\%$.

interfacial tension is foams. These features bring complexity in predicting realistic kinetic evolutions. Experiments with emulsions of variable continuous phase volume fraction are scarce. They, however, also suggest that $f_3(\phi)$ does not change rapidly with ϕ (it increases by less than a factor 2 between $\phi = 0.90$ and $\phi = 0.98$ in [63]). Like emulsions, bubbly liquids are simpler model systems than alloys, because each phase and their interface are ideally homogeneous and isotropic.

We recall that, in the dilute limit, the coarsening rate is $K_0 = \frac{8}{9}\gamma D H_e v_m$ (cf. Eq. 1.24), where γ is the surface tension at the gas/surfactant/liquid interface, D is the diffusion coefficient, He the gas solubility, $v_m = 0.024m^3/mol$ the gas molar volume. For $\gamma = 37.1mN/m$ [13], $D = 2\ 10^{-9}m^2/s$ [64], $H_e = 7.6\ 10^{-6}$ [65], we estimate $K_0 = 12.1\mu m^3/s$. We find one order of magnitude of difference with the experimental values of $\Omega_{c,R_{10}}$, much more than what the majority of the theories predict for the coarsening enhancement factor $f_3(\phi)$, as shown in Fig. 2.6. The prediction that most closely matches the observed data range comes from the Modified LSW (MLSW) model [24], but the data points are concentrated in a range of ϕ that is too narrow to allow for a meaningful comparison. Further experiments are needed in the liquid fraction range of $50\% < \phi < 100\%$ to determine which theory best applies to bubbly liquids.

2.2.3 Coarsening rates in the foam regime

We show in Fig. 2.7 the coarsening rates $\Omega_{p,R_{32}}$ as a function of the liquid fraction ϕ. We observe that, like in bubbly liquids, the coarsening rate decreases with ϕ. This is agreement with the theories developed for dry and moderately-wet foams (cf. Section 1.2.3). In foams, gas diffuses between bubbles across the contact films. In the dry limit $\phi \to 0$, the complete surface area of the bubbles is covered by films. As the liquid fraction increases, the Plateau borders thicken and the surface area covered by films decreases, reducing

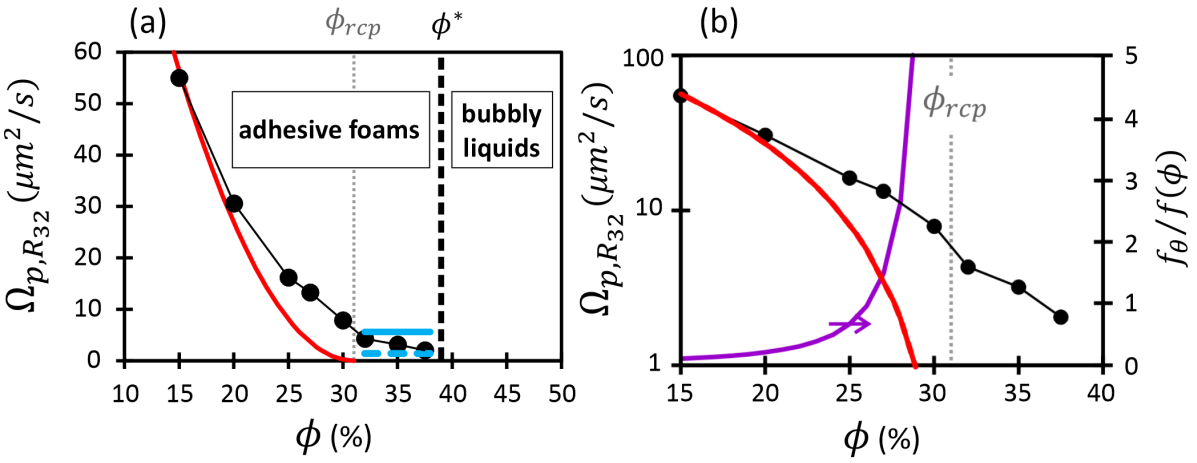

Figure 2.7: Coarsening rates $\Omega_{p,R32}$ as a function of the liquid fraction ϕ, for wet foams presented in: (a) linear scale; (b) logarithmic scale. The red line represents the theoretical prediction, i.e. Eqs. 1.39 and 1.41, evaluated as explained in the text with $\phi_{\rm rcp}$ =31%, $k = 4.75$. The horizontal blue lines correspond to the expected coarsening rates due solely to adhesion-induced contact films between bubbles (cf. Eq. 2.2), assuming respectively 12 (continuous line) and 3 (dashed line) contacts per bubble. In (b), the purple curve represents the ratio of film areas induced solely by adhesion forces (Eq. 2.2) and those induced solely by the osmotic pressure (Eq. 1.41).

proportionally the gas flux between bubbles. Thus, the decrease of the coarsening rate with the liquid fraction is captured by $f_2(\phi)$, the fraction of surface area covered by films (cf. Eq. 1.39). The function $f_2(\phi)$ is set by the osmotic pressure of the foam (cf. Eqs. 1.6 and 1.41), and it vanishes when the liquid fraction reaches the random close packing fraction $f_2(\phi_{rcp}) = 0$. For monodisperse spheres randomly packed, $\phi_{rcp} = 0.36$; for polydisperse or ordered systems this value can be lower than that [10]. In the case of a coarsened foam, as it will be discussed in the next Section, we found $\phi_{rcp} = 0.31$ [19].

Surprisingly, the experimental observations of $\Omega_{p,R_{32}}$ do not vanish for $\phi > \phi_{rcp}$, up to $\phi^* \approx 0.39$. Indeed, the prediction underestimates the experiments in the range of liquid fractions $\phi \geq 25\%$, as we show in Fig. 2.7. We deduce that an additional mechanism raises $f_2(\phi)$ in our foams, for liquid fractions $\phi \geq 20\%$. We will address this effect more broadly later on Section 3.3.1, and specifically, we will show that it is justified to neglect it for liquid fractions close to 15% From Eq. 1.39, we get $\Omega_0 = \Omega_{p,R_{32}}(R_{21}/R_{32})^2/f_2(0.15) \approx 214 \pm 21 \mu m^2/s$. First, we compare it with previous experiments in quasi two-dimensional foams, where the capillary pressure was maintained constant in a range comparable to our experiments [69]. The result of this work, $\Omega_0 = 256 \mu m^2/s$, is in good agreement with our estimation in view of the experimental uncertainties. Then, we consider the physical-chemistry of the foam. We recall that, in the dry limit, the coarsening rate is $\Omega_0 = 2\gamma D H_e v_m/h$ (cf. Eq. 1.40), where h is the film thickness. Using $\gamma = 37.1\ mN/m$ [13], $D = 2\ 10^{-9} m^2/s$ [64], $H_e = 7.6\ 10^{-6}$ [65], and $h \approx 35\ nm$ [13], we estimate $\Omega_0 = 390\ \mu m^2/s$. This is larger than what we deduced from the experiments, with the higher uncertainty residing in the estimation of the film thickness h.

We explain the anomalous evolution of $\Omega_p(\phi)$ as an effect of the weak adhesive forces observed between contacting bubbles, as shown in Fig. 2.8(left). Here, we assume weak adhesion forces between contacting bubbles, so that $f_2(\phi) = f_{2,\theta}$ for $\phi \geq \phi_{\rm rcp}$. We estimate $f_{2,\theta}$ for $\phi \geq \phi_{\rm rcp}$ using the following relation:

$$f_{2,\theta} = \frac{z A_c}{4\pi R^2} = \frac{z\, sin^2(\theta)}{4} \tag{2.2}$$

where θ is the contact angle between two bubbles, and z is the average number of contacts

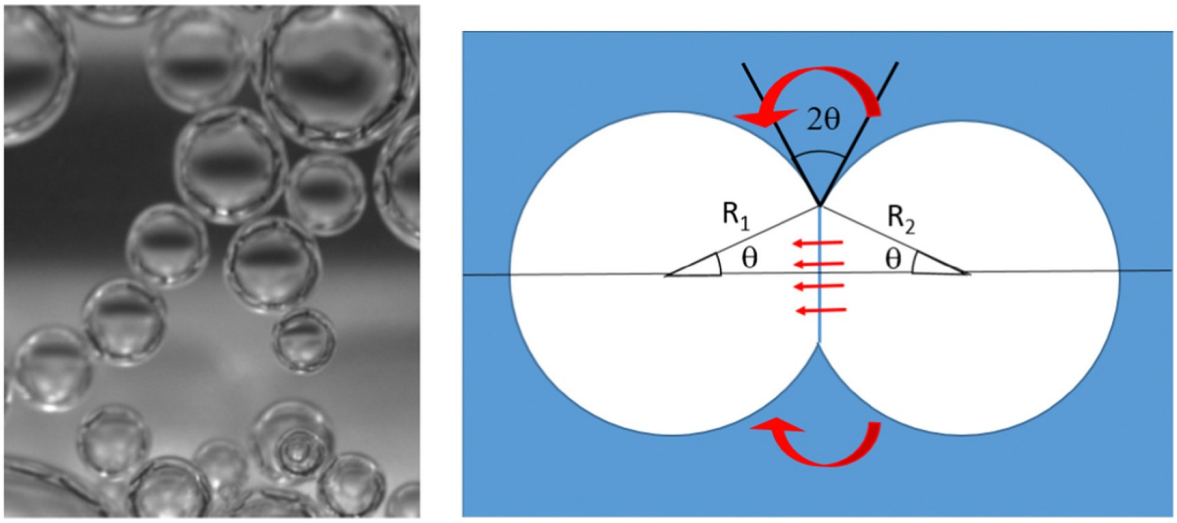

Figure 2.8: (left) Picture of a bubble cluster surrounded by foaming liquid, spontaneously formed during our measurements in microgravity. (right) Side view of two adhesive bubbles, of radii R2oR1, both very close to their average R. In this schematic illustration, the contact angle y is much larger than the value that we determined experimentally and that we consider in our model, and the radii are too close to be distinguished. Figures from [13].

per bubble. The contact angle can be measured from the outline of two bubbles of equal size in contact, in conditions of in static equilibrium (cf.Fig. 2.8 (right)). By using an image analysis technique described in [70], we get a contact angle of $3.6 \pm 1°$. As a reference, this angle is larger than the one of $1.1 \pm 1°$ reported for Sodium Dodecyl Sulfate (another ionic surfactant) at similar concentrations. The estimation of the number of contacts z is more complex. For dry foams, the average number of faces lays in the range $12 \leq z \leq 15$ [1], with lower values for more polydisperse and disordered foams. In the range of liquid fractions $\phi_{rcp} \leq \phi \leq \phi^*$ we expect it to decrease with the liquid fraction, but we lack the support of simulations or experiments providing a scaling. In Fig. 2.7(a) we plot Eq. 1.39, using Eq. 2.2 and two reference values $z = 4, 12$. We observe that the variation of Ω_p in the range of liquid fraction $\phi_{rcp} \leq \phi \leq \phi^*$ is compatible with the proposed expression.

In the next section, we focus on the study of the bubble size distributions. In doing so, we provide also a better measurement of the gap between the random close packing fraction ϕ_{rcp} and the jamming transition ϕ^*.

2.3 Hierarchical bubble size distributions in coarsening wet liquid foams

We reprint here the article that we published on the bubble size distributions of wet foams [19]. Additionally, we give space to additional details which could not be discussed in the published content.

PNAS RESEARCH ARTICLE | PHYSICS

Hierarchical bubble size distributions in coarsening wet liquid foams

Nicolò Galvani[a,b], Marina Pasquet[c], Arnab Mukherjee[a], Alice Requier[c], Sylvie Cohen-Addad[a,d], Olivier Pitois[b], Reinhard Höhler[a,d], Emmanuelle Rio[c], Anniina Salonen[c], Douglas J. Durian[e,f], and Dominique Langevin[c,1]

Edited by David Weitz, Harvard University, Cambridge, MA; received April 21, 2023; accepted August 7, 2023

Coarsening of two-phase systems is crucial for the stability of dense particle packings such as alloys, foams, emulsions, or supersaturated solutions. Mean field theories predict an asymptotic scaling state with a broad particle size distribution. Aqueous foams are good model systems for investigations of coarsening-induced structures, because the continuous liquid as well as the dispersed gas phases are uniform and isotropic. We present coarsening experiments on wet foams, with liquid fractions up to their unjamming point and beyond, that are performed under microgravity to avoid gravitational drainage. As time elapses, a self-similar regime is reached where the normalized bubble size distribution is invariant. Unexpectedly, the distribution features an excess of small roaming bubbles, mobile within the network of jammed larger bubbles. These roaming bubbles are reminiscent of rattlers in granular materials (grains not subjected to contact forces). We identify a critical liquid fraction ϕ^*, above which the bubble assembly unjams and the two bubble populations merge into a single narrow distribution of bubbly liquids. Unexpectedly, ϕ^* is larger than the random close packing fraction of the foam ϕ_{rcp}. This is because, between ϕ_{rcp} and ϕ^*, the large bubbles remain connected due to a weak adhesion between bubbles. We present models that identify the physical mechanisms explaining our observations. We propose a new comprehensive view of the coarsening phenomenon in wet foams. Our results should be applicable to other phase-separating systems and they may also help to control the elaboration of solid foams with hierarchical structures.

foams | coarsening | Ostwald ripening

Significance

Coarsening is a ubiquitous phenomenon in phase separations. It is widely observed in alloys, polymers, emulsions, foams, and even in biological systems. However, coarsening of materials where the two phases have comparable volume fractions is still poorly understood. To fill this gap, we performed coarsening experiments on aqueous foams in microgravity—free from gravity-driven destabilization. We discovered that coarsening naturally produces, besides large jammed bubbles, a significant proportion of small roaming bubbles. This hierarchical size distribution is surprising but could be general and exist in other coarsening systems. Foaming being a generic method to produce solid cellular materials with many applications, making use of these roaming bubbles opens up a new way of designing hierarchical materials.

Liquid-phase separation is a common phenomenon in material processing or aging. In the late stages of separation, the dispersed domains grow, in order to decrease interfacial energy. This often occurs as the dispersed phase diffuses through the continuous phase. This process, known as coarsening or Ostwald ripening, is sometimes referred to as "thermodynamic capitalism" (1), where big entities get bigger at the expense of small entities which disappear.

Coarsening kinetics determines the microstructure of the materials, i.e., the average domain size and size distribution, which is why it has been studied in widely varying contexts. The coarsening of alloys has been extensively studied (2), but coarsening also affects crystallization of proteins (3), separation by chirality (4), synthesis of small particles of controlled microstructure including quantum dots (5–7), stability of foams and emulsions (8–10) as well as other complex liquid–liquid phase separations (11). Coarsening has recently emerged as an important route to protein compartmentalization within living cells (12).

The theoretical description of coarsening goes back to Lifshitz and Slyozov (13), and to Wagner (14), and is usually referred to as "LSW theory". This theory is only valid in the limit of high volume fraction ϕ of the continuous phase. Nonetheless, the LSW theory correctly predicts the coarsening behavior in numerous systems, namely, that the time-dependent average domain radius increases with time as $t^{1/3}$ and that the normalized size distribution of the domains (PDF) is invariant with time. Many efforts were subsequently made to account for the behavior at smaller ϕ by means of theoretical methods and by computer simulations (15, 16). However, the evolution of the growth regime in $t^{1/3}$ toward the so-called "grain growth regime" in $t^{1/2}$ established for vanishing ϕ remains mostly unexplored, both experimentally and theoretically. In view of the large variety of phase-separating systems and their existing and potential applications, improving the knowledge on this transition is highly desirable. We have chosen liquid foams as model systems because the domains are fluid and isotropic.

Liquid foams are metastable dispersions of gas bubbles in a liquid matrix (8–10). They are not only interesting model systems for coarsening studies, but also they have

Author contributions: S.C.-A., O.P., R.H., E.R., A.S., and D.L. designed research; N.G., M.P., A.M., A.R., S.C.-A., O.P., R.H., E.R., A.S., and D.L. performed research; R.H. contributed analytic tools; N.G., M.P., A.M., S.C.-A., O.P., and R.H. analyzed data; and N.G., M.P., S.C.-A., O.P., R.H., E.R., A.S., D.J.D., and D.L. wrote the paper.

The authors declare no competing interest.

This article is a PNAS Direct Submission.

Copyright © 2023 the Author(s). Published by PNAS. This article is distributed under Creative Commons Attribution-NonCommercial-NoDerivatives License 4.0 (CC BY-NC-ND).

[1]To whom correspondence may be addressed. Email: dominique.langevin@universite-paris-saclay.fr.

This article contains supporting information online at https://www.pnas.org/lookup/suppl/doi:10.1073/pnas.2306551120/-/DCSupplemental.

Published September 14, 2023.

Downloaded from https://www.pnas.org by 90.92.98.18 on September 15, 2024 from IP address 90.92.98.18.

numerous practical applications. Solidifying the continuous phase of liquid foams yields solid materials which inherit the structure of their precursors. Solid foams are widely used for packaging, insulation, or as lightweight construction materials such as foamed cement or metallic foams. Their solid volume fraction is frequently chosen between 20% and 50%, to confer sufficient mechanical strength (17). The solid foam microstructure has an impact on its mechanical properties, for a given density. Hierarchical foam structures were predicted to have an order of magnitude improvement of mechanical strength-to-density ratio with just two levels of hierarchy (18). Therefore, such hierarchical structures self-assembled by foam coarsening, as we report here, could be of great interest for applications.

When the liquid volume fraction ϕ is large, the bubbles are spherical and isolated, and the dispersions are called "bubbly liquids" rather than foams. Coarsening is expected to lead to a bubble growth proportional to $t^{1/3}$, as in Ostwald ripening. When the liquid fraction ϕ is decreased below a critical value, ϕ_{rcp}, contacts between neighboring bubbles are formed and their shapes progressively evolve from spheres to polyhedra in the limit $\phi \to 0$ (8–10). Equilibrium films separating neighboring bubbles have generally thicknesses of a few tens of nanometers. They are connected three by three to channels called Plateau borders, themselves connected at vertices. For disordered monodisperse foams, $\phi_{rcp} \approx 36\%$, and ϕ_{rcp} is expected to decrease slightly as polydispersity increases (19). Experiments with 3D foams of small liquid fractions have shown that the average bubble radius grows at long times as $t^{1/2}$ (20–23), in contrast with the $t^{1/3}$ scaling observed in the case of Ostwald ripening. The value of the exponent is related to the mechanism of gas transfer between bubbles. In dry foams, it occurs mostly through the thin films between bubbles, whereas in bubbly liquids, gas is transferred through bulk liquid (24). Another important feature of coarsening is the shape of the bubble size distribution that is also expected to change with liquid fraction. Several experimental and numerical works (21, 25–29) show that the normalized distribution is asymmetric, of the Weibull or lognormal type, in the regime associated with the $t^{1/2}$ growth law, whereas for the $t^{1/3}$ regime, it is more symmetric and narrower (13).

Foams evolve with time not only because of coarsening but also due to gravity drainage (8–10) and possibly due to rupture of liquid films separating neighboring bubbles, called coalescence. Since gravity drainage and coarsening are coupled, studying and modeling coarsening requires gravity drainage to be suppressed. Pioneering foam coarsening experiments were performed with dry horizontal 2D foams (single layers of bubbles) where drainage was not an issue (31). Studies of 3D foams on Earth are generally restricted to small liquid fractions $\phi \ll 0.1$, where drainage is slow enough (20, 32).

To rule out artifacts related to gravity in 3D foams whatever the liquid fraction, we have performed foam coarsening experiments in microgravity, on board the International Space Station (ISS), where drainage is suppressed. Samples with arbitrary liquid volume fractions ϕ can thus be studied over long times, up to several days, as required to investigate the Scaling State of foam containing a significant fraction of liquid.

1. Results and Discussion

A. Excess of Small Bubbles. We have investigated foam coarsening for liquid fractions between 15% and 50% using the instrument described in ref. 33. Details can be found in the *Materials and Methods*. The evolution of the bubble size has been studied elsewhere (34, 35). From the sample surface observations (a typical image is shown in Fig. 1*A*), we measure the bubble sizes using image analysis and determine the bubble size distributions of the radius normalized by its average $\rho = R/\langle R \rangle$. The initial size distributions produced by our experimental setup are asymmetric (positive skew) with a maximum at $\rho \approx 0.6$ (see Fig. 1*B* for foam with 15% liquid fraction as an example). The normalized size distributions broaden with time, and a sharp peak builds up progressively for small bubble sizes, i.e., $\rho \approx 0.3$, until a stationary form is reached, indicating a Scaling State. This is shown in Fig. 1*B* for times $t > 2{,}000$ s. This evolution is typical of the measurements we have made for foams with liquid fractions within the range $15\% \leq \phi < \phi^*$, with $\phi^* \approx 39\%$. The small bubbles corresponding to the peak in the distribution are highlighted in Fig. 1*A*. After an increase in the transient regime,

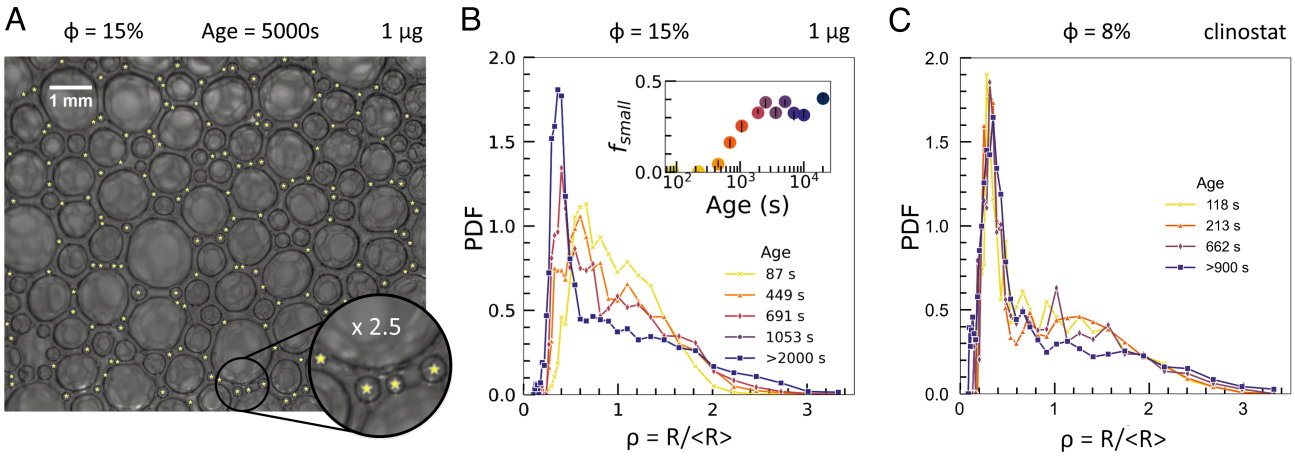

Fig. 1. Excess of small bubbles. (*A*) Image of foam surface ($\phi = 15\%$) in the Scaling State regime. Yellow stars have been superimposed on the image to highlight the small bubbles corresponding to the sharp peak in the distribution shown in (*B*). (*B*) Probability density function of normalized bubble radius $\rho = R/\langle R \rangle$ at different foam ages as indicated, for a foam with liquid fraction $\phi = 15\%$. The curve corresponding to age > 2,000 s represents the Scaling State regime, for which the normalized distribution no longer evolves. *Inset*: evolution of the proportion of small bubbles as a function of time. The number fraction f_{small} is obtained by dividing the number of bubbles with radius $R < R_t$ by the total number of bubbles in the sample (see Section B for details). A change in R_t by ±5% induces a variation of f_{small} smaller than the point size. (*C*) Probability density function of normalized bubble radius at different ages as indicated, for a sample with liquid fraction $\phi = 8\%$ studied on ground.

Downloaded from https://www.pnas.org by 90.92.98.18 on September 15, 2024 from IP address 90.92.98.18.

they finally represent about 35% of the total bubble population in the scaling state (inset of Fig. 1*B*). We also measured the number of those small bubbles per foam vertex to reach a maximum average value of 1.5, due to space limitation in the vertices. As a consequence, the size distribution becomes invariant in time (statistically self-similar) as observed.

Up to now, such an excess of small bubbles has not been reported in the literature (21, 25, 27, 29). In order to check whether distributions with an excess of small bubbles are also found in drier foams, we have performed coarsening experiments using the same surfactant and a liquid fraction of 8%, low enough for gravity effects to be compensated in a ground-based experiment by rotating the cell around a horizontal axis (clinostat). As shown in Fig. 1*C*, we observed a similar excess of small bubbles. The small bubbles were thus seemingly present but not detected in previous studies. This is probably because high spatial resolution together with a careful image analysis is needed (36). The only experimental work we have found that indirectly relates to this is that of Feitosa and Durian (25), which reports the development of transient bidispersity for initially monodisperse bubbles in a steady state column, where drainage and coarsening occur simultaneously. In their simulations of 2D foam coarsening, Khakalo et al. (37) have observed an excess of small bubbles but the gas transfer through interstitial bulk liquid was not taken into account. Other peculiar size distributions such as "Apollonian" distributions were observed during the decay of beer foam (38) and with emulsions (39). In contrast to what happens in our systems, they arose from coalescence events.

For $\phi > \phi^*$, we have observed a different scenario: the initial bubble size distribution shrinks until a steady state is reached where the size distribution is notably narrow (*SI Appendix*, Fig. S1). The latter distribution is reminiscent of the theoretical distribution predicted for the Ostwald regime (13). Around ϕ^*, a change in the growth laws for the average bubble size is also shown for the same foam samples (34, 35):

$$R_{32}^2(t) = R_{32}^2(0) + \Omega_p\, t \qquad \text{for} \quad \phi < \phi^*, \qquad [1]$$

$$R_{32}^3(t) = R_{32}^3(0) + \Omega_c\, t \qquad \text{for} \quad \phi > \phi^*. \qquad [2]$$

The Sauter mean radius $R_{32} = \langle R^3 \rangle / \langle R^2 \rangle$ is defined as the ratio of third to second moments of the bubble radius distribution.

B. Transition from Jammed Bubbles to Roaming Bubbles. To clarify the origin of the hierarchical bubble population, we have identified bubbles that eventually disappear and tracked the evolution of their area. Fig. 2*A* shows examples of such measurements in a foam with $\phi = 15\%$. Similar data are shown for other liquid fractions between $\phi = 20\%$ and $\phi = 33\%$ in *SI Appendix* (cf. *SI Appendix*, Fig. S2). Over time, the individual bubble area can either increase or decrease, depending on the bubble's gas exchanges with its neighbors, but most of the observed bubbles eventually shrink (Fig. 2*A*). The magnitude of the shrinking rate appears to be initially similar to that characterizing the initial growing rate. Then, a transition occurs and the area decreases much more slowly. Actually, the shrinking after this transition can be extremely slow, and we think this is the underlying mechanism explaining why a peak at smaller than average bubbles builds up in the size distribution. Remarkably, the bubble radius at the transition, R_t, is such that its area $A_t = \pi R_t^2$ increases linearly with time, which is similar to the evolution of the squared mean radius in the Scaling State (Eq. **1**). Moreover, the transition to the very small shrinking rate appears to occur when the bubble has become so small that it fits inside the interstice between three larger bubbles at the surface and possibly loses contacts with them as sketched in Fig. 2*B*. (Movies S1–S3). They are free to move throughout the interstice without being pressed against multiple neighbors. Such small bubbles can have different configurations in the interstice, i.e., near the center of the interstice or in contact with one bubble or two bubbles, but these configurations do not last for the entire life of the bubbles because their positions are jostled as the jammed bubbles intermittently rearrange due to the coarsening-induced dynamics (9, 40). We call the small bubbles roaming bubbles. Note that they are reminiscent of rattlers (grains carrying no force) in granular media (41). We conjecture that the bubble size at the transition, R_t, should scale as the maximum radius of a sphere that can be trapped in such an interstice at the wall surface.

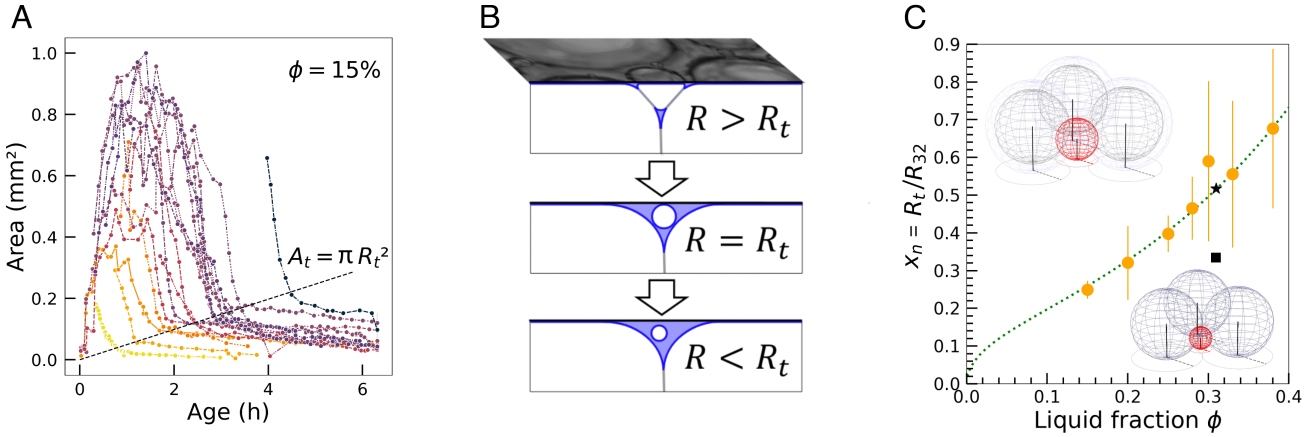

Fig. 2. Roaming transition: (*A*) Evolution of the area of individual bubbles as a function of foam age measured as the time elapsed since the end of the foam sample production, for $\phi = 15\%$. The area $A_t = \pi R_t^2$ denotes the bubble area at the wall when its shrinking abruptly slows down (*Text*). Each label corresponds to a different bubble. (*B*) The transition to the very small shrinking rate was observed to occur when the foam bubble has become so small that it fits inside the interstice between neighboring larger bubbles. The corresponding geometrical transition can therefore be described as follows: When its radius is larger than R_t, the small bubble is a foam bubble, in the fact that it shares thin liquid films with its neighbors. In contrast, as its radius reaches values smaller than R_t, the bubble loses its contacts with its neighbors: it becomes a roaming bubble and its shrinking rate is strongly decreased. (*C*) Coefficient $x_n = R_t/R_{32}$ as a function of ϕ. Filled orange disks: values deduced from the tracking of individual bubbles. Error bars show $\pm 3SD$, to highlight the observed variability. Black stars/drawings: calculation of x_n from the size of a hard sphere (in red) that can be inserted into the interstice formed by three spheres at the wall, assuming either a compact bubble cage (*Bottom*) or slight loosening (*Top*) of the latter. The dotted line corresponds to Eq. **4** with $\xi = 2.2$.

Downloaded from https://www.pnas.org by 90.92.98.18 on September 15, 2024 from IP address 90.92.98.18.

In a coarsening foam that has reached the Scaling State, there is only one independent length scale of the bubble packing structure. Since the bubbles that form the interstices are bigger than the encaged roaming bubbles, we chose to characterize their average size by the Sauter mean radius. With respect to $\langle R \rangle$, R_{32} indeed represents mainly the average radius of the larger bubbles of the distribution and minimizes the contribution of the small bubbles. At a time t, the maximum radius of a sphere trapped in such a vertex can be written, on average:

$$R_t(t, \phi) = x_n(\phi) R_{32}(t), \quad [3]$$

where $x_n(\phi)$ is a dimensionless geometrical coefficient. We show in *SI Appendix*, Fig. S3 the plots of R_t versus R_{32} for each liquid fraction. The plots are reasonably described by Eq. **3**, allowing the determination of the average coefficient x_n for each liquid fraction (Fig. 2*C*). $x_n(\phi)$ varies from 0.25 to 0.55 as ϕ varies from 15% to 38%, respectively. Using those x_n values, the transition radii R_t collapse on a linear master curve when plotted versus $x_n(\phi)R_{32}$ (cf. *SI Appendix*, Fig. S3).

We have performed a geometrical calculation of the size of the interstice between a plane and three perfect spheres of equal radius R_{32} in contact together and with the plane (Fig. 2*C*). This leads to $x_n = 1/3$. This value is smaller than what is measured for liquid fractions corresponding to the bubble random close packing fraction, i.e., $\phi_{\text{rcp}} \approx 31\%$ (see Section D for more details), beyond which the bubbles are spherical. As the liquid fraction gets close to ϕ_{rcp}, the foam osmotic pressure, which pushes neighboring bubbles against each other at contacts, becomes very low, and it can be inferred that the cage formed by the triplets of bubbles of radius R_{32} loosens. Note that such a geometrical loosening effect is general and independent of friction (42). Therefore, as a correction to the previous calculation, a distance ϵR_{32} is added around each sphere (Fig. 2*C*). The coefficient now reads: $x_n = \frac{\epsilon(2+\epsilon)+\frac{4}{3}(1+\epsilon)^2}{2(2+\epsilon)} \approx \frac{1}{3} + \epsilon$, and it increases significantly due to the loosening effect: assuming a moderate loosening $\epsilon \approx 0.2$ gives $x_n \approx 0.5$ which is in better agreement with our measurements (Fig. 2*C* and Movie S2). It is reasonable to assume that polydispersity may also impact the size of the interstice. This effect can be estimated by considering two bubbles of size R_{32} and a third one with size βR_{32}. It can be shown that in such a case, the coefficient reads $x_n \approx \frac{1}{3} + 0.11(\beta - 1)$. Therefore, the magnitude of the polydispersity effect is much weaker than the previous one, in addition to the fact that it can work in both directions, depending on the value of β, which we observed to vary in the range $0.3 < \beta < 1.5$ (*SI Appendix*, Fig. S4). However, it is worth noting that a significant fraction of bubbles have a radius larger than R_{32}, i.e., $1 \leq \beta \leq 1.5$, and that almost half of the nodes are bounded by one such large bubble (see *SI Appendix*, Fig. S4 as an example for foam with 15% liquid). These findings suggest that the effect of polydispersity is only slightly positive and should only slightly increase x_n, i.e., the size of the wall interstice. We conclude that the loosening of the bubble packing is the main effect accounting for the measured x_n values.

To extend our prediction to any liquid fraction $\phi \leq \phi_{\text{rcp}}$, we turn to ref. 43, where the radius of passage of a hard sphere through the liquid channels so-called Plateau borders was determined as a function of ϕ and bubble radius R in a monodisperse foam. Due to the uniformity of the capillary pressure through the foam, which sets the radius of curvature of the channels, and thus their cross-section, the bubble radius at the transition R_t should be proportional to this radius of passage. Following the approach proposed in ref. 43 we refer to the effective pore radius introduced by Johnson et al. (44): $\Lambda \approx (8\tilde{k}/\tilde{\sigma})^{1/2} R$, where $\tilde{k}$ is the dimensionless liquid Darcy's permeability through the foam structure, i.e., k/R^2, and $\tilde{\sigma}$ is the ratio of the electrical conductivity of the foam to that of the foaming liquid. Therefore, the expression sought for x_n is

$$x_n = \xi(8\tilde{k}/\tilde{\sigma})^{\frac{1}{2}}, \quad [4]$$

where ξ is a geometrical coefficient to be determined. Note that the latter is expected to account for the loosening and polydispersity effects discussed previously. To continue, we now need expressions for $\tilde{k}$ and $\tilde{\sigma}$. Since Λ was initially proposed for solid porous media, the permeability should correspond to foam having rigid interfaces to mimic solid-like boundary conditions. As studied by Rouyer et al. (45), its expression is given by $\tilde{k} = \phi^2/(312(1 - 2.15\phi + 1.37\phi^2)^2)$ within the range of liquid fractions $1\% \leq \phi \leq 40\%$. For foams and bubbly liquids, Feitosa et al. (46) proposed an approximate analytical expression for $\tilde{\sigma}$, i.e., $\tilde{\sigma} = 2\phi(1 + 12\phi)/(6 + 29\phi - 9\phi^2)$. Using these expressions, we set $\xi = 2.2$ in Eq. **4** in order to get a predicted value of x_n close to the measured value 0.53 for $\phi \approx \phi_{\text{rcp}}$ (Fig. 2*C*). Remarkably, the agreement with our experimental data is very good over the whole range of liquid fractions, which reinforces the physical picture that R_t actually corresponds to the size of the interstices formed by the jammed bubbles around the roaming bubbles. Note that in all of the above, nothing is really specific to the fact that we are looking at the wall. In bulk, typical interstices are formed by four bubbles in a tetrahedral assembly. The geometrical calculation for four bubbles in contact gives $\sqrt{\frac{3}{2}} - 1 \approx 0.225$, compared to 1/3 at the wall. Therefore, we can estimate x_n for bulk by using Eq. **4** with coefficient $\xi = 2.2 \times (0.225/0.333) \approx 1.5$. Provided this value is used, the behavior observed at the wall should be similar to the behavior observed in the bulk of the foam.

C. Dissolution Rate of the Roaming Bubbles. In this section, we focus on the dissolution rate of the roaming bubbles in the range $\phi < \phi^*$. We first consider the data for times longer than those that mark the intersection of the dissolution curve with $A(t) = \pi R_t^2$ (Fig. 2*A* and *SI Appendix*, S2). We follow the evolution of the radius of roaming bubbles $R(t)$ for $R(0) \lesssim R_t$. For comparison, we similarly analyze individual bubbles roaming in the bubbly liquids ($\phi > \phi^*$), from the instant they start to continuously shrink. Several examples of the curves are presented in Fig. 3*A*. We observe that the following function fits well all the curves (48, 49):

$$R^2(t) = R^2(0) - \Omega_r t, \quad [5]$$

where the only fitted parameter Ω_r represents the dissolution rate of the roaming bubble. Such fits were performed for all the liquid fractions and the average values of Ω_r are presented in Fig. 3*B*. Ω_r is found to depend only weakly on liquid fraction: $\Omega_r \approx 1$ to 2 $\mu m^2/s$. We also plot on Fig. 3*B* the growth rate Ω_p that characterizes the coarsening of the foam in the Scaling State (Eq. **1**). It appears that $\Omega_p \gg \Omega_r$ for $\phi \lesssim \phi_{\text{rcp}} \approx 31\%$, and $\Omega_p \approx \Omega_r$ for $\phi_{\text{rcp}} < \phi < \phi^*$. This comparison reinforces our discussion in Section A: The size of the roaming bubbles, represented on the *Left* side of the distribution, varies more slowly than the average bubble size. As a result, the roaming bubbles accumulate in the interstices formed by the larger bubbles.

Downloaded from https://www.pnas.org by 90.92.98.18 on September 15, 2024 from IP address 90.92.98.18.

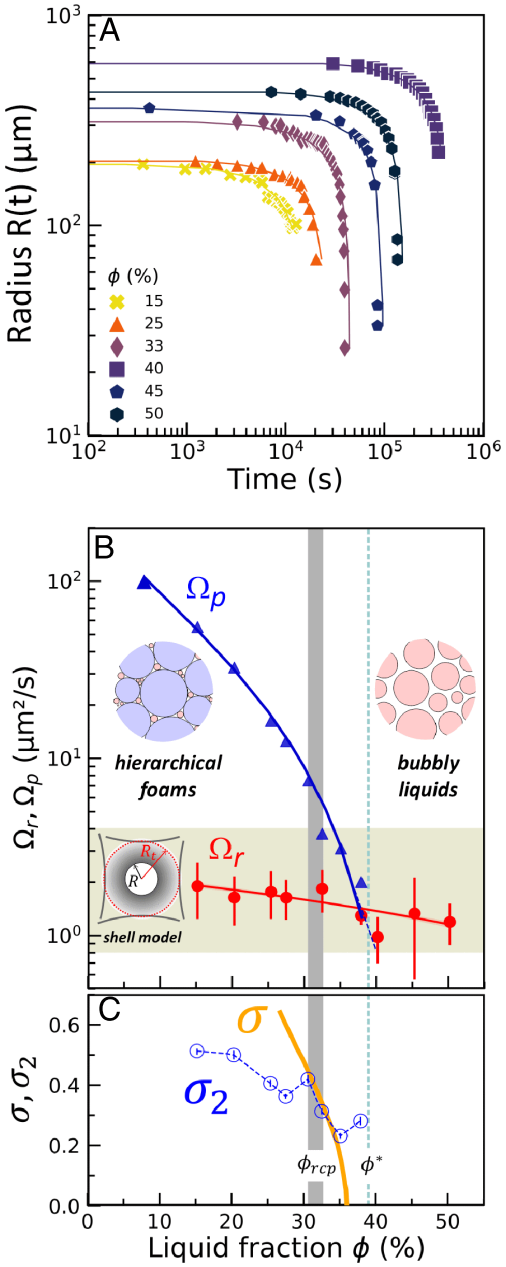

Fig. 3. Roaming bubble dissolution: (*A*) Radius evolution of dissolving roaming bubbles where each curve represents a single bubble. The solid lines correspond to fits of Eq. **5**. (*B*) Average shrinking rate of roaming bubbles Ω_r as a function of liquid fraction compared to the growth rate of average bubble size in the foam Ω_p (Eq. **1**, data from ref. 34). The lines are guides to the eye. Ω_r values fall within the range (highlighted in green) predicted by the shell model (*SI Appendix*, Eq. 1), schematically illustrated by the inside drawing. Error bars correspond to $\pm 1SD$. The growth rate Ω_p is strongly dependent on the liquid fraction, at the difference of the dissolution rate Ω_r. (*C*) Measured shape parameter σ_2 of the jammed bubbles size distribution (*SI Appendix*, Eq. 6) as a function of liquid fraction (blue circles). The (orange) continuous line represents the maximum packing volume fraction predicted for a lognormal distribution of spheres with shape parameter σ (19, 47). The gray vertical area highlights the range where σ and σ_2 coincide, from which we deduce $\phi_{rcp} \approx$ 30 to 32%. This also corresponds to the range of liquid fractions where Ω_r is comparable to Ω_p in *B*.

As the dissolution rate Ω_r plays a crucial role in the accumulation mechanism of the roaming bubbles, we seek here to understand this value. The starting point is the comparison of our data with theory for the dissolution of isolated bubbles (48, 49), which gives the steady dissolution rate far enough from the final instant of bubble disappearance as $\Omega_r = -dR^2/dt = 2D_m V_m\,(c(R) - c_\infty) = 2D_m V_m \mathrm{He} P_0 (1-\zeta)$, where the saturation parameter $\zeta = c_\infty/\mathrm{He}P_0$ characterizes the gas saturation of the liquid environment, $c(R)$ and c_∞ are, respectively, the gas concentrations in the liquid at the bubble surface and at infinity, P_0 is the gas pressure at infinity, and He and D_m are, respectively, the Henry solubility and the diffusion coefficient of the air molecules in the foaming solution. V_m is the molar volume of the gas at the pressure P_0. From the measured Ω_r, we deduce an effective value for the saturation parameter: $\zeta = 0.973 - 0.987$, which suggests that the bubbles dissolve faster than if they were isolated, and despite the presence of the large neighboring bubbles which impose at their interface a gas concentration larger than $\mathrm{He}P_0$. To explain this apparent contradiction, it is important to understand that the gas transfer is controlled by the concentration gradient and not only by the concentration difference. Due to the short distances involved between the roaming bubble interface and the interfaces of the large neighboring bubbles, the concentration gradient around the roaming bubble reaches relatively high values compared to the case of the isolated bubble. Therefore, to mimic this situation, we consider the configuration illustrated in the *inset* of Fig. 3*B*, where a roaming bubble of radius R is centered in a cavity of radius R_t and is surrounded by a liquid shell of thickness $R_t - R$. The local concentration at the outside boundary of the shell is estimated as that at the surface of a bubble of average size R_{32}. From Fick's first law, we then predict the bubble dissolution rate Ω_r in that shell environment (see more details in *SI Appendix*). For the range of values of R_{32} in the scaling state in our experiments and typical ratio R/R_t, we expect $\Omega_r \approx$ 0.75 to 4 $\mu m^2/s$ which provides boundaries consistent with the measured values of Ω_r (cf. Fig. 3*B*).

A drawback of this shell-like model is that the roaming bubble is assumed to remain at the center of the interstice, which is not always the case. Indeed, we often noticed transient apparent contacts between the roaming bubble and either one of the bubbles delimiting the interstice or two larger bubbles forming a corner. These transient contacts can result from adhesive forces. We have indeed observed that under microgravity conditions, persistent aggregates form spontaneously in dilute bubble dispersions. In complementary ground-based experiments, we have observed a contact angle close to $3-4^o$ (34). The underlying configuration may be an adhesive contact with the formation of a liquid film that slightly flattens the bubbles or it can be a near-contact with a small separation distance so that the roaming bubble is spherical. Since it was not possible to distinguish between these two types of contact, we estimated the dissolution rate for both cases (see details of the calculation in *SI Appendix*). In the range of average bubble sizes R_{32} of our experiments, assuming a film thickness effective for the transport of gas of the order of 40 to 60 nm (34), we found that the expected rates fall within the range of values measured for Ω_r. This remains broadly true if the bubble is in a corner, where the corresponding dissolution rate is twice larger. Therefore, whatever the configuration considered for the roaming bubble in the interstice, we find values for its dissolution rate that are compatible with our measurements, which gives robustness to the proposed mechanism based on the accumulation of long-lasting roaming bubbles in the foam interstices.

D. Bubble Size Distributions and Random Close Packing Fraction in the Scaling State. Let us analyze now the role of liquid fraction on the distribution shape. Details on the analysis are given in *SI Appendix*. Fig. 4 shows the normalized bubble size

Downloaded from https://www.pnas.org by 90.92.98.18 on September 15, 2024 from IP address 90.92.98.18.

distributions observed in the Scaling State for each sample liquid fraction.

The PDF for $\phi = 15\%$ is the same as that of Fig. 1 in the Scaling State. It exhibits a prominent narrow peak, that we identified to the roaming bubble population in Section A, followed by a broad peak for the foam jammed bubble population. These features qualitatively persist up to $\phi < 38\%$ but the narrow peak progressively shifts toward larger ρ while its height decreases. For $\phi \geq 40\%$, PDFs exhibit a single peak, which is consistent with the fact that all bubbles should be roaming bubbles. PDFs become narrower as ϕ increases and their peak height increases. This qualitative change is also captured by the abrupt variation of statistical quantities like polydispersity (cf. *SI Appendix*, Fig. S5). None of the existing theories predict such distributions (15). These findings indicate a cross-over between qualitatively different PDFs occurring for a liquid fraction $\phi^* \approx 39\%$. This transition coincides with the observed change of growth laws Eqs. **1** and **2** and it is attributed to the onset of the formation of a foam gel due to weak attraction between bubbles as evidenced by finite contact angle at films junctions (34).

The expected jamming liquid fraction for randomly close-packed monodisperse hard spheres is $\phi_{rcp} = 36\%$. However, polydispersity will reduce this value since smaller bubbles can fit into the interstices between larger ones. This effect has been predicted by numerical simulations of polydisperse close packings of spherical particles with lognormal PDF, as a function of the shape parameter σ (19, 47). In our foams, the close packing concerns the population of jammed bubbles, which are connected to each other *via* films. Therefore, we compare the measured shape parameter of the foam bubble distribution σ_2 to the predicted ones (cf. Fig. 3*C*). We find them to coincide within the range $\phi = 30\%$ and $\phi = 32\%$: We expect the close packing fraction ϕ_{rcp} of our foams to lay inside the range between these 2 values.

To provide an independent result of the close packing fraction of frictionless spheres with the polydispersity observed in our samples in the Scaling State, we have performed molecular dynamics simulations. Since here we are only interested in the geometrical sphere packing problem at the jamming point where the confinement pressure and interaction forces drop to zero with increasing ϕ, we expect the nature of the interaction law used in the simulations to have only a minor impact. Using Hertzian interactions, in the framework of the molecular dynamics code LAMMPS (*Materials and Methods*), we obtained ϕ_{rcp} =31.0 $\pm$0.5%, in remarkable agreement with our analysis based on

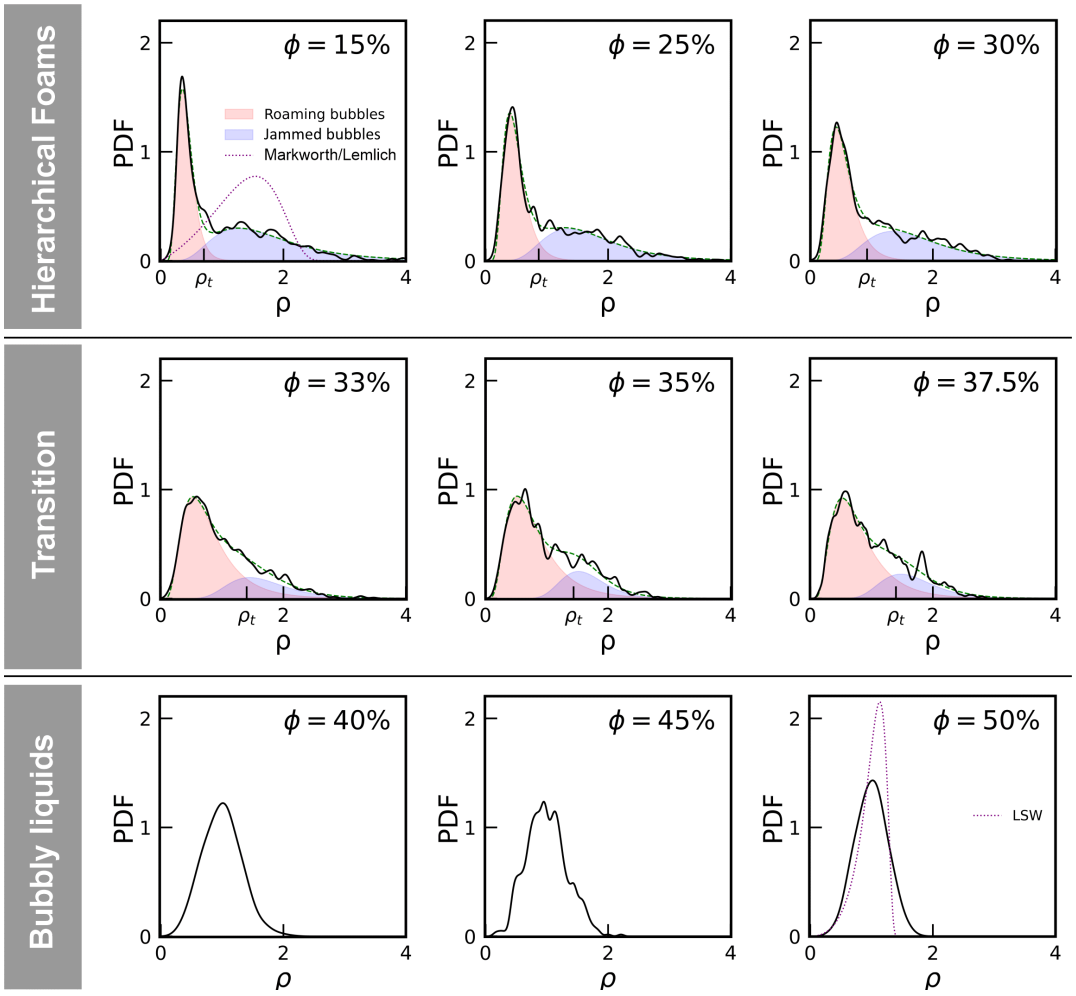

Fig. 4. Bubble size distributions of normalized radius $\rho = R/\langle R \rangle$ for each liquid fraction as labeled. The data are represented by black continuous lines. The green dashed lines represent the bilognormal PDFs (*SI Appendix*, Eq. 6) fitted to the data. The red (resp. blue) shaded area corresponds to the roaming bubble PDF $w\ \mathcal{L}(r; m_1, \sigma_1)$ (resp. to the foam bubble PDF $(1-w)\ \mathcal{L}(\rho; m_2, \sigma_2)$) with the parameters given in *SI Appendix*, Fig. S5. In the plots for ϕ up to 38%, the width of the roaming bubble distributions is characterized by ρ_t, defined in *SI Appendix*, Eq. 8. For $\phi = 15\%$, the dotted line is the PDF predicted for wet foams by Markworth (50) based on Lemlich's model (51) for that ϕ. As a comparison, for $\phi = 50\%$, the dotted line is the LSW prediction (15) ($\phi = 1$).

Downloaded from https://www.pnas.org by 90.92.98.18 on September 15, 2024 from IP address 90.92.98.18.

the work of Farr and Groot (19). Note that strictly speaking, our simulations only provide an upper bound for the optimal random close packing fraction of such polydisperse spheres, which may be obtained by more sophisticated simulation procedures described in the literature (52). However, in the context of our experiments, the truly relevant packing fraction is the one of a coarsening foam. In this case, we expect a local packing which is not exactly the most compact possible one. A jammed foam regularly undergoes rearrangements, helping it to settle into new minimal energy configurations. This implies that in between rearrangements, the packing is not always optimally close-packed. Simulations of this where we also replace the Hertzian interaction by the more realistic Morse Witten law (53, 54) are the subject of ongoing work.

E. Potential Consequences on Foam Properties. The roaming bubbles represent a significant proportion of the total number of bubbles. As a result, exclusion of the roaming bubbles from the determination of the average radius leads to an up to 3-fold overestimation of coarsening rates, depending on the liquid fraction (34).

In terms of volume fraction with respect to the liquid volume, the roaming bubbles represent up to ten percent depending on ϕ. It can therefore be expected that their impact is important for certain properties. Roaming bubbles can also modify foam drainage, where they slow down the flow of the liquid. A study with solid spheres, located in the nodes of the liquid network of the foam, showed that such an amount of particles in the liquid could reduce the permeability of the foam by 40% (55). This shows the bias of systematically ignoring their presence. Let us mention that to date, this effect has never been taken into account in permeability modeling.

The presence of the roaming bubbles can be highly detrimental for applications of foams where the microstructure is an important parameter, all the more so if they migrate and accumulate in large proportions in certain places. Moreover, for a number of these applications, the interstitial liquid is a complex fluid, possibly with yield stress properties that will prevent gravity from evacuating the roaming bubbles: One expects to find relatively high volume fractions of roaming bubbles in such systems.

By examining some recent papers on foamed construction materials, we recognized traces of the presence of such roaming bubbles. For example in ref. 56, very small pores can be seen in the bulk nodes of cement foam solidified after coarsening, as revealed by the microtomography image. There is every reason to believe that literature is full of such examples.

On the other hand, one can make use of these roaming bubbles. Note that the stakes are high in terms of producing solid foam structures with hierarchical porosity, including both macro- and microscaled pores. Such structures have recently been produced by 3D printing (57) and they were found to present enhanced energy absorption properties and enhanced mechanical resistance to cyclic loading.

2. Conclusions

Studies of foam samples where the liquid fraction remains constant over periods of several days, without any confounding effects of gravitational drainage, reveal that, as demonstrated earlier for dry foams, wet foams evolve toward a Scaling State. In this state, the bubble size distributions show a well-defined peak toward smaller than average sizes, i.e., an excess of bubbles for sizes close to $0.3\langle R\rangle$. This feature is not predicted by existing theories. During coarsening, as shrinking bubbles become smaller than the size of interstices between the larger bubbles, they can move independently from the jammed bubble network to become roaming bubbles. Surprisingly, although we have been able to reproduce this effect on Earth, no previous experimental study mentions the presence of these small bubbles, except for a study of draining foams (25) but where roaming bubbles have not been identified as such. This suggests that, although their study has been underestimated, hierarchical bubble size distributions can build up on Earth if drainage is not too fast compared to dissolution and coarsening.

The dissolution rate of these roaming bubbles is approximately constant, whatever the liquid fraction of the samples. The dissolution rate is consistent with calculations based on the gas transfer through the liquid shell that surrounds the roaming bubble, or through the "contact" between one roaming bubble and larger jammed bubbles surrounding them. The key point in the accumulation of the small bubbles in the interstices formed by the larger bubbles, is the fact that the rate of disappearance of these bubbles is much smaller than the average growth rate of the jammed bubbles. This behavior is observed for foams with liquid fractions smaller than the random close packing fraction ϕ_{rcp}. For ϕ between ϕ_{rcp} and ϕ^*, where the bubble assembly approaches the regime of bubbly liquids, the rate of dissolution of the roaming bubbles reaches progressively the growth rate of the jammed bubbles, which suppresses the accumulation mechanism. As a consequence, the peak initially observed for liquid fractions $\phi < \phi_{rcp}$ shifts toward $\langle R\rangle$ and a distribution almost centered on $\langle R\rangle$, characteristic of bubbly liquids, is eventually observed. For ϕ above ϕ^*, none of the bubbles are confined.

In closing, we have shown the existence of naturally developed hierarchical bubble size distributions in coarsening foams. We present a comprehensive view of coarsening of wet foams, completely different from expectations, with a persistent coexistence of jammed bubbles with small roaming bubbles, and the existence of a range between ϕ_{rcp} and ϕ^* where foam bubbles are still jammed although not close-packed. These findings challenge our current understanding of foam coarsening and have potential implications in the design and performance of foamy materials. This view should not be restricted to foams but also be applicable to other two-phase systems driven by interfacial effects, such as emulsions, alloys, and binary fluid/polymer mixtures. It should be mentioned that recent studies of alloys with small volume fraction of the continuous phase suggest that the Ostwald ripening regime persists when ϕ is smaller than ϕ_{rcp} (16). The difference between coarsening of foams and alloys remains to be clarified.

3. Materials and Methods

The foams were made with aqueous solutions of an ionic surfactant, tetradecyltrimethyl-ammonium bromide (TTAB), with purity $\geq$ 99% and used as received from Sigma–Aldrich. It was dissolved at 5 g/L in ultrapure water (resistivity 18.2 MΩ cm). This concentration is 4 times larger than the critical micellar concentration and large enough to prevent coalescence. The surface tension of the TTAB solution measured at room temperature is $\gamma = 37.1$ mN/m. The Henry solubility coefficient of the air molecules in the foaming solution is $He = 7.4\,10^{-6}$ mol m^{-3} Pa^{-1} and their diffusion coefficient in the foaming solution is $D_m = 2.0\,10^{-9}$ m^{2}s^{-1} (34).

The majority of the experiments were performed on board the International Space Station using the experiment container described in ref. 33. In this environment, the residual gravity acceleration fluctuations are reported to be on the order of or less than a μg, for frequencies below 0.01 Hz (58). Each foam cell was filled on Earth with a given volume of foaming solution (measured by weight at controlled temperature) and air, then hermetically sealed. The liquid volume fraction ϕ contained in each cell was deduced from the liquid volume and the total cell volume. After the completion of the experiments, the cells were

Downloaded from https://www.pnas.org by 90.92.98.18 on September 15, 2024 from IP address 90.92.98.18.

sent back to Earth and we checked that their weight had varied by less than 1%. All the experiments were repeated three times and found reproducible, even a few months apart.

In addition, we made on Earth a clinostat experiment with a foaming liquid of composition identical to that of the ISS experiments. The foams were produced with the double-syringe method (36) filled with air and a volume of the foaming solution in order to set the liquid fraction to $7.8\% \pm 0.2\%$. Note that the initial bubble size distribution with this foam production is close to that of the Scaling State. The sample was placed in a cylindrical cell (diameter 30 mm, thickness 12.8 mm) with transparent flat faces. The cell was kept with its symmetry axis aligned in the horizontal direction and rotated about this axis with a speed of rotation equal to 15 rpm.

Foam age is counted from the instant when the foaming process stops. Bubbles at the surface of the sample are recorded using a video camera. Every image (such as the one shown in Fig. 1*A*) was analyzed as described in ref. 36. We checked that the radial profile of liquid fraction remained constant throughout the measurement duration, indicating that the effect of gravity drainage was indeed counteracted and that the rotation did not induce radial drainage either in the clinostat. The bubble area A was deduced from the area inside the contour of the bubbles measured using the ellipses method (36). Finally, the bubble radius is calculated as $R = \sqrt{A/\pi}$. In the ISS experiments, simultaneously to the video recording, the intensity of light transmitted through the sample was recorded, which provided the average bubble size in the bulk of the sample as explained in ref. 36. Our results showed that the evolution of the average bubble radius measured either at the surface or in the bulk is similar.

We also performed numerical simulations to evaluate the random close packing liquid fraction of the bubbles. In the framework of the molecular dynamics code LAMMPS (59), a cubic simulation box was filled by spheres with repulsive, Hertzian interactions with radii randomly chosen from a distribution corresponding to the one we observe experimentally for $\phi = 33\%$ in the Scaling State (Fig. 4). The number of spheres was of the order of 2,000, similar to our foam coarsening experiments at the largest investigated foam ages. To fill the simulation cell, we started with an initial cell volume so large that the sphere dispersion was highly diluted. Using the pressostat provided by LAMMPS, we then shrunk the cubic cell and compacted these structures until a very small osmotic pressure appeared. We then turned off the pressostat and equilibrated the sample for imposed simulation box volumes, varied by small steps around the previous value. The close packing fraction was estimated by plotting confinement pressure versus packing fraction and by detecting the ϕ value where zero pressure is reached within numerical accuracy. We did this for 5 different initial random seeds and found $\phi_{rcp} = 31.0 \pm 0.5\%$. The way you compact a packing has a large impact on the final close packing fraction in frictional granular materials and to a lesser extent also in frictionless systems. To investigate this effect, we applied simulated gravity to dilute sphere dispersions as an alternative to the initial pressostat procedure. Kinetic energy was dissipated by introducing viscous friction in the contact law. This procedure mimics foams that form when a bubbly liquid is subjected to buoyancy, as it is common on earth. Once equilibrium was reached, we switched off gravity and simulated pressure versus packing fraction as previously. The final values of ϕ_{rcp} are within experimental error the same as those obtained with the pressostat.

Data, Materials, and Software Availability. All study data are included in the article and/or *SI Appendix*.

ACKNOWLEDGMENTS. We acknowledge funding by European Space Agency and Centre National d'Etudes Spatiales (via the projects "Hydrodynamics of Wet Foams") focused on the Soft Matter Dynamics instrument and the space mission Foam-C, as well as NASA via grant number 80NSSC21K0898. Marina Pasquet, Nicolò Galvani, and Alice Requier benefited from CNES and ESA PhD grants. We are grateful to the Belgian User Support and Operations Centre team for their invaluable help during the International Space Station experiments. We also want to warmly thank Marco Braibanti and Sébastien Vincent-Bonnieu from ESA, Christophe Delaroche from CNES and Olaf Schoele-Schulz from Airbus for their continuing support.

Author affiliations: [a]Sorbonne Université, CNRS, Institut des NanoSciences de Paris, Paris 75005, France; [b]Lab Navier, Univ Gustave Eiffel, Ecole Nationale des Ponts et Chaussées, CNRS, Champs-sur-Marne 77420, France; [c]Université Paris-Saclay, CNRS, Laboratoire de Physique des Solides, Orsay 91405, France; [d]Université Gustave Eiffel, Champs-sur-Marne 77420, France; [e]Department of Physics and Astronomy, University of Pennsylvania, Philadelphia, PA 19104; and [f]Center for Computational Biology, Flatiron Institute, Simons Foundation, New York, NY 10010

1. K. Wang, M. Glicksman, Phase coarsening in thin films. *JOM* **67**, 1905–1912 (2015).
2. P. W. Voorhees, Ostwald ripening of two-phase mixtures. *Annu. Rev. Mater. Sci.* **22**, 197–215 (1992).
3. C. N. Nanev, Recent experimental and theoretical studies on protein crystallization. *Cryst. Res. Technol.* **52**, 1600210 (2017).
4. W. L. Noorduin, E. Vlieg, R. M. Kellogg, B. Kaptein, From Ostwald ripening to single chirality. *Angew. Chem. Int. Ed.* **48**, 9600–9606 (2009).
5. J. M. Asua, Ostwald ripening of reactive costabilizers in miniemulsion polymerization. *Euro. Polym. J.* **106**, 30–41 (2018).
6. J. Huo *et al.*, Hollow ferrocenyl coordination polymer microspheres with micropores in shells prepared by Ostwald ripening. *Angew. Chem.* **122**, 9423–9427 (2010).
7. F. Ross, J. Tersoff, R. Tromp, Coarsening of self-assembled Ge quantum dots on Si (001). *Phys. Rev. Lett.* **80**, 984 (1998).
8. D. L. Weaire, S. Hutzler, *The Physics of Foams* (Oxford University Press, 2001).
9. I. Cantat *et al.*, *Foams: Structure and Dynamics* (OUP Oxford, 2013).
10. D. Langevin, *Emulsions, Microemulsions and Foams* (Springer International Publishing, 2020).
11. K. A. Rosowski *et al.*, Elastic ripening and inhibition of liquid-liquid phase separation. *Nat. Phys.* **16**, 422–425 (2020).
12. A. A. Hyman, C. A. Weber, F. Jülicher, Liquid-liquid phase separation in biology. *Annu. Rev. Cell Dev. Biol.* **30**, 39–58 (2014).
13. I. Lifshitz, V. Slyozov, The kinetics of precipitation from supersaturated solid solutions. *J. Phys. Chem. Solids* **19**, 35–50 (1961).
14. C. Wagner, Theorie der alterung von niederschlägen durch umlösen. *Z. Elektrochem.* **65**, 581–591 (1961).
15. A. Baldan, Review progress in Ostwald ripening theories and their applications to the γ'-precipitates in nickel-base superalloys part ii nickel-base superalloys. *J. Mater. Sci.* **37**, 2379–2405 (2002).
16. H. Yan, K. Wang, M. Glicksman, Microstructural coarsening in dense binary systems. *Acta Mater.* **233**, 117964 (2022).
17. L. J. Gibson, M. F. Ashby, *The Mechanics of Foams: Basic Results, Cambridge Solid State Science Series* (Cambridge University Press, ed. 2, 1997), pp. 175–234.
18. R. Lakes, Materials with structural hierarchy. *Nature* **361**, 511–515 (1993).
19. R. S. Farr, R. D. Groot, Close packing density of polydisperse hard spheres. *J. Chem. Phys.* **131**, 244104 (2009).
20. D. Durian, D. Weitz, D. Pine, Multiple light-scattering probes of foam structure and dynamics. *Science* **252**, 686–688 (1991).
21. J. Lambert *et al.*, Coarsening foams robustly reach a self-similar growth regime. *Phys. Rev. Lett.* **104**, 248304 (2010).
22. N. Isert, G. Maret, C. M. Aegerter, Coarsening dynamics of three-dimensional levitated foams: From wet to dry. *Euro. Phys. J. E* **36**, 116 (2013).
23. A. T. Chieco, D. J. Durian, A simply solvable model capturing the approach to statistical self similarity for the diffusive coarsening of bubbles, droplets, and grains. arXiv [Preprint] (2023). http://arxiv.org/abs/2303.09612 (Accessed 16 March 2023).
24. W. W. Mullins, The statistical self-similarity hypothesis in grain growth and particle coarsening. *J. Appl. Phys.* **59**, 1341–1349 (1986).
25. K. Feitosa, O. L. Halt, R. D. Kamien, D. J. Durian, Bubble kinetics in a steady-state column of aqueous foam. *Europhys. Lett. (EPL)* **76**, 683–689 (2006).
26. J. Lambert *et al.*, Experimental growth law for bubbles in a moderately "wet" 3D liquid foam. *Phys. Rev. Lett.* **99**, 058304 (2007).
27. S. Magrabi, B. Dlugogorski, G. Jameson, Bubble size distribution and coarsening of aqueous foams. *Chem. Eng. Sci.* **54**, 4007–4022 (1999).
28. G. L. Thomas, J. M. Belmonte, F. Graner, J. A. Glazier, R. M. de Almeida, 3D simulations of wet foam coarsening evidence a self similar growth regime. *Colloids Surf. A Physicochem. Eng. Asp.* **473**, 109–114 (2015).
29. D. Zimnyakov *et al.*, Self-similarity of bubble size distributions in the aging metastable foams. *Physica D* **398**, 171–182 (2019).
30. A. Saint-Jalmes, M. L. Peugeot, H. Ferraz, D. Langevin, Differences between protein and surfactant foams: Microscopic properties, stability and coarsening. *Colloids Surf. A: Physicochem. Eng. Asp.* **263**, 219–225, A collection of papers presented at the 5th European Conference on Foams, Emulsions, and Applications, EUFOAM 2004, University of Marne-la-Vallee, Champs sur Marne (France), 5-8 July, 2004. (2005).
31. J. Stavans, The evolution of cellular structures. *Rep. Progr. Phys.* **56**, 733 (1993).
32. Z. Briceño-Ahumada, D. Langevin, On the influence of surfactant on the coarsening of aqueous foams. *Adv. Colloid Interface Sci.* **244**, 124–131, Special Issue in Honor of the 90th Birthday of Prof. Eli Ruckenstein. (2017).
33. P. Born *et al.*, Soft matter dynamics: A versatile microgravity platform to study dynamics in soft matter. *Rev. Sci. Inst.* **92**, 124503 (2021).

Downloaded from https://www.pnas.org by 90.92.98.18 on September 15, 2024 from IP address 90.92.98.18.

34. M. Pasquet *et al*., Coarsening transitions of wet liquid foams under microgravity conditions. *Soft. Matter.* **19**, 6267–6279 (2023).
35. D. J. Durian, Effective exponents for the diffusive coarsening of wet foams and analogous materials. arXiv [Preprint] (2023). http://arxiv.org/abs/2304.00415 (Accessed 1 April 2023).
36. M. Pasquet *et al*., Aqueous foams in microgravity, measuring bubble sizes. *C. R. Méc.* **351**, 1–23 (2023).
37. K. Khakalo, K. Baumgarten, B. Tighe, A. Puisto, Coarsening and mechanics in the bubble model for wet foams. *Phys. Rev. E* **98**, 012607 (2018).
38. S. Sauerbrei, E. Haß, P. Plath, The apollonian decay of beer foam bubble size distribution and the lattices of young diagrams and their correlated mixing functions. *Discrete Dyn. Nat. Soc.* **2006** (2006).
39. S. Kwok, R. Botet, L. Sharpnack, B. Cabane, Apollonian packing in polydisperse emulsions. *Soft Matter* **16**, 2426–2430 (2020).
40. S. Cohen-Addad, R. Höhler, Bubble dynamics relaxation in aqueous foam probed by multispeckle diffusing-wave spectroscopy. *Phys. Rev. Lett.* **86**, 4700–4703, TY - JOUR (2001).
41. I. Agnolin, J. N. Roux, Internal states of model isotropic granular packings. I. Assembling process, geometry, and contact networks. *Phys. Rev. E* **76**, 061302 (2007).
42. F. De Larrard, *Concrete Mixture Proportioning: A Scientific Approach* (CRC Press, 1999).
43. N. Louvet, R. Hohler, O. Pitois, Capture of particles in soft porous media. *Phys. Rev. E* **82**, 041405 (2010).
44. D. L. Johnson, J. Koplik, L. M. Schwartz, New pore-size parameter characterizing transport in porous media. *Phys. Rev. Lett.* **57**, 2564–2567 (1986).
45. F. Rouyer, O. Pitois, E. Lorenceau, N. Louvet, Permeability of a bubble assembly: From the very dry to the wet limit. *Phys. Fluids* **22**, 043302 (2010).
46. K. Feitosa, S. Marze, A. Saint-Jalmes, D. J. Durian, Electrical conductivity of dispersions: From dry foams to dilute suspensions. *J. Phys.: Condens. Matter* **17**, 6301 (2005).
47. R. S. Farr, Random close packing fractions of lognormal distributions of hard spheres. *Powder Technol.* **245**, 28–34 (2013).
48. P. S. Epstein, M. S. Plesset, On the stability of gas bubbles in liquid-gas solutions. *J. Chem. Phys.* **18**, 1505–1509 (1950).
49. S. Michelin, E. Guérin, E. Lauga, Collective dissolution of microbubbles. *Phys. Rev. Fluids* **043601**, 043601 (2018).
50. A. J. Markworth, Comments on foam stability, Ostwald ripening, and grain growth. *J. Colloid Interface Sci.* **107**, 569–571 (1985).
51. R. Lemlich, Prediction of changes in bubble size distribution due to interbubble gas diffusion in foam. *Ind. Eng. Chem. Fund.* **17**, 89–93 (1978).
52. A. R. Kansal, S. Torquato, F. H. Stillinger, Computer generation of dense polydisperse sphere packings. *J. Chem. Phys.* **117**, 8212–8218 (2002).
53. D. Morse, T. Witten, Droplet elasticity in weakly compressed emulsions. *Europhys. Lett.* **22**, 549 (1993).
54. R. Höhler, D. Weaire, Can liquid foams and emulsions be modeled as packings of soft elastic particles? *Adv. Colloid Interface Sci.* **263**, 19–37 (2019).
55. F. Rouyer, B. Haffner, N. Louvet, Y. Khidas, O. Pitois, Foam clogging. *Soft Matter* **10**, 6990–6998 (2014).
56. B. Feneuil *et al*., Stability criterion for fresh cement foams. *Cem. Concr. Res.* **125**, 105865 (2019).
57. Q. Chen, P. F. Cao, R. C. Advincula, Mechanically robust, ultraelastic hierarchical foam with tunable properties via 3D printing. *Adv. Funct. Mater.* **28**, 1800631 (2018).
58. NASA, Acceleration environment (2015).
59. A. P. Thompson *et al*., LAMMPS - a flexible simulation tool for particle-based materials modeling at the atomic, meso, and continuum scales. *Comp. Phys. Comm.* **271**, 108171 (2022).

Downloaded from https://www.pnas.org by 90.92.98.18 on September 15, 2024 from IP address 90.92.98.18.

Supporting Information Text

Dissolution rate models

We consider the configuration illustrated in the inset of Figure 3b, where a roaming bubble of radius R is centered in a cavity of radius R_t and surrounded by a liquid shell of thickness $R_t - R$. Denoting r the radial distance from the bubble center, the gas concentrations at $r = R$ and $r = R_t$ are imposed by the bubble Laplace pressures, i.e. $c(R) = He\ (P_0 + 2\gamma/R)$ and $c(R_t) = He\ (P_0 + 2\gamma/R_{32})$, where the *local* concentration at the outside boundary of the shell is estimated as that at the surface of a bubble of average size R_{32}. With these boundary conditions, the dissolved gas concentration profile is only a function of the radial coordinate r. It is a solution of the steady diffusion equation and is given by $\frac{c(r)-c(R)}{c(R_t)-c(R)} = \frac{R_t}{R_t-R}(1 - R/r)$. From Fick's first law, the molar rate of gas transfer outwards from the roaming bubble is equal to $-4\pi R^2 D_m (dc/dr)_{r=R}$, and the resulting dissolution rate is:

$$\Omega_r = \frac{4\gamma D_m V_m He}{R} \frac{(\frac{1}{R} - \frac{1}{R_{32}})}{(\frac{1}{R} - \frac{1}{R_t})} \quad [1]$$

Values provided by equation 1 depend on estimates of the different radii that have been introduced. We choose R_{32} within the range of values corresponding to our experiment in the Scaling State, i.e. $300\ \mu m \lesssim R_{32} \lesssim 500\ \mu m$ (1), and we limit the ratio R/R_t within the range $0.2 - 0.8$ (for $R/R_t \lesssim 0.2$ the size of roaming bubbles is measured with less precision, and for $R/R_t \gtrsim 0.8$ it is difficult to be sure that the tracked bubble is still a roaming bubble). Thus, we get values for Ω_r within the range $0.75 - 4\ \mu m^2/s$, as represented in Figure 3b.

As explained in the main text, we noticed transient apparent contacts between the roaming bubble and either one of the bubbles delimiting the interstice or two larger bubbles forming a corner. The underlying configuration may be a real contact, i.e. with the formation of a liquid film that slightly flattens the bubbles, or it can be a near-contact with a small separation distance, in which case the roaming bubble remains spherical. Since it is not possible to distinguish between these two types of contact, we estimate the dissolution rate for both cases. First we consider the case of the near-contact. We refer to the work of Schimming & Durian (2), who considered the so-called *kissing bubbles* configuration, where the distance h between the two spherical bubbles is such that $h/R \ll 1$. We assume two bubbles of radii $R \approx R_t/2 \approx R_{32}/6$ and R_{32} (radius of surrounding jammed bubbles). The dissolution rate of the small bubble then writes:

$$\Omega_r \approx 2\gamma D_m V_m He \left(\frac{1}{R} - \frac{1}{R_{32}}\right) \times \ln\left(0.8 + 0.6\frac{R_{32}}{3\ h}\right) \approx \frac{10\gamma D_m V_m He}{R_{32}} \ln\left(0.8 + 0.6\frac{R_{32}}{3\ h}\right) \quad [2]$$

Because of the logarithm values provided by equation 2 are weakly dependent on h. A typical value for Ω_r is $2\ \mu m^2/s$.

Now we consider the case of a small bubble of radius R and a big bubble of radius R_{32} sharing a film, of thickness h and area A, which meets the free surface of the bubbles with a contact angle θ (3) (cf. Fig. S7). The dissolution rate of the small bubble is set by the Laplace pressure difference ΔP between both bubbles, which drives the gas transfer through the contact film and sets its curvature. It writes:

$$\Omega_r \approx \frac{D_m V_m He}{2\pi\ R\ h} \Delta P\ A \quad [3]$$

The film is a spherical cap surface with its radius of curvature $R^\star$ (cf. Fig. S7) given by:

$$\Delta P = \frac{4\gamma}{R^\star} = 2\gamma\left(\frac{1}{R} - \frac{1}{R_{32}}\right) \quad [4]$$

The surface area $A = 2\pi R^{\star 2}\,(1 - cos(\psi/2))$. Taking the same range of bubble radii as above $R \approx R_t/2 \approx R_{32}/6$ and for the small contact angles considered here, geometrical considerations shows that at leading order $\psi/2 \approx 5\theta/7$, thus $A \approx \frac{\pi}{2} R^{\star 2}\theta^2$. Then the dissolution rate(Eq. 5) writes:

$$\Omega_r \approx \frac{12\gamma D_m V_m He}{5\ h}\ \theta^2 \quad [5]$$

Values provided by Eq. 5 depend on the film thickness and contact angle. For our foams, we have $\theta \approx 4°$ (1). We remark that an effective film thickness in the range $h \approx 40 - 60$ nm gives a dissolution rate close to the rate calculated for the *kissing bubbles* configuration, i.e. $\approx 2.6 - 4\ \mu m^2/s$. Note that the effective thickness accounts for both the aqueous core film thickness and the effective length related to gas transfer resistance from the two surfactant monolayers. Therefore, $h \approx 40 - 60$ nm may well correspond to either a Newton Black Film (NBF) with significant monolayer effect, or to a Common Black Film (CBF) with limited monolayer effect. It seems difficult to go further in this quantitative analysis but it is in good agreement with the effective thickness obtained from the foam coarsening rate with the same solution (1).

To estimate the dissolution rate when the bubble is in a corner, we can, as a first approximation, multiply the previous values by a factor of two. For the *kissing bubbles* configuration we get a dissolution rate equal to the upper range of values provided by the shell-model, i.e. $4\ \mu m^2/s$. Values for roaming bubbles sharing two liquid films with neighboring larger bubbles exceed a little bit that range, i.e. $5 - 8\ \mu m^2/s$. As we did not measure such high values, it suggests that such a configuration, if it really exists, is rather rare.

Therefore, whatever the configuration considered for the roaming bubble in the interstices, we find values for its dissolution rate that are compatible with our measurements, which gives robustness to the proposed mechanism based on the accumulation of long-lasting roaming bubbles in the foam interstices.

Analysis of bubble size distributions

We first transformed the measured discrete histograms into continuous PDFs using a Gaussian Kernel estimation (with bandwidth equal to 2.5 the image pixel size ≈ 14 μm). We then described the two bubble populations (either roaming bubble or jammed bubble) in the domain $\phi < \phi^\star$ with a bimodal lognormal PDF defined as:

$$\mathcal{F} = w \cdot \mathcal{L}(\rho; m_1, \sigma_1) + (1 - w) \cdot \mathcal{L}(\rho; m_2, \sigma_2) \quad [6]$$

where w is the proportion of roaming bubbles in the foam, and $\mathcal{L}$ is a lognormal distribution parameterized as:

$$\mathcal{L}(\rho; m, \sigma) = \frac{1}{\rho\sigma\sqrt{2\pi}} \exp\left[-\frac{\log^2(\rho/m)}{2\sigma^2}\right]. \quad [7]$$

where the shape parameter σ is the log-scale standard deviation and m is the linear-scale median. We fitted the bimodal function to the measured PDFs, and observed that the parameter $m_2 = 1.66 \pm 0.03(SEM)$ is almost independent of the liquid fraction. In the following, we fix $m_2 = 1.66$ and fit the other parameters. Their variations with liquid fraction are given in Fig. S5. The results of the Kolmogorov-Smirnov statistical test (4) applied to the bimodal lognormal fits provide quantitative evidence for fit quality: no fit could be rejected according to the 5% rule, and many are above 40% (with the exceptions of $p(\phi = 15\%) = 21\%$ and $p(\phi = 25\%) = 14\%$).

Finally, since R_t should represent the maximum size of the roaming bubbles, we conjecture that it should be correlated to the width of the roaming bubble PDF. To test this, we measure the width at the foot of the PDF $\mathcal{L}(\rho; m_1, \sigma_1)$ by the normalized radius ρ_t estimated such that number of roaming bubbles with $\rho > \rho_t$ equals the number of jammed bubbles with $\rho < \rho_t$:

$$(1 - w) \int_0^{\rho_t} \mathcal{L}(\rho; m_2, \sigma_2) = w \int_{\rho_t}^{\infty} \mathcal{L}(\rho; m_1, \sigma_1). \quad [8]$$

We have estimated $\rho_t(\phi)$ up to $\phi = \phi^*$, and in Figure S6 we compare it to $x_n(\phi)$. Since we employed R_{32} as the reference radius in the estimation of x_n, we must rescale ρ_t by R_{32} for a comparison with x_n. In the range of liquid fractions up to $\phi = \phi_{\mathrm{rcp}}$, we find $\rho_t \langle R\rangle / R_{32} \approx x_n$, which is consistent.

Additional Figures

The additional figures support discussions in the main text. We did not include text there, the captions being self-explanatory.

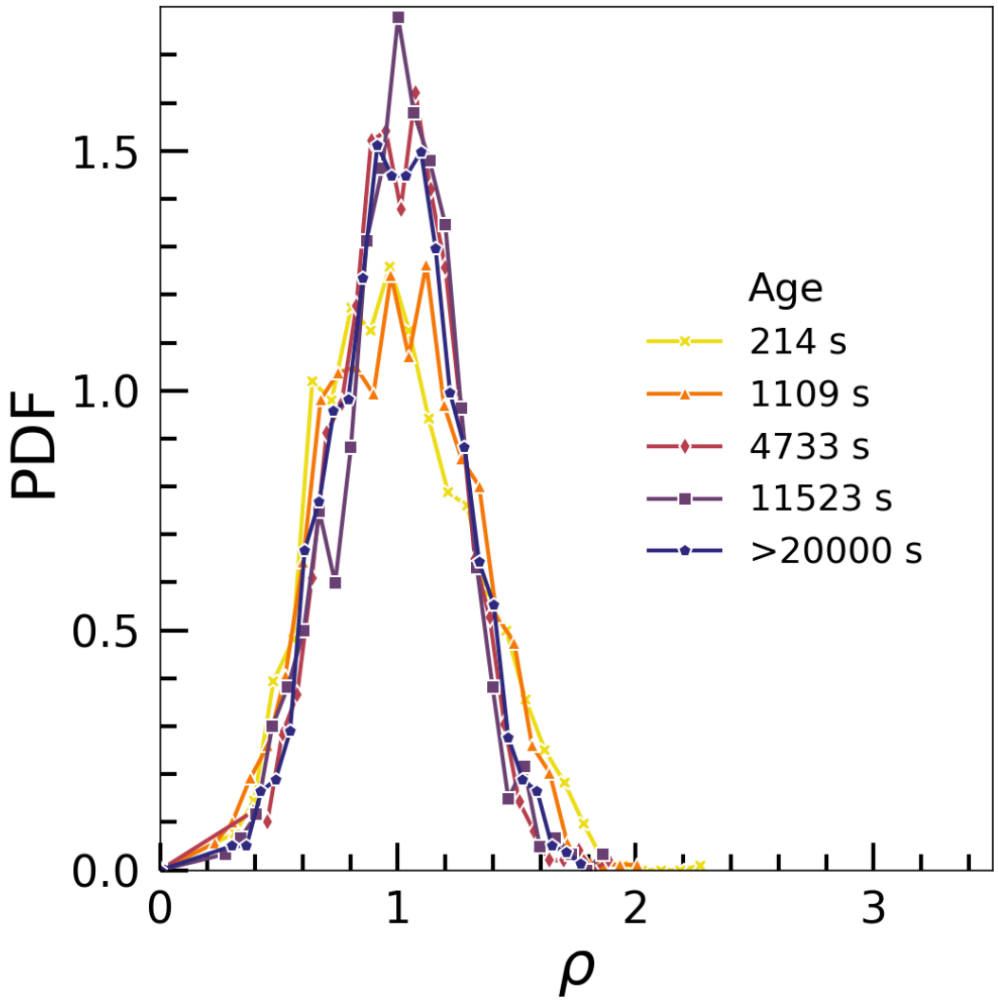

Fig. S1. Probability density function of the normalized bubble radius $\rho = R/\langle R \rangle$ at different foam ages as indicated, for a foam with liquid fraction $\phi = 50\%$. The curve corresponding to age $>$ 20000 s represents the Scaling State regime (observed up to 300000s - end of the experiment), for which the normalized distribution no longer evolves. This distribution is an example of a concentrated bubbly liquid, with a single peak and a narrow distribution with bubble sizes strictly smaller than $\rho = 2$.

Nicolo Galvani[2,3], Marina Pasquet[1], Arnab Mukherjee[2] Alice Requier[1], Sylvie Cohen-Addad[2,4], Olivier Pitois[3], Reinhard Höhler[2,4], Emmanuelle Rio[1], Anniina Salonen[1] Douglas J.Durian[5], Dominique Langevin[1]

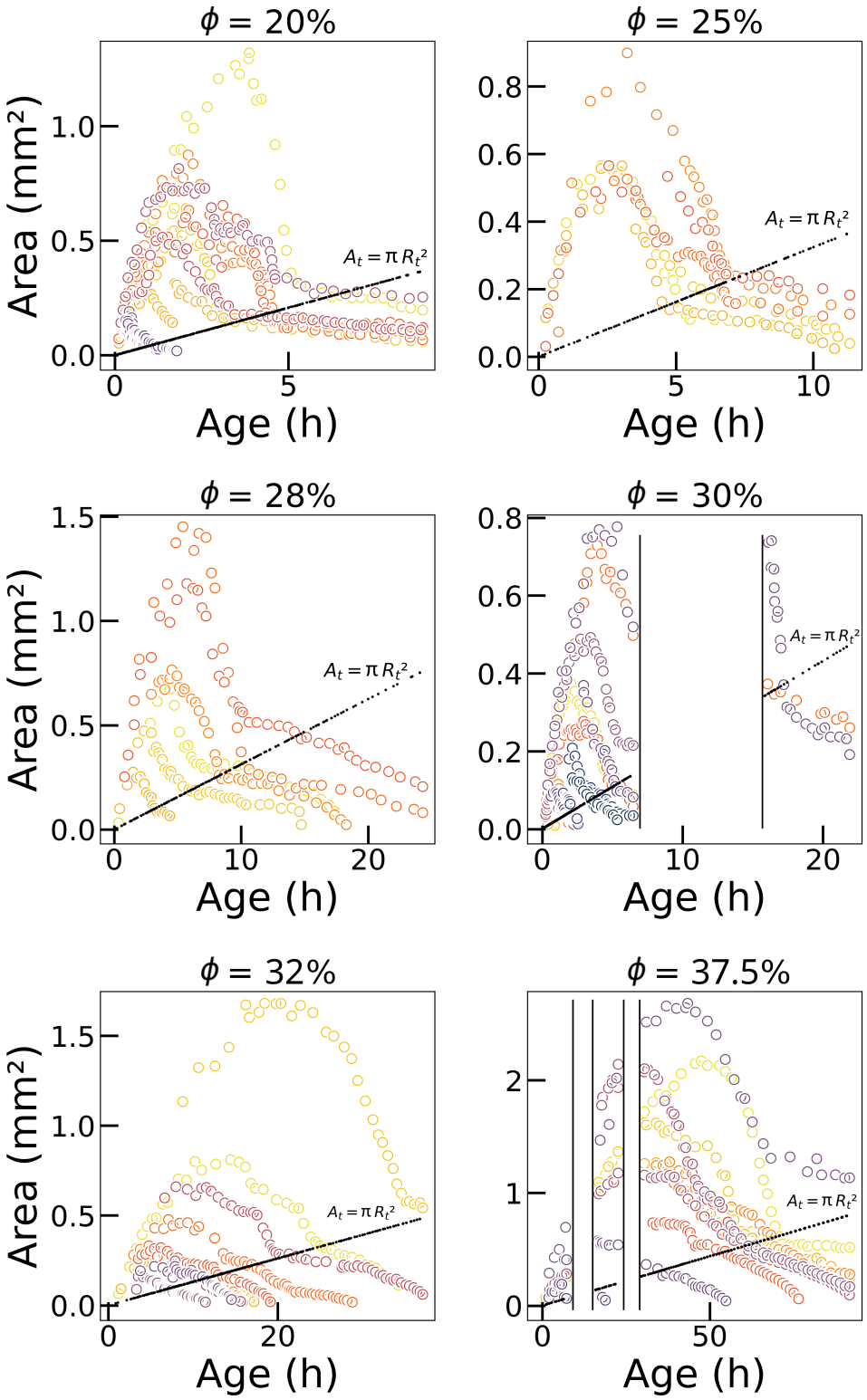

Fig. S2. Evolution of the area of individual bubbles as a function of foam age versus the time elapsed since the end of the foam sample production, for a series of liquid fractions. The area $A_t = \pi R_t^2$ denotes the bubble area when its shrinking abruptly slows down (see text). Each color corresponds to the evolution of a different bubble. For samples with $\phi = 30\%$ or 38%, data were acquired in parallel with other samples. As a consequence, there are some blanks in the image in between the vertical lines.

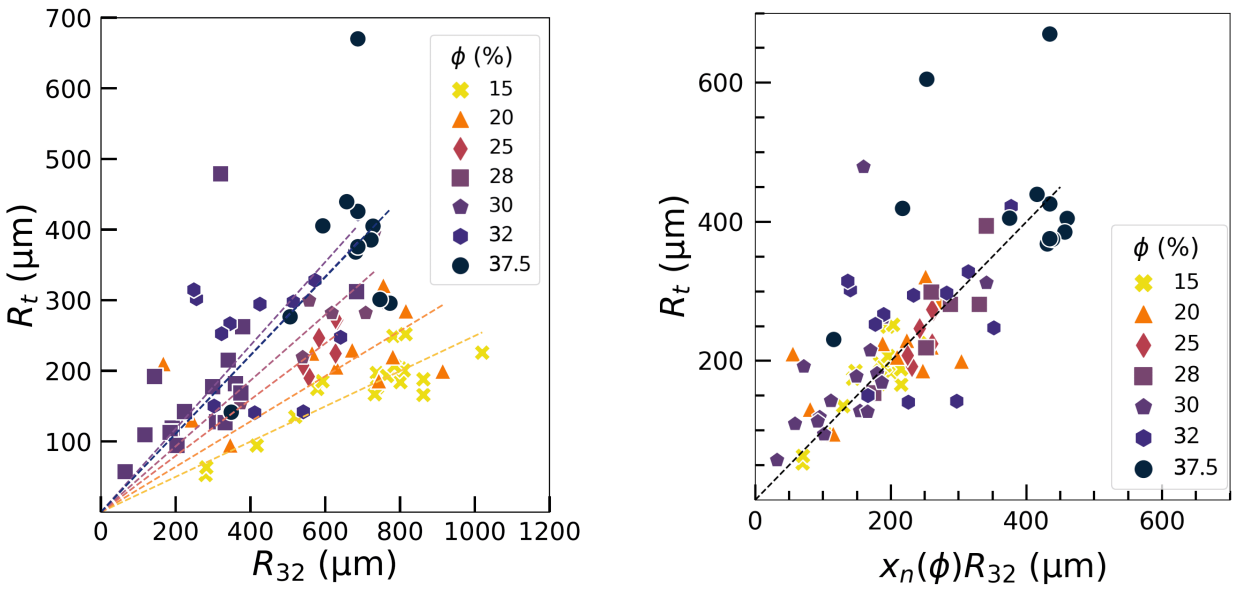

Fig. S3. (left) Bubble radius R_t as a function of the Sauter mean radius R_{32}, measured at the instant of the transition where the shrinkage rate slows down and the bubble starts to roam. A linear relation (dashed line) is fitted to the data for each liquid fraction ϕ, to determine the coefficient $x_n(\phi)$ defined in Eq. 3. (right) Master curve of the bubble radius R_t plotted as a function of $x_n(\phi)\ R_{32}$. The dotted line has a slope equal to unity.

Nicolo Galvani[2,3], Marina Pasquet[1], Arnab Mukherjee[2] Alice Requier[1], Sylvie Cohen-Addad[2,4], Olivier Pitois[3], Reinhard Höhler[2,4], Emmanuelle Rio[1], Anniina Salonen[1] Douglas J.Durian[5], Dominique Langevin[1]

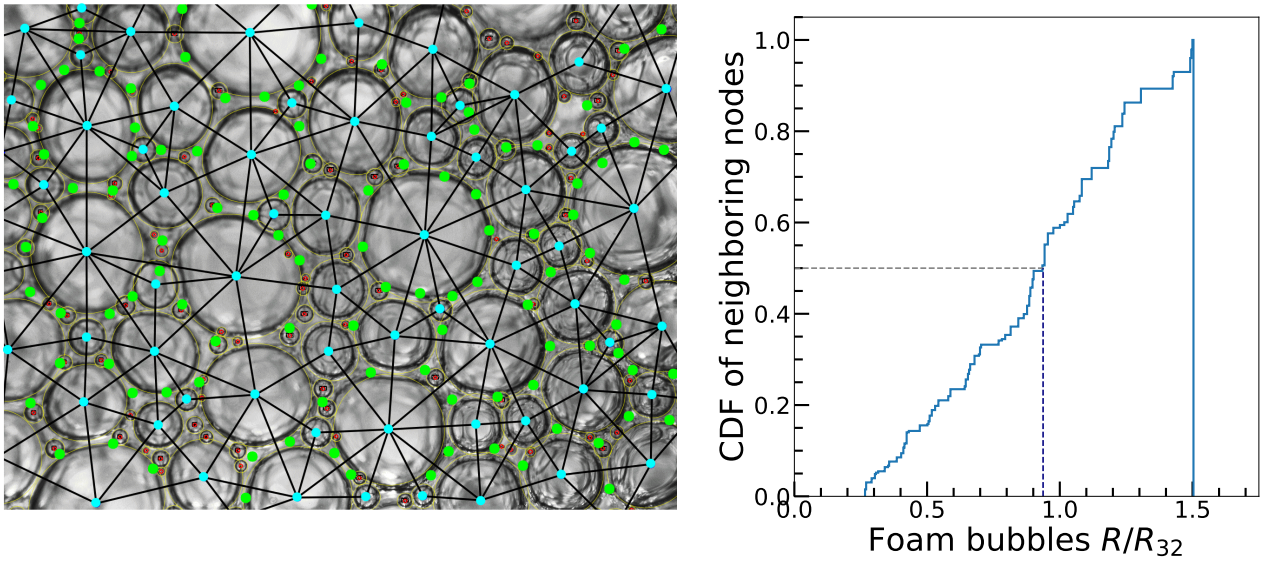

Fig. S4. Image of a sample with $\phi = 15\%$ in the Scaling State (foam age $t = 9645s$). The maximum radius of a roaming bubble, R_t, at this foam age is predicted from the value of R_{32} at this age using Eq. 3. Each bubble is then classified as a roaming (resp. foam) bubble if its radius is smaller (resp. bigger) than R_t. In the figure, roaming (resp foam) bubbles are identified by red (resp. cyan) spots at their centers. We used the jammed bubbles' center positions to analyze the foam structure by triangulation (black lines joining the centers in overlay). We estimated the number of surface nodes, identified by green spots, and localized at the barycenter of the triangles. On average, we counted 1.5 roaming bubbles per node, and 1.2 nodes per jammed bubble. (right) CDF of the number fraction of nodes around bubbles as a function of their normalized radius R/R_{32}, evaluated for the sample shown in the left. We see that the median is very close to $R = R_{32}$ which means that nearly half of the nodes are delimited by a jammed bubble larger than R_{32}. This is consistent with the choice of R_{32} as the characteristic radius of jammed bubbles constituting the nodes. Similar findings are found for liquid fractions up to $\phi_{rcp} \approx 31\%$.

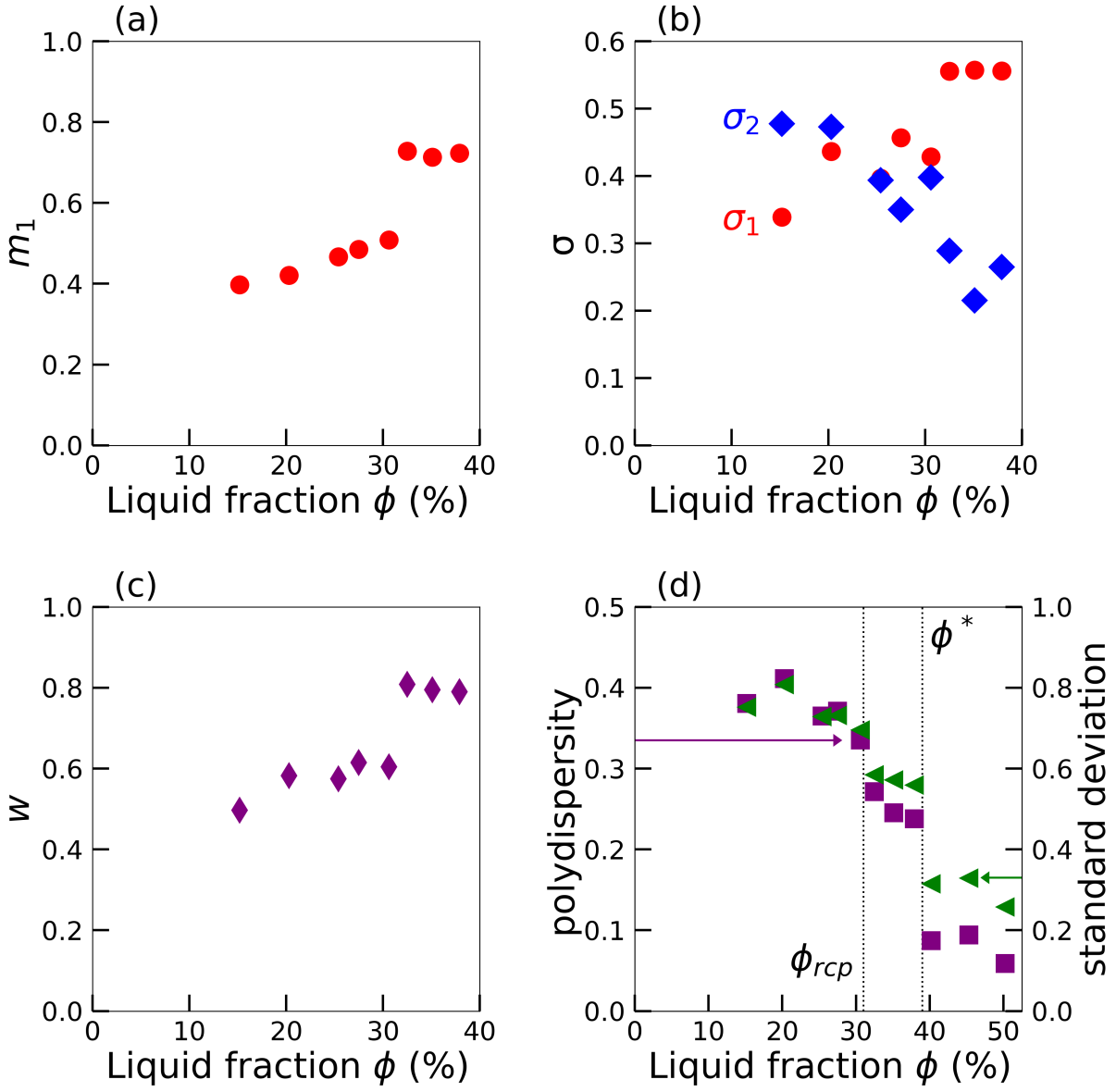

Fig. S5. Variation of the fitted PDF parameters, as defined in the text (Eq. 6 and 7), with liquid fraction. a) Natural-scale median m_1 of the roaming bubbles (the median $m_2 = 1.66$ is fixed). b) Logarithmic-scale standard deviation : σ_1 for the roaming bubble PDFs (red disks), σ_2 for the jammed bubble PDFs (blue diamonds). c) Relative weight w of the roaming bubble distribution. d) Polydispersity (squares), defined as $R_{32}/\langle R^3\rangle^{1/3} - 1$, and standard deviation (triangles) evaluated from raw data. Error bars are of the size or smaller than the symbol size.

Nicolo Galvani[2,3], Marina Pasquet[1], Arnab Mukherjee[2] Alice Requier[1], Sylvie Cohen-Addad[2,4], Olivier Pitois[3], Reinhard Höhler[2,4], Emmanuelle Rio[1], Anniina Salonen[1] Douglas J.Durian[5], Dominique Langevin[1]

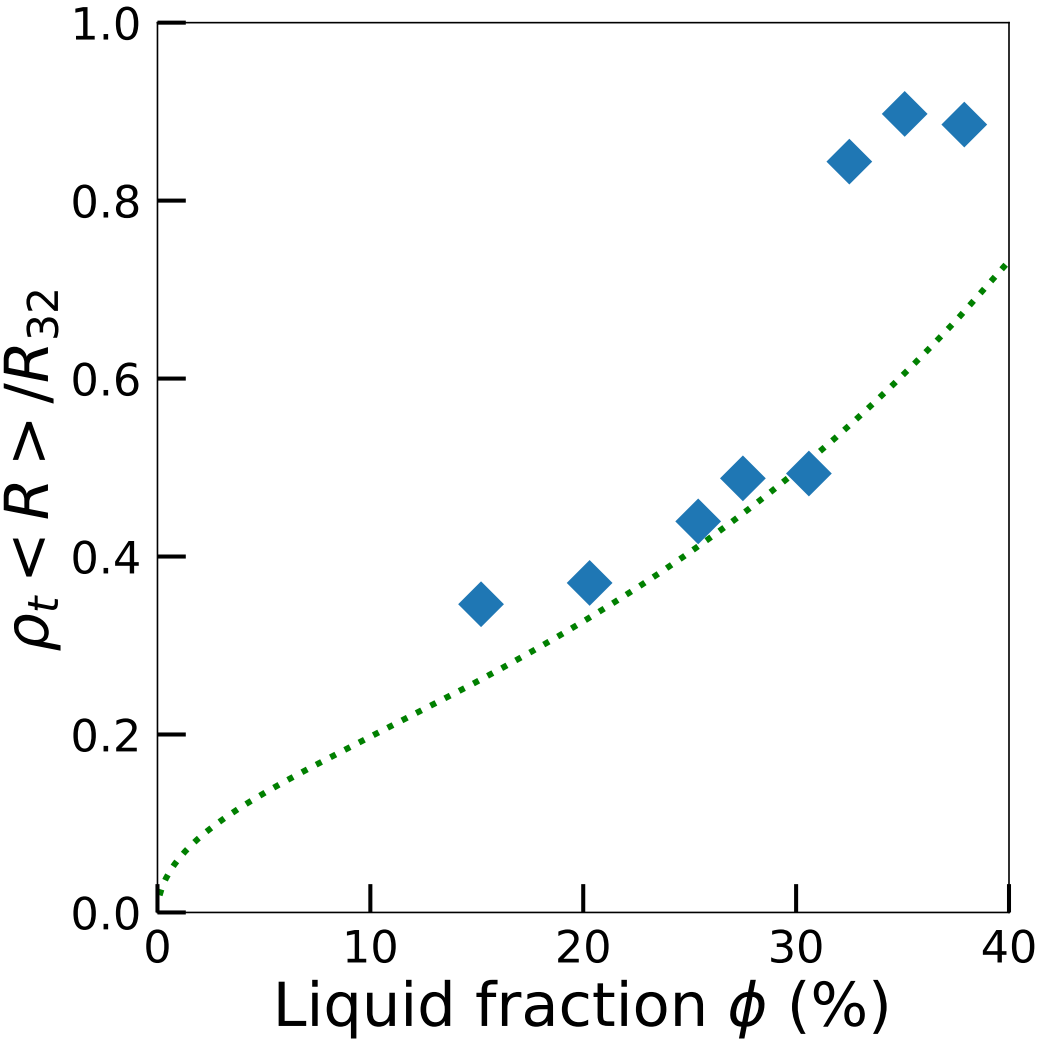

Fig. S6. Characteristic width of the roaming bubble PDFs ρ_t (defined by Eq. 8) rescaled by $\langle R \rangle / R_{32}$ as a function of the liquid fraction. The dotted line represents Eq. 4 with $\xi = 2.2$ as in fig 2c.

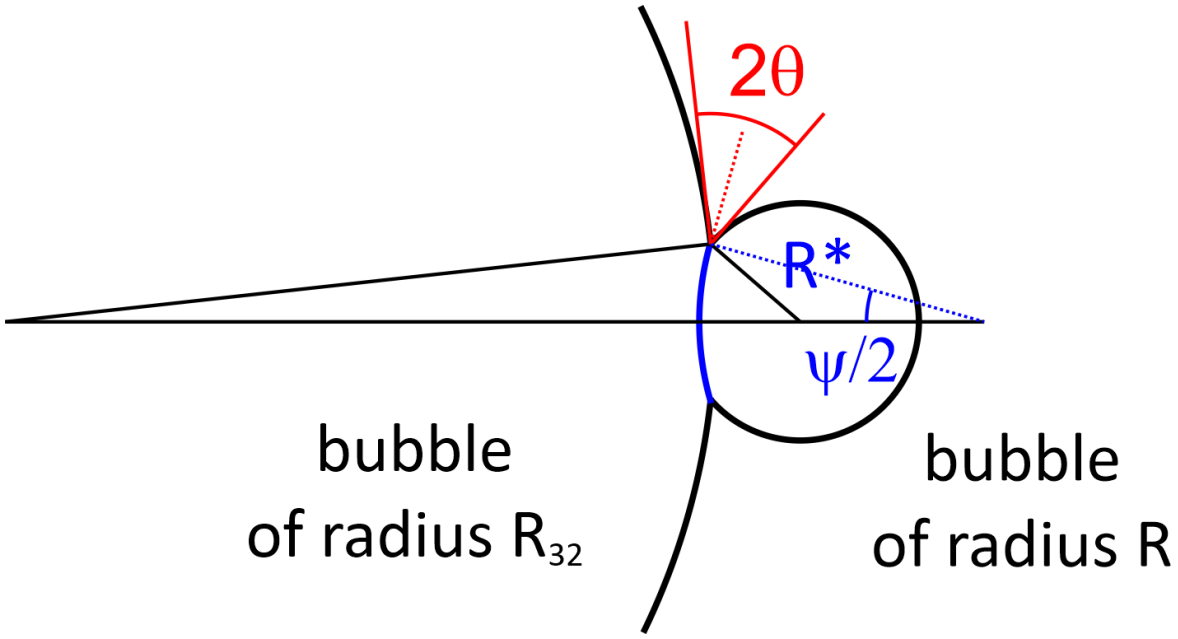

Fig. S7. Bubbles of radii R and R_{32} sharing a film (in blue) due to adhesion forces accounted for by the contact angle θ. $R^{\star}$ is the radius of curvature of the shared film.

Nicolo Galvani[2,3], Marina Pasquet[1], Arnab Mukherjee[2] Alice Requier[1], Sylvie Cohen-Addad[2,4], Olivier Pitois[3], Reinhard Höhler[2,4], Emmanuelle Rio[1], Anniina Salonen[1] Douglas J.Durian[5], Dominique Langevin[1]

Movie S1. 15.mov: overview movie of a foam coarsening in microgravity with $\phi = 15\%$. After $t \approx 2000s$ the foam reaches the scaling state, and we can appreciate the presence of small bubbles filling the foam interstices. These bubbles can be followed while roaming in the nodes and in the liquid channels, due to the rearrangements in the foam structure.

Movie S2. 38.mov: overview movie of a foam coarsening in microgravity with $\phi = 38\%$. After $t \approx 100'000s$ the foam reaches the scaling state. In this sample we can appreciate the role of adhesion: the spherical bubbles tend to stick together forming chains, in a gel-like behaviour. In the liquid space between the chains individual bubbles can be found, slowly dissolving similarly to roaming bubbles or bubbly liquids.

Movie S3. 50.mov: overview movie of a bubbly liquid coarsening in microgravity with $\phi = 50\%$. After $t \approx 20'000s$ the foam reaches the scaling state. The overall appearance is more homogeneous than in the previous cases.

References

1. M. Pasquet, N. Galvani, S. Requier, A.and Cohen-Addad, O. Pitois, R. Höhler, E. Rio, A. Salonen, and D. Langevin. Coarsening transitions of wet liquid foams under microgravity conditions. arXiv:2304.11206, 2023.
2. C. D. Schimming and D. J. Durian. Border-crossing model for the diffusive coarsening of two-dimensional and quasi-two-dimensional wet foams. Phys. Rev. E, 96:032805, Sep 2017. . URL https://link.aps.org/doi/10.1103/PhysRevE.96.032805.
3. Frits Huisman and Karol J. Mysels. The contact angle and the depth of the free-energy minimum in thin liquid films. their measurement and interpretation. The Journal of Physical Chemistry, 73:489–497, 1969. .
4. Encyclopedia of Mathematics. Kolmogorov–smirnov test, 2010. URL http://encyclopediaofmath.org/index.php?title=Kolmogorov%E2%80%93Smirnov_test&oldid=22660.

2.3.1 Addenda: effect of polydispersity on the wall node size

In Section 1-B of the article, we compare the experimental determination of x_n, the ratio between the maximum radius of a sphere trapped in a vertex of the packing R_t and the characteristic size of the packing R_{32}, with geometrical considerations. We present here a geometrical estimation of x_n, for any combination of sphere sizes, in the general case of a vertex formed by three spheres and a plane.

Let's consider 3 spheres of radii R_A, R_B, R_C, constrained to remain in contact with each other, as well as in contact with a plane. The problem asks to determine the maximum size that a sphere of radius R_0 can have, while sharing contacts with the three caging spheres and the plane, as shown in Fig. 2.9(left). If R_A is the typical size of the sphere packing, the determination of R_0/R_A is equivalent to the determination of x_n in a polydisperse foam. The problem is solved by imposing three sets of constraints, which ensure that the spheres are touching the plane, that they are in contact, and that the projections of their centers on the plane generate triangles respecting the law of cosines:

$$\begin{aligned} d_{i,p} &= R_i \\ d_{i,j} &= R_i + R_j \\ d^2_{i\perp,j\perp} &= d^2_{i\perp,0\perp} + d^2_{j\perp,0\perp} - 2d_{i\perp,0\perp} \cdot d_{j\perp,0\perp} \cos i\hat{0}j \end{aligned}$$

where index p refers to the plane, index 0 to the trapped sphere, and i, j to the spheres creating the cage, and $\perp$ to the projections on the plane. For convenience, we rescale all lengths by the typical size of the sphere packing R_A:

$$\alpha = \frac{R_B}{R_A} \quad \beta = \frac{R_C}{R_A} \quad \delta = \frac{R_0}{R_A}. \tag{2.3}$$

By applying the constraints expressed above, we get an expression for δ as a function of α, β:

$$\delta = \frac{1 + \frac{\alpha+\beta}{\alpha\beta} - \sqrt{3}\sqrt{2\frac{\alpha+\beta}{\alpha\beta} - 1 - (\frac{\alpha-\beta}{\alpha\beta})^2}}{2[1 - \frac{\alpha+\beta-1}{\alpha\beta} + (\frac{\alpha-\beta}{\alpha\beta})^2]} \tag{2.4}$$

whose solutions are shown in Fig. 2.9(right). For a monodisperse packing, with $\alpha = \beta = 1$, we obtain the classical result $\delta = 1/3$. For $\alpha = 1 \neq \beta$, we get an expression well approximated by $\delta \approx 1/3 + 0.11(\beta - 1)$, as written in the text. More in general, even larger values of δ can be reached if the cage presents bubbles bigger than average. However, for the range of $0.5 \leq \alpha|\beta \leq 1.5$ experimentally observed, the increase of δ is not sufficient to explain the x_n observed.

The loosening of the cage can also be taken into account. The spheres are no more in contact with each other, but an additional thin shell of liquid separates the surfaces. For a shell of thickness $R\epsilon$, where $\epsilon \geq 0$ is the loosening factor, we rewrite the second constraint as: $d_{i,j} = (R_i + R_j)(1 + \epsilon)$. The solution δ of this problem can be numerically computed as a function of α, β, ϵ. We find that the effect of ϵ can be approximated as a multiplicative factor, dependent itself on α and β. For $\alpha \geq \beta$, the effect of loosening is well approximated in the range $1 \leq \alpha/\beta \leq 4$ by:

$$\frac{\delta(\epsilon)}{\delta(0)} \approx 1 + (3 + \frac{\alpha}{4\beta})\epsilon \tag{2.5}$$

which gives in the monodisperse limit $\alpha = \beta = 1$: $\delta(\epsilon) \approx \frac{1}{3} + \epsilon$, as predicted. Thus, even a small deviation of the parameters from the average $\alpha = 1.25$, $\beta = 0.8$, $\epsilon = 0.1$ is compatible with the measured $x_n(0.36) = 0.5$.

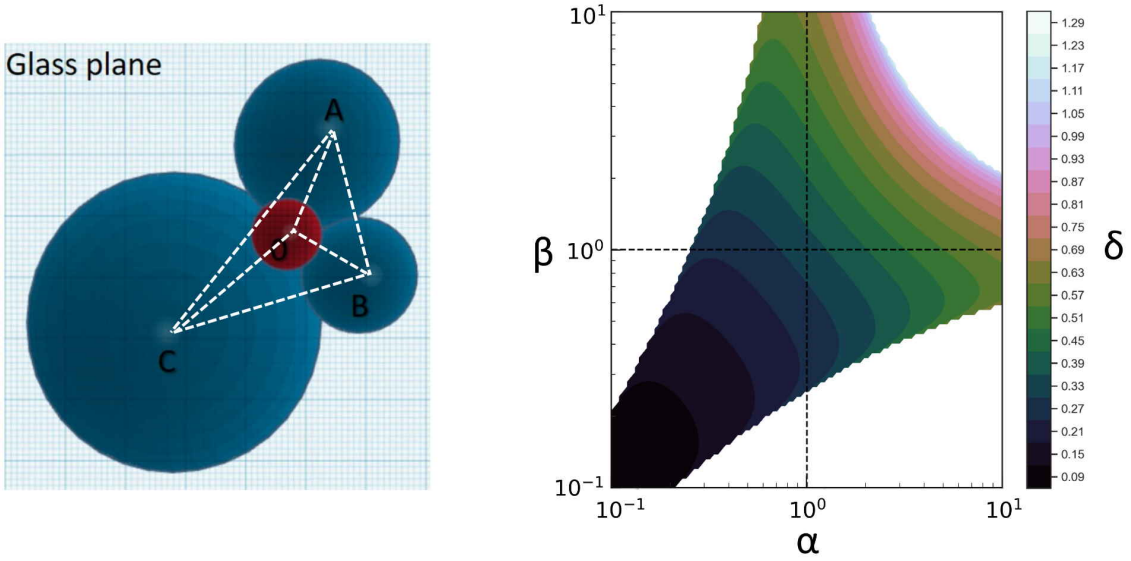

Figure 2.9: (left) Scheme of a cage composed by three spheres (A,B,C) and a place, for the sphere 0. This problem is equivalent to the problem of a roaming bubble in a surface vertex. Like in real foam videomicroscopy, the point-of-view is set behind the plane corresponding to the window. The white lines highlight the projections of the sphere centers on the plane, and the 4 triangles generated. (right) Values of δ estimated by Eq. 2.4, as a function of the parameters α, β defined in Eq. 2.3. The white areas correspond to combinations of $\alpha|\beta$ not admitted by the constraints.

2.4 Summary: the jamming transition between foam and bubbly regimes

In this chapter, we present the results of a series of experiments conducted in microgravity conditions to study the coarsening of foams and bubbly liquids, and determine the coarsening behaviour across the jamming transition.

In Section 2.1.1, we describe the experimental conditions of the microgravity experiments. To ensure that videomicroscopy observations accurately represent the bulk evolution of coarsening foams, we first conducted laboratory experiments to compare bubble size distributions at the surface with those within the foam's bulk. Unlike dry foams, where surface measurements may not reflect bulk behavior, we determined that in wet foams, surface observations are representative just after the foaming process (cf. Fig. 2.2). Furthermore, we compared the mean Sauter radius obtained from surface videomicroscopy with data from Diffused Transmitted Microscopy (DTS), which tracks the evolution of average bubble size by analyzing the temporal variation in transmitted light. Our findings show that even during coarsening, the videomicroscopy measurements are consistent with bulk-specific techniques (cf. Fig. 2.3), confirming the validity of surface-based observations throughout the coarsening process.

In Section 2.2, we study the growth laws of wet foams and bubbly liquids. Our microgravity experiments reveal that wet foam coarsening exhibits an average bubble radius growth following $t^{1/2}$, as seen in dry foams. The transition to the Ostwald ripening regime, characterized by $t^{1/3}$ growth, occurs sharply at a liquid fraction $\phi^* = 39\%$, significantly higher than the random close packing fraction for monodisperse hard spheres ($\phi^* = 36\%$) and well above the random close packing fraction for spheres with a polydispersity similar to that of the coarsening foams in their scaling state $\phi_{rcp} = 31\%$ (cf. Fig. 2.4). This value of ϕ_{rcp} was consistently determined using both simulations and theoretical models linking the observed polydispersity to the packing fraction (cf. Section 2.3). At liquid fractions

below 25%, our measured coarsening rates agree with prior models, but some discrepancies may arise due to the influence of surfactant monolayers on film permeability, or the presence of non-equilibrium films with increased thickness (cf. Fig. 2.7). However, for liquid fractions above 25%, and particularly near ϕ_{rcp}, we observed much faster coarsening rates than predicted by models that consider gas transfer solely through films. The persistent $t^{1/2}$ scaling observed up to $\phi = 39\%$ suggests that gas transfer is still dominated by thin thin films (whose thickness does not depend on ϕ). We attribute these findings to weak attractive interactions between bubbles, evidenced in ground-based experiments. Such interactions enhance contact film areas for $\phi \geq \phi_{rcp}$, forming a gel-like network of bubbles, observable in the absence of gravity. Experimental results compare well with the predictions that we provide for the effect of adhesion. The sharp transition to Ostwald ripening at ϕ^* and the unexpectedly large prefactor for the growth of bubbly liquids (cf. Fig. 2.7) suggest the need for further investigation to fully understand the mechanisms at play.

In Section 2.3, we study the bubble size distributions developed by wet foams and bubbly liquids. We show that, similar to dry foams, wet foams evolve towards a Scaling State. In this state, the bubble size distribution develops a well-defined peak, representing an excess of smaller bubbles ($\approx 0.3\overline{R}$), a feature not predicted by current coarsening theories. These small bubbles, termed *roaming bubbles*, shrink but persist within the interstices of larger *jammed bubbles*. Their dissolution rate is nearly constant across different liquid fractions, and significantly slower than the average growth rate of the jammed bubbles, leading to the buildup of a hierarchical bubble size distribution in foams with $\phi < \phi_{rcp}$. As the liquid fraction increases toward ϕ^*, the rate of roaming bubble dissolution gradually approaches the growth rate of the jammed bubbles, reducing their accumulation and shifting the distribution peak toward the mean bubble size $\overline{R}$. At $\phi > \phi^*$, none of the bubbles remain confined, and the size distribution becomes centered around $\overline{R}$, resembling that of bubbly liquids. These findings challenge the current understanding of foam coarsening. We have demonstrated the natural formation of hierarchical bubble size distributions, particularly in the range between ϕ_{rcp} and ϕ^*, where foam bubbles are jammed but not densely packed. The coexistence of jammed bubbles with smaller roaming bubbles highlights an unexpected complexity in foam coarsening dynamics.

This comprehensive perspective has broader implications, potentially extending beyond foams to other two-phase systems where interfacial dynamics are pivotal, such as emulsions, alloys, and polymer mixtures. To fully develop this understanding, further experiments are essential. In particular, to quantify the role of adhesion and determine a definitive expression for $f_2(\phi, \theta)$, we need to measure the coarsening rates Ω_p of foams with the same surfactant in the liquid fraction range $\phi < 15\%$, where adhesion effects are negligible. Similarly, for a deeper understanding of bubbly liquids, experiments at higher liquid fractions $\phi > 50\%$ are required, allowing direct comparisons with existing models.

In the next chapter, we will address these key points. We will specifically investigate how to replicate the absence of gravitational drainage in laboratory experiments conducted under normal gravity conditions. To achieve this, we will explore the preparation of foamed emulsions where the continuous phase exhibits intrinsic elastoplastic properties, focusing on their coarsening dynamics in conditions where they replicate analogous simple foams.

Chapter 3

Coarsening in a bubble dispersion stabilized against drainage

Contents

In the previous chapter, we studied the coarsening of wet foams in microgravity. Here we focus on foamed emulsions: we study the limits of foamability of emulsions depending on their physicochemical characteristics. Then we show that when foaming emulsions with a low enough yield stress gravity drainage can be counteracted without impacting the foam coarsening dynamics. Finally we take benefit of such a property to study the coarsening growth laws of bubble dispersions from the dilute to the dry liquid fractions in conditions similar to zero-gravity. Our results are validated by comparison with data previously obtained in the ISS. We establish the dependency of the coarsening rate with the liquid fraction over its full range and compare it with theoretical predictions.

3.1 Experimental details

3.1.1 Emulsion: preparation and characterization

3.1.1.1 Emulsion production

We elaborate in our laboratory quasi monodisperse oil-in-water emulsions with micrometric size droplets using a Couette mill [71]. We start from a *mother aqueous phase* constituted of a TTAB surfactant (tetradecyltrimethylammonium bromide, reference 8.40006

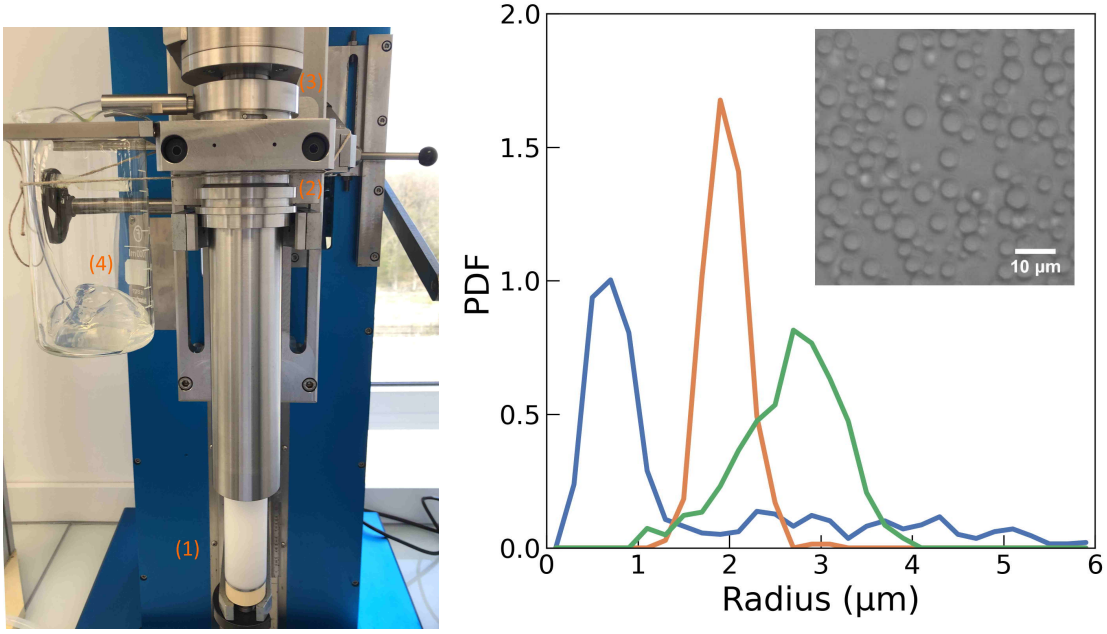

Figure 3.1: (left) Couette mixer: (1) container of the *coarse emulsion*, (2) static cylinder, (3) rotating cylinder, (4) monodisperse fine *mother emulsion* at $\varphi = 0.90\%$. It looks transparent as refractive indexes of oil and water/glycerol solution are matched. (right) Droplet size distributions of three different *mother emulsion* with polydispersity, defined in Eq. 1.3: (blue) $p_{32} = 0.70$, (green) $p_{32} = 0.04$, (orange) $p_{32} = 0.01$. In the inset, a picture of the oil droplets diluted from a mother emulsion and observed by videomicroscopy.

from Aldrich, purity 99%, used as received) solution at a concentration of $\mathcal{C} = 30\ g/L$, dispersed in a glycerol/water mixture with $\mathcal{G} = 52$ %wt glycerol. Note that the TTAB concentration is large, 24 times the critical micellar concentration in water $cmc_{TTAB} = 1.243$ g/L. This solution is sonicated for 5 minutes to break up the flocks in suspension. A *coarse emulsion* is obtained by incorporating silicon oil with viscosity 350 cSt (Rhodorsil Si 47V350 from Bluestar Silicones) in the *mother aqueous phase*, with a target oil fraction in the range $\varphi = 0.86 - 0.90$. The mixing is performed by hand, drizzling the oil over the aqueous phase while shearing with a spatula. The shear should be strong enough to avoid phase inversion but weak enough to avoid making droplets smaller than about 10 µm, which would alter the final monodispersity. The preparation is put in a bell jar under low vacuum for 2 minutes twice, halfway and at the end of the mixing, to remove part of the air bubbles incorporated during the mixing.

To obtain micrometric droplet sizes, the *coarse emulsion* is strongly sheared in a Couette mill (mixer[72] from Transmissions Service Roulements) as shown in Figure 3.1(a)) with a rotor-stator gap of $d = 100\ \mu$m and a rotation speed of 600 rpm . The output monodisperse emulsion is then diluted using a surfactant-free aqueous solution with $\mathcal{G} = 52$ %wt glycerol in order to reduce the TTAB concentration to $\mathcal{C} = 18$ g/L and the oil fraction to a controlled oil fraction in the range $\varphi = 0.800 - 0.825$. We call this the *mother emulsion*.

Afterward, smaller oil fractions are prepared by dilution of the *mother emulsion* with an aqueous solution of TTAB (same concentration $\mathcal{C} = 18$ g/L) and glycerol with a concentration which is slight adjusted around $\mathcal{G} = (52 \pm 0.5)\%$ in order to obtain a transparent emulsion. Indeed, as will be discussed in Section 3.1.3, diffuse scattering from the emulsion is detrimental to the videomiscroscopy observations of the foamed emulsion structure. Therefore the refractive index of the continuous phase of the emulsion needs is matched to that of the silicone oil (measured under visible light: $n_{oil} = 1.403$). After the dilution, each emulsion is centrifuged for runs of 1 minute, starting from 500 rpm

and increasing the speed at each run by steps of 200 rpm, not exceeding a maximum value of 2000 rpm, such that all the undesired incorporated bubbles migrate to the top of the sample. In this range of rotation speed, the centrifugal pressure is large enough to overcome the emulsion yield stress and to entrain the air bubbles.

3.1.1.2 Droplet size characterization

To characterize the droplet size distribution, we dilute the *mother emulsion* with pure water to get an oil fraction of $\varphi \approx 1-5\%$ so that the index is again mismatched between the droplets and the suspending phase. The dispersion is placed in a thin capillary with rectangular cross section and observed under a microscope (cf. Fig. 3.1). From the analysis of such images, we determine the droplet radius distribution (shown in Fig. 3.1), from which we evaluate the average Sauter radius r_d and the polydispersity p_{32} (defined in Eq. 1.3). The properties of each emulsion are summarised in Table 3.1. Note that from one mother emulsion to the other, there are significative differences in the size distributions that we attribute to the refinement of the preparation protocol over time.

3.1.1.3 Emulsion rheological characterization

Protocol for rheological measurements

We study the rheological properties of our emulsions using a rheometer equipped with a cone-plate geometry, particularly suitable for nonlinear rheology since it insures a uniform shear stress across the gap (cone angle equal to 2° or 4°). We used roughened surfaces to prevent wall slip by mechanical interlocking with the oil droplets [73]: The surface of the cones are sand blasted (6μm for the cone with 2° angle), while waterproof sand paper is glued on the plate surface (roughness 15μm). We find no significant differences between oscillatory or steady flow measurements with each cone angle, and conclude that wall slip is indeed suppressed.

Before using an emulsion, it is gently centrifuged (cf. Section 3.1.1.1) to remove residual trapped air bubbles easily observable since the emulsion is transparent. A small drop of emulsion is then gently placed at the center of the plate, and the cone is slowly lowered to avoid entrapping bubbles. Visual inspection before and after the measurements confirms the absence of bubbles. The rheometer cell is closed with a lid and the air inside saturated with humidity using wet sponges. The temperature is kept constant at 20°. To erase rheological memory inherited from the flow as the emulsion is poured in the

Label	r_d (μm)	p_{32}	φ	$\mathcal{G}$ (%wt)	γ_{WO} (mN/m)
A	1.9	0.7	0.60-0.75	52	4.5
B	2.9	0.7	0.66-0.84	52	4.5
C	2.0	0.01	0.70	52	4.5
D	2.9	0.03	0.70 or 0.90	52	4.5
E	3.0	-	0.73 or 0.87	8 or 50	5.9 or 4.5
F	3.2	0.06	0.70 or 0.80	7 or 11	5.9
G	3.3	-	0.70-0.87	50	4.5

Table 3.1: Emulsion characteristics: average Sauter radius r_d, polydispersity p_{32} (Eq. 1.3), range of oil volume fractions studied φ, glycerol concentration in the continuous phase $\mathcal{G}$. The first group (A-D) includes the emulsions used in foamed emulsions experiments; the second group (E-G) includes emulsions used for the rheological characterization only to verify the generality of the scaling laws we tested.

rheometer cell, we apply a preshear with a strain rate ramp increasing from 1 s^{-1} to 100 s^{-1} in 45 s, followed by a constant strain rate of 100 s^{-1} during 6 s. Then oscillatory or steady shear measurements are performed as described below.

For each sample we repeat three times the measurement, cleaning the instrument from the previous test and taking a new portion of the sample each time. In this way the final emulsion properties that we measure are the average among three repetitions, and we are able to estimate the sample homogeneity from the standard deviations we get.

Strain sweep oscillatory measurements of viscoelastic properties

After the pre-shear, we apply for 12 s an oscillatory strain of small amplitude $\varepsilon = 0.01\%$, at a frequency $f = 1$ Hz. We increase the strain amplitude with a logarithmic ramp of 26 points up to $\varepsilon = 1000\%$; for each point the stress amplitude and phase difference between strain and stress is evaluated over 10 s to deduce the complex shear modulus $G^*(\varepsilon) = G'(\varepsilon) + iG''(\varepsilon)$ where G' is the storage modulus and G'' the loss modulus. In Fig. 3.2a, we show G' and G'' measured at increasing strain, for different dilutions of emulsion B with $\varphi = 0.82$. In the limit of small strains i.e. linear elastic response, the storage modulus exhibits a plateau from which we deduce the static elastic modulus G as the average of $G'(\varepsilon)$ in the range $\varepsilon \leq 0.1\%$. In the limit of large strains, $G'(\varepsilon)$ decreases following a power law with exponent -1.5 as expected for elastoplastic behavior [74] (as illustrated by the straight line with slope -1.5 in Fig. 3.2). We determine the yield strain ε_y as the strain amplitude at the cross over between the two asymptotic limits: the low amplitude plateau and the large amplitude power law; we deduce the yield stress τ_y as proposed in [75] by:

$$\tau_y = |G^*(\varepsilon_y)|\varepsilon_y. \tag{3.1}$$

Note that the yield strain corresponds to a peak of G'' thus a maximum of mechanical dissipation.

Fig. 3.2(b,c) shows $G'(\varepsilon)$ and $G''(\varepsilon)$ for different dilutions of emulsion A. For concentrated emulsions in the range $0.64 \leq \varphi \leq 0.75$, we observe features similar to those of emulsion B. For emulsions with $0.6 \leq \varphi \leq 0.64$ we still observe an elastoplastic behaviour, but the response differs by the apparition of two kinks in G' and two peaks in G'' at strain values ε_1^* and ε_2^*, indicating that the yielding becomes a 2-step process. This behavior is similar to that reported previously for attractive emulsions [76]. Since our emulsions contain a large amount of surfactant, there must be attractive forces between the droplets due to micellar depletion, and we expect similar behavior. The peak at ε_1^* is due to the weak adhesive bonds arising between the droplets; as such it is constant in its position and height regardless of the oil fraction. It is the dominant peak for $\varphi \leq 0.65$, but it is overshadowed for larger φ by the peak at ε_2^*, due to the droplet compression, which raises by one order of magnitude according to the oil fraction.

We show in Fig. 3.3 the variations of G and τ_y as a function of the oil volume fraction, for the emulsions described in Table 3.1. Both quantities increase as the oil fraction increases, but present a level of dispersion which reflects the differences in droplet size and in interfacial tension between the oil and aqueous phases, γ_{WO}. In the case where capillary repulsion between droplets dominates (which here corresponds to $\varphi \geq 0.65$), G and τ_y are predicted by Eq. 1.47 and Eq. 1.48. The tension γ_{WO} is affected by the glycerol concentration, and at an aqueous/oil interface saturated with TTAB we expect it to lay in the range $1 - 10$mN/m [77].

Since emulsions A,B, C, D and G have almost the same glycerol concentration ($\mathcal{G} \approx 52\%wt$), they should have the same γ_{WO}. Therefore, according to Eq. 1.48, for all these emulsions the quantity $\tau_y r_d/\beta$ should follow a unique scaling with φ where γ_{WO} is the only unknown. Setting the values of $\beta = 0.5$ and $\varphi^* = 0.634$ (assuming that the variation of polydispersity as small enough to consider that β and φ^* are constant), compatible with the behaviour of disordered emulsions[1], we determine $\gamma_{WO} \approx 4.5mN/m$ which is in

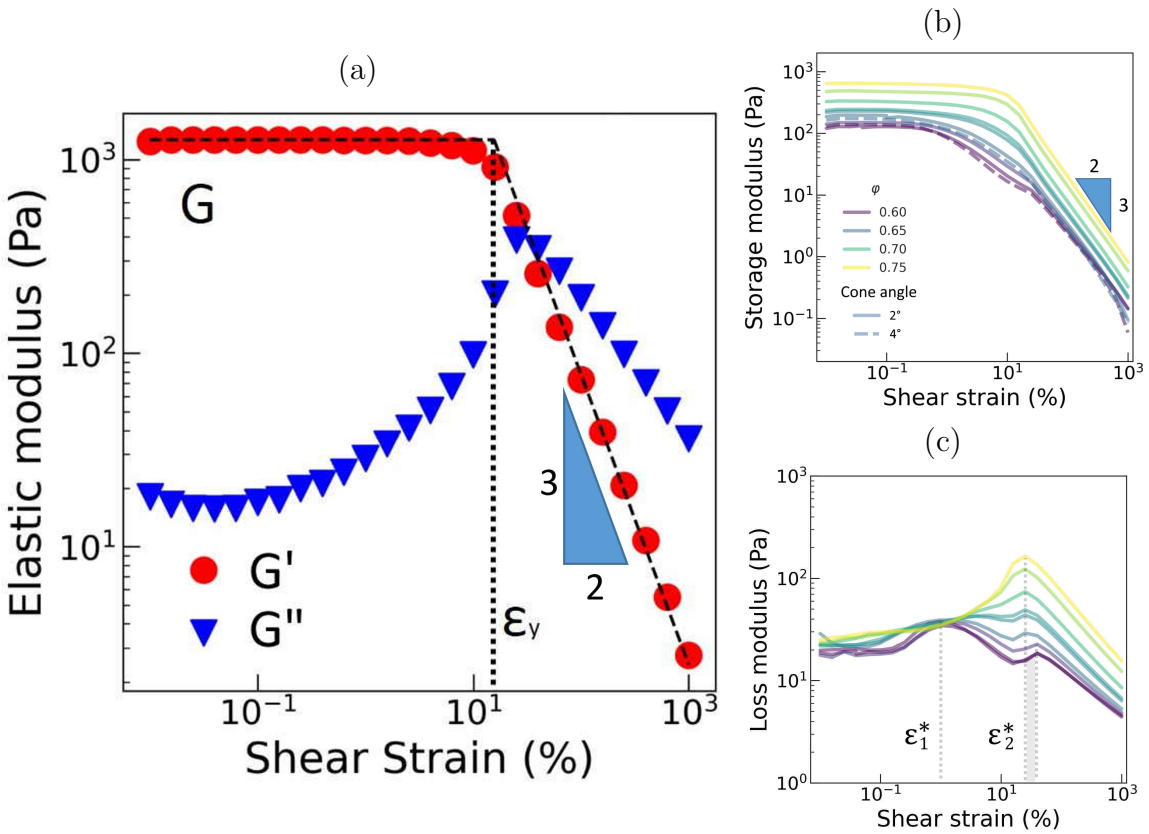

Figure 3.2: Viscoelastic properties of the emulsions determined from oscillatory measurements (at 1Hz, two different cone angles as labelled). Storage modulus G' and loss modulus G'' of: (a) Emulsion B with $\varphi = 0.82$; (b, c) Emulsion A for 8 dilutions with φ varying between 0.60 and 0.75. Emulsions constitutions are specified in Table 3.1.

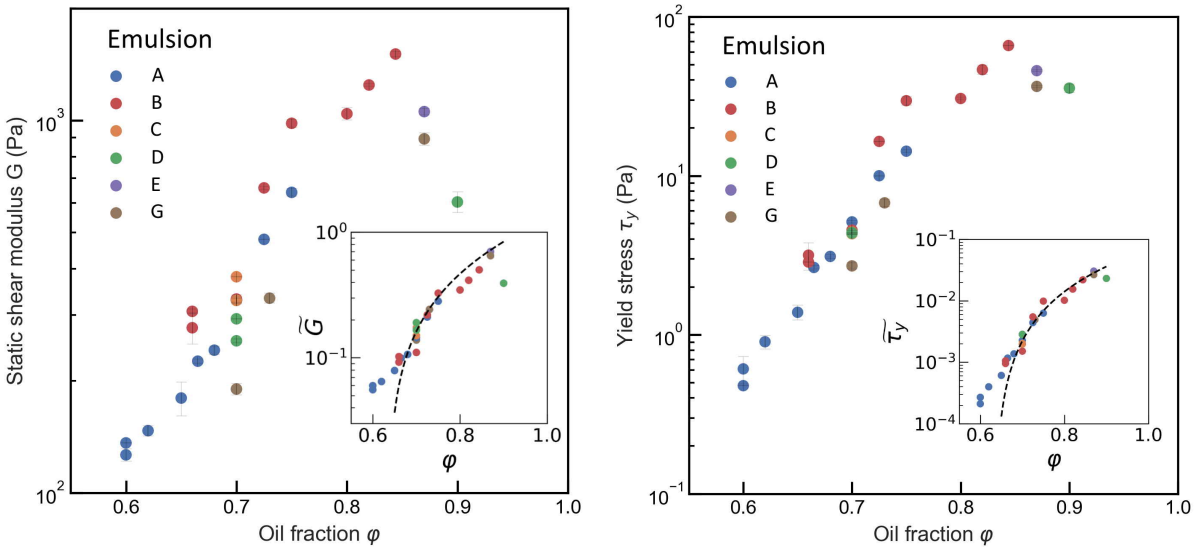

Figure 3.3: Rheological parameters determined from amplitude sweep experiments: (left) static shear modulus G and (right) yield stress τ_y, as a function of the oil fraction. The markers show the average of 3 measurements, with error bars to show the standard deviation. The insets show the same quantities normalised by γ_{WO}/r_d. The black dashed lines show respectively Eqs. 1.47 and 1.48, using $\alpha = 3.5$, $\beta = 0.5$, $\varphi^* = 0.634$ (see text).

the expected range. Knowing γ_{WO}, using the same set of data, we can now determine the prefactor α of the shear modulus in Eq. 1.47: $\alpha \approx 3.5$, which is compatible with values from the literature [30]. We do the same determination of γ_{WO} for emulsions E, F and G ($\mathcal{G} \approx 9\%wt$), keeping $\beta = 0.5$ and $\varphi^* = 0.634$, we find: $\gamma_{WO} \approx 5.9mN/m$. This value is larger than that found for a larger glycerol concentration. This can be attributed to the fact that the glycerol tends to adsorb at the oil/water interface. This is related to the decrease we observed in the surface tension at the interface between water/glycerol/TTAB and air, compared to water/TTAB and air interface (private communication).

In the insets of Fig. 3.3 we show the static modulus $\widetilde{G}$ and the yield stress $\widetilde{\tau_y}$ normalized by the capillary pressure γ_{WO}/r_d as a function of φ. For each, the data collapse on a master curve, which is well described by the respective laws , Eq. 1.47 and Eq. 1.48 in the range $\varphi \geq \varphi^*$. With this information we are able to interpolate the elastic properties of our emulsions, when we do not dispose of the complete set of measurements.

For the further study of coarsening in foamed emulsions, we will need to estimate the level of strain N_Y that the emulsion is able to sustain before yielding (cf. section 1.4.4), and that increases with φ as:

$$N_Y \equiv \frac{\tau_y}{G} = \frac{\beta}{\alpha}\frac{(\varphi - \varphi^*)}{\varphi}. \tag{3.2}$$

In the range $0.65 \leq \varphi \leq 0.95$ we determine the bounding values for all our studied emulsions: $0.004 \leq N_Y \leq 0.05$.

For the study of foamability, we will use emulsions in the range of oil fraction $0.10 \leq \varphi \leq 0.87$. Since for $\varphi = 0.60$ we measure $\tau_y = 0.5$ Pa, we consider more concentrated emulsions $\varphi \geq 0.60$ as yield stress fluids, and more diluted emulsions $\varphi < 0.60$ as simple fluids.

Steady shear measurement of flow curve

After the pre-shear, we apply a logarithmic ramp of decreasing strain rate, from $\dot{\varepsilon} = 100s^{-1}$ to $\dot{\varepsilon} = 0.0001s^{-1}$; the duration of each measurement increases logarithmically from $10s$ to $30s$, to partially compensate the difference in the strain rate. We checked that there is no relevant hysteresis when applying an increasing strain rate ramp just after the decreasing one. We show in Fig. 3.4 the flow curves obtained with emulsions A and B. For concentrated emulsions $\varphi \geq \varphi^*$, we observe a shear-thinning behavior with a yield stress in the limit of low strain rate. The Hershel-Bulkley constitutive law Eq. 1.45 can be fitted to the stress-strain rate curves with a power index $n = 0.5$, yielding the dynamic yield stress τ_y^{flow} and the emulsion consistency κ. This is consistent with previous measurements [34]. With an oil fraction slightly below the jamming transition $\varphi = 0.634$, we observe a similar behavior although with a lower reproducibility. In this case, the yield stress must be due to the adhesion between oil droplets. To characterize it, we also fit Herschel–Bulkley to those data. The Hershel-Bulkley consistency κ and the dynamic yield stress τ_y^{flow} are respectively plotted in Fig. 3.4(c,d). The dynamic yield stresses τ_y^{flow} are systematically larger than the yield stress determined from the amplitude sweep $\tau_y^{flow} = 2.2\tau_y$. In the foamed emulsion experiments, we will always refer to the oscillatory estimation.

To determine the scaling between the emulsion consistency κ and its properties we plot in Fig. 3.4(b) the adimensional viscous stress as previously proposed in [78] (for $R = r_d$):

$$\widetilde{\tau_{vf}} \equiv \frac{\tau - \tau_y^{flow}}{\gamma/r_d} \tag{3.3}$$

as a function of the capillary number:

$$Ca = \frac{\eta_c r_d \dot{\varepsilon}}{\gamma} \tag{3.4}$$

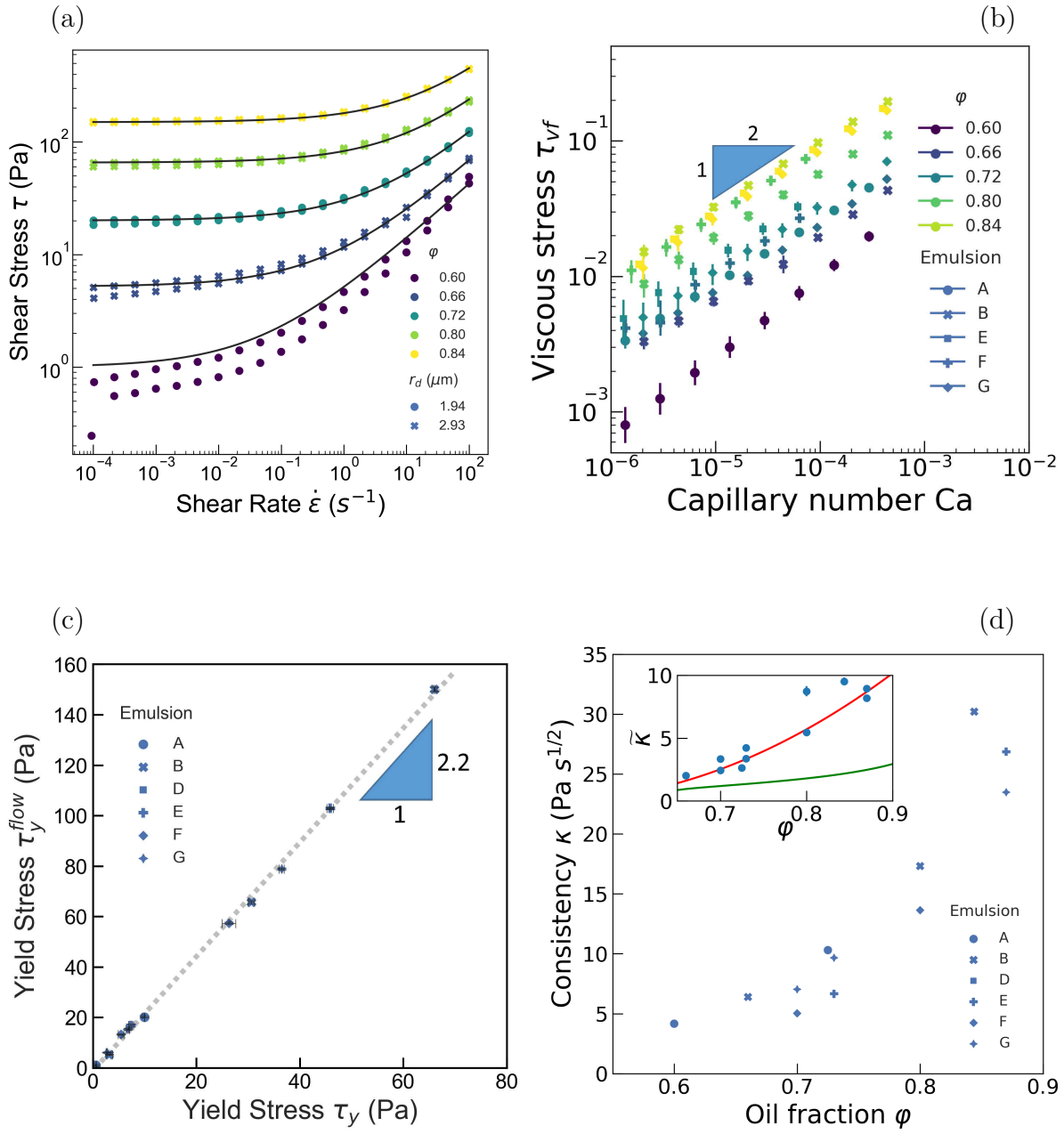

Figure 3.4: Flow curves obtained by means of steady shear measurements. (a) Shear stress as a function of the applied shear rate, for dilutions of Emulsions A, B (see Table 3.1). For each sample we see 2-3 experiments. The continuous lines represent the Herschel–Bulkley model (Eq. 1.45) with $n = 0.5$ fitted on each sample. (b) Viscous stress (Eq. 3.3) as a function of the capillary number (Eq. 3.4), where we recover the scaling $\tau_{vf} \propto Ca^{0.5}$ for $\varphi \geq \varphi^*$. (c) Dynamic yield stress τ_y^{flow} as a function of the static yield stress τ_y: all the points align on the proportionality $\tau_y^{flow} = 2.2\tau_y$. (d) Herschel-Bulkley consistency κ as a function of the oil fraction. In the inset the normalized consistency $\widetilde{\kappa}$ (defined in Eq. 3.6) is plotted as a function of the oil fraction. The green curve is Eq. 1.49, the red curve is an empirical scaling corresponding to Eq. 3.7.

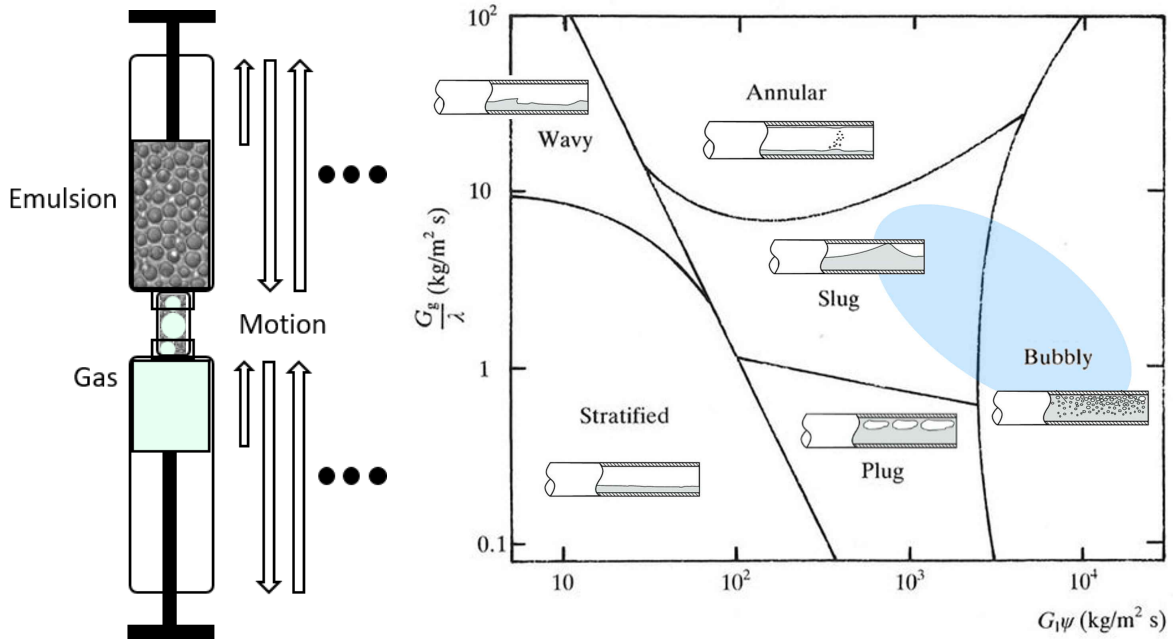

Figure 3.5: (left) Schematic representation of the double syringe method. (right) Baker map [79] for the two-phase flow in a horizontal pipe, adapted from [80]: it shows the flow regimes according to (y-axis) the gas mass speed G_g, divided by the density ratio $\lambda = \sqrt{\frac{\rho_G}{\rho_{air}}\frac{\rho_L}{\rho_{water}}}$, and (x-axis) the liquid mass speed G_l, multiplied by the liquid parameter $\psi = \frac{\gamma_{water}}{\gamma}\sqrt[3]{\frac{\eta_L}{\eta_{water}}\sqrt{\frac{\rho_{water}}{\rho_L}}}$. The colored area identifies the region of this parameter space that we experimentally probe.

where η_c is the dynamic viscosity of the continuous phase. With these quantities, the Herschel-Bulkley law writes:

$$\widetilde{\tau_{vf}} = \frac{\kappa}{\gamma/r_d} Ca^n \left(\frac{\gamma}{\eta_c r_d}\right)^n \tag{3.5}$$

For capillary numbers $Ca > 10^{-6}$ we recover the scaling $\tau_{vf} \propto Ca^{0.5}$, in the range $0.66 \leq \varphi \leq 0.85$. In this range we can evaluate the adimensional consistency:

$$\widetilde{\kappa} = \tau_{vf}/Ca^{0.5} \approx \kappa\sqrt{\frac{r_d}{\eta_c \gamma_{WO}}} \tag{3.6}$$

and plot it in the inset of Fig. 3.4(d) as a function of the oil fraction. We observe that Eq. 1.49, analytically derived for concentrated repulsive droplets, fails to catch the experimental scaling. Thus, we determine an empirical relation inspired by the scaling of yield stress with oil fraction:

$$\widetilde{\kappa} = \alpha_\kappa(\varphi - \varphi_\kappa)^2 \tag{3.7}$$

where $\alpha_\kappa = 60$ and $\varphi_\kappa = 0.5$ are valid for the complete range of φ, r_d, $\mathcal{G}$ that we studied.

3.1.2 Foam preparation

All the foams studied in our lab have been produced with the *double syringe method* [7]. Its schematic representation is shown in Fig. 3.5.

To produce a foam with the desired liquid fraction ϕ, a syringe (Fisherbrand™ Plastic PP Syringe, Luer Lock) is filled with a volume $V_l = \phi V_T$ of the foaming solution, where V_T is the total volume of foam one wants to produce. We employed "10 mL" syringes,

capable to reach a maximum $V_T = 12$ mL. The solution is sucked slowly from the center of the bottle with the aid of a plastic tube connected to the tip of the syringe. Once the desired volume V_l is reached, the plastic tube at the syringe tip is replaced with a female-female Combifix Adapter Luer-Lock connector. The syringe is filled up to V_T with the desired gas. If air is used it is drawn from the environment. For other gases (e.g. $N_2, CO_2, Air + C_6F_{14}$...) the connector is attached to the gas reservoir. Next, an empty second syringe is quickly attached to the connector to minimize gas contamination. If a different gas pressure than 1 atm is required, a three-way luer-lock connector can be used to ensure both syringes and the gas reservoir remain connected, preventing leaks.

The foaming happens by shearing the two fluids between the syringes: pushing the plunger of the full syringe and pulling the plunger of the empty syringe in a back-and-forth motion. This procedure is performed at 30-60 cycles per minute for 2 to 10 minutes. We consider a sample to exhibit *good foaming* if the following three criteria are satisfied:

- The full volume of one syringe is filled with foam if its plunger is at V_T and the other syringe is emptied.
- The foam remains stable when gently transferred between syringes for a few cycles, maintaining the first criterion.
- The foam transmits light uniformly upon visual inspection.

Otherwise, we consider it as a *bad foaming* sample. For simple fluids, two minutes of cycling is usually sufficient to determine if the solution can foam with the desired liquid fraction ϕ or if the liquid volume is insufficient to embed all the gas. In contrast, complex fluids require ten minutes of cycling before a sample can be declared non-foaming. While an automated approach using a computer-controlled mechanical syringe pusher was tested, manual foaming of yield stress fluids proved to be more effective. This manual approach benefits from varying the rhythm and applied pressure during cycles, leading to better results.

Applying continuous pressure on both syringes from the start reduces momentarily the gas volume. This decrease in gas volume aids in mixing the liquid with all the gas. As the gas incorporates, the pressure should be gradually reduced cycle by cycle until atmospheric pressure is reached again. The slow reduction of pressure allows bubbles to expand without breaking the foam, while subsequent shearing cycles break overly large bubbles into smaller ones until a steady-state bubble size distribution is achieved [7].

The initial 30 seconds of cycles should be performed at a high frequency (1 cycle per second), then progressively slowed down to a low frequency (0.25 cycles per second) over the next 30 seconds. In the following minutes, alternate two cycles at high frequency with several cycles at low frequency. From the Baker map (Figure 3.5 from [79]) we understand that a bubbly flow is achieved when the liquid flows with the gas at a large flow rate. For yield stress fluids, achieving this condition at low frequencies can be challenging, as the gas may flow ahead of the liquid by finding a free path or piercing through the fluid. Therefore, initiating mixing at high frequency is crucial. Once the bubbly emulsion forms, its yield stress is lower than that of the fluid alone, so slower speeds can be used and prevent foam breakage. If gas incorporation fails, the process should be retried at higher speeds.

3.1.3 Experimental setup: the Clinostat

Experiments conducted in microgravity are subjected to a long list of constraints: on the sample composition, on the duration of experiments, on the number of parameters under study, etc. We tried to overcome these issues and study nonetheless coarsening of 3D

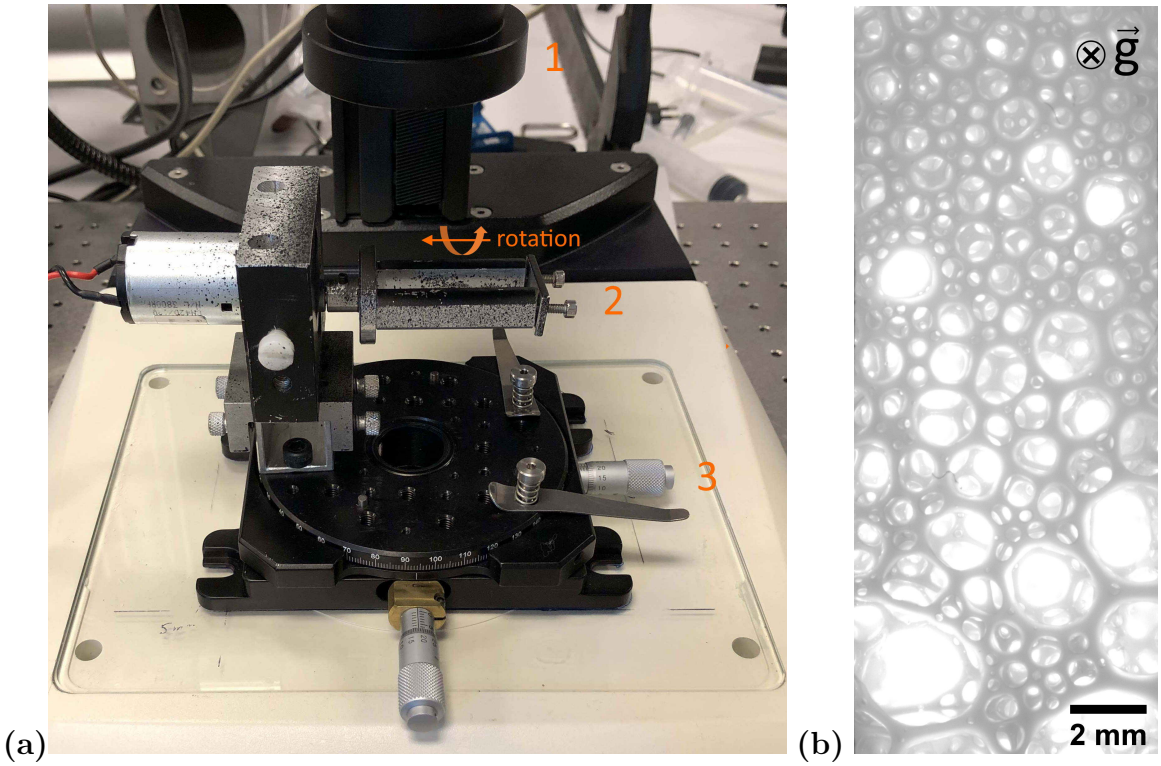

Figure 3.6: (a) Microscopy setup composed by: 1) Microscope objective, 2) cuvette holder, 3) translation stage. (b) Microscope image of a foamed emulsion with $\phi = 0.15, \varphi = 0.60$ taken after 70 minutes of aging. The cuvette is kept perpendicular to gravitational field, and the picture is taken from above.

foam samples without the problem of drainage. We designed a cell with dimensions large enough so that the sample is representative of a bulk sample. To do so, we designed and perfected over time a new experimental setup in the lab.

The first iteration of this setup is shown in Figure 3.6 (a): a 3.5mL transparent cuvette (internal dimensions: height 35mm, length 10mm, width 10mm) is filled with foam and it is fixed with two screws in a custom-made holder. The holder is connected to a rotating motor, which generates a continuous rotation at 10 rounds per minute (rpm) around an horizontal axis. The holder is placed on top of a Two-Axis Linear Translation Stage, to guarantee a precise control in the horizontal XY plane of the cell position under a microscope. The holder is painted in black to minimize light reflection. The rotation can be stopped with the cell in a horizontal position to acquire pictures of the sample surface on the two sides, illuminating the sample from below with diffused light. The main concept was on point, but we identified a series of features to improve:

- it takes 5 minutes to fill the cuvette and put it into position, losing information of the initial coarsening stage;
- the cuvette size limits the maximum bubble size under study;
- images appeared noisy, as light was not diffused enough by the foam itself;
- a small tilt in the axis of rotation determined at long times drainage along the axis (see in Figure 3.6 (b));
- the acquisition is not synchronized with the rotation and it requires to first stop the rotation, moreover the simple motor we used was not able to stop always at the same position, and it required manual operation;

- no parallelization in the measurements is possible.

We solved step by step these issues and developed our final *clinostat* setup, shown in Figure 3.7. The sample is kept inside a 10 mL cylindrical cell (inside diameter $\oslash$ = 30.0 mm, height L =10.8 mm). The cell is made of PVC, with transparent plastic windows on the flat sides for the sample observation. The windows are removable to ensure an easy cleaning, and are kept into position by two PVC covers, with O-ring to seal the gaps. The back cover is hold to the central body with 6 M3 screws. The front cover has a threaded section, to screw it directly into the central body and lock the window in a matter of seconds. We have 10 of these custom cells, to perform experiments in parallel.

The cup is attached to a step motor (Module Midi-Ingénierie MAC23), fixed so that its axis of rotation is maintained horizontal at $\pm 0.01°$ by a micrometric rotation stage (Newport TR120BL Rotation Stage). It is coupled to a reductor which allows rotation speed from 0.1 to 20 rounds per minute. An external LED source of light is positioned in front of a lateral aperture ($\oslash$ = 10mm) in the cup, aligned to a 45° mirror located inside, to transmit light to the sample at each rotation. A camera is mounted on a horizontal linear stage for the focus, looking at the 'front' face of the sample cell. According to the stage of the foam evolution we mount one of three objectives on the camera, to vary the magnification in the range $2.41 - 9.47$ μm/pixel to maximize the resolution and keep hundreds of bubbles in the field of view. A custom script written in C controls the motor rotation speed, allows to record images at instants synchronized with the instants when the aperture is facing the source of light, according to the set speed of rotation and desired frequency and duration of acquisition. The reasoning behind the determination of the appropriate rotation speed for a specific sample is detailed in next section.z

In a coarsening experiment, the foam is prepared with the double syringe method and injected inside the cell directly from the syringe, with the help of a thin plastic tube. The time when the foaming ends is noted, to work as a reference for foam aging. To fill the cell, close it, and secure it in the cup it takes 90-120 s. For short experiments (up to 2 days), the sample cell is kept under observation up to the end of the experiment. For longer experiments where differences in the foam properties must be measured in days or weeks, the sample cell can be removed and put in standby in a tube roller, where it rotates at 6 rounds per minute (rpm) until the need to acquire a new picture. With this system we were able to study coarsening of foamed emulsions up to 6 months after their preparation.

3.1.4 Avoiding drainage in a coarsening foam

As explained in the premises, the purpose of this setup is the study of foam coarsening while preventing drainage. First, we describe how drainage is impeded statically in yield stress fluids, thanks to plasticity. Then, for simple foams, we explore the possibility to delay the effects of drainage by rotating the sample continuously, and therefore varying the direction of gravity.

3.1.4.1 Avoiding drainage with yield stress

As discussed in Section 1.4.3, the yield stress of the continuous phase is able to stop drainage in foamed emulsions, be it bubble rise in bubbly emulsions or liquid flow in the channels of foamy emulsions. Experiments and simulations determined the maximum bubble size for the entrapment of bubbles in a yield stress fluid R_M^{bubble} (cf. Eq. 1.55), dependent on the yield stress of the medium τ_y and the density difference between the two phases $\Delta\rho$.

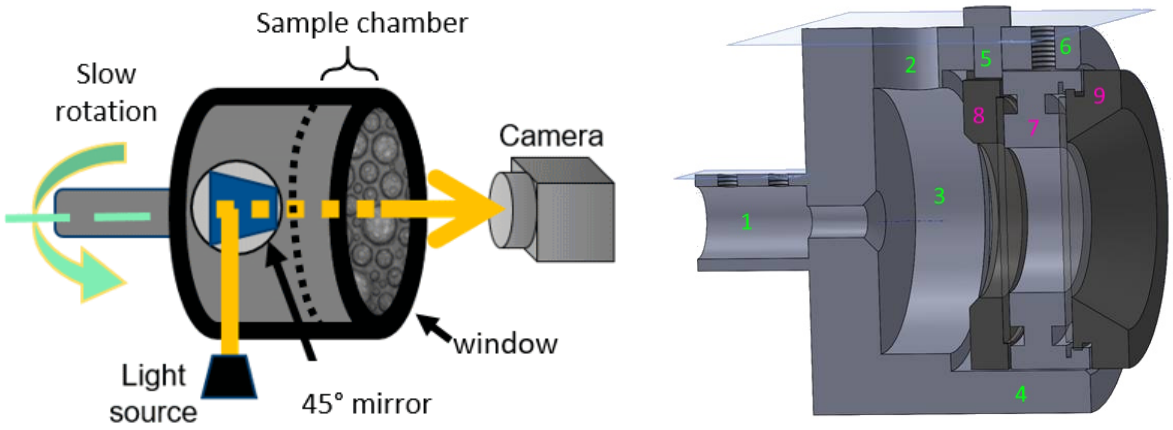

Figure 3.7: Clinostat setup: (left) drawing of the setup in operation, (right) cut-view scheme of the tailor-made pieces. The cylindrical cell, filled with the sample, is inserted in the rotating cup; at each rotation the light can enter in the cup through an aperture, and a 45° mirror reflects it toward the sample. On the other side, a camera records images of the sample surface. In the scheme we can identify the cup, whose elements (1-6) are numbered in green, and the cylindrical cell, whose numbers (7-9) are colored in magenta. We highlight: 1) housing of the motor axis of rotation; 2) hole for light transmission; 3) housing for the mirror; 4) housing for the cell; 5) stopper to put the cell every time in the same position; 6) screw-hole, to lock the two pieces; 7) body of the cell, which contains the foam in between two plastic windows, sealed by o-rings held into position by the 8) back and 9) front covers.

In foamy emulsions, we know that drainage can be stopped if the yield stress is of the order of magnitude of or larger than the hydrostatic pressure in the channels (cf. Eq. 1.56)[45], but we lack a more precise estimation. Simulations and experiments [81] studied the flow of yield stress fluids through porous media, as a function of the non-dimensional pressure difference:

$$\widetilde{\Delta P} = \frac{\Delta P}{L}\frac{\lambda}{\tau_y} \tag{3.8}$$

where ΔP is the applied pressure, L is the total length of the medium, and λ is the characteristic length of the channels. According to the packing type they measured different critical values $\widetilde{\Delta P_c}$; for a random close packing of hard spheres ($\phi = \phi_{rcp}$) the simulations yielded $\widetilde{\Delta P_c} = 4.56$. We can transpose this result into wet foams ($\phi \sim \phi_{rcp}$): the pressure gradient is of gravitational nature $\frac{\Delta P}{L} = \rho g$, and the length of the Plateau borders can be approximated to the average bubble size $\lambda \approx R_{32}$. With these elements we can estimate the maximum for the average bubble size in a foamed emulsion, for it to be stabilized against drainage:

$$R_M^{foam}(\tau_y) \approx \frac{\tau_y}{\rho g}\widetilde{\Delta P_c}. \tag{3.9}$$

This must be considered as an upper limit for R_M^{foam}, since the value of $\widetilde{\Delta P_c}$ is valid for no-slip boundary conditions. We can notice the similarity with Eq. 1.55, and in view of the identity $1/\widetilde{\Delta P_c} \approx 0.22 \approx Y_{gc}$ we link the two cases:

$$R_M^{bubble} \approx \frac{3}{2} R_M^{foam}. \tag{3.10}$$

As an order of magnitude, for a reference yield stress $\tau_y = 1$ Pa, we predict a foamed emulsion to be stable up to $R_M^{foam} \approx 450$ μm.

3.1.4.2 Avoiding drainage through rotation

In a free drainage experiment [29] the vertical pressure gradient $\frac{\partial P}{\partial z} = \rho g$ generates a downward liquid flow, with an average speed u described by Darcy's law (cf. Eq. 1.9). As the foam coarsens (cf. Chapter 2), the average speed u increases over time $u \propto R_{32}^2 \propto t^{\alpha}$, where $\alpha = 1$ in foams and $\alpha = 2/3$ in bubbly liquids. This flow induces a vertical gradient in the foam liquid fraction.

What we want to do here is to retard the inset of drainage, in simple foams and in foamed emulsions with small Y_{gc}. Let's consider a foam placed inside an horizontal cylinder, with its axis of symmetry perpendicular to the gravitational field directed along $\hat{z}$, and rotating with period T. In the reference frame of the cylinder, the rotation varies with time the direction of gravity $\mathbf{g} = -g\cos\left(2\pi\frac{t}{T}\right)\hat{z}$. Additionally, the liquid residing in the foam is subjected to a centrifugal acceleration $\mathbf{a} = r\left(\frac{2\pi}{T}\right)^2\hat{r}$, where r is the radial distance from the axis of rotation. In the limit $|\mathbf{g}| >> |\mathbf{a}|$, which is justified for the clinostat size ($R_{clinostat} = 0.015$ m) as long as $T >> \frac{1}{4}$s, we can neglect the contribution of the centrifugal acceleration and focus only on gravity.

We assume that, to have an irreversible variation of the liquid fraction ϕ in an oscillating gravitational field $\mathbf{g}$, the liquid must flow radially across a characteristic distance L. For a given T, it exists a range of bubble sizes such that the time required to the liquid with speed u to move across that distance L, L/u, is long compared to T. In this situation the liquid flows over a shorter distance back and forth during each rotation, with a net movement equal to zero over a period. In this configuration the rotation prevents foam drainage. Over time the same foam will coarsen, and u will increase up to a point where, in a fraction of a rotation, the liquid flows for larger distances and the liquid fraction develops a radial gradient. The consequent permeability gradient hinders the liquid from flowing back to the core of the foam when gravity reverses its direction, and radial drainage builds up at each rotation.

3.1.4.3 Experiments

We performed a series of coarsening experiments in the clinostat, at a constant period of rotation $T = 5$ s. The samples are simple aqueous foams, with a surfactant (TTAB) concentration $\mathcal{C} = 5$g/L, at a constant liquid fraction $\phi = 0.08$. The experiment last ≈ 1 h, after which the bubble size and the polydispersity were too large to measure a minimum of N=100 bubbles. At the end of the experiment we could observe a layer of pure liquid at the rim of the foam, which accumulated at the bottom when the cell was stopped. By watching the videos, we observed that at around 30 min the foam started to slowly turn with respect to the reference frame of the camera, set to always take a picture with the foam in the same position. We interpreted it as an effect of the wall slip of the foam, due to the presence already at that time of a thin layer of liquid. Then, we varied the period of rotation in the range $4 \leq T \leq 120$ s, and observed a qualitative difference in the timing of these phenomena, but lacked a quantitative measurement of it.

We repeated the experiments with a slight modification in the setup, as shown in Fig. 3.8 (a): we used a transparent (refractive index n =1.5) bi-layer tape to fix a 45° prism, at the center of the front window, occupying an area of 1.2 cm (width) x 1 cm (height). We adjusted also the orientation of the light source and the camera (perpendicular to the prism faces) to perform observations of the foam surface in reflection [69]. As illustrated, the light rays reach the glass/liquid interface at the window at an incident angle $\theta = 45°$. The consequent refraction ensures that they reach the liquid/gas interface with an angle of incidence $\theta_i > \theta_c$, the critical angle for total reflection. Using water we get $\theta_i = 52° > 49° = \theta_c$; in glycerol solutions $\theta_i = 49° > 46° = \theta_c$. If they hit a liquid

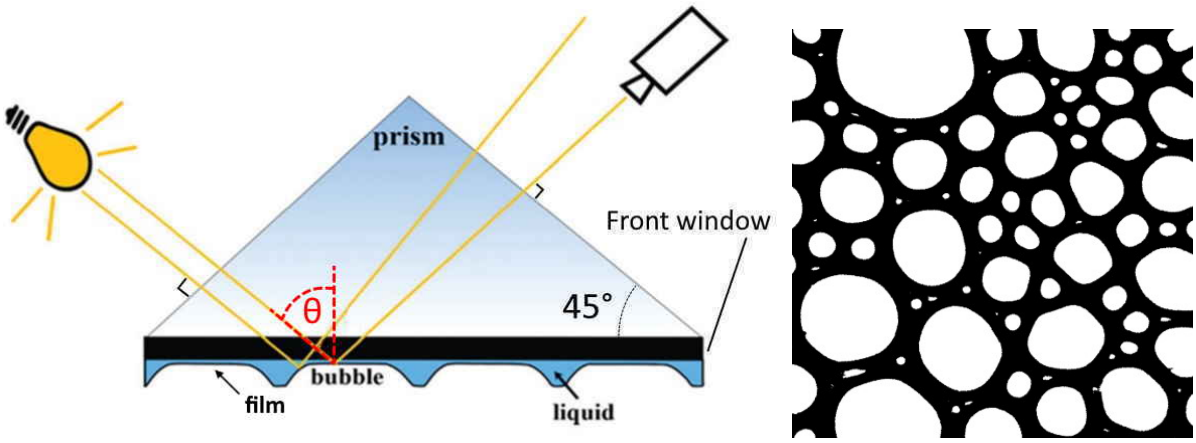

Figure 3.8: (left) Schematic drawing of the configuration for measurements in reflection, adapted from [69]: ray paths passing through a prism are used to observe bubbles at the wall. (right) Binarized picture of the foam surface in reflection: only the surface films reflect light and produce white areas.

film formed at the contact between the bubble and the window, they reach the camera. If instead they hit a curved liquid region, they are transmitted or deviated away. The prism serves to avoid refraction at the air-glass interface, and the camera is equipped with a telecentric objective to reduce the aberrations in the image due to the angle. The resulting images can be easily treated to become binarized, like in Fig. 3.8(b): the surface films (in white) identify the bubbles against the background of nodes and Plateau borders (in black). In these images, the ratio of black pixels over the total is used to determine the surface liquid fraction $\phi_s = \frac{A_{liquid}}{A_{foam}}$, which is directly linked to the volume liquid fraction ϕ by [82] :

$$1 - \phi_s = k\frac{(1-\phi)(\phi-\phi^*)^2}{k(\phi-\phi^*)^2 + 2(1-\phi)\sqrt{\phi}} \tag{3.11}$$

where k is given by: Eq. 1.7 [13].

We can also measure the bubble size from these pictures through ellipse fitting, using the Hough transformation algorithm [83]. We compare in Fig. 3.9 the evolution of the average Sauter radius measured either with the videomicroscopy set-up (cf. Section 2.1.2) or in repetitions of the same experiment with the reflection set-up. The radius determined from reflection measurement underestimates by a constant factor 1.43 the radius determined by videomicroscopy. This difference is expected: the white area measured in reflection corresponds to the contact films at the wall, which have a smaller area than the dark rings identifying the bubble planar projection, measured in videomicroscopy. Taking that into account, we are able to measure at the same time the bubble size and the average liquid fraction in the foam.

We show in Figure Fig. 3.10(a) the temporal evolution of the surface fraction ϕ_s measured for simple foams with the same initial ϕ and increasing rotation periods. Initially all samples have the same φ_S, but after an ageing time t^*, φ_S departs from its initial value which indicates that the foam under the field of view starts loosing its liquid. We observe that t^* decreases as T increases: the slower the rotation, the earlier gravity drainage destabilizes the foam: the sample with the faster rotation ($T = 4$ s) has $t^* \approx 2000$ s, and the sample with the slower rotation ($T = 120$ s) starts draining around $t^* \approx 400$ s.

Then, using Eq. 3.11 and the Sauter radius measured at the instant t^* (Fig. 3.9), we can estimate the foam permeability at this instant from Eq. 1.11. Finally, using Darcy's equation Eq. 1.9, we deduce the average speed of the liquid u^* at the onset of drainage. This quantity is connected to T by introducing a characteristic distance, L, which is

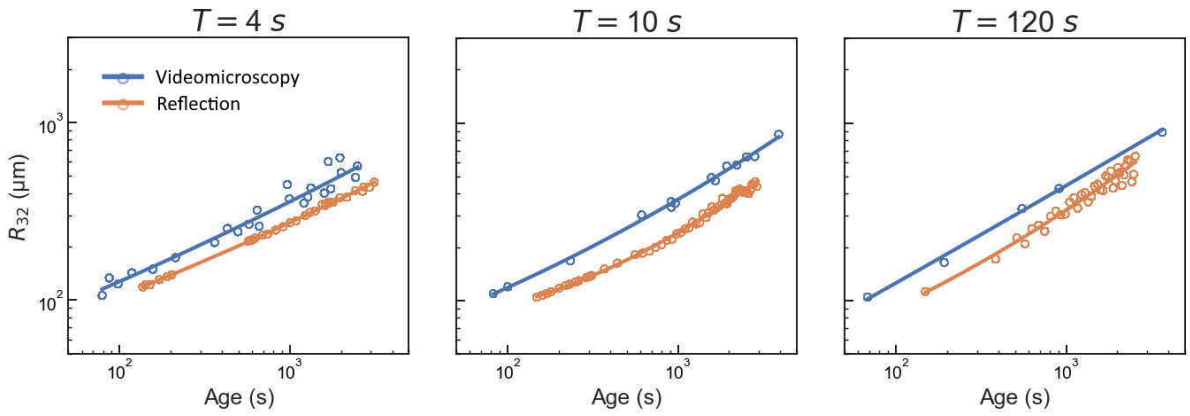

Figure 3.9: Average Sauter radius R_{32} versus coarsening age, for different rotation periods T. The empty circles show the experimental results obtained: (blue) by videomicroscopy or (orange) by reflection experiments. The dispersion among the points shows the reproducibility of the experiments; the solid lines are guides for the eye, and averaging between the repetitions.

evidenced by plotting u^* as a function of T in Fig. 3.10(b). This distance appears to be the proportionality constant $L = u^*T = (1.2 \pm 0.2)$ mm. ~~, and it approximates the height of the foam region under observation $H = 1$ mm. This value is compatible with the framework: the liquid can flow fast enough to go from the center to the lower border in half a period, and the drainage becomes visible.~~ To revise: H is 1 cm. For 8%, $L \approx 2R_{32}$, which would make sense. For the others? Would it be better to plot u^*T as a function of R^*_{32}?

The competition between drainage and rotation could be developed more in detail: simulations can be done of the radial drainage, taking into account the centrifugal acceleration and the sinusoidal variation of gravity; this is anyway outside the scope of this preliminary experiment. We are satisfied with the empirical relation $L = u^*T$, valid in the context of our setup, and combine it with Eq. 1.9 to determine the maximum bubble radius which can be studied avoiding drainage:

$$R_M(T, \phi) = \sqrt{\frac{L\eta}{TK\tilde{(}\phi)\rho g}} \tag{3.12}$$

where η is the dynamic viscosity of the liquid, $\tilde{K}(\phi) = K(\phi)/R^2$ the dimensionless foam permeability (cf. Eq. 1.11), g the gravitational acceleration. We show in Fig. 3.10(c) the predicted values of $R_M(T, \phi)$, for an aqueous foam rotating in a system of given L/T.

3.2 Foamability of emulsions

In this section we describe the experiments performed to assess the conditions by which an emulsion, either with a dilute oil volume fraction or with a concentrated one exhibiting a yield stress, can be foamed efficiently.

3.2.1 Introduction

In order for a liquid to foam, gas must be entrapped in the shape of bubbles, and the liquid-gas interfaces must be stabilized by the adsorption of surfactant molecules [1]. If $\mathcal{C}$ denotes the surfactant concentration dispersed in the bulk aqueous phase, and *cmc* its critical micellar concentration, $\mathcal{C} - cmc$ is the concentration of surfactant in the aqueous

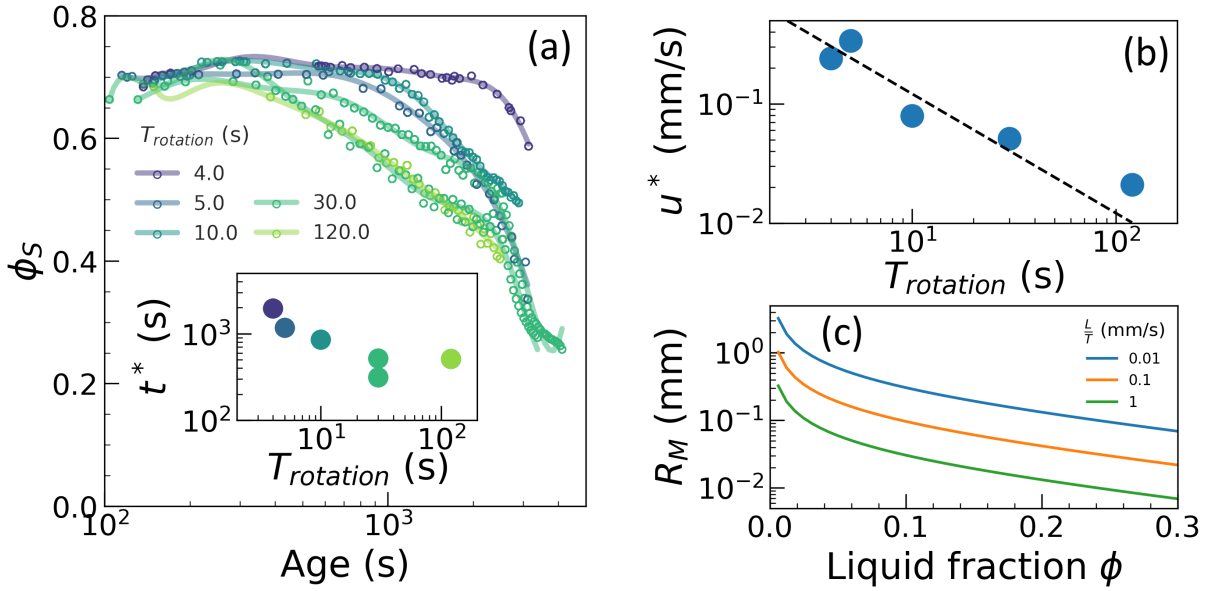

Figure 3.10: (a) Surface liquid fraction φ_S measured as a function of coarsening time (age) using the reflection set-up (cf. Fig. 3.8). The samples are simple foams with a constant liquid fraction $\phi = 0.08$. The inset shows the instant t^* where φ_S departs from its initial value, as a function of the period T of the applied rotation decreases. (b) Flow speed at the inset of drainage u^*, as a function of the period of rotation T. The points show the averages u^* among the experiments performed for a given T. The dashed is $u^* = L/T$, with fitted $L = (1.2 \pm 0.2$ mm. (c) Maximum bubble radius stable against drainage R_M as a function of the liquid fraction ϕ. The lines correspond to Eq. 3.12, for different values of the parameter L/T as indicated.

reservoir available for adsorption. Let's call Γ_∞ the surface concentration of adsorbed surfactant at saturation. The criterion of saturated surface coverage of a monodisperse dispersion of bubbles, of radius R, in a foam of liquid volume fraction ϕ can be written as [84, 85]:

$$\frac{\mathcal{C} - cmc}{\Gamma_\infty}\phi \geq \frac{3}{R}(1-\phi). \tag{3.13}$$

In the case where the foaming liquid is made of an emulsion, the oil/water interfaces must remain saturated by adsorbed surfactant molecules for the emulsion to remain stable upon foaming as pointed out by [37]*. This means that there should be enough surfactant available to saturate both oil/water interfaces and water/gas interfaces (in the case of an oil in water emulsion). Introducing $v_w = \phi(1-\varphi)$, $v_o = \phi\varphi$ and $v_g = 1-\phi$ the volume fractions in the total foam volume of the water phase, the oil phase and the gas respectively, the criterion for saturated surface coverage now becomes:

$$\frac{\mathcal{C} - cmc}{\Gamma_{cmc}} v_w \geq 3\left(\frac{v_g}{R} + \frac{v_o}{r_d}\right) \tag{3.14}$$

for a monodisperse emulsion of droplet radius r_d. Let's define the *saturation radius* $R_s = 3\frac{\Gamma_{cmc}}{(\mathcal{C}-cmc)}$, the characteristic radius of a sphere such that the amount of surfactant available in its volume is equal to the amount of surfactant needed to saturate its surface. In our systems, we have oil droplet radius $r \approx 3\mu$m, the bubble size measured just after foaming $R \approx 30\mu$m, and with $\mathcal{C} = 18$ g/L, $R_s \approx 0.6\mu$m. Then Eq. 3.14 simply writes:

$$\frac{v_w}{R_s} \geq 3\left(\frac{v_g}{R} + \frac{v_o}{r_d}\right) \tag{3.15}$$

*In ref [37], the authors considered the oil/water interfaces only, neglecting the water/air interface coverage

By applying the identity $v_w + v_g + v_o = 1$, we can finally rewrite Eq. 3.15 as a criterion for the maximum gas volume fraction allowing foaming:

$$v_g \leq v_g^{max} \equiv \frac{1 - v_o(1 + \frac{R_s}{r_d})}{1 + \frac{R_s}{R}}. \tag{3.16}$$

We expect the maximum gas fraction v_g^{max} which can be foamed to decrease linearly with the oil fraction in the foam v_o, according to the surfactant properties (bulk concentration $\mathcal{C}$, surface concentration Γ_∞) and the droplet size r_d.

Furthermore, it has been showed that foaming could also be restricted by dynamical effects, intrinsic to the mixing process, which limits the capability to entrap gas in the liquid phase [2]. Foaming experiments [6] with a simple shear mixing have proven an interdependence between the final liquid fraction ϕ, the bubble size R and the continuous phase viscosity η. We will consider also these kind of phenomena in determining what limits the foam production.

3.2.2 Results

We perform a series of foaming experiments with the double syringe method: we set the emulsion properties, a target liquid fraction ϕ, and we try to foam the emulsion following the protocol described in Section 3.1.2. The test is repeated varying the target liquid fraction ϕ, to identify the boundary between *good foaming* and *bad foaming*, according to the criteria defined in Section 3.1.2.

We perform our tests on three sets of foaming samples: Set I : surfactant solutions; Set II : emulsions without yield stress ($\varphi < 0.60$); Set III : emulsions with yield stress ($\varphi \geq 0.60$) (cf. Section 3.1.1.3). In the first set we vary the surfactant concentration $\mathcal{C}$ and the glycerol concentration $\mathcal{G}$. In the second set we fix the droplet size $r_d = 3.2\mu$m (Emulsion F cf. Table 3.1), while the oil concentration φ, $\mathcal{C}$ and $\mathcal{G}$ are varied. In the third set we fix $c = 18$ g/L and $\mathcal{G} = 52\%$wt, while varying φ and r_d (emulsion F of cf. Table 3.1).

The foamability diagram for the three sets is plotted as a function of oil fraction φ in Fig. 3.11(a). We observe that emulsions with a given oil fraction φ foam more easily at larger liquid fractions ϕ. We call ϕ^{min} the boundary between bad foaming and good foaming behaviors. Additionally, ϕ^{min} increases for larger φ. For both sets II and III, the boundary ϕ^{min} exhibits some scatter: this indicates that ϕ^{min} doesn't scale only with φ, but that it also depends on the parameters r_d, $\mathcal{G}$, and $\mathcal{C}$. Since data of set I are indistinguishable in this graph, we plot them as a function of the surfactant concentration $\mathcal{C}$ in Fig. 3.11(b). Here we see that, for a given viscosity η, you need to increase the surfactant concentration $\mathcal{C}$ to reach good foaming at smaller liquid fractions ϕ. Nonetheless, the boundary between good and bad foaming depends also on the viscosity of the continuous phase η_c.

To test Eq. 3.16, we first consider dataset III, and plot v_g as a function of v_o in Fig. 3.12(a). The boundary between good and bad foaming follows a straight line, consistently with Eq. 3.16. By grouping data according to R_S/r_d, we plot the predicted boundary v_g^{max}, using our experimental parameter $R_S/R = 0.02$. Without fitting parameters, we find that it is in good agreement with the observed boundary, which means that surface coverage is here the limiting parameter for foaming.

However, the same analysis cannot be applied neither to set I, where the viscosity of the continuous phase η_c is relevant, nor to set II, where the variation of v_g is incompatible with the negligible variation of v_o. If the surface coverage is not the limiting factor, we need to identify a different criterion. We search for a scaling of the minimum liquid fraction ϕ^{min} with the viscosity of the foaming solution η and the surfactant concentration

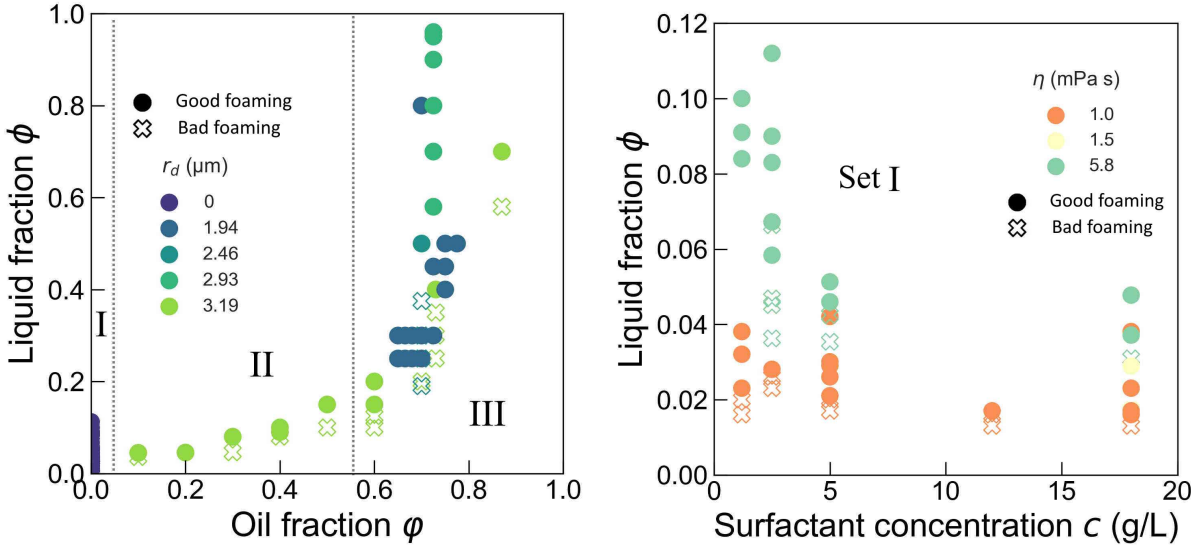

Figure 3.11: Foamability diagram with the double syringe method. (left) Liquid fraction ϕ as a function of the oil fraction φ, for the three sets of experiments: I) surfactant solutions, II) dilute emulsions ($\varphi < 0.60$), III) yield-stress emulsions ($\varphi \geq 0.60$). The colorscale identifies the droplet size, with $r_d = 0$ for simple foams. (right) Liquid fraction ϕ as a function of the surfactant concentration $\mathcal{C}$, for set I (surfactant solutions), below and above the $cmc = 1.24 g/L$. The colorscale shows the viscosity of the continuous phase η, modified by varying the glycerol concentration $\mathcal{G}$. In both graphs, filled circles identify good foaming, and empty crosses bad foaming.

$\mathcal{C}$. With an empirical approach, we normalize these quantities by two reference physical constants $\eta_{water} = 1$ mPa.s and $cmc = 1.24$ g/L, and write a general power law:

$$\phi^{min} \propto \left(\frac{\eta}{\eta_{water}}\right)^{p} \left(\frac{\mathcal{C}}{cmc}\right)^{q}. \tag{3.17}$$

For dataset I, the viscosity η is simply that of the aqueous phase, which varies with the glycerol concentration $\mathcal{G}$, while for dataset II, the viscosity is that of dilute emulsions, evaluated using the modified Krieger-Dougherty Eq. 1.44. For both sets, varying the surfactant concentration $\mathcal{C}$, the liquid viscosity η and the oil fraction $\varphi < 0.60$, a unique equation with $p = 1/2$ and $q = -1/3$ describes the boundary between good and bad foaming:

$$\phi^{min} = A \left(\frac{\eta}{\eta_{water}}\right)^{1/2} \left(\frac{cmc}{\mathcal{C}}\right)^{1/3} \tag{3.18}$$

with an adimensional prefactor $A \approx 0.03$. This empirical law is consistent with all the data, except for the surfactant solution at cmc without glycerol (corresponding to $(\eta/\eta_{water})^{1/2}(cmc/\mathcal{C})^{1/3} = 1$).

We consider the physical processes involved, to search an explanation of this empirical criterion. By comparing our experimental conditions to the general behaviour of two phase flow in a horizontal pipe (cf. Fig. 3.5(b)), we deduce that they lie in the domain where the two phases are able to mix during the flow, and air entrapment can't be a limiting factor. Previous work proposed that foaming using the double syringe method results from hydrodynamic processes occurring in the constriction connecting the two syringes, in two steps: first, air pockets are entrapped by the liquid during the biphasic flow; then, the shear breaks the air pockets into smaller bubbles, until a characteristic average bubble size $\overline{R}$ is reached [7]. Let us now consider the bubble breaking mechanism induced by viscous friction.

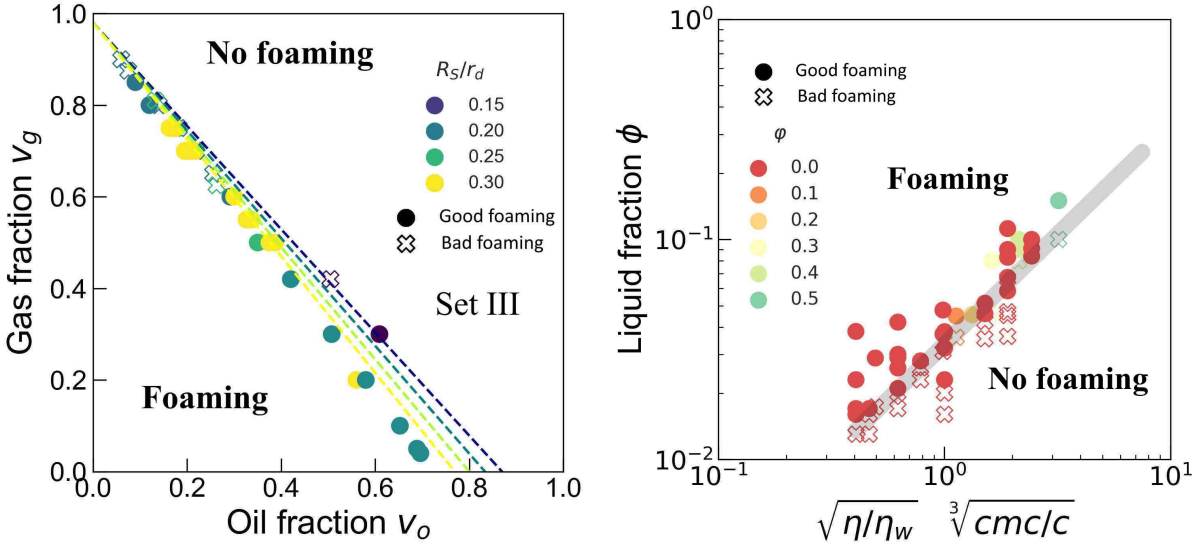

Figure 3.12: (left) Gas fraction v_g as a function of the oil fraction v_o, in foamed emulsions exhibiting yield stress, with $\varphi \geq 0.60$ (data set III from Fig. 3.11). The surfactant concentration is set at $\mathcal{C} = 18g/L$ ($R_S/R = 0.02$), with the exception of the two isolated purple points, at $\mathcal{C} = 30g/L$ ($R_S/R = 0.01$). The dashed lines show the maximum gas fraction $v_g^{max}(v_o)$ predicted by Eq. 3.16, evaluated for the appropriate R_S/R and the 4 values of R_S/r_d shown in the colorscale. (right) Liquid fraction ϕ as a function of a scaling parameter determined empirically, where η is the viscosity of the water-glycerol phase for surfactant solutions and the suspension viscosity for dilute emulsions. The transparent gray line is the linear scaling Eq. 3.18 with prefactor $A \approx 0.03$.

A single bubble in a shear flow is predicted by Grace to break when the viscous shear stress τ normalized by the capillary pressure γ/R is larger than a critical value $\tilde{\tau}_{CR} = \tau R/\gamma$, which depends on the ratio between the viscosity of the dispersed phase and that of the continuous phase $\lambda = \eta_d/\eta_c$ [86]. In flowing dry foams, the bubble breaking mechanism is modified by the presence of other bubbles around. Golemanov *et al* measured a normalized critical shear stress for bubble breaking, $\tilde{\tau}_{CR} \approx 0.4$ [87]. They reported that $\tilde{\tau}_{CR}$ is independent from the ratio between the viscosity of the dispersed phase and the effective viscosity of the foam η_{eff}: $\lambda_{foam} = \eta_d/\eta_{eff}$. Since foams have shear thinning behaviour, they evaluated it as $\eta_{eff} \cong \tau_{VF}/\dot{\varepsilon}$, where τ_{VF} is the viscous shear stress and $\dot{\varepsilon}$ the shear rate, and a Herschel-Bulkley constitutive law Eq. 1.45. Qualitatively, the viscous shear stress τ_{VF} increases as ϕ decreases (cf. Eq. 1.49), because the liquid in the foam interstices becomes more confined, and the local velocity shear rate increases. Thus, for increasing ϕ, τ_{VF} will not be large enough to overcome the Laplace pressure and induce bubble breaking. If this process were the limiting foaming factor, we would expect a maximum liquid fraction for good foaming, which is the opposite of our observations (cf. Fig. 3.12(right)).

Instead, we consider a foaming criterion where a liquid film should embed a bubble to stabilize it after its formation. Assuming spherical bubbles of radius R, the minimum liquid fraction required to cover them with a liquid shell of thickness e writes:

$$\phi_{min} \equiv e\frac{3(1-\phi)}{R} \tag{3.19}$$

thus the foaming criterion requires $\phi \geq \phi_{min}$:

$$\phi \gtrsim \frac{3e}{R}. \tag{3.20}$$

The dynamic thickness e, as the two bubbles approach to each other and the liquid interstice thins, should be given by the Stefan-Reynolds law [35]: $e \propto RCa^{1/2}$, where $Ca = R\eta\dot{\varepsilon}/\gamma$ is the capillary number, and η the viscosity of the foaming solution. Thus we expect:

$$\phi \geq \phi_{min} \propto Ca^{1/2}. \tag{3.21}$$

We estimate that in the constriction between the syringes the shear rates varies in a limited range $10^3 \leq \dot{\varepsilon} \leq 10^4 s^{-1}$, and that the bubbles size after foaming R does not depend strongly on the liquid fraction. In these conditions, the observed scaling $\phi_{min} \propto \eta^{1/2}$ is in qualitative agreement with the foaming criterion Eq. 3.21. As an order of magnitude, $e \lesssim r_d$. If the oil droplets are squeezed in these liquid layers (films) they could break them; only the films containing only the aqueous phase are stable. This is in agreement with the larger number of back-and-forth cycles (cf. Section 3.1.2) required to foam concentrated emulsions: at each cycle, a fraction of the new films is not stable, and break.

To summarize, we determine two criteria which together describe successfully the foamability with the double-syringe method of simple solutions, dilute emulsions and yield stress emulsions. In our experiments the transition from one criterion to the other is empirically linked to the existence of yield stress. The minimum liquid fraction that can be foamed is given by:

$$\phi_{min} = \begin{cases} 0.03(\frac{\eta}{\eta_{water}})^{1/2}(\frac{\mathcal{C}}{cmc})^{-1/3}, & \tau_y = 0 \\ \\ \frac{R_S}{R}[1 + \frac{R_S}{R} - \varphi(1 + \frac{R_S}{r_d})]^{-1}, & \tau_y > 0. \end{cases} \tag{3.22}$$

Further analysis could test the limits of application for this condition, by changing the nature of the suspension (solid particles, polymers...). Experiments with a control of the shear rate and of the stress could verify if the dependency of the empirical scaling is explained by Eq. 3.21 as conjectured. Additionally, testing with multiple surfactants could help to determine the dependency with its concentration that we measure. Another topic to scrutiny more is the transition between the two cases: we find it to coincide with the appearance of yield stress, which is consistent with a change in the flow dynamic. Nevertheless, we cannot exclude that the main difference were the crossover between the two limiting factors.

Simple foams										
ϕ (%)	2.6	3	5	5	8	8	8	-	-	-
T_{rot} (s)	5	5	5	5	4	4	4	-	-	-
Ω_p (μm^2/s)	192±3	144±5	119±9	110±6	93±2	98±2	130±3	-	-	-
R_{32}/R_{21}	1.1	1.2	1.2	1.2	1.3	1.3	1.3	-	-	-
Bubbly emulsions with the same small yield stress										
ϕ (%)	45	45	58	65	70	75	80	90	95	96
T_{rot} (s)	10	10	10	10	10	10	10	10	10	10
Ω_c (μm^3/s)	99±4	91±7	60±2	49±2	51±2	37±3	34±3	25±1	22±1	23±4

Table 3.2: Foam samples studied using the clinostat: liquid volume fraction ϕ , period of rotation T_{rot}, measured coarsening rate. The simple foams are prepared from a TTAB (5 g/L) aqueous solution; the surface tension of the TTAB aqueous solution at the air-liquid interface is $\gamma = 37$ mN/m. The emulsion is made of silicone oil droplets (350 cP viscosity) in a TTAB (18 g/L) glycerol aqueous mixture (52wt% glycerol). All the experiments are made from emulsion B, with $\varphi = 0.725$ and $\tau_y = 16.5$ Pa. The surface tension of the TTAB/glycerol aqueous solution at the air-liquid interface is $\gamma = 32$ mN/m. See more details in Sections 3.1.1 and 3.1.1.2.

3.3 Coarsening from dry foams to dilute bubbly suspensions

We studied in Chapter 2 the dependency of the coarsening rate of average bubble growth on the liquid fraction ϕ [13], thanks to experiments with aqueous foams placed in microgravity. We aim here to extend our investigations either in drier or more dilute samples, using the clinostat setup described in Section 3.1.3, in order to obtain a complete view valid from the dry limit to the dilute limit. The studied samples are described in Table 3.2. Examples of pictures of coarsening foams and bubbly liquids are showed in Fig. 3.13. In moderately wet foams $\phi \leq 8\%$ the continuous rotation is sufficient to avoid drainage. To study coarsening in bubbly liquids up to $\phi = 96\%$, we substitute the simple aqueous solution with a concentrated emulsion, with a yield stress $\tau_y = 16.5$ Pa large enough to stabilize the dispersions against drainage (cf. Sections 3.1.1 and 3.1.4.1).

We keep the same surfactant at the same concentration in the two cases, and we study the bubble growth only in a range of bubble sizes such that $\tau_y \ll \gamma/R$. Thus, we expect to observe the same coarsening growth law as that of a simple bubbly liquid, with a difference only in the prefactor $K_0 = \frac{8}{9}\gamma H_e D v_m$ (cf. Eq. 1.24). We discuss in Section 3.3.2.3 the difference that we can theoretically expect. We will compare quantitatively the relative variations in the coarsening rate Ω as a function of the liquid fraction ϕ.

3.3.1 Foam coarsening in the presence of adhesive forces

We studied the coarsening of simple foams (cf. Table 3.2) around the dry/wet boundary $\phi \approx 0.05$. We stabilized them against drainage by keeping the samples under continuous rotation (cf. Section 3.1.4). In the Lemlich model for dry foam coarsening [27] (cf. Section 1.2.3), the critical radius for foam coarsening is predicted to be R_{21}. Nevertheless, the coarsening rate itself is governed by the osmotic pressure of the foam Π (cf. Eq. 1.6), which scales with the mean Sauter radius R_{32}. Thus, in analogy with experiments performed in microgravity (cf. Chapter 2), we employ as average the mean Sauter radius R_{32} of the foam, and consider the ratio R_{32}/R_{21} in the discussion. First, we propose a model of foam coarsening in the presence of adhesive forces, which quantifies the variation in

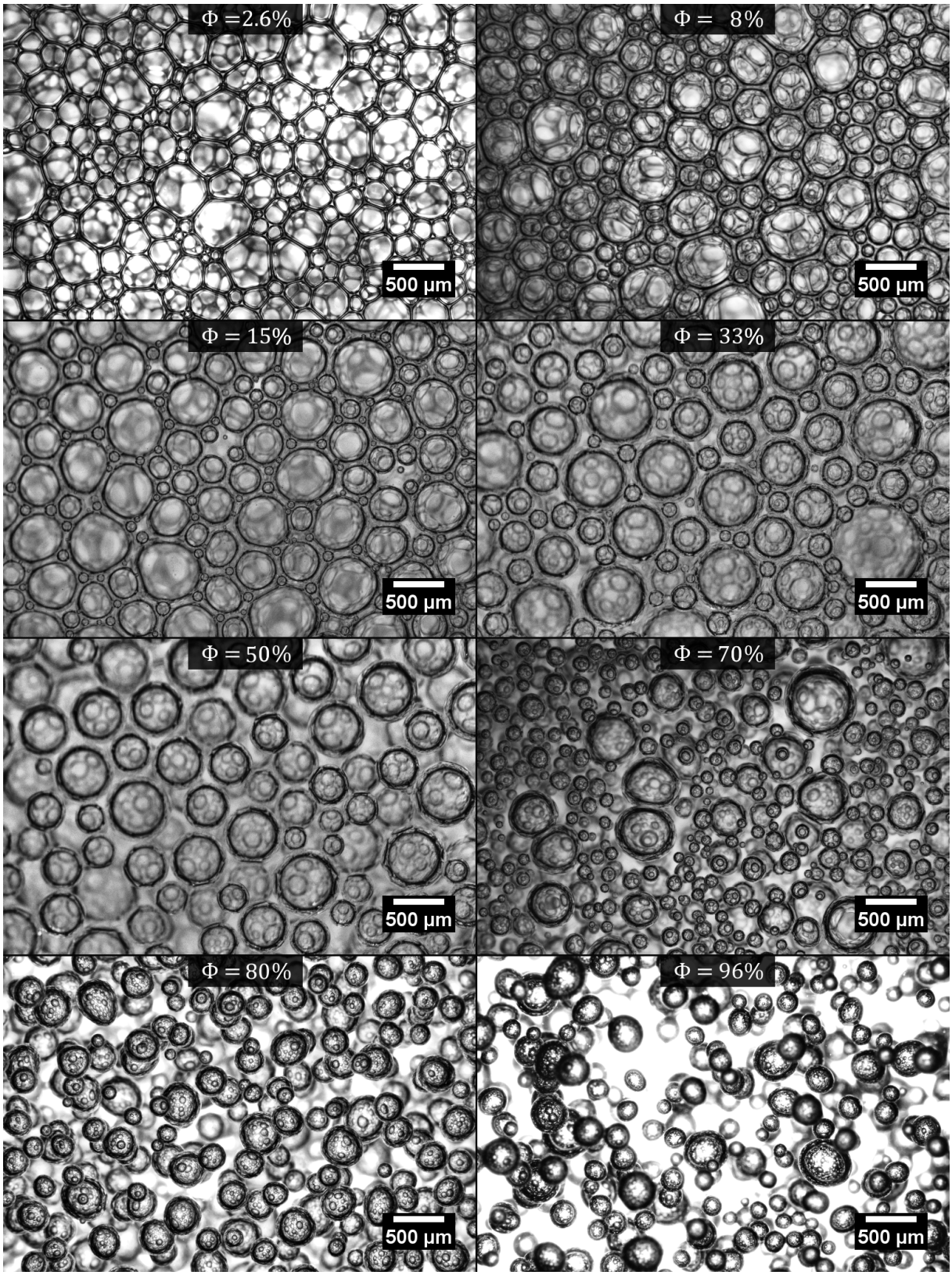

Figure 3.13: Pictures of foams and bubbly dispersions with liquid fractions ϕ ranging from the dry to the dilute limits, as indicated. The samples belong to three groups of experiments: ($\phi \leq 8\%$) dry foams studied on ground (cf. Table 3.2), ($15\% \leq \phi \leq 50\%$) wet foams and bubbly liquids studied in microgravity (cf. Table 2.2), ($\phi \geq 70\%$) bubbly emulsions studied on ground (cf. Table 3.2).

the coarsening rate due to these forces. Then, we discuss the experimental results and we compare them to the new model.

3.3.1.1 Modelisation

The steady state coarsening process of liquid foams can be described by a parabolic law, *i.e.* $\langle R(t)\rangle^2 = \overline{R_0}^2 + \Omega_p(t - t_0)$, with(cf. Section 1.2.3):

$$\Omega_p = C\Omega_0 \, f_2(\phi) \tag{3.23}$$

where $f_2(\phi)$ is the fraction of the bubble area covered by thin films [13], C is a constant depending on the type of the average performed for the radius ($C = (\langle R\rangle / R_{21})^2$), and Ω_0 is the coarsening constant that depends on the physico-chemical properties of the foaming liquid (cf. Eq. 1.40).We recall that a theoretical function for $f_2(\phi)$ has been proposed for arbitrary polydispersity and for liquid fractions up to the the random close packing [14], i.e. for $0 < \phi \leq \phi_{\text{rcp}}$:

$$f_2(\phi) = \frac{\tilde{\Pi}}{\tilde{\Pi} + 2(1-\phi)}. \tag{3.24}$$

$\tilde{\Pi}$ is the foam osmotic pressure, normalized by $\gamma/\langle R\rangle$. The following semi empirical relation describes experimental and simulation data for disordered foams over the full range of foam liquid fractions [12]:

$$\tilde{\Pi} = \frac{k(\phi - \phi_{\text{rcp}})^2}{\sqrt{\phi}} \tag{3.25}$$

For a disordered assembly of monodisperse bubbles $\phi_{\text{rcp}} = 0.36$, $k = 3.2$ (cf. Eq. 1.7). In polydisperse coarsened foam (steady state), it has been shown that $\phi_{\text{rcp}} = 0.31$ and $k = 4.75$ [13]. Note that Eq.1.41 vanishes at $\phi = \phi_{\text{rcp}}$.

The compressive force F_Π experienced by the bubbles at their contact facets as they are compressed under an osmotic pressure Π can be expressed as:

$$\Pi = \frac{1-\phi}{4\pi \langle R\rangle^2} z F_\Pi \tag{3.26}$$

where z is the number of contacts per bubble.

We recall that the strength of the forces between bubbles is characterized by the Young-Dupré contact angle θ (cf. Fig. 2.8). In the presence of adhesion, the bubbles are pressed against each other by an additional force F_θ, which increases their contact area compared to the case without adhesion. As a consequence, the adhesion creates an additional contribution σ_θ to the confinement pressure similar to Eq. 3.26. We write the total effective confinement pressure:

$$\sigma^*(\phi, \theta) \simeq \Pi(\phi) + \sigma_\theta = \Pi(\phi) + \frac{1-\phi}{4\pi \langle R\rangle^2} z F_\theta \tag{3.27}$$

According to [88, 89], the adhesion force F_θ is independent of the liquid fraction and given by:

$$F_\theta = 2\pi \langle R\rangle \, \gamma sin^2\theta \tag{3.28}$$

By reporting this expression in the effective pressure, we get:

$$\tilde{\sigma}^*(\phi, \theta) \simeq \tilde{\Pi}(\phi) + \frac{1}{2}(1-\phi) z sin^2\theta \tag{3.29}$$

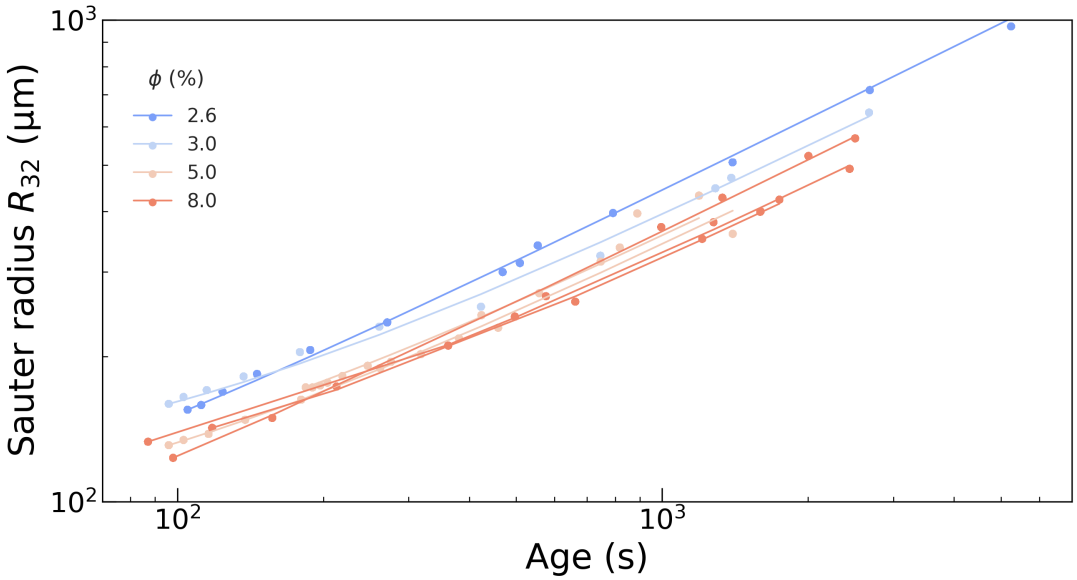

Figure 3.14: Mean Sauter radius R_{32} as a function of the foam age, for simple liquid foam studied in the clinostat (cf. Table 3.2). The continuous lines represent growth laws obtained by fitting a parabolic law (cf. Eq. 1.38) to the data.

and reporting $\tilde{\sigma}^*(\phi, \theta)$ in Eq. 1.41, we predict the fraction of film area as a a function of ϕ and the contact angle θ:

$$f_2(\phi, \theta) \simeq \frac{\tilde{\sigma}^*(\phi, \theta)}{\tilde{\sigma}^*(\phi, \theta) + 2(1 - \phi)} \tag{3.30}$$

Note that for $\phi = \phi_{\text{rcp}}$, $\tilde{\Pi}(\phi_{\text{rcp}}) = 0$ and $f_2(\phi_{\text{rcp}}, \theta) \simeq z sin^2\theta/4$, which is consistent with Pasquet *et al* [13].

The number of contacts per bubble, z, is expected to be in the range $12 \leq z_0 \leq 15$ for $\phi \ll \phi_{\text{rcp}}$. On the other limit, as ϕ gets close to ϕ_{rcp}, z should reach $z(\phi_{rcp}) \approx 6$ due to isostaticity [90]. In a repulsive foam, z discontinuously drops to 0 for larger liquid fractions $\phi > \phi_{rcp}$. In the presence of adhesion, we expect a smoother decrease, down to $z \simeq 0 - 2$ at $\phi^* \simeq 0.39$, above which Ostwald coarsening is observed and the associated cubic law replaces the parabolic law [13]. This evolution can be captured, for example, by a sigmoid function:

$$z(\phi) = \frac{z_0}{1 + exp[a(\phi - \phi_{rcp})]} \tag{3.31}$$

where a is a parameter which dictates the rate of variation of z.

3.3.1.2 Results

We show the evolution of the mean Sauter radius R_{32} as a function of foam age, in Fig. 3.14. For any liquid fraction ϕ, we observe an increase of R_{32} with time which follows the parabolic growth law expected for foams (cf. Eq. 1.38). We fit Eq. 1.38 to each curve. The fitted coarsening rates Ω_p are reported in Table 3.2. We observe that the coarsening rate decreases with the liquid fraction, which is consistent with a decrease of the contact area between neighbouring bubbles.

To gain more insight in the dependency with the liquid fraction, we combine our new measurements of the coarsening rate Ω_p with the measurements previously made on the same system previously in microgravity (cf. Chapter 2). We fit Eq. 3.23 to both sets of data, using Eqs. 3.30 and 3.31. We fix $\phi_{rcp} = 0.31$ [19] and $z_0 = 12$, and get

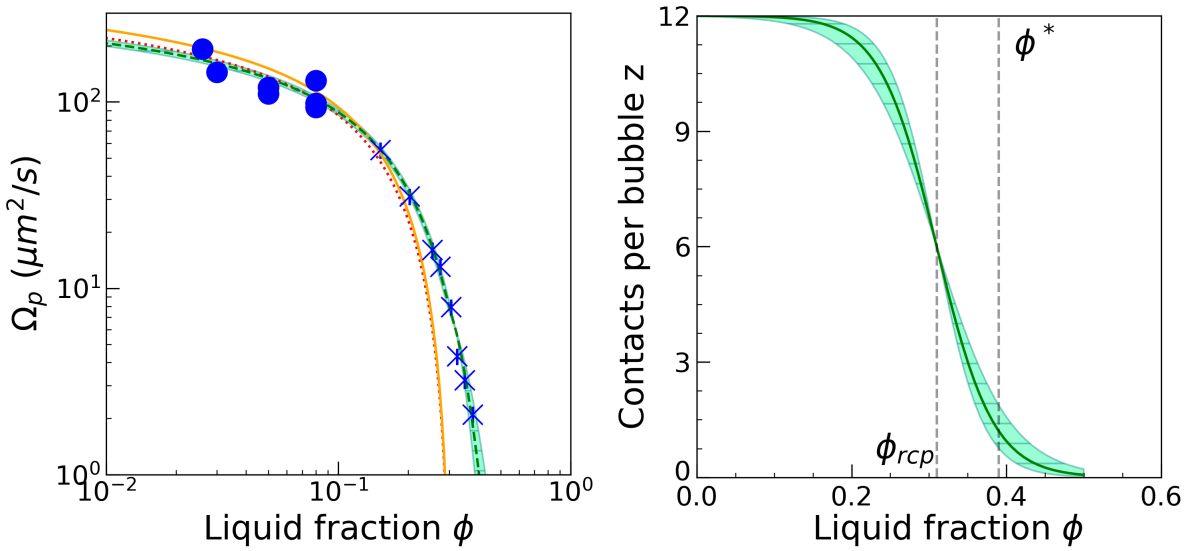

Figure 3.15: (left) Coarsening rate Ω_p (cf. Eq. 3.23) as a function of the liquid fraction, for simple liquid foams prepared from a TTAB (5 g/L) aqueous solution: (disks) studied in the clinostat, (X) studied in microgravity (cf. Table 2.2). The lines represent Eq. 3.23, with $\phi_{rcp} = 0.31$, using: (solid orange) Eq. 3.24, with $C\Omega_0 = 362$ μm^2/s [13] (cf. Chapter 2); (dotted red) Eq. 3.24, with fitted $C\Omega_0 \approx (330 \pm 20)$ μm^2/s; (dashed green) Eqs. 3.30 and 3.31, with contact angle $\theta = 3.6°$, and fitted $C\Omega_0 \approx (300 \pm 10)$ μm^2/s and $a = 27 \pm 6$. (right) Average coordination number z as a function of the liquid fraction, using Eq. 3.31 with $a = 27 \pm 6$ and $\phi_{rcp} = 0.31$. The green area corresponds to the variation in a for $\pm 1\sigma$.

$C\Omega_0 \approx (300 \pm 10)$ μm^2/s and $a = 27 \pm 6$. We show the good agreement between the fit and the evolution of Ω_p with ϕ in Fig. 3.14.

Thanks to the new data close to the dry limit, the value of $C\Omega_0$ is 17% smaller than that determined from microgravity data only where we found $C\Omega_0 \approx 360$ μm^2/s. From complementary laboratory experiments (cf. Appendix A) we have an updated estimation of $\Omega_0 \approx 240$ μm^2/s. From our clinostat measurements, we deduce $C = (R_{32}/R_{21})^2$ in the range $1.21 \leq C \leq 1.44$. Thus, our estimation $C\Omega_0 \approx 300$ μm^2/s is in good agreement with the updated value for $C \approx 1.25$. We conclude that the fitted coarsening constant Ω_0 is consistent with the equations, and we study the dependency of the dimensionless quantity $f_2 = \Omega_p / C\Omega_0$ with the liquid fraction.

In the regime where repulsive bubble interactions are dominant, i.e. up to $\phi \leq 0.15$, the difference between both predictions of $f_2(\phi)$ and $f_2(\phi, \theta)$ using Eq. 3.30 and Eq. 3.24 is negligible, as shown in the Fig. 3.15(left). For larger ϕ, it is necessary to consider the effect of adhesion to explain the data. We observe that, in fitting f_2, the agreement is not sensitive to a $\pm 20\%$ variation of the parameter a. The same is true for the average number of contacts per bubble $z(\phi)$, shown in Fig. 3.15 (right).For a different choice of $z_0 = 14$, we get a consistent value of $a \approx 31 \pm 7$, and a smaller $C\Omega_0 \approx 296 \pm 11$, which is still compatible with $\Omega_0 \approx 240$ with a smaller value of C.

We conclude that $f_2(\phi, \theta)$ describes really well the evolution of the coarsening rate Ω_p with respect to ϕ, in adhesive foams from the dry limit to the jamming transition $\phi = \phi^*$. It does not require fine-tuning of the parameters, and it is consistent with the physical framework of sphere packings. Experiments performed with a different chemical composition, and with variable contact angles θ, could test this law. Simulations could provide a more refined expression for Eq. 3.31, and a physical interpretation for a.

3.3.2 Coarsening in a bubbly emulsion

We study the coarsening of bubbly emulsions (cf. Table 3.2), with liquid fractions $0.45 \leq \phi \leq 0.96$. The yield stress of the emulsion, $\tau_y = 16.5$ Pa, stabilizes them against drainage (cf. Section 3.1.4). Since in Ostwald ripening the critical radius for coarsening is predicted to be the average radius $\overline{R}$, we will prefer it to R_{32} in the study of the growth laws.

3.3.2.1 Coarsening models for bubbly liquids

Over the years, following the classical Lifshitz-Slyozov-Wagner (LSW) model, which addresses bubble ripening in the dilute limit, a series of models have emerged to account for the effects of the liquid fraction ϕ (cf. Section 1.2.2)[25]. Each of these models builds upon the foundational principles established by LSW, yet they diverge in how they incorporate the influence of the finite distance between bubbles, on the solute concentration gradients surrounding each bubble, and the method of resolution for the diffusion problem. In the LSW model, the infinite dilution assumption simplifies the treatment of bubble interactions, as bubbles are assumed to be sufficiently far apart to neglect any overlap in concentration fields. However, as ϕ decreases, this assumption no longer holds, and the concentration gradient near one bubble can be significantly perturbed by the presence of nearby bubbles. Thus, the need arises for more sophisticated models that account for this proximity effect in order to predict the increase of coarsening rate as the liquid fraction decreases.

In the following, we consider four among them which have the most pertinent hypothesis for the case of bubbles - which is simplest than alloys or solid precipitates systems:

- In the modified LSW (MLSW) model [24], the average solute concentration in the continuous phase is not set at infinity, but on the surface of an 'influence sphere' centered around each bubble, with a radius r' (cf. Eq. 1.26), which depends on both the bubble size R and the average distance $\bar{l}$ between neighboring bubbles. Here, the distance $\bar{l}$ is estimated by assuming that the bubbles are monodisperse and randomly distributed throughout the continuous phase. The diffusion problem is treated with a mean-field approximation.

- In Tsumuraya-Miyata (TM) theory[91], 6 models are proposed taking into account different hypothesis for the spatial distribution of the particles, and how this affects the radius of the influence sphere r'. We will consider here the TM3 model, which assumes disposition of the bubbles in the continuous phase more ordered with respect to MLSW premises, as a result of the nucleation process (here the foaming process). Again, in TM3 model the diffusion problem is treated with a mean-field approximation.

- In Voorhees-Glicksman (VG) model [68], the mean-field approximation for the diffusion process is abandoned in favour of computer simulation techniques, which provide approximated solutions to the multiparticle-diffusion problem.

- In the Streitenberger (PS) model [92], a family of analytical solutions to the Ostwald ripening problem is derived based on four hypotheses: (1) the growth rate $\dot{V}$ depends only on the ratio $R/\overline{R}$; (2) there exists a critical bubble size R_c such that $\dot{V}(R_c/\overline{R}) = 0$; (3) the bubble size distribution has an upper bound characterized by $R_{max}/\overline{R}$; and (4) the growth rate $\dot{V}$ can be approximated by a second-order polynomial in $R/\overline{R}$. The approximate solution emerges from physical constraints established by previous theories and experimental observations. From it, the model predicts the evolution of the bubble size distribution and the coarsening rate as a function of the liquid fraction ϕ.

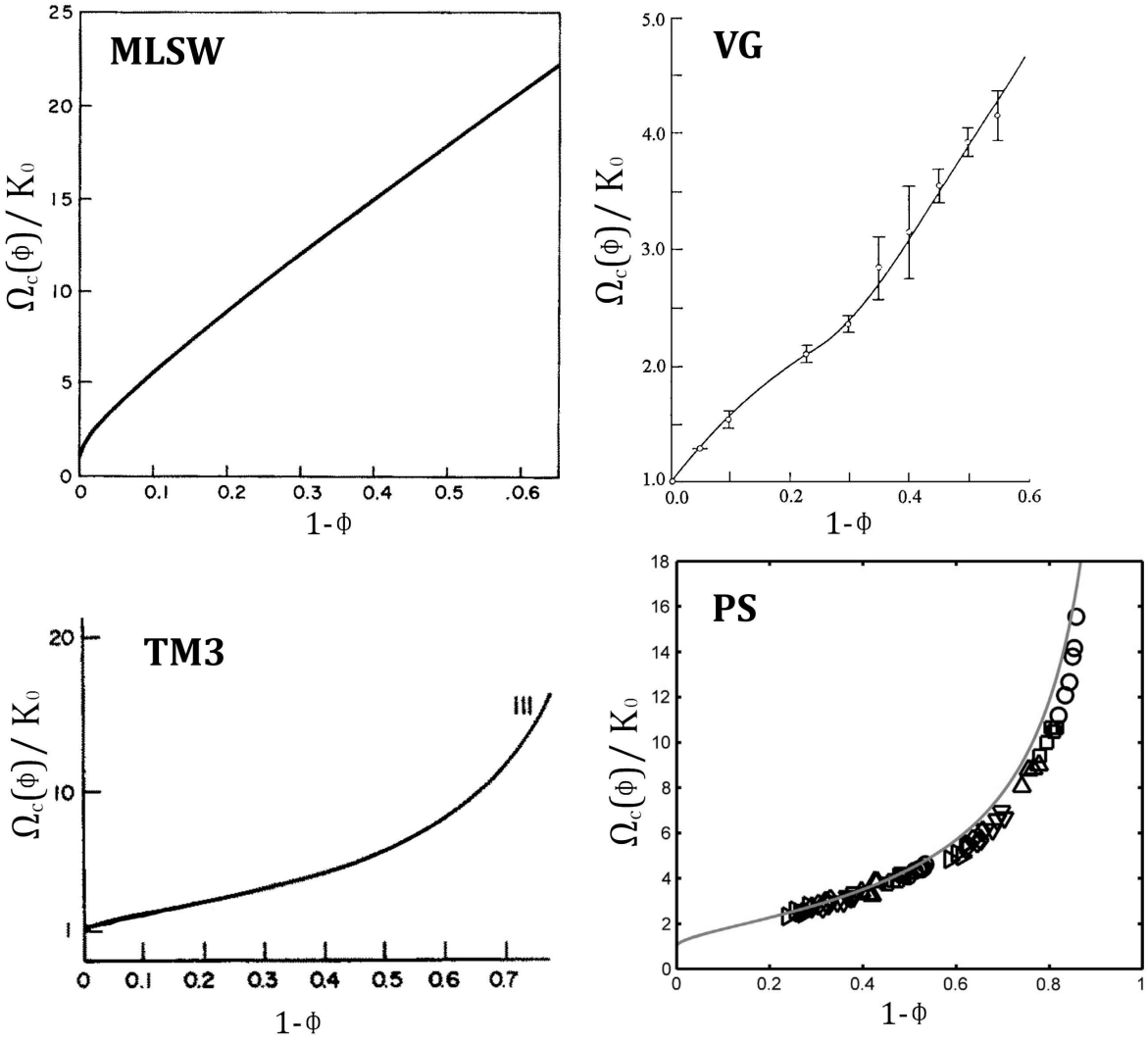

Figure 3.16: Evolution of the coarsening rate Ω_c as a function of the gas fraction $1-\phi$, according to 4 models (top to bottom, left to right): MLSW [24]; TM3 [91]; VG [68]; PS [92]. In VG and PS, the points represent simulations. The plots come from the cited articles.

For any given model, it is expected that the coarsening rate of the average bubble radius increases from the dilute value K_0, determined from the LSW model with Eq. 1.24, for increasing (resp. decreasing) gas fractions $1-\phi$ (resp. liquid fraction ϕ) (cf. Section 1.2.2). Similarly to what is done in foams, we introduce the *coarsening enhancement factor* $f_3(\phi)$, which describes the relative variation of the coarsening rate with ϕ:

$$\Omega_c(\phi) = C_3 K_0 f_3(\phi) \tag{3.32}$$

where C_3 is a constant depending on the type of the average performed for the radius ($C_3 = (< R > / \overline{R})^3$). By construction, $f_3(\phi = 1) = 1$. We plot the predictions of the four models in Fig. 3.16. Note that, for a given model, $f_3(\phi)$ is uniquely defined without additional parameters.

3.3.2.2 Results

We show the evolution of the mean radius $\overline{R}$ as a function of foam age, in Fig. 3.17(a). For any liquid fraction ϕ, we observe an increase of $\overline{R}$ with time which follows the cubic growth

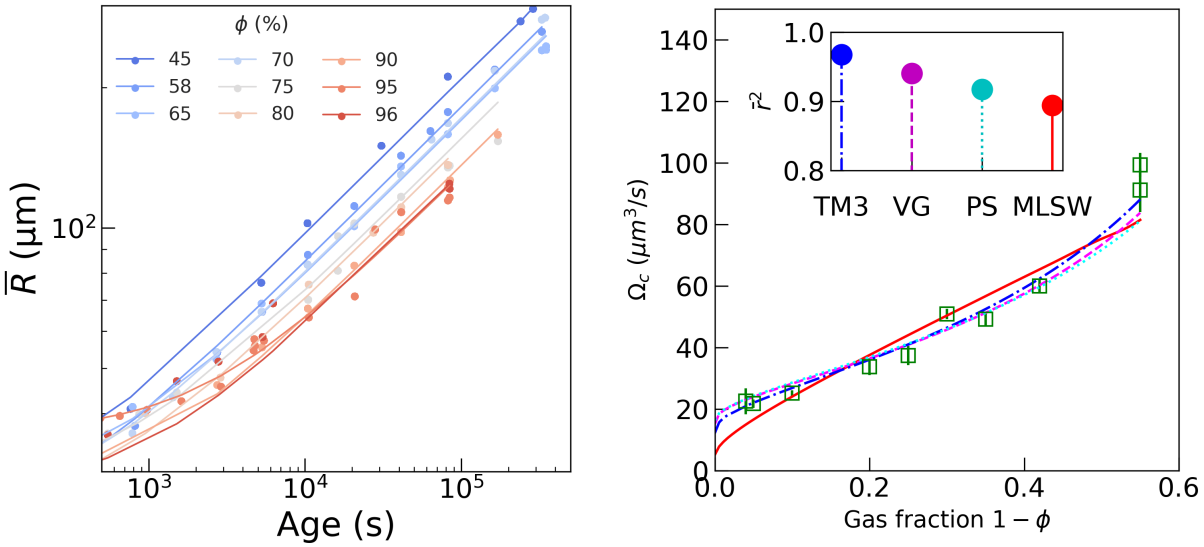

Figure 3.17: (left) Mean radius $\overline{R}$ as a function of the foam age, for bubbly emulsions studied in the clinostat (cf. Table 3.2). The continuous lines represent growth laws obtained by fitting a cubic law (cf. Eq. 1.23) to the data.(right) Coarsening rate Ω_c as a function of the gas fraction $1-\phi$. The lines show *Eq.* 1.24 fitted on the data, using for f_3: (dash-dotted blue) TM3 [91]; (dashed magenta) VG [68]; (dotted cyan) PS [92]; (solid red) MLSW [24]. In the inset we show the adjusted coefficient of determination $\overline{r}^2$, estimated for the 4 models. The values of K_0, $\overline{r}^2$ are reported in Table 3.3.

law expected for bubbly liquids (cf. Eq. 1.23). Remarkably, we observe that the plasticity of the continuous phase does not exhibit an influence on the growth law, at this stage of coarsening. Indeed, for each experiment; the average bubble size reaches a maximum value $\overline{R} \approx 200\mu$m, which corresponds to a capillary pressure $\Pi_c = 2/\gamma/\overline{R} \approx 300$Pa. This value is much larger than the emulsion yield stress $\tau_y = 16.5$ Pa and bubbles keep there spherical shape. We measured the bubble radius distribution and observe that the dispersions reach a scaling state for coarsening times $t \gtrsim 10^4$s. The PDF are given in Appendix B. We fit Eq. 1.23 to each curve. The fitted coarsening rates Ω_c are reported in Table 3.2. We observe that the coarsening rate increases for decreasing liquid fraction, as expected according to all the models for coarsening in bubbly liquids.

For the smallest liquid fraction corresponding to a bubbly liquid studied with the clinostat, we find : $\Omega_c \approx 95$ μm^3/s (here $C_3 = 1$)(Table 3.2). The equivalent simple bubbly liquid measured in microgravity yields $\Omega_c = \Omega_{c,R32}/C_3^3 \approx 163$ μm^3/s (Table 2.2). Thus the bubbly emulsion must have a coarsening constant ≈ 1.7 times smaller than the simple bubbly liquid. This suggests that gas diffusion is slower in the bubbly emulsion than in the simple surfactant solution. This will be studied in detail in Section 3.3.2.3.

We compare now the evolution of the coarsening rate Ω_c with the gas fraction $1-\phi$ to the four predictions described in the previous section. Each model provides numerical results for f_3 at different gas fractions $1-\phi$, which we interpolate with cubic splines on our values of $1-\phi$. We fit Eq. 1.30 to Ω_c as a function of the gas fraction $1-\phi$, fixing $C = 1$ and $f_3(1-\phi)$ with one of the predicted expressions at a time; letting K_0 be a free parameter. The fitted values of K_0 are presented in Table 3.3. We compare in Fig. 3.17(b) the models and the experimental results. We see that MLSW predicts a linear scaling in the range of gas fractions under study, which is incompatible with the observations. On the contrary, the other three models exhibit a good agreement with the experiments, with a flex point around $1-\phi = 0.20$ and an increasing slope after that point. To provide a quantitative comparison, we compute for each fit the adjusted coefficient of determination

Model	TM3 [91]	VG [68]	PS [92]	MLSW [24]
K_0 (μm^3/s)	12.1 ± 0.3	15.1 ± 0.5	16.2 ± 0.6	4.2 ± 0.2
$\bar{r}^2$	0.97	0.94	0.92	0.89

Table 3.3: Fitted coarsening rate in the dilute limit K_0 and adjusted coefficient of determination $\bar{r}^2$, for 4 models of the coarsening enhancement factor f_3, fitted to the experimental values of the coarsening rate Ω_c.

$\bar{r}^2$, and show it in Table 3.3 and in the inset of Fig. 3.17(b). The use of $\bar{r}^2$ is justified in this situation, by treating $f_3(1-\phi)$ as a transformed variable and Eq. 1.30 as a regression linear in the parameter K_0. We find that TM3 model correlates better with the data among the four models tested, with a score $\bar{r}^2 = 0.97$. Qualitatively, the main difference between TM3 and the two closest models, VG and PS, is that it predicts a faster evolution of Ω_c in the range $1 - \phi > 0.4$, in agreement with the data.

Thus, we consider the prediction from TM3 of coarsening rate in the dilute limit, $K_0 = (12.1 \pm 0.3)$ μm^3/s, as the most accurate. Now, we can now fit Eq. 1.30 to the coarsening rates of simple bubbly liquids, using the f_3 expression of TM3 model. We get $K_0^{simple} \approx (29 \pm 5)$ μm^3/s, with a large uncertainty due to the limited range of liquid fractions $0.40 \leq \phi \leq 0.50$ of those data. It is a value ~ 2.4 times larger than what is predicted by the mean-field approximation in the LSW model $K_0^{simple,th} \approx 12$ μm^3/s, taking into account the physical-chemistry of the system (cf. Section 3.3.2.3). In view of the good agreement in Section 3.3.1.2 between the experimental and the theoretical values of Ω_0, we exclude that this factor 2.4 could be an artifact of surface observations.

We conclude that bubbly emulsions coarsen following the same growth law as simple bubbly liquids, as long as capillary pressure dominate over plastic stresses. We find that TM3 model describes really well the evolution of the coarsening rate Ω_c with respect to ϕ, in bubbly liquids spanning the full range of liquid fractions from the jamming transition $\phi = \phi^*$ to the dilute limit $\phi \to 1$. We estimate for the bubbly emulsions under study the coarsening rate in the dilute regime, $K_0 = (12.1 \pm 0.3)$ μm^3/s; in the next section we discuss the physical-chemistry of diffusion in such a medium.

3.3.2.3 Gas diffusion through emulsions

In this section, we try to estimate the coarsening rate corresponding to the dilute limit of bubbles in emulsions $K_0 = 8/9\gamma D H_e v_m$ (cf. Eq. 1.24), where D is the diffusion coefficient, He the Henry constant of gas solubility, $v_m \approx 0.024$ m^3/mol the gas molar volume. The diffusion of air inside an emulsion is an open physical problem: it involves 2 gas species (N_2, O_2) diffusing inside 2 immiscible liquid phases (the glycerol aqueous solution $Gly52/H_2O$ and the silicon oil). The liquid phases themselves are structured like a porous medium, with the oil phase dispersed inside the aqueous one. In the following we first determine K_0 for the two liquid phases, with the information gathered from literature, and then we consider the effect of the porous structure. We report the relevant physico-chemical properties of the liquid phases in Table 3.4, estimated for $T = 25°C$. To distinguish the gas and liquid species involved, we will use subscripts to index the gas phase, and superscripts to index the liquid phase.

For Gly/H_2O solutions, the surface tension is modified by the presence of glycerol at the interface; in absence of more specific measurements we consider $\gamma^{\mathcal{G}52} \approx \gamma^{\mathcal{G}20} = 33.4$ mN/m. The diffusion coefficient is inversely proportional to the liquid viscosity $D \propto 1/\eta$: at that temperature the dynamic viscosity η of aqueous glycerol solutions is given by [93]:

$$\eta(\mathcal{G}) = 0.91 e^{-6.9(1-\mathcal{G}+1.37\mathcal{G}(1-\mathcal{G})/0.66\mathcal{G}+2.1(1-\mathcal{G}))}. \tag{3.33}$$

Liquid phase	η	He_{N2}	He_{O2}	He_{Air}	D_{Air}	γ	K_0^{th}	K_0^{exp}
	mPa s	10^{-6} mol Pa^{-1}m^{-3}			10^{-9}m^{2}s^{-1}	mN m^{-1}	μm^{3}s^{-1}	
Pure water	1	6.5	12.7	7.6	2	37.5	*12*	29 ± 5
Solution $\mathcal{G} = 0.20$	1.5	3.5	8.2	*4.5*	*1.3*	33.4	*4.2*	-
Solution $\mathcal{G} = 0.52$	5.6	2	*6*	*3*	*0.36*	*33.4*	*0.8*	-
Silicon oil	350	69	110	77	*0.006*	-	*0.3*	-
Emulsion $\varphi = 0.725$	-	-	-	*57*	*0.011*	*33.4*	*0.45*	12.1 ± 0.3

Table 3.4: Chemical properties relevant to gas diffusion, in a series of liquids , at a temperature $T = 25°C$. Values gathered from literature are in plain text, those estimated in the text are in *italic*. Data for silicon oil come from [97]. Dynamic viscosity η, estimated for glycerol solutions interpolating values from [95] using Eq. 3.33. Gas solubility He, determined for three gases (di-nitrogen, di-oxygen, air) as explained in the text; for glycerol solutions we use values from [95] (N_2) or [96] (O_2), and estimate the missing values as explained in the text. Diffusion coefficient of air in the liquid D_{Air}. Surface tension at the interface between gas/TTAB/continuous phase γ; measurements for TTAB at $\mathcal{C} = 5$ g/L (cf. Appendix A).Theoretical coarsening rate in the dilute limit rate K_0^{th}, determined from Eq. 1.24; for silicon oil and the emulsion we give an effective value, as explained in the text. Experimental coarsening rate in the dilute limit K_0^{exp} determined by fitting Eq. 1.30 to experimental measurements in previous section, assuming that f_3 follows TM3 model.

The solubility of a gas g, He_g, in a mixture of liquid solvents $1, 2$ scales with the molar ratios x of each solvent [94]:

$$He_g^{1,2}(x_1, x_2) = (He_g^1)^{x_1}(He_g^2)^{x_2} e^{a^{12} \cdot x_1 \cdot x_2} \tag{3.34}$$

where He_g^i is the solubility of the gas g in the pure solvent $i = 1, 2$, and a^{12} is the interaction parameter between the solvent phases $1, 2$. We fit Eq. 3.34 to the measurements of solubility in glycerol solutions for N_2 [95] or O_2 [96], and plot the solubilities as a function of the glycerol concentration in Fig. 3.18(a). To obtain He_{O_2} at $\mathcal{G} = 0.52$ we need to extrapolate the fitted law. We determine He_{Air} as the sum of the individual solubilities, weighted by the respective molar fractions: $He_{Air} = (0.78He_{N_2} + 0.21He_{0_2})/0.99$. We can finally determine K_0 as a function of the glycerol concentration, and we report it in Table 3.4 for 2 reference glycerol concentrations $\mathcal{G} = 0.20$ or 0.52. The bubble liquid/gas interfaces have the same surface tension as the glycerol solutions: $\gamma = 33.4$ mN/m. For diffusion only through silicon oil, we estimate an effective $K_0^{oil} \approx 0.3$ μm^3/s. This value is about half the coarsening constant value expected for our glycerol solutions: $K_0^{\mathcal{G}52} \approx 0.8$ μm^3/s. The large viscosity of the oil phase has been partially compensated by the large solubility of air in it. Therefore, we expect the oil droplets to contribute to the diffusion process.

We adapt here Zhang's review on diffusion in heterogeneous media [98]. We consider the problem of parallel diffusion in a biphasic system. The effective solubility in the medium is the sum of the solubilities of the two phases, weighted by their volume fractions:

$$He^{emulsion} = He^{oil}\varphi + He^{aq}(1 - \varphi). \tag{3.35}$$

When the two phases are separated and diffusion can proceed in parallel, the effective diffusion coefficient of the medium is again the sum of the diffusion coefficients of the two phases, weighted by their solubilities and volume fractions:

$$D^{emulsion} = \frac{D^{oil}He^{oil}\varphi + D^{aq}He^{aq}(1 - \varphi)}{He^{emulsion}}. \tag{3.36}$$

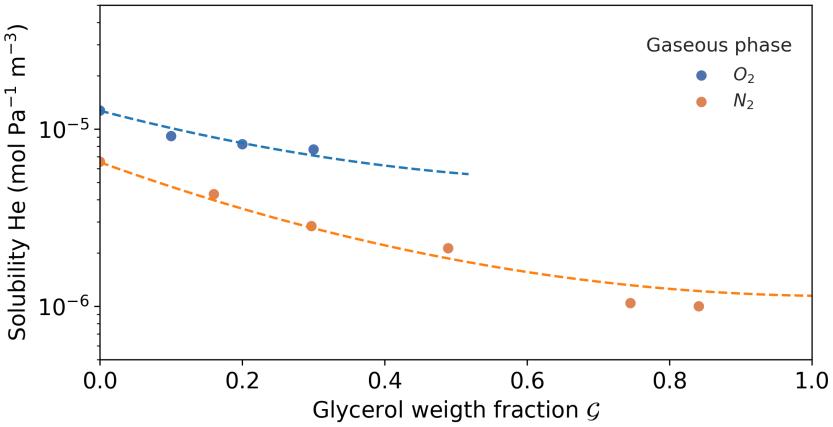

Figure 3.18: Solubility He of water/glycerol solutions, as a function of the glycerol weight fraction $\mathcal{G}$, for: N_2 [95], O_2 [96]. The dashed lines show Eq. 3.34 fitted to the data, with: fixed parameters $He_{N_2}^{H_2O} = 6.5 \cdot 10^{-6}$ mol Pa^{-1} m^{-3}, $He_{O_2}^{H_2O} = 12.7 \cdot 10^{-6}$ mol Pa^{-1} m^{-3}; free parameters $He_{N_2}^{Gly} = 1.1 \cdot 10^{-6}$ mol Pa^{-1} m^{-3}, $He_{O_2}^{Gly} = 5.6 \cdot 10^{-6}$ mol Pa^{-1} m^{-3}, $a^{H_2O,Gly} = -1.6$.

For $\varphi = 0.725$, using Eqs. 1.24, 3.35 and 3.36, we get: $He^{emulsion} \approx 57 \cdot 10^{-6}$ mol Pa^{-1}m^{-3}, $D^{emulsion} \approx 0.011 \cdot 10^{-9}$m^{2}s^{-1}, $K_{0,th}^{emulsion} \approx 0.45$ μm^3/s. This value is 27 times smaller than the experimental result $K_{0,exp}^{emulsion} \approx 12.1$ μm^3/s. Taking into account the factor $K_{0,exp}^{H_2O}/K_{0,th}^{H_2O} \sim 2.4$, the ratio becomes ~ 11. We could refine the model of parallel diffusion, taking into account the tortuosity arising from the porous structure of the emulsion. Nevertheless, that would provide only a small correction to $K_{0,th}^{emulsion}$. The gap between $K_{0,exp}^{emulsion}$ and $K_{0,th}^{emulsion}$ cannot be explained either by the choice of coarsening model: the most conservative estimation, $K_{0,exp}^{emulsion} \approx 4.2$ μm^3/s, is 4 times bigger than expected.

In view of this unexpected result, and the lack of previous studies of the subject, we conclude that diffusion in emulsions cannot be completely explained by the usual physical-chemistry arguments. The porous structure created by oil droplets determines a diffusion faster than the continuous phase alone. As we have reported, this effect does not impact the nature of the growth laws, but only the common factor. We propose two hypotheses for this behaviour, for future experiments or theories to test:

- **Surface diffusion**. In solid porous media with slow bulk diffusion, one can measure an anomalous diffusion of solute across the medium. This results from the solute 'jumping' along the interface in adsorption/desorption cycles, and generating a fast effective diffusion along the pore surface [99].

- **Droplets as a solute reservoir**. Oil droplets present a gas solubility constant He 26 larger than that of the glycerol solution, with a diffusivity D 60 times smaller. Moreover, the oil droplets are not connected, and the parallel diffusion through the two phases could be unjustified. Instead, diffusion could happen mainly through the glycerol solution, and the oil droplet could behave as a gas reservoir in view of their disproportionate capability to accumulate the solute. This would increase the average solute saturation.

3.4 Summary: coarsening from foams to the dilute limit

In this chapter, we developed the knowledge and the techniques necessary to mitigate gravity-driven drainage, and to study coarsening of foams and bubbly liquids outside the microgravity conditions described in the previous chapter.

A significant aspect of the study involved the design of the Clinostat setup, described in Section 3.1.3. It allows to accurately perform videomicroscopy on foams samples for bubbles sizes spanning two orders of magnitude, $5\mu m \leq \overline{R} \leq 1mm$, and over 5 orders of magnitude for foam age. We show in Section 3.1.4 that the continuous rotation of the foam is able to delay the insurgence of drainage. We experimentally determine that foams are stabilized against drainage as long as their average bubble size is smaller than a maximum radius $R_M(T, \phi)$, which is a decreasing function of both the liquid fraction in the foam ϕ and of the period of rotation T (Eq. 3.12). In the clinostat setup, this method is sufficient to study the coarsening of foams up to the inset of the wet regime $\phi \leq 10\%$. For larger liquid fraction, the needed period of rotation T would become small enough to generate a centrifugal acceleration, detrimental for coarsening. For wet foams and bubbly liquids, drainage can be delayed by employing a yield stress fluid, like an emulsion, as the effective continuous phase of the dispersion. In Section 3.1.4.1, we show that for both kind of systems it is predicted a maximum radius $R_M(T, \phi)$ scaling with the yield stress of the emulsion τ_y: at $\tau_y \sim 3Pa$, millimetric bubbles should be stable.

In Section 3.2, we study the conditions for good foaming with the double syringe method, for both simple liquids and emulsions. We observe that, for a given sample, it exists a minimum liquid fraction ϕ_{min}, below which the result is not stable and homogeneous. For concentrated emulsions, we determine that ϕ_{min} is set by the scarcity of surfactant, and the bubble interfaces cannot be stabilized (Eq. 3.13). In simple surfactant solutions and dilute emulsions, we find an empirical criterion which gives a dependency of ϕ_{min} from the viscosity of the solution η (Eq. 3.18). We show that this condition is compatible with a physical principle: bubbles need to be covered by a shell of liquid, whose thickness has the same dependency from η (Eq. 3.21). Eq. 3.22 summarises our knowledge of good foaming with the double syringe method.

In Section 3.3.1, we study the coarsening of adhesive foams as a function of ϕ. We observe that the average bubble radius grows according to a parabolic law, as expected in the foam regime. The coarsening rate Ω_p decreases with the liquid fraction ϕ, following the same trend that we found in wet foams in Section 2.2. We propose a new model, which extends the consolidated predictions for the evolution of the fraction of contact film area in bubbles $f_2(\phi)$ with ϕ, incorporating adhesion effects (cf. Section 3.3.1.1). We see that the dependency of Ω_p from ϕ is well described by our model, for both these samples and the ones studied in the previous chapter (cf. Fig. 3.14 (b)).

In Section 3.3.2, we study the coarsening of bubbly emulsions in the capillary regime ($\gamma/R \gg \tau_y$) as a function of ϕ, at constant τ_y. The range of liquid fraction under study, $0.45 \leq \phi \leq 0.96$, has never been studied in long coarsening experiments. We observe that the average bubble radius grows according to a cubic law, as expected in the dilute regime. The coarsening rate Ω_c decreases with the liquid fraction ϕ, and we compare its evolution with the prediction given by 4 models (cf. Fig. 3.17(b)). We find that the best prediction is given by the TM3 mean-field coarsening model. We fit the coarsening rate for the bubbly emulsions in the dilute limit, K_0, and compare it with the theoretical predictions (cf. Section 3.3.2.3). We observe a significant gap between the two values, indicating the presence of additional mechanisms that enhance diffusion rates in emulsions. Two potential explanations for this phenomenon were proposed, though further experimental work is required for confirmation.

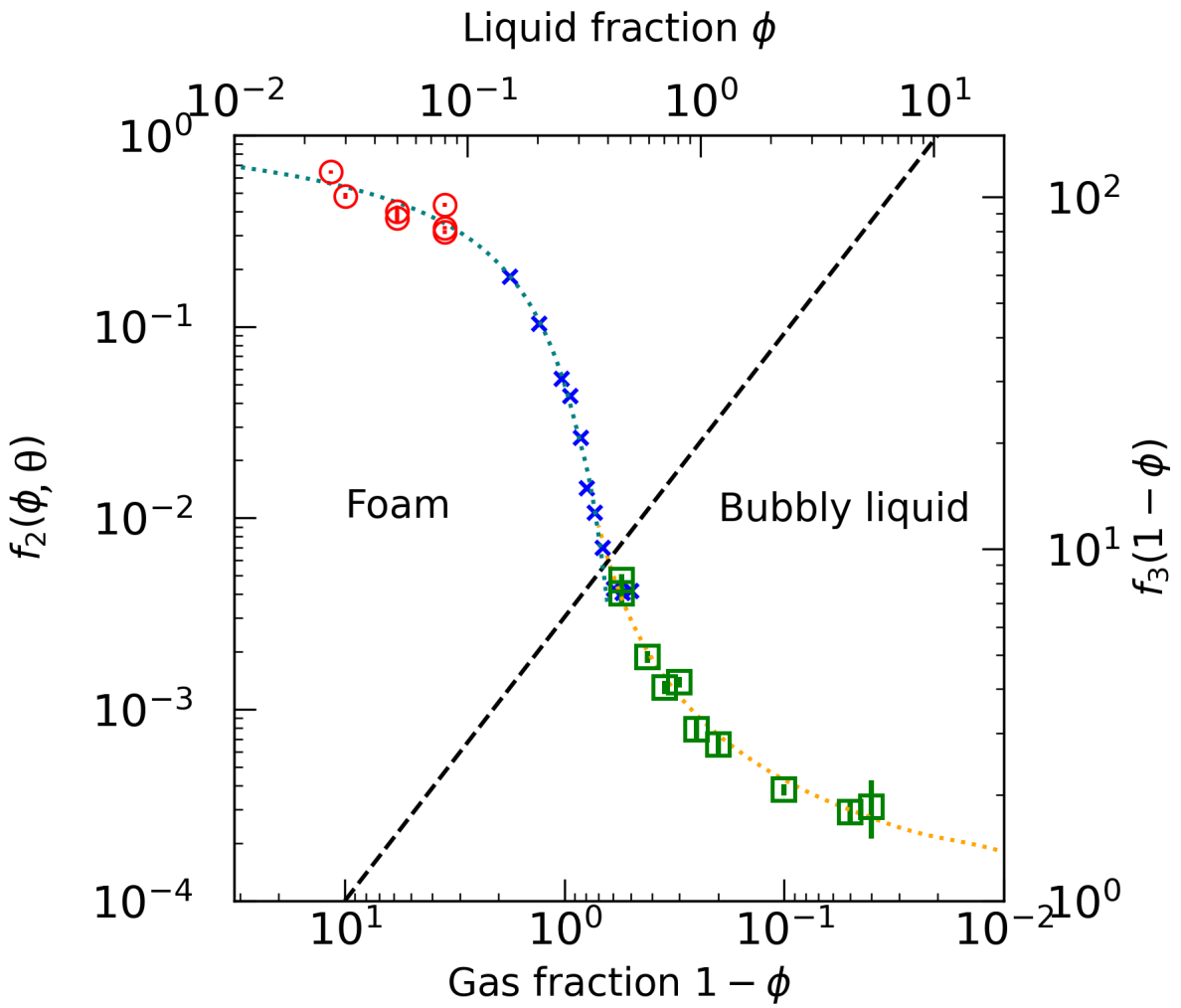

Figure 3.19: Dependency of the normalized coarsening rate with the volume fraction of the continuous/dispersed phase in bubble dispersions, from the dry limit to the dilute limit. (top left) Evolution of the fraction of bubble surface area covered by the films $f_2(\phi, \theta)$ with the liquid fraction ϕ of the foam. (bottom right) Evolution of the coarsening enhancement factor $f_3(1-\phi)$ with the gas fraction $1-\phi$ of the bubbly liquid. The points are experimental results, determined normalizing Ω_p (resp. Ω_c) by the dry limit value Ω_0 (resp. the dilute limit value K_0), for: (red circles) foams on ground (cf. Fig. 3.14), (blue crosses) adhesive wet foams or bubbly liquids in microgravity (cf. Figs. 2.6 and 2.7), (green squares) bubbly emulsions on ground (cf. Fig. 3.17). Coarsening rates are determined for the mean Sauter radius R_{32} in foams and for the average radius $\overline{R}$ in bubbly liquids. The blue dotted line shows Eq. 3.24, with parameters $\theta = 3.6°$ and $a = 27$. The dotted orange line shows the predictions of f_3 given by TM3 model [91] (cf. Fig. 3.16). The two x-axes are aligned on the common value $\phi = 1-\phi = 0.5$. The two y-axes are aligned on the simple bubbly liquid closer to the jamming transition $\phi^* \approx 0.40$ where $f_2 = 4 \cdot 10^{-3}$ and $f_3 = 7.5 \pm 0.4$.

We summarise these findings in Fig. 3.19, which shows how the coarsening rate of a bubble dispersion varies for any range of liquid fractions. We hope that, by providing experimental observations on both sides of the jamming transition ($\phi = \phi^*$), we will help theoreticians in modeling the jamming transition even for adhesive foams.

In the next chapter, we will study coarsening of foamed emulsions outside the capillary limit ($\tau_y \sim \gamma/R$), to investigate the effects of plasticity.

Chapter 4

Morphological and kinetic modifications in a plastic foam undergoing coarsening

Contents

In the previous chapter, we discussed the preparation of foamed emulsions, and studied their coarsening in conditions such that plasticity affects only drainage. In this chapter we consider instead a wider range of Bingham capillary numbers, to detail the difference these foams develop with respect to their simple counterparts. Finally, we combine all these features in a unique map, describing the coarsening regimes of foamed emulsions.

4.1 Materials and Experimental setup

As discussed in section 3.2, the foamability of an emulsion with a yield stress larger than about 20 Pa remains challenging, and constitutes an obstacle that needs to be overcome to study coarsening arrest. A simple argument [45] suggests that coarsening should be stopped when the foam plasticity becomes stronger than capillarity, e.g. when the Bingham capillary number $Bi = \tau_y R/\gamma \approx 1$. In a typical clinostat experiment (cf. section 3.1.3), we have $Bi \approx 0.1$. Thus we need to increase by at least one order of magnitude either the average bubble size R reached at the end of coarsening or the emulsion yield stress τ_y. To study bubbles 10 times larger while keeping the same number of bubbles as in the clinostat would require to increase by ten times the cell radius and height, generating a consumption of 10 L of foam per experiment instead of the usual (and affordable) 10 mL. Therefore we discarded that idea and developed a new setup where we increase the emulsion yield stress after the foam production using an osmotic cell that allows the continuous phase of the emulsion to be withdrawn from the sample. In the following, we describe the studied samples, the osmotic cell set-up and its validation using a numerical simulation. Finally we present the image analysis tools we developed in the framework of the automatic segmentation model YOLO to analyse images of the foam structure recorded at the surface of the sample, and which allow radius and contour shape of thousands of bubbles to be determined and tracked at each instant along coarsening.

4.1.1 Emulsion and foam samples

Monodisperse transparent emulsions constituted of silicone oil droplets dispersed in a TTAB and glycerol aqueous solution are prepared as described in section 3.1.1. Their characteristic properties are given in table 4.1. They are foamed with air using the double-syringe method (cf. 3.1.2) which allows to probe the parameter space of liquid volume fraction in the foam ϕ and oil volume fraction in the emulsion φ comprised between $0.25 \leq \phi \leq 0.96$, $0.65 \leq \varphi \leq 0.80$ (cf. table 4.1). These samples are placed in the clinostat cell, slowly rotated along its horizontal axis at a speed of 6 rpm as described in Section 3.1.3. In addition, samples prepared with the double syringe with initial oil fraction $60\% \leq \varphi \leq 70\%$ and liquid fraction $30\% \leq \phi \leq 95\%$ are injected in the osmotic cell, also slowly rotated along its horizontal axis at a speed of X tr/min. After liquid withdrawing, the final reached oil and liquid volume fractions are respectively $86\% \leq \varphi \leq 96\%$ and $23\% \leq \phi \leq 94\%$, as indicated in Table 4.2.

4.1.2 Osmotic cell

We now describe the osmotic cell designed in collaboration with Brice Saint-Michel at Laboratoire Navier. As schematically represented in Figure 4.1, The cell has a cylindrical shape with dimensions similar to those of the clinostat (inside diameter $D_{int} = 47.0$ mm, height $L = 11.7$ mm). It is delimited on one side by a rigid fixed semipermeable membrane, whose pores block the passage of air bubbles and oil droplets letting only the aqueous phase to flow through (membrane Sartorius 11107–47–N reference with pore size = 0.2 µm). The other side of the cell is delimited by a rigid transparent sliding window which allows videomicroscopy observations. This window, properly lubricated on its sides with the same silicon oil we employ for the emulsion, is free to move and to account for the progressive sample volume variation as the aqueous phase is withdrawn. The sample is in contact with a liquid reservoir containing the same solution as the continuous phase of the emulsion through the membrane. The reservoir is connected to a syringe pump (Standard Infuse/Withdraw PHD ULTRA™ Syringe Pumps, Harvard Apparatus) using a

Clinostat							
Foam regime				**Bubbly regime**			
ϕ (%)	φ (%)	Emulsion	τ_y (Pa)	ϕ (%)	φ (%)	Emulsion	τ_y (Pa)
25	65	A	1.4 ± 0.2	45	72.5	A	10.0 ± 0.2
25	65	A	1.4 ± 0.2	45	72.5	B	16.47 ± 0.01
25	66.5	A	2.65 ± 0.07	45	75	A	14.3 ± 0.3
25	68	A	3.11 ± 0.08	58	72.5	B	16.47 ± 0.01
25	70	G	2.7 ± 0.1	65	72.5	B	16.47 ± 0.01
30	65	A	1.39 ± 0.2	70	72.5	B	16.47 ± 0.01
30	66.5	A	2.65 ± 0.07	80	72.5	B	16.47 ± 0.01
30	68	A	3.11 ± 0.08	90	72.5	B	16.47 ± 0.01
30	70	A	5.1 ± 0.1	95	72.5	B	16.47 ± 0.01
30	70	A	5.1 ± 0.1	96	72.5	B	16.47 ± 0.01
30	72.5	A	10.0 ± 0.2				
30	75	A	14.3 ± 0.3				
35	75	A	14.3 ± 0.3				

Table 4.1: Foam samples studied using the clinostat: liquid volume fraction ϕ, oil volume fraction φ, emulsion yield stress τ_y. The emulsion is made of silicone oil droplets (350 cP viscosity) in a TTAB (18 g/L) glycerol aqueous mixture (52wt% glycerol). The characteristics of the specific emulsions are detailed in Table 3.1. The surface tension of the TTAB/glycerol aqueous solution at the air-liquid interface is $\gamma = 34.3$ mN/m. See more details in Sections 3.1.1 and 3.1.1.2.

Osmotic cell							
φ^0 (%)	ϕ^0 (%)	τ_y^0 (Pa)	Emulsion	Π_{set} (kPa)	φ^f (%)	ϕ^f (%)	τ_y^f (Pa)
65	30	0	C	10	92	23	91
70	40	4	C	10	95	33	115
70	40	3	D	10	91	34	63
70	40	4	C	33	88	35	66
70	50	4	C	10	92	43	94
70	60	4	C	1	84	55	108
70	60	4	C	10	94	53	110
70	60	3	D	10	95	53	83
70	60	3	D	10	95	52	36
70	80	4	C	1.5	88	76	67
70	80	4	C	10	87	76	65
70	88	4	C	10	86	86	58
70	88	3	D	10	93	85	69
70	95	4	C	33	96	93	118

Table 4.2: Foam samples studied using the osmotic cell: initial liquid volume fraction ϕ^0, initial oil volume fraction φ^0, initial emulsion yield stress τ_y^0, osmotic pressure Π_{set}, final liquid volume fraction ϕ^f, final oil volume fraction φ^f, final emulsion yield stress τ_y^f. The emulsion is made of silicone oil droplets (350 cP viscosity) in a TTAB (18 g/L) glycerol aqueous mixture (52wt% glycerol). The characteristics of the specific emulsions are detailed in Table 3.1. The surface tension of the the TTAB/glycerol aqueous solution at the air-liquid interface is $\gamma = 34.3$ mN/m. See more details in sections 3.1.1 and 3.1.1.2.

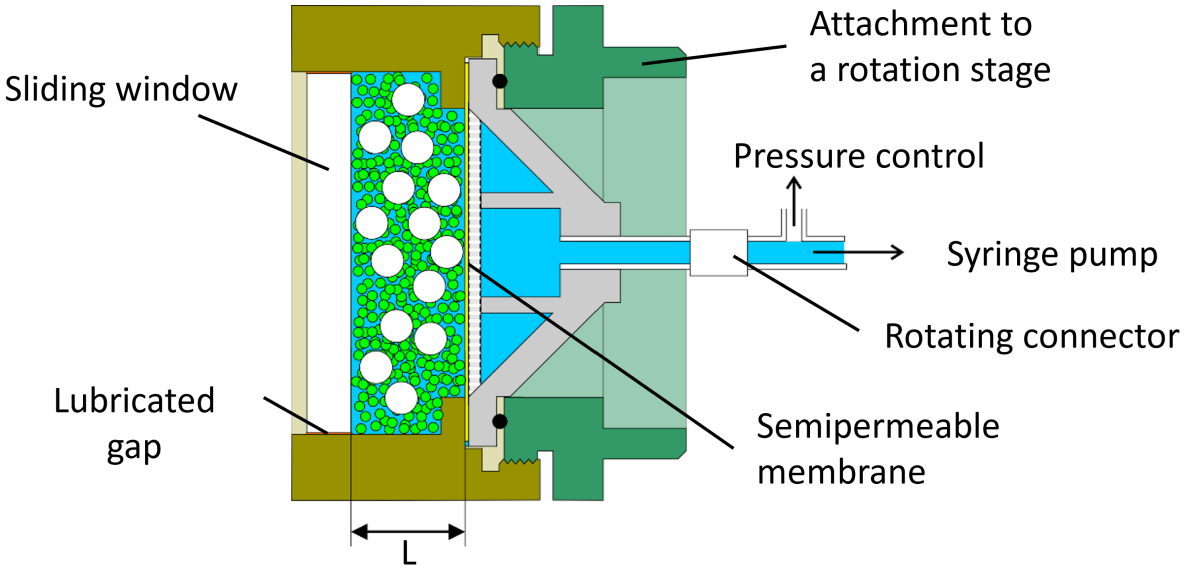

Figure 4.1: Schema of the cylindrical osmotic cell used to increase *in situ* the emulsion yield stress of a foamed emulsion. The three phases of the foamed emulsion are highlighted in different colors: air bubbles (white), oil droplets (green), aqueous phase (blue). While the aqueous phase is sucked out through the membrane under the effect of the depression applied by the syringe pump, the sample thickness L decreases with time, and the transparent window slides. The membrane is kept in position by a 3D-printed reinforcement structure (gray), which prevents also its deformation under large pressure differences. The cell features a threaded section (zigzag line) designed to be compatible with a 3D-printed attachment to the rotation stage (green), enabling the rapid and secure assembly of the two by simply screwing them together. An O-ring (black) is compressed during the locking procedure between the reinforcement structure and the attachment to the rotation stage, sealing the cell. The cell presents and the attachments present compatible threads, to allow one to screw them The cell is maintained under rotation along its axis of symmetry (in the horizontal direction).

rotating connector. The pump is used to suck liquid from the reservoir by applying a given depression between the foam and the liquid reservoir (i.e. a given osmotic pressure). The cell is mounted on a rotation stage (URS75-BCC) to rotate the cell around its horizontal symmetry axis with a speed 10 tr/min (as for the clinostat).

Observations of the foam surface are performed with an objective mounted on a camera. Images are acquired at a frequency of 4 pictures per minute. To ensure that the camera remains focused, it is mounted on a motorized linear stage (Newport UTS100-CC) to maintain it at a constant distance from the sliding window. For a test experiment with pure emulsion (in absence of bubbles), we draw a sharp mark on the external side of the window, to ensure that the camera can focus on it and measure $\Delta L(t)$.

A python script controls the syringe pump, in order to keep constant the pressure measured by a sensor, the rotation stage speed, the linear stage position, and it triggers the camera. For each image acquisition, the script saves into a file the following measurements: time elapsed since the beginning of liquid withdrawal, camera position from which we deduce at that time the real position of the sliding window, the theoretical volume of liquid retrieved from the pump, and the environmental temperature kept at $T = 22 \pm 1°\text{C}$.

To determine the displacement $\Delta L(t)$ of the window we measure two quantities: the variation of the camera position $\Delta x(t)$, which gives $\Delta L(t) = \Delta x(t)$, or the volume of liquid extracted from the syringe pump $\Delta V_L(t)$, which gives $\Delta L(t) = 4\Delta V_L/\pi D_{int}^2$. The former gave us a better estimation than the latter, with less noise and a more precise determination of the offset. In the following section the experimental values of ΔL are estimated from the camera position only.

4.1.3 Simulating drainage in the osmotic cell

In contrast to the preceding experiments with the clinostat (cf. Section 3.1.3), the bubbles here ripen in a medium with a time-dependent yield stress. In order to relate our observations at the cell window to relevant quantities, like the Bingham capillary number Bi, we need to estimate how the yield stress varies in time in the vicinity of the window. We model the evolution of the oil volume fraction in the emulsion and that of the liquid volume fraction in the foam as a free drainage problem and give a numerical resolution of it.

Description of the problem

The cell contains three phases: the gas bubbles, the oil droplets, and the aqueous phase of the emulsion. Initially, their volume fractions are uniform over the sample with values ϕ^0, φ^0, and φ_l^0, where we define for convenience the aqueous volume fraction in the emulsion $\varphi_l = 1 - \varphi$. At time $t = 0$ a constant depression Π_{set} is applied to the membrane. As time progresses, the air bubbles and the oil droplets stay in place, while the aqueous phase undergoes a free drainage through the emulsion under the constant applied pressure, which sets the osmotic pressure Π of the emulsion in the cell. This is similar to the free drainage of a simple aqueous foam [1]. The oil droplets constitute a porous medium for the flow of the aqueous phase. In contrast, since the air bubbles are much bigger than the oil droplets ($R \gg r_d$), they behave as inclusions in the porous medium and induce a hydrodynamical tortuosity of the system.

Thanks to the cylindrical symmetry of the cell we can work on it as a 1-dimensional problem. With reference to the cell schemed in Figure 4.1, we define the coordinate x along the axis of revolution, with origin at the center of the semipermeable membrane, directed toward the window. The sliding window is located at $x = L(t) = L_0 - \Delta L(t)$. The average superficial speed V_l of the aqueous phase flow through the emulsion toward the membrane is modeled using Darcy's law [1]:

$$V_l = \frac{K}{\eta}\frac{\partial \Pi}{\partial x} \tag{4.1}$$

where η is the shear viscosity of the aqueous phase and K is the permeability of the emulsion. The osmotic pressure of the emulsion is given by Eq. 1.6:

$$\Pi = k\frac{\gamma_{O/W}}{r_d}\frac{(\varphi_l^* - \varphi_l)^2}{\sqrt{\varphi_l}} \tag{4.2}$$

where $\varphi_l^* = 0.36$ is the random close packing fraction of the emulsion, $\gamma_{O/W}$ is the surface tension at the oil/water interface, r_d is the Sauter mean radius of the droplets, and the geometrical prefactor for a polydisperse packing with such a random close packing is given by Eq. 1.7: $k(0.36) = 3.2$.

The Darcy permeability of the emulsion, assuming non-mobile oil/water interfaces in view of the high viscosity ratio $\eta_o/\eta_w = 350$, is given by Eq. 1.10. The flow of the aqueous phase in the emulsion is hindered also by the presence of gas bubbles, which increase the tortuosity of the medium compared to the bulk case. To account for it, the permeability must be multiplied by the semi-empirical coefficient C_g [100, 101], valid in the range $0 \leq \phi \leq 1$:

$$C_g = \frac{2\phi(1+12\phi)}{6+29\phi-9\phi^2}. \tag{4.3}$$

As the aqueous phase drains out of the emulsion, the foam liquid fraction ϕ decreases from its initial value ϕ^0 according to:

$$\frac{\phi}{\phi^0} = \left\{1 + [1-\phi^0]\left[\frac{1-\varphi_l}{1-\varphi_l^0} - 1\right]\right\}^{-1}. \tag{4.4}$$

Finally, the continuity equation for the conservation of the aqueous phase in the foamed emulsion writes:

$$\phi\frac{\partial \varphi_l}{\partial t} + \frac{\partial}{\partial x}\left(\frac{K}{\eta}\frac{\partial \Pi}{\partial x}\right) = 0 \tag{4.5}$$

Its solution determines the spatio-temporal variation of the aqueous phase fraction $\varphi_l(x,t)$, with the following boundary conditions:

- The liquid velocity is zero at the window at any time

$$V_l(L,t) = 0 \tag{4.6}$$

- The pressure at the membrane is constant, set by the applied pressure

$$\Pi(0,t) = \Pi_{set}. \tag{4.7}$$

Numerical resolution

We solve the drainage equation 4.5 by the *finite difference method*. We introduce the parameters Δt, which is the time interval, and $\Delta l(x,t)$, the thickness of the slices dividing the sample along the x axis which varies with x and t to account for the variable flow of the aqueous phase and the consequent reduction of the cell volume. We write the drainage equation 4.5 for the superficial velocity of the aqueous phase V_l (Eq. 4.1):

$$\phi(x,t)\Delta l(x,t)[\varphi_l(x,t+\Delta t) - \varphi_l(x,t)] + [V_l(x+\Delta x,t) - V_l(x,t)]\Delta t = 0 \tag{4.8}$$

After a time step Δt, the oil volume of each slice is conserved, which writes:

$$(1-\varphi_l(x,t))\phi(x,t)\Delta l(x,t) = (1-\varphi_l(x,t+\Delta t))\phi(x,t+\Delta t)\Delta l(x,t+\Delta t) \tag{4.9}$$

and similarly, the gas volume is conserved:

$$(1-\phi(x,t))\Delta l(x,t) = (1-\phi(x,t+\Delta t))\Delta l(x,t+\Delta t). \tag{4.10}$$

By combining Eq. 4.9- 4.10, we get:

$$\frac{1}{(1-\phi(x,t+\Delta t))} = 1 + \frac{1-\varphi_l(x,t)}{1-\varphi_l(x,t+\Delta t)}\frac{\phi(x,t)}{(1-\phi(x,t))}. \tag{4.11}$$

Finally, we can express the relative change in the slices' thickness as:

$$\frac{\Delta l(x,t+\Delta t)}{\Delta l(x,t)} = \frac{1-\phi(x,t)}{1-\phi(x,t+\Delta t)} = 1-\phi(x,t)+\phi(x,t)\frac{1-\varphi_l(x,t)}{1-\varphi_l(x,t+\Delta t)}. \tag{4.12}$$

At each time step, we compute for each slice the aqueous phase speed V_l, its aqueous phase volume fraction $\varphi_l(x,t)$ (Eq. 4.8), its liquid fraction $\phi(x,t)$ (Eq. 4.11), and its thickness $\Delta l(x,t)$ (Eq. 4.12). This iteration is repeated until the desired final time is reached. We also evaluate the total cell thickness $L(t) = \sum_x \Delta l(x,t)$.

We performed such simulations for a cell with initial thickness $L_0 = 11.7$ mm using a grid of 100 slices of initial thickness $\Delta l(x,0) = L_0/100$, with a time step increasing logarithmically from 0.02 s to 2.6 s at a final time of $5 \cdot 10^6$ s. We did these simulations for each sample listed in Table 4.2.

Simulation results

Figure 4.2(left) shows an example of the simulated spatial dependency of the aqueous phase volume fraction for different drainage times. The position of the window is represented by the terminal dot at the end of each curve. From the very beginning, the aqueous phase volume fraction in the vicinity of the membrane drops from φ_l^0 to a much smaller value, with a sharp step in the profile. As time progresses, the windows recedes towards the membrane (as its position drifts towards smaller values of x), the drainage front moves toward the window and the profile becomes smoother. For the longest time, the aqueous fraction at the window has decreased by 33%. At anytime we measure an approximately uniform volume fraction for the continuous phase, $\varphi_l(x,t) \approx \varphi_l(L,t)$ in the region of the sample experimentally probed, i.e. close to the window, and over a depth much larger than the average bubble radius. Thus, the volume fraction profiles close to the window $\varphi_l(L,t)$ and $\phi(L,t)$ are sufficiently uniform to consider that the coarsening of bubbles in this region occurs without being affected by the variations of the profile closer to the membrane.

To calibrate our simulations, we compare the predicted variation of the window position $\Delta L(t)$ with experimental measurements for three samples: a pure emulsion, a bubbly emulsion, and a foamed emulsion with the smallest investigated liquid fraction, as illustrated in Figure 4.2(right). The experiments performed twice with pure emulsion show the good reproducibility of the measurements, and a very good agreement with the simulation over almost four decades in time. We observe that the drainage of the foamed emulsion is much slower than those of the bubbly liquid or the pure emulsion, as it is expected since the tortuosity induced by the bubbles hinders the flow. Overall we observe that experiments and simulation coincide, without further adjustment of the initial valus of the chosen coefficients. The low level of noise can be due to the window stopping momentarily due to friction, or to issues in the camera focus.

We focus now on the foamed emulsion at the window. Figure 4.3(a) shows φ_l as a function of time. The drainage front reaches the window at a drainage time $t \approx 10^4$ s, after which the aqueous volume fraction decreases over time. For small applied pressures $\Pi_{set} \approx 1kPa$, the aqueous fraction reaches a plateau value $\phi_l = \phi_l^{osm}$, which is the equilibrium

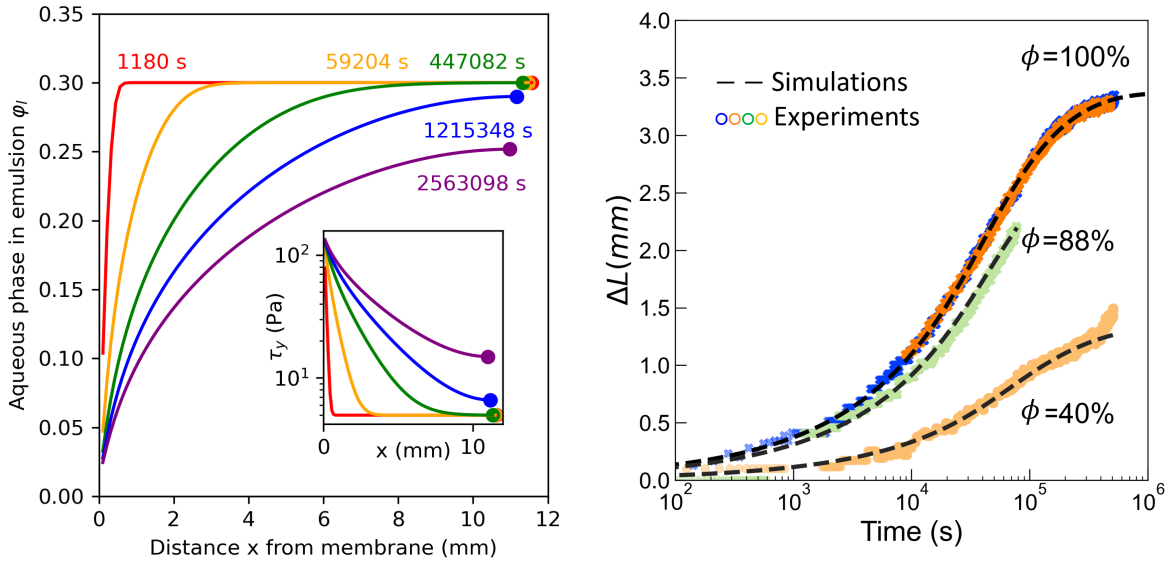

Figure 4.2: (left) Profiles of the aqueous phase volume fraction $\varphi_l(x,t)$ for a foamed emulsion with parameters $\phi^0 = 0.40$, $\varphi_l^0 = 0.30$, $r_d = 2$ μm, $\Pi_{set} = 10$ Pa. For each time t as labelled, a dot marks the total length of the cell $L(t)$ which corresponds to the position of the window. At all times the profiles become asymptotically flat for $x \to L(t)$, over a depth in the sample larger than the instantaneous average bubble radius $\overline{R}$; the same is true for the emulsion yield stress τ_y, plotted in the inset for the same reference times. (right) Variation of the cell thickness ΔL over time, for three samples: pure emulsion ($\phi^0 = 1$), bubbly emulsion ($\phi^0 = 0.88$), foamed emulsion ($\phi^0 = 0.40$). The estimations provided by simulations (dashed lines) coincide with the experimental measurements (colored symbols). Each color correspond to a different experiment.

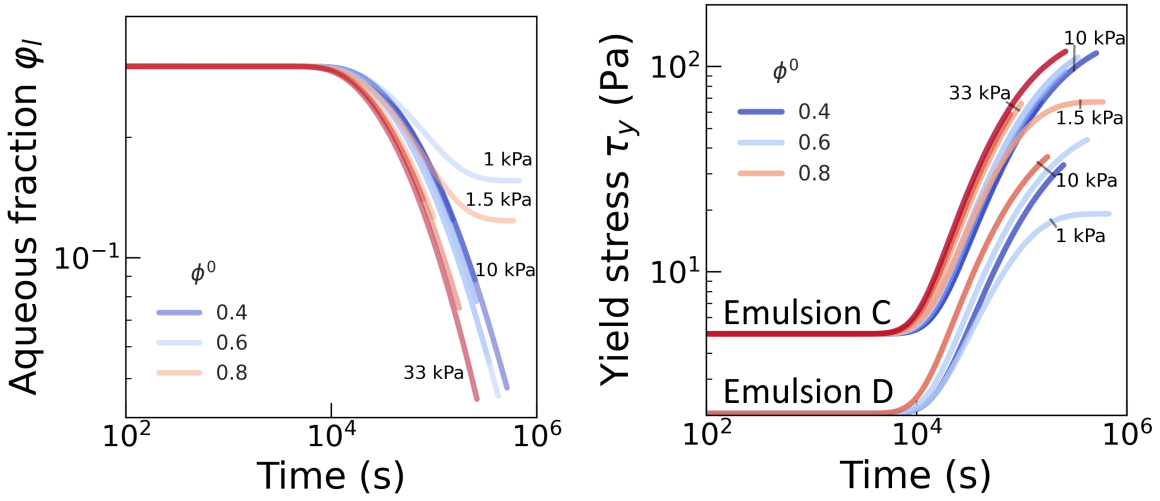

Figure 4.3: Predicted values at the window of the (left) aqueous volume fraction and (right) yield stress, varying ϕ^0 at a fixed $\varphi^0 = 0.70$, for the range of droplet size and osmotic pressures experimentally studied. The curves stop at the time where the associated experiment ends. The emulsion label and the applied pressure is specified near the corresponding curves. The yield stress is evaluated from the oil volume fraction by using Eq. 1.48, using the appropriate parameters determined by the rheological characterization (cf. 3.1.1.2): $\alpha = 0.31$, $\gamma_{O/W} = 4$mN/m.

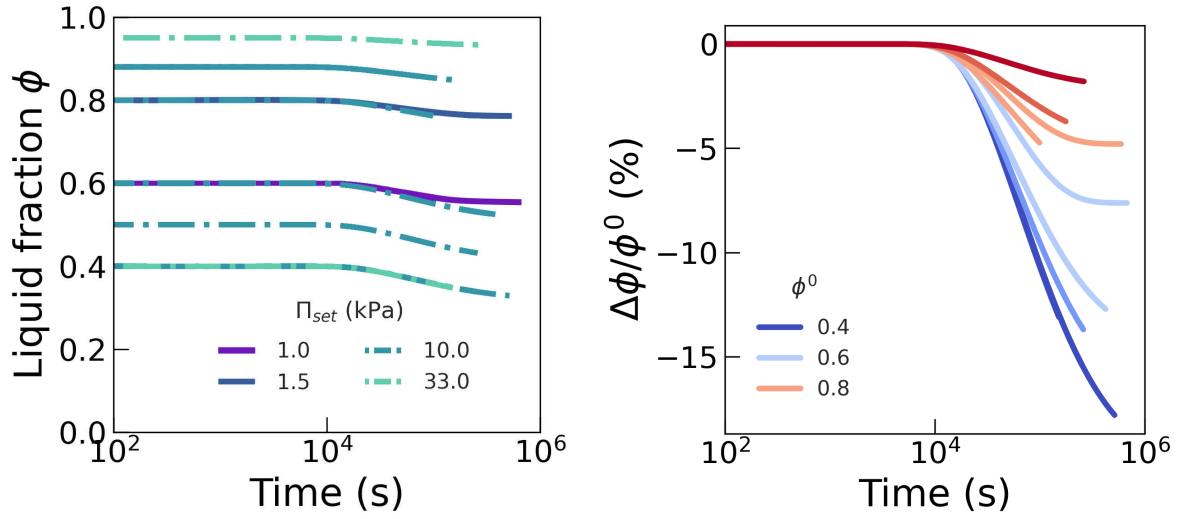

Figure 4.4: Predicted values at the window of (left) the liquid volume fraction and (right) the relative variation of the liquid fraction, at a fixed $\varphi^0 = 0.70$, for the range of droplet size and osmotic pressures experimentally studied. The curves stop at the time where the associated experiment ends. In the left graph, the lines corresponding to $\Pi = 10, 33$ kPa are dot-dashed to show better where multiple curves superimpose.

fraction, corresponding to the applied osmotic pressure according to Eq.1.6. For larger pressures the curves are far from the equilibrium and the evolution is independent from Π_{set}. In these conditions, the drainage speed is mainly dependent on the initial liquid fraction ϕ^0, and only marginally by the droplet size.

From the simulated emulsion aqueous fraction $\varphi_l(L,t)$, we can predict the emulsion yield stress using Eq. 1.48 and the emulsion characteristic parameters (cf. 3.1.1.2). We show in 4.3(b) the predicted yield stress at the window for emulsions with a fixed $\varphi^0 = 0.70$. The temporal evolution of τ_y is similar to that of φ_l regarding the dependency with ϕ^0, which increases the rate of variation, and with Π_{set}, which determines the limit value at the end of drainage. The droplet size introduces only a multiplicative factor in the yield stress.

Figure 4.3 shows the simulated evolution of the foam liquid fraction ϕ at the window, for different initial liquid fractions ϕ^0 for the same emulsion, determined from Eq. 4.4. Again, the applied pressure Π_{set} is relevant only if the drainage is reaching the equilibrium condition, in the experiments with $\Pi_{set} \approx 1kPa$. We see that the variation of the liquid fraction is really small compared to the aqueous or the oil fractions; to quantify it better we show also the relative variations of ϕ, $\frac{\Delta\phi}{\phi^0}$. In the case of dilute bubbly emulsions ($0.8 \leq \phi \leq 0.95$) the variations are smaller than 5%, and thus negligible. In more concentrated foams we get larger variations: at the end of the drainage and for the smallest investigated liquid fraction $\phi^0 = 0.40$, the variation reaches $\approx 15\%$. Therefore for $\phi^0 \leq 0.60$, we will need to take into account the instantaneous value of ϕ when studying coarsening in the osmotic cell.

Note that with such simulations, we can identify time lapses where the relative variations of the liquid fraction are small enough to be considered as constant. This will allow for the instantaneous average growth rate to be studied as a function of liquid volume fraction or emulsion yield stress, as we will do in Section 4.2.4.

4.1.4 Bubble segmentation, shape analysis and tracking using YOLO

In Chapters 2 and 3 we focused on the evolution of the average bubble size and of the bubble size distribution; these tasks required to extract only the bubble area A, on images logarithmically spaced in time. To probe different aspects of foam evolution, such that the bubble morphology and the foam dynamics, we need more information. The first task requires a finer study of bubble contours in the images, which cannot be satisfied by simple ellipse fitting. The second task requires the analysis of a multitude of images, finely spaced in time, which requires a larger degree of automation to be feasible in the timescale of the PhD.

As detailed in Section 2.1.4, bubbles in a wet foams are difficult to identify in an image: the background is not uniform, lightning conditions can vary between images, and the bubbles themselves act as lenses for the deep layers. We searched in literature for automatic methods for the recognition of bubbles in an image, and could not find satisfaction for our specific problem in the available solutions [102–104]. The breakthrough was the release in 2023 of the real-time object detector YOLOv8 (You Only Look Once) [105, 106]. We found this multi-purpose, trainable model ideal for our goal: its "Segment" task defines for each identified object a polygonal mask, whose number of vertices adapts to the object complexity, and can capture the level of detail we desire. Each mask is assigned with a score which represents the estimated probability of good detection. After the detection, it is easy to set a threshold based on this score and filter the results. Additionally, its python-compatibility makes it easy to implement it in the analysis pipeline. It can take only 1 minute to analyse an image containing ≈ 1000 bubbles. With this powerful instrument at hand, we still had to train a foam-specific model of it, and to define the pre- and post-processing routines.

4.1.4.1 Model training

The training of whatever kind of machine learning requires the preparation of a training set. For object detection models, it is composed of a long series of images containing the objects you want to identify, in different environmental conditions and (generally) from different perspectives; each image must be paired to a text file, containing the labels of each object inside that image. A label for segmentation consists of two elements: a class identifier, which specifies the quality of the specific object (bubble, car, balloon, dog...), and the mask, the coordinates in image units of the vertices of the polygon inscribing the object.

To train a model it is recommended to employ thousands and thousands of labels for each class; thanks to previous experiments detailed in Chapter 3 we already have such an information for more than 10^5 bubbles analysed in images with different liquid fractions and lightning conditions. Additionally, we doubled the number of bubbles and the variability of the experimental conditions by employing a non-trainable segmentation model, Fast Segment Anything Model (FastSAM) [107]. This model produces quickly good quality masks (polygons with a large number of vertices), but its lack of specificity for bubbles made it prone to false positives in detection, and to miss the smaller bubbles of the image.

By visual inspection of these false positives, shown in Fig. 4.5, we determined two geometrical features ideal to describe their anomalous shape:

$$Circularity = \frac{P_{CH}^2}{2\pi A} \in [0, 1] \tag{4.13}$$

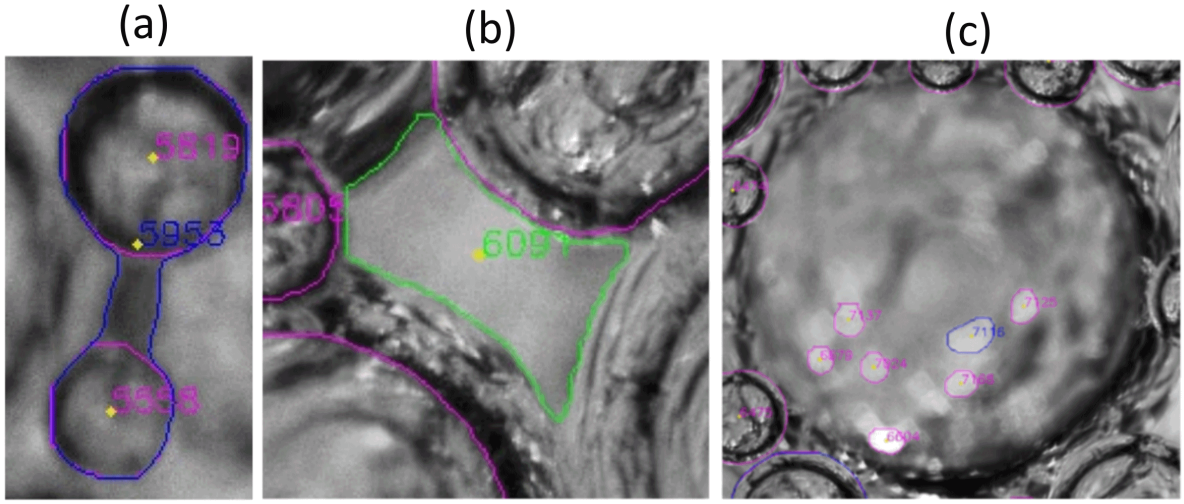

Figure 4.5: Examples of false positives in automatic detection using FastSam: (a) a doublet of small bubbles (in blue), characterized by high Eccentricity; (b) a large 'void' space in the first layer of bubbles (in green), characterized by low Circularity; (c) bright spots inside a large bubble, solvable with proper image treatment.

$$Eccentricity = \sqrt{\left(\frac{a}{b}\right)^2 - 1} \in [0, 1] \tag{4.14}$$

where A is the area of the polygon, P_{CH} the perimeter of the polygon's convex hull, and a and b are respectively the major and minor semi-axis of an ellipse fitted to the polygon.

We determined that the true positives could be better discriminated using two threshold values, $c_{min} = 0.86, e_{max} = 0.6$, which maximize the sensitivity to true positives of the recognition and minimize the retention of false positives. As a result, we derived a *Shape-based cleaning algorithm*, detailed in Algorithm 1, which we applied to the FastSAM-derived dataset to improve its quality.

To prepare the first dataset, based on ellipse fitting, we needed instead to first convert the ellipses into polygonal masks, and then to correct the vertices positions to follow with higher fidelity the bubble shape. Algorithm 2 details the *Contour refinement algorithm*: from the polygon centroid we 'shoot rays' at 360°, and move the contour to the darkest point in its (radial) vicinity; the resulting profile is smoothed and converted into vertices coordinates.

4.1.4.2 Pipeline for bubble recognition

Images are treated with a Python script, which implements algorithms from open-CV library[108]. Figure 4.6 shows the three steps of image preparation:

- Denoise: the "Non Local Means Denoising" algorithm [109] homogenizes the pixels' intensity on a fine scale. By applying a small window we reduce the relevance of out-of-focus bubble layers, while maintaining the level of detail needed to identify the smallest bubbles.

- Contrast enhancement: uneven illumination in the image is corrected through "Contrast Limited Adaptive Histogram Equalization" (CLAHE) algorithm [110].

- Edge enhancement: the "Laplacian filtering" algorithm extracts sharp edges from the image, ignoring finer details. By adding its result to the image itself we increase contours' definition.

Algorithm 1: Shape based cleaning algorithm

Input: Masks $\boldsymbol{p_i}$
$\mathcal{B} = []$ `Approved bubbles`
`Determine geometrical features`
forall $i \in [1, ...N]$ **do**
  A $= \frac{1}{2}\sum_j (x_{j+1} - x_j)(y_{j+1} + y_j)$, vertices j
  `Evaluate the polygon's convex hull to estimate circularity`
  $\boldsymbol{p'_i} = ConvexHull(\boldsymbol{p_i})$
  $P_{CH} = \sum_j \sqrt{(x'_{j+1} - x'_j)^2 + (y'_{j+1} - y'_j)^2}$, vertices j
  Circularity $= \frac{P_{CH}^2}{2\pi A}$
  `Fit an ellipse on the polygon to estimate eccentricity`
  Semi-axes $a, b = EllipseFitting(\boldsymbol{p_i})$
  Eccentricity $= \sqrt{\left(\frac{a}{b}\right)^2 - 1}$
  `Compare the descriptors with threshold values, and keep if passes the tests`
  if *Circularity* $< c_{min}$ **then**
    Void space, discard
  else if *Eccentricity* $> e_{max}$ **then**
    Bubble doublet, discard
  else
    $\mathcal{B} \leftarrow \boldsymbol{p_j}$
end
Output: $\mathcal{B}$

Algorithm 2: Contour refinement for masks

Input: mask $\boldsymbol{p_0}$, Image I
`Determine the radial profile with Algorithm 3`
$R(\theta) = RadialProfile(\boldsymbol{p_0})$
`Interpolate pixel values in the image at` $360°$ `from the polygon centroid up to a distance` $r = 1.1R(\theta)$
$I(\theta, r) = Interpolate(\theta, r, I)$
`For each angle` θ`, determine the` r `coordinate of the darkest point, corresponding to the contour position.`
$r_{edge}(\theta) = min(I(r; \theta))$
`Dampen the radial profile in the frequency domain, to smooth the contour and get the corrected radius` R^c
$R(\theta^{-1}) = \mathcal{F}(r_{edge}(\theta))$
$R^c(\theta) = \mathcal{F}^{-1}(R(\theta^{-1}) \cdot Gauss(\theta^{-1}))$
`Transfer the new radial profile back to Cartesian coordinates`
forall $\theta \in [1, 2, ...360]$ **do**
  $x_\theta^c = X + R_\theta^c cos(\theta)$
  $y_\theta^c = Y + R_\theta^c sin(\theta)$
  $\boldsymbol{p_c}[\theta] \leftarrow (x_\theta, y_\theta)$
end
Output: $\boldsymbol{p_c}$

Algorithm 3: Radial profile

Input: mask $\boldsymbol{p_0}$, Image I

`Determine the polygon centroid`

$X = \sum_j (x_{j+1}y_j - x_j y_{j+1})(x_i + x_{i+1})/6A$ for j in $\boldsymbol{p_0}$

$Y = \sum_j (x_{j+1}y_j - x_j y_{j+1})(y_i + y_{i+1})/6A$ for j in $\boldsymbol{p_0}$

`Determine` $R(\theta)$

$\theta_j = mod(arctan2(\frac{y_j - Y}{x_j - X}), 2\pi)$

$R_j = \sqrt{(x_j - X)^2 + (y_j - Y)^2}$

$R(\theta) = Interpolate(\theta_j, R_j)$

Output: $R(\theta)$

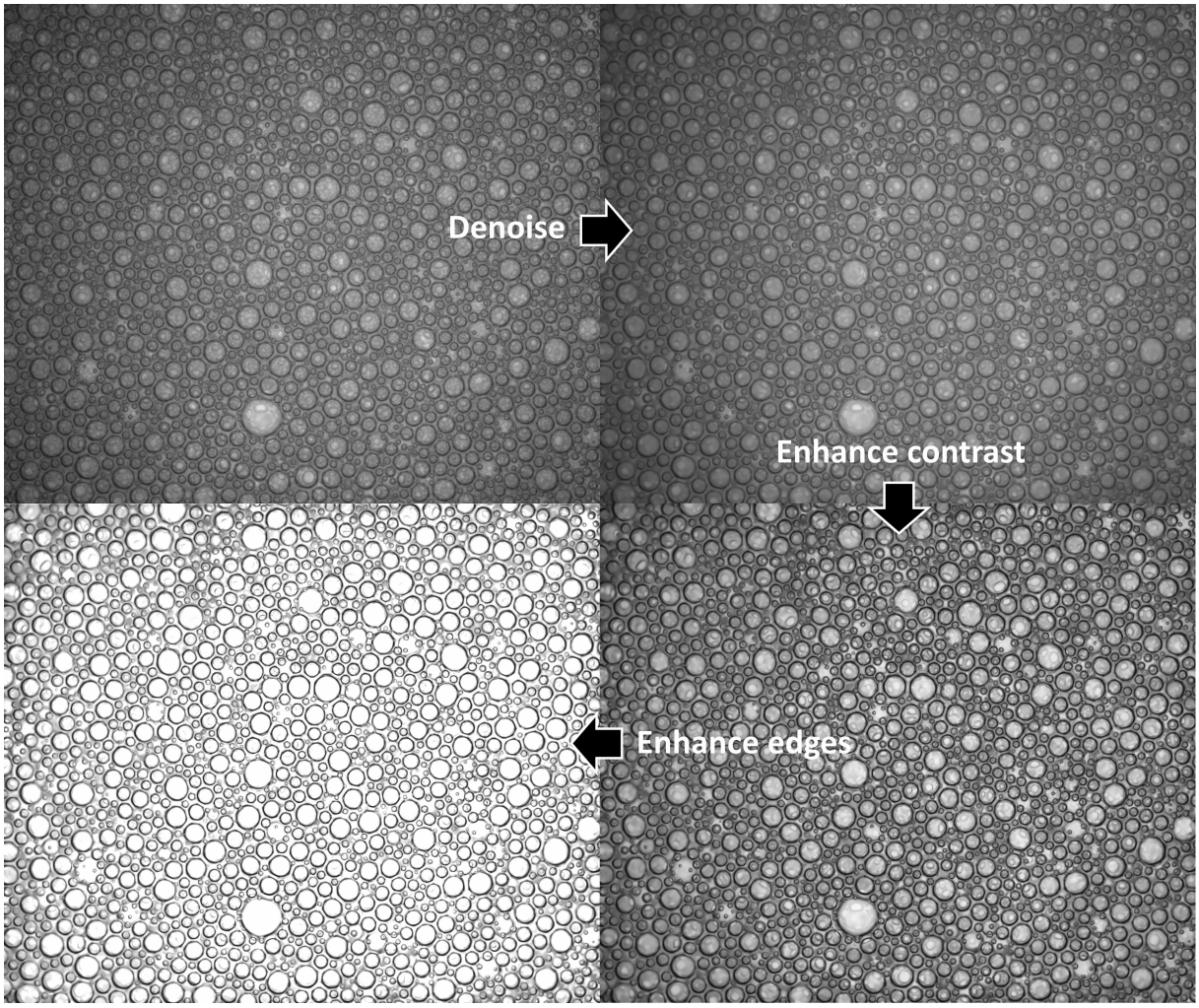

Figure 4.6: Step-by-step pretreatment of a foamed emulsion with $\phi = 30\%, \varphi = 75\%$. From top right, clockwise: raw image, after denoising, after contrast enhancement, after edge enhancement (ready for the recognition).

Images can now be analysed by our segmentation model. Our foam samples have a large polydispersity, and it is easy to miss the smaller bubbles in the image [19]; if we simply applied the recognition on the whole image we detect only big- and medium-sized bubbles. To overcome it, we employ Slicing Aided Hyper Inference (SAHI) algorithm [111]: the image is divided into overlapping tiles, on which the recognition is applied; the results of all the tiles are merged avoiding double counting. Figure 4.7 shows our routine. First, the recognition is applied on the pretreated image, to detect the larger bubbles. Then, SAHI algortithm is applied to detect the smaller bubbles in the image. The masks found with the two methods are compared, and if multiple masks overlap on the same object, the mask with the highest score is kept. By integrating the 'tiled-detection' with the 'overall-detection' we are able to detect bubbles of multiple scales without additional supervision, and output a csv file containing, for each bubble, the position of the vertices inscribing the polygon.

The post-processing employs again Algorithms 1-2 to ensure the best data quality. We apply this procedure to all the images captured for an experiment, and we employ a linking algorithm [112] to identify the single bubbles in successive images, tracking their position, size and shape in time.

4.1.4.3 Local curvature and bumps identification

In Section 4.3.3 we will study the bubble morphology, with particular regard for *bumps* appearing on the profile of bubbles bigger than average (like in Figure 4.8(a)). Here we explain the methods employed to analyse them: the whole procedure is summarized in Algorithm 4.

The bumps are identify as peaks in the bubble profiles $R(\theta)$, determined with Algorithm 3. To detect them, we employ a peak detection algorithm from the Scipy python library. The post-processing procedures have already smoothed the bubble profile, but it naturally contains oscillations of smaller amplitude which we want to exclude from the detection. We also want to exclude from the identification of bumps the two extremes of elongated bubbles: we observe bubbles smaller than average to have that elliptical-like shape, and we feel that they would need a separate treatment. To filter out these possible sources of noise we require from the algorithm to respect a set of parameters: i) the peak *prominence*, the height of the peak with respect to its lowest foot, must be a relevant fraction of the bubble size $\geq 15\% < R(\theta) >_\theta$; ii) two peaks must not be too close in the angular profile, with a minimum peak-to-peak angle $\geq 60°$; iii) the peak must be limited in its angular size, with a full width half maximum $\leq 120°$.

After the identification of bumps, we perform additional quantitative measurements. We take as the bump size the radius of curvature of the bubble contour, at the angle θ_b where the bump exhibits a maximum in the profile. To measure it, we differentiate twice the function $R(\theta)$ at the angle of the bump θ_b. Then, we search for the presence of a neighbouring bubble along the direction of the bump. Among all the other bubbles, we consider the ones whose center is located at an angular distance from θ_b smaller than a threshold $\Delta\theta = 10°$, and determine which is the closest to the reference bubble. Of this neighbour, we keep note of its size and surface-to-surface distance.

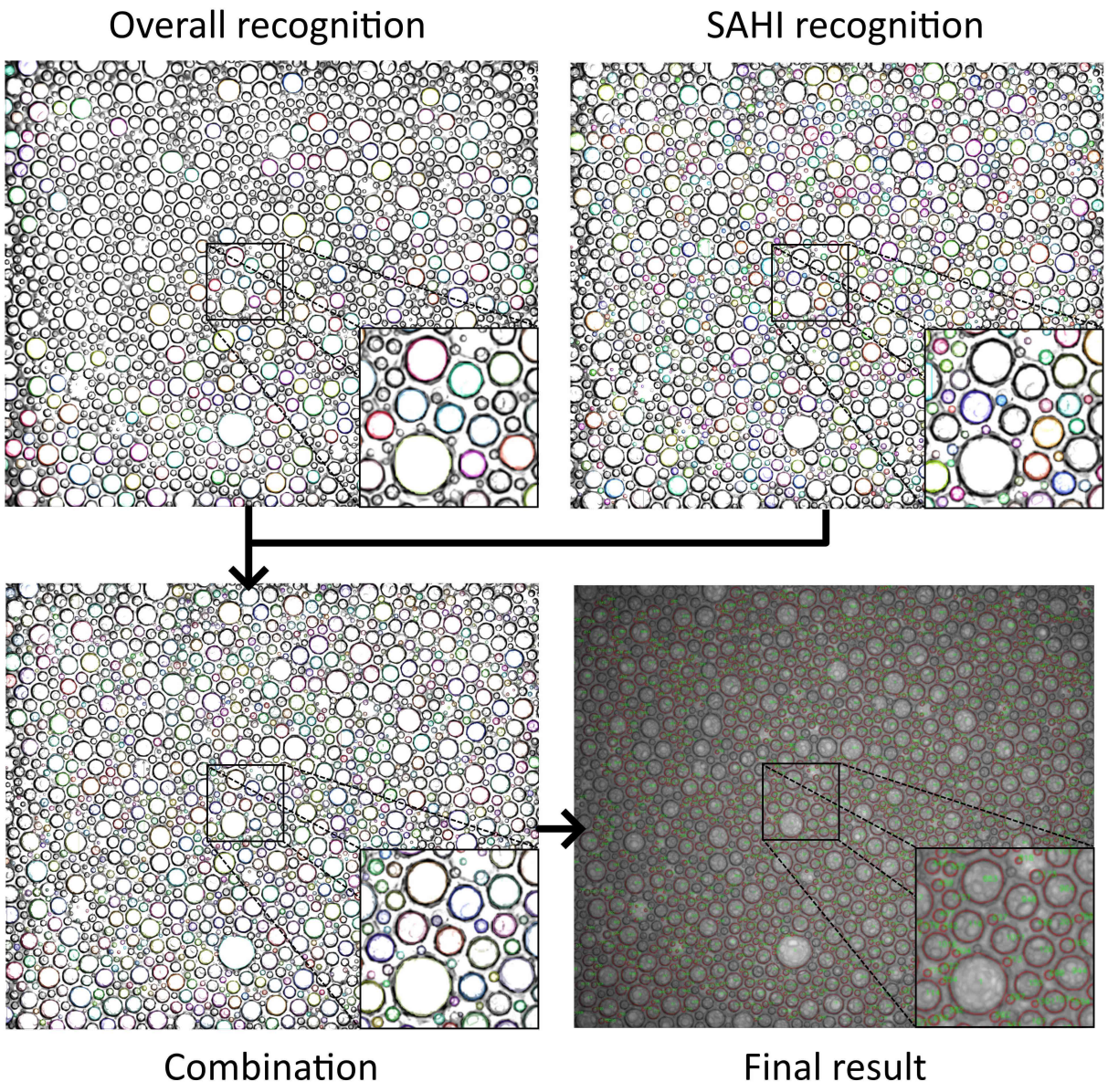

Figure 4.7: Two-scale automatic segmentation of a $\phi = 30\%, \varphi = 75\%$ foam: (top left) recognition applied on the complete image, (top right) recognition applied on overlapping windows thanks to SAHI algorithm, (bottom left) combination of the two results, (bottom right) final result, with cleaned contours superimposed to the non-treated image. In the first three pictures the contour of the recognized bubbles is randomly colored. In the first picture, mainly bubbles larger than average are detected, and smaller ones are missed. In the second picture, the opposite happens. In the third picture, all kind of bubbles are correctly recognized. By zooming in the third picture, we can observe that the colored masks have a low definition at the pixel level, with a polyhedral shape. On the contrary, in the last picture the contours are all smooth.

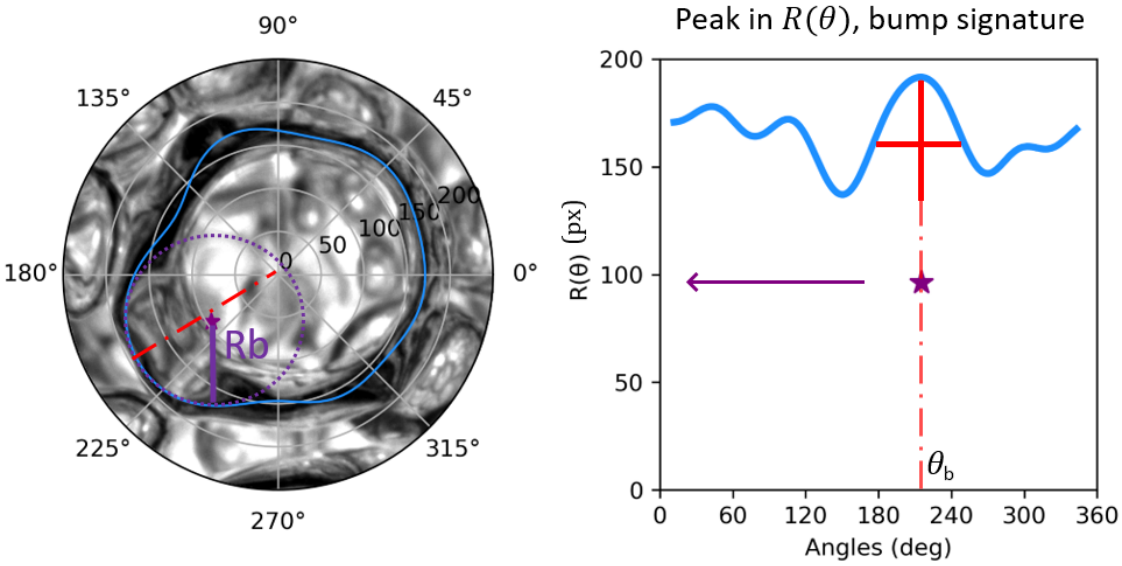

Figure 4.8: (left) Picture of a bumpy bubble in a coarsened foamed emulsion where the contour profile determined by the automatic treatment is superimposed (blue curve); (right) bubble profile plotted in polar coordinates $R(\theta)$. The prominent peak in the function $R(\theta)$ at the angle θ_b is a signature of a bump; its prominence and full width half maximum (FWHM) are highlighted by red solid lines. The value of the bump radius of curvature R_b is marked by a purple star in the plot, and a circumference with that radius is drawn on the image.

Algorithm 4: Bump characterization

Input: Bubble positions $(\boldsymbol{x},\boldsymbol{y})$, corrected profiles $\boldsymbol{R(\theta)}$
`Define the parameters`
Prom $= 0.15 \cdot \langle R(\theta)_i \rangle_\theta$
MinPeakD $= 60°$
MaxWidth $= 120°$
$\Delta\theta = 10°$
$\mathcal{B} = []$ `Dictionary of bubbles:bumps`
forall *bubbles* i **do**
  `Determine the relative angle and distance of the other bubbles`
  $\boldsymbol{\alpha} = arctan2(\boldsymbol{y} - y_i, \boldsymbol{x} - x_i)$
  $\boldsymbol{d} = \|\boldsymbol{y} - y_i, \boldsymbol{x} - x_i\|$
  `Search for bumps`
  $\mathcal{B}_i = []$ `List of bumps with properties`
  $\theta^b = \text{FindPeak}(R(\theta)_i, \text{Prom}, \text{MinPeakD}, \text{MaxWidth})$
  forall *bump* j **do**
    $R_j^c = R''(\theta_j^b)$ `bump size`
    $\mathcal{N} = []$ `list of candidate neighbours`
    forall *other bubbles* k **do**
      if $|\alpha_k - \theta_j^b| < \Delta\theta$ **then**
        $\mathcal{N} \leftarrow k$
      end
    end
    $kj = k : d(k) = \min(d(k)) \quad \forall k \in \mathcal{N}$
    $r_j = \langle R(\theta)_{kj} \rangle_\theta$ `Neighbour size`
    $d_j = d_{kj} - r_j - R(\theta_j^b)$ `Neighbour distance`
    $\mathcal{B}_i \leftarrow (R_j^c, d_j, r_j)$
  end
  $\mathcal{B} \leftarrow (i, \mathcal{B}_i)$
end
Output: $\mathcal{B}$

4.2 Coarsening arrest in bubbly yield stress fluids

This section focuses on the coarsening experiments performed in foamed emulsions in the *bubbly regime* ($\phi > 0.40$). The coarsening is studied using two experimental setups, the clinostat and the osmotic cell, described respectively in Sections 3.1.3 and 4.1.2. The complete list of experimental parameters is detailed in Tables 4.1 and 4.2. Exemplar pictures of bubbly emulsions coarsening in the clinostat are showed in Fig. 4.9.

4.2.1 Damped growth law

In Chapter 3, we studied the coarsening of bubbly emulsions, using the clinostat set-up, for average bubble sizes $\overline{R}$ small enough to remain in the capillary regime i.e. for small average Bingham number $\overline{Bi} = \tau_y \, \overline{R}/\gamma \leq 0.05$. We recall that in this set-up the emulsion yield stress τ_y is kept constant. We showed that the normalized bubble size distributions become independent of aging time demonstrating that the system has reached a scaling state and we studied the average bubble radius growth law as a function of the liquid fraction, over a range of liquid fraction considerably larger than the one we were able to investigate in microgravity experiments. By extending the duration of these experiments, up to $t \sim 10^7 s$, we let the foam reach a mean bubble size $\overline{R}$ (and so a $\overline{Bi}$) large enough to observe a modification of the growth laws, that we attribute to the plasticity of the continuous phase.

We show in Fig. 4.10 the corresponding evolutions of the mean bubble size $\overline{R}$ as a function of the foam age. We observe that the growth slows down after a given time, and that it is no longer described by a cubic growth law with exponent 1/3. Instead we fit Eq. 2.1, a general power law, to the data at long times $t \gtrsim 10^5$ s, where we observe a clear deviation from the cubic law. The fitted exponent α is shown in the inset of Figure 4.10. With the exception of two samples $\phi = 0.45$, $\phi = 0.70$, where the damping is not so obvious, we get $\alpha \approx 1/4 < 1/3$ independently of the liquid fraction.

We believe we have identified the reasons for the discrepancies observed for these two samples. For $\phi = 0.70$, at times $t \sim 10^6$ s, close inspection of the images reveals sparse coalescence phenomena happening in the second layer of bubbles below the window, which could affect the later stages of coarsening. For $\phi = 0.45$, which in simple foams with the same surfactant is close to the unjamming transition $\phi^* = 0.39$ [13] (cf. Section 2.2), we notice on the images the apparition of a few contacts between bubbles, reminiscent to those in foams. These contacts could be favoured by the 'bumpy' bubble morphology, discussed in Section 4.3.3. The presence of contacts should fasten the coarsening

We studied the normalized bubble size distributions obtained at long times $t \gtrsim 10^5$ s, and compared them to those determined at earlier ages in the scaling state in Fig. 4.11. Remarkably, for a given liquid fraction, the distributions determined at later ages do not significantly differ from those in the cubic growth regime. We are then tempted to consider the change of exponents as a continuous damping process, rather than a sharp transition in the coarsening behaviour.

4.2.2 Discussion

To explain the damped average bubble growth we propose a semi-quantitative model, based on the assumption that the damping originates from the plastic response of the emulsion surrounding the bubbles. We neglect the emulsion elastic response since our analysis of the ripening of a single bubble in an yield stress emulsion, following Venerus model, shows that a relative variation of bubble radius of the order of 1.5% (cf. Eq. 1.71 is sufficient to yield the medium around it.

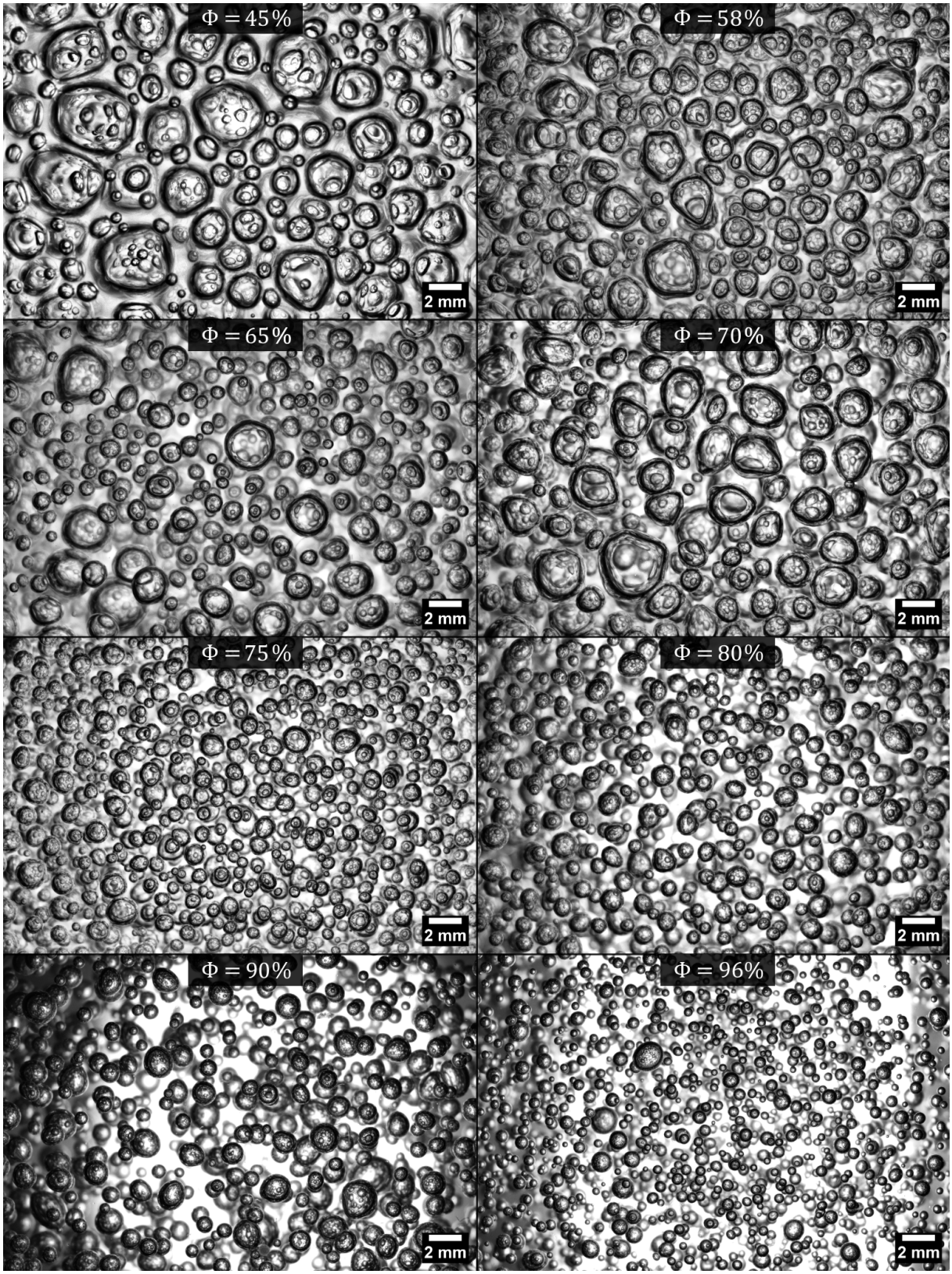

Figure 4.9: Pictures of bubbly emulsions with constant $\tau_y = 16.5\ Pa$, and varying liquid fractions ϕ as indicated. The samples are dilutions of emulsion B coarsening in the clinostat (cf. Table 4.1). The pictures show the samples at the end of the corresponding experiment, at a time $2\ 10^6 \leq t < 2\ 10^7 s$ (cf. Fig. 4.10).

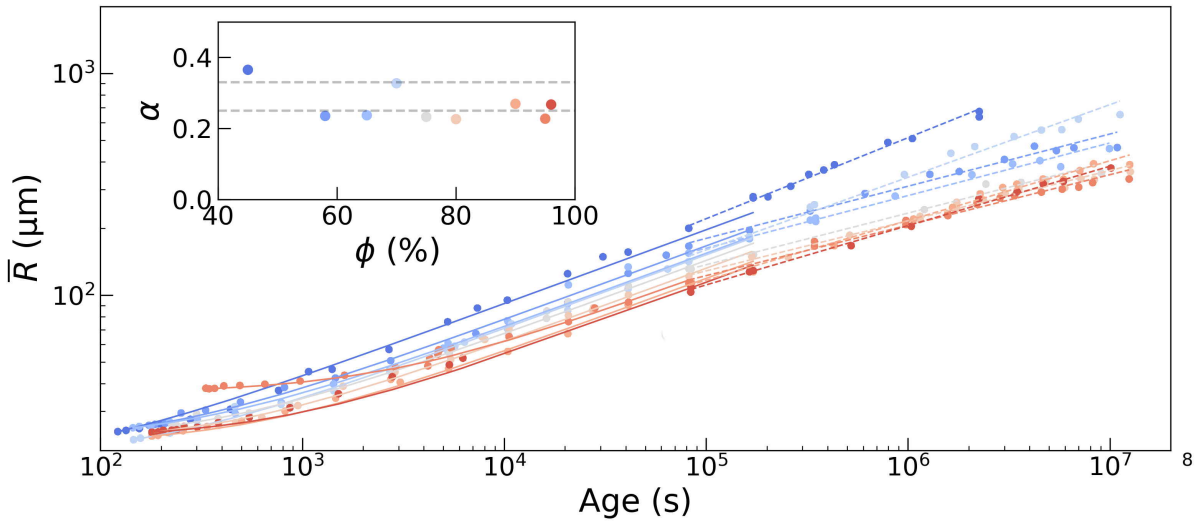

Figure 4.10: Mean radius $\overline{R}$ as a function of foam age in bubbly emulsions ($\phi > 0.40$), coarsening in the clinostat. Samples are made of dilutions of emulsion B (cf. Tables 3.1 and 4.1). For long times $t \gtrsim 10^5$ s, the growth laws show a clear deviation from the classic scaling $R \propto t^{1/3}$ (Eq. 1.23). The solid lines show Eq. 1.23 fitted to data for times $t \leq 2 \cdot 10^5$ s. The dashed lines represent the power law (Eq. 2.1) fitted to the data for times $t \geq 10^5$ s; we show in the inset the effective exponent α yielded by the fit. The grey dashed lines in the inset correspond to $\alpha = 1/3$ and $\alpha = 1/4$.

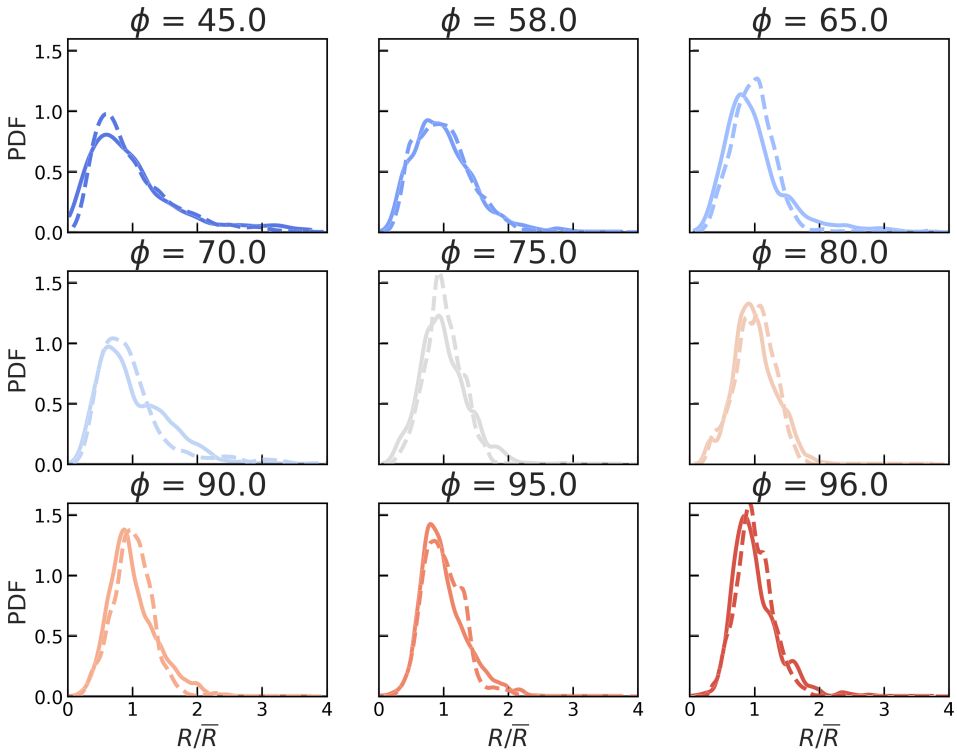

Figure 4.11: Bubble size distributions of $R/\overline{R}$ of bubbly emulsions coarsening in the clinostat (i.e. with constant emulsion yield stress $\tau_y = 16.5$ Pa) (same samples as in Fig. 4.10). The solid lines show distributions measured in the scaling state when the growth law is cubic ($\alpha = 1/3$), and dashed lines correspond to distributions at long times times $t \gtrsim 10^5$ s when the growth exponent is $\alpha \approx 1/4$ (cf. Fig. 4.10).

Liquid fraction ϕ	0.45	0.58	0.65	0.70	0.75	0.80	0.90	0.95	0.96
Ω_c (μm^3/s)	100 ± 10	60	47 ± 4	41	40 ± 3	31	22	27	22
Bi^*	1 ± 0.8	0.32 ± 0.03	0.30 ± 0.06	1 ± 0.5	0.19	0.18	0.23	0.16	0.20

Table 4.3: Coarsening rate Ω_c and critical Bingham $Bi^*(\phi)$ determined by fitting Eq. 4.15 to the growth curves shown in Fig. 4.12. The uncertainty on the parameters is, unless specified, on the order of 5%. All the presented bubbly emulsions are prepared from emulsion B; its specifics are detailed in Table 3.1.

In a coarsening bubbly liquid in the scaling state, the bubbles bigger than or equal to average bubble size can grow thanks to the dissolution of the smaller bubbles. From simulations we can deduce that the shrinkage of an individual bubble can be arrested if its Bingham number $Bi \sim 1.3$ *. We assume that, if some of the smaller bubbles in the dispersion stop dissolving, the gas oversaturation in the continuous phase decreases and the average growth will be damped. Ultimately, if dissolution is totally arrested, the average bubble size will stop growing. In the capillary limit ($\overline{Bi} \to 0$) the growth law should be that of a simple bubbly liquid (Eq. 1.23). We conjecture the existence of a critical Bingham $Bi^*(\phi)$, which sets the plastic limit ($\overline{Bi} \to Bi^*(\phi)$) where coarsening arrests ($d\overline{R}/dt \to 0$). This behaviour is captured by the simple expression:

$$\overline{R}^3 - \overline{R_0}^3 = \Omega_c(t - t_0)\left(1 - \frac{\overline{Bi}}{Bi^*(\phi)}\right)\mathcal{H}(Bi^* - \overline{Bi}) \tag{4.15}$$

where $\left(1 - \frac{\overline{Bi}}{Bi^*(\phi)}\right)\mathcal{H}(Bi^* - \overline{Bi})$ describes the damping effect due to the plasticity of the continuous phase. $\mathcal{H}$ is the Heaviside step function, which mathematically ensures that coarsening stops for $\overline{Bi} \geq Bi^*$. In the investigated range of bubble size $\overline{R}$ and yield stress τ_y, we expect all of our samples to start coarsening in the capillary limit, and to undergo later a progressive damping as the bubble size increases. That would appear as a power law with an exponent decreasing over time $\alpha < 0.33$. We fit Eq. 4.15 to each growth curve, using as free parameters the coarsening rate Ω_c and the critical Bingham $Bi^*(\phi)$. Fig. 4.12 shows the good agreement between the fit and the observed growth for each liquid fraction. Nevertheless, for the same liquid fractions which presented an effective growth exponent α different than the others $(0.45, 0.70)$, the data present a less pronounced curvature with respect to the other experiments, and the fitted curves are straight lines. The fitted parameters are given in Table 4.3. For those two experiments, the fit yields $Bi^* \sim 1$, which is anomalous with respect to the other data. Thus, we will exclude them from the analysis of the fitted parameters, and concentrate on the similarities between the others.

The critical Bingham $Bi^*(\phi)$ is plotted in Fig. 4.13(a): for large liquid fractions $\phi \geq 0.75$ we find a constant $Bi^* \approx 0.2$; for smaller liquid fractions $\phi \leq 0.70$, $Bi^*(\phi)$ increases with the decrease of liquid fraction. To account for this evolution, we find that the simplest empirical law is:

$$Bi^*(\phi) = Bi^*_{dilute} + A(1 - \phi)^3 \tag{4.16}$$

where the best fitting parameters are $Bi^*_{dilute} \approx 0.17 \pm 0.01$, $A \approx 2 \pm 1$. The bubbles in the emulsion weaken its mechanical response. We expect its effective yield stress $\tau_y^{eff}(\phi)$ to decrease from τ_y as ϕ decreases. Thus, the average size of the bubbles whose coarsening can be counteracted by the plasticity of the surrounding medium should be larger. Qualitatively, Bi^* should increase as ϕ decreases.

To test this hypothesis, we describe the bubbly emulsion as an effective medium whose effective yield stress $\tau_y^{eff}(\phi)$ is given by Eq. 1.53 in the semi-dilute limit (cf. Section 1.4.2).

*cf. Fig 9 in [46], note that $Bi = R\tau_y/\gamma$ is written as $\frac{R}{R_0}\frac{N_\sigma N_{Ca}}{N_{De}}$ in the author's notation

We assume that this expression is valid down to $\phi \approx 0.58$, and we compute the Bingham number of the effective medium:

$$Bi_{eff}(Bi, \phi) = Bi\ \tau_y^{eff}(\phi)/\tau_y. \tag{4.17}$$

On figure Fig. 4.13(b), we show the effective Bingham $Bi_{eff}(Bi^*, \phi)$ evaluated for values of Bi^* shown in Table 4.3: we observe that it is independent from the liquid fraction, with an average value $Bi^*_{eff} \approx 0.15 \pm 0.01$. We deduce that the critical Bingham for coarsening arrest is governed by the yield stress of the effective medium. We propose a criterion for coarsening arrest, for a dispersion of bubbles in an emulsion with a given (ϕ, τ_y):

$$Bi_{eff}(Bi, \phi) \geq Bi^*_{eff} \approx 0.15 \tag{4.18}$$

The coarsening rate Ω_c is plotted as a function of the liquid fraction ϕ in Fig. 4.13(c). Similarly to what we did in the capillary limit (cf. Section 3.3), we assume that the coarsening rate follows $\Omega_c = K_0 f_3(\phi)$ (cf.Eq. 1.30), where K_0 is the coarsening rate in the LSW dilute limit (Eq. 1.24). The function $f_3(\phi)$ takes into account the increase in the coarsening rate Ω_c due to the finite distance between bubbles in a dispersion with $\phi^* \leq \phi < 1$, predicted by the TM3 model [91] (cf. Fig. 2.6). By fitting K_0 to the data, we obtain $K_0 \approx 11.5 \pm 0.8 \mu m^3/s$. This value is in good agreement with what we determined in the capillary limit in Section 3.3, where we find $K_0^{capillary} \approx 12.1 \pm 0.3 \mu m^3/s$ (cf. Table 3.3).

We conclude that the interplay between plasticity and capillarity inside a bubbly emulsion leads to the damping of coarsening, and Eq. 4.15 describes well this behaviour. We remain with the question: can we observe the arrest of coarsening in a bubbly emulsion, in the limit $\overline{Bi} \to Bi^*$?

4.2.3 Arrested coarsening

Here we present experiments performed in the osmotic cell which allows large emulsion yield stress to be reached: $\tau_y \cong 100$ Pa. We recall that with this set-up, foamed emulsions undergo a combination of foam coarsening and emulsion drainage, the latter being discussed in Section 4.1.3. Fig. 4.14 shows the evolution of the average bubble radius $\overline{R}$ with time for foamed emulsions, aging under a constant applied liquid depression. The composition of the samples is specified in Table 4.2. The final liquid fractions ϕ_f span the range $0.23 \leq \phi_f \leq 0.93$. Note that these samples are either bubbly liquids for $\phi_f > \phi^* = 0.40$ or foams for $\phi_f < \phi^*$. For all samples, we observe that as time progresses, $\overline{R}$ increases until it reaches a plateau. These growth curves show that coarsening progressively slows down up to the point when it is finally arrested. We notice that the average radius reached at the arrest increases as the liquid fraction decreases: larger radius are necessary to halt coarsening in foams than in bubbly liquids. Exemplar pictures of foamed emulsions after the coarsening arrest are showed in Fig. 4.15.

Even when the coarsening has stopped, the Bingham number of the samples increases, due to the continuous drainage of the emulsion undergoing in the osmotic cell. We plot the Bi values measured in the growth plateau as a function of the liquid fraction ϕ in Fig. 4.16(a). We observe that the minimum of Bi is constant for dilute samples $\phi > 0.7$, and it increases for decreasing liquid fractions ϕ. This is reminiscent of the evolution of the critical Bingham for coarsening arrest Bi^*, determined from the damped growth laws in bubbly emulsions (cf. Fig. 4.13). We compare the new data and the previous prediction (cf. Eq. 4.16), and find a very good agreement even for samples which have reached the foam regime. Previously, we conjectured that the yield stress of the effective medium is responsible for the ripening arrest. Thus, we determine the Bingham number

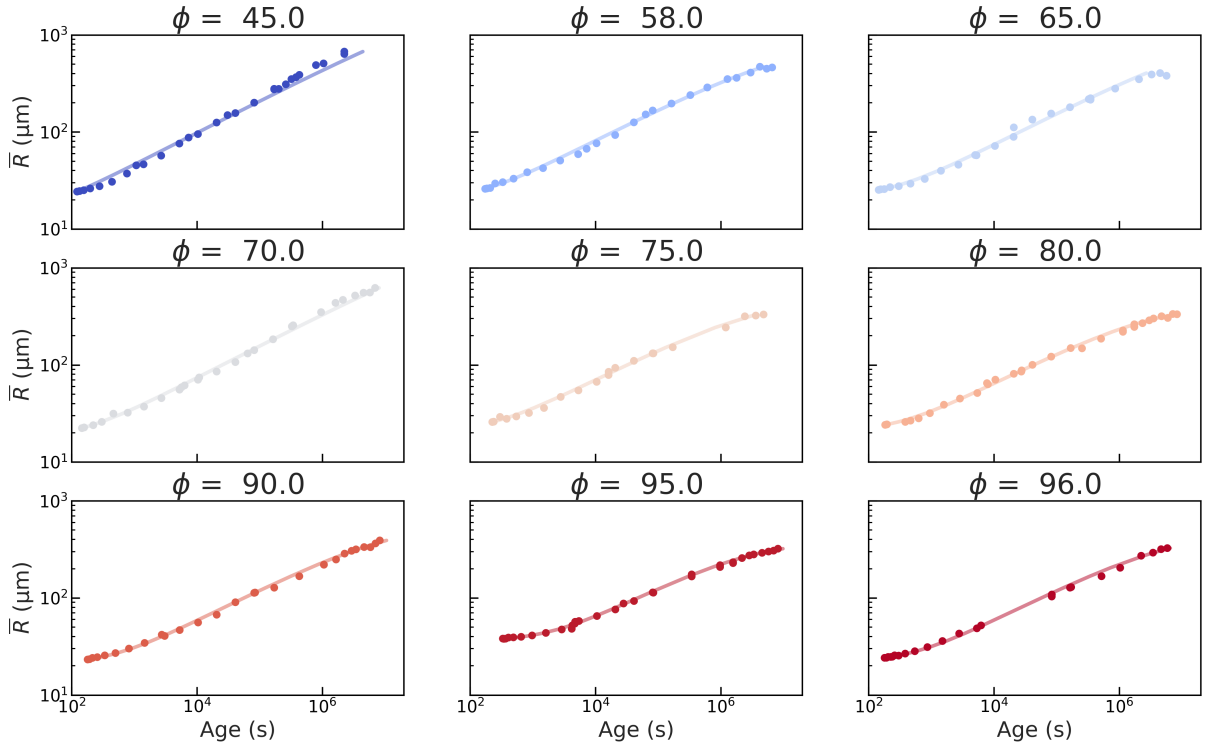

Figure 4.12: Mean bubble radius $\overline{R}$ as a function of foam age in bubbly emulsions coarsening in the clinostat (same data as in Fig. 4.10), for different liquid fractions ϕ as indicated. With the emulsion yield stress $\tau_y = 16.5$ Pa, and the surface tension $\gamma = 33.4$ mN/m, $\overline{Bi} = \overline{R}\tau_y/\gamma$ starts for each sample around $\overline{Bi} \approx 0.01$ (at $\overline{R} \approx 25$ μm), and increases linearly with $\overline{R}$.

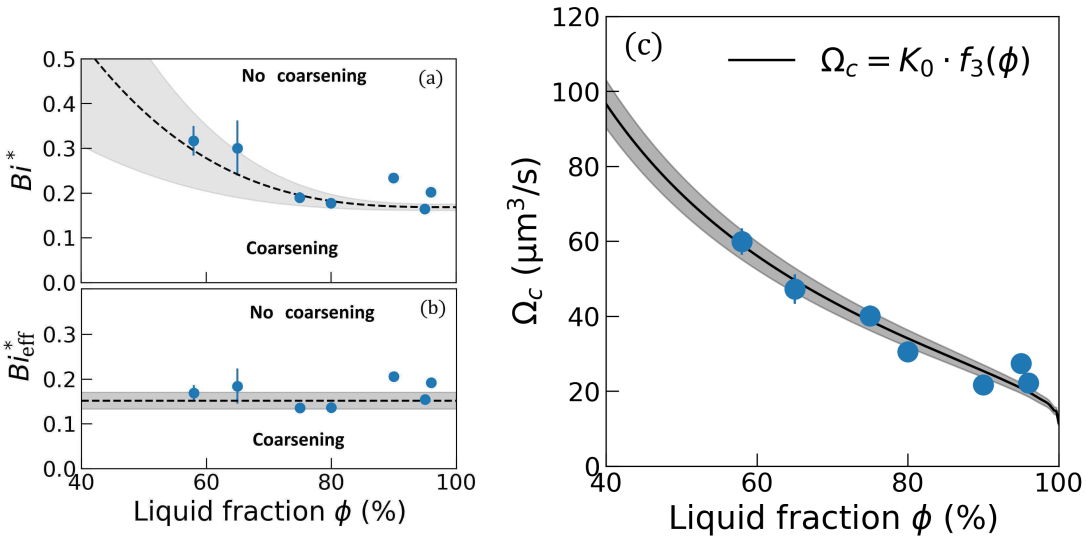

Figure 4.13: Parameters determined by fitting Eq. 4.15 to the measured growth laws shown in Fig. 4.12. (a) Critical Bingham for coarsening arrest, Bi^*, as a function of the liquid fraction ϕ. The dashed line shows Eq. 4.16, using the parameters $Bi^*_{dilute} \approx 0.17 \pm 0.01$, $A \approx 2 \pm 1$. The gray area shows 1 standard deviation (confidence interval 68%) around Bi^*_{dilute}, A. (b) Effective critical Bingham for coarsening arrest, Bi^*_{eff}, as a function of the liquid fraction ϕ. The black dashed line shows the average value $Bi^*_{eff} \approx 0.15 \pm 0.01$. (c) Coarsening rate Ω_c measured as a function of the liquid fraction ϕ. The continuous line shows the rate predicted by the TM3 model [91] (cf.Eq. 1.30), with the fitted parameter $K_0 = 11.5 \pm 0.8$ $\mu m^3/s$. The gray area shows 1 standard deviation (confidence interval 68%) around K_0.

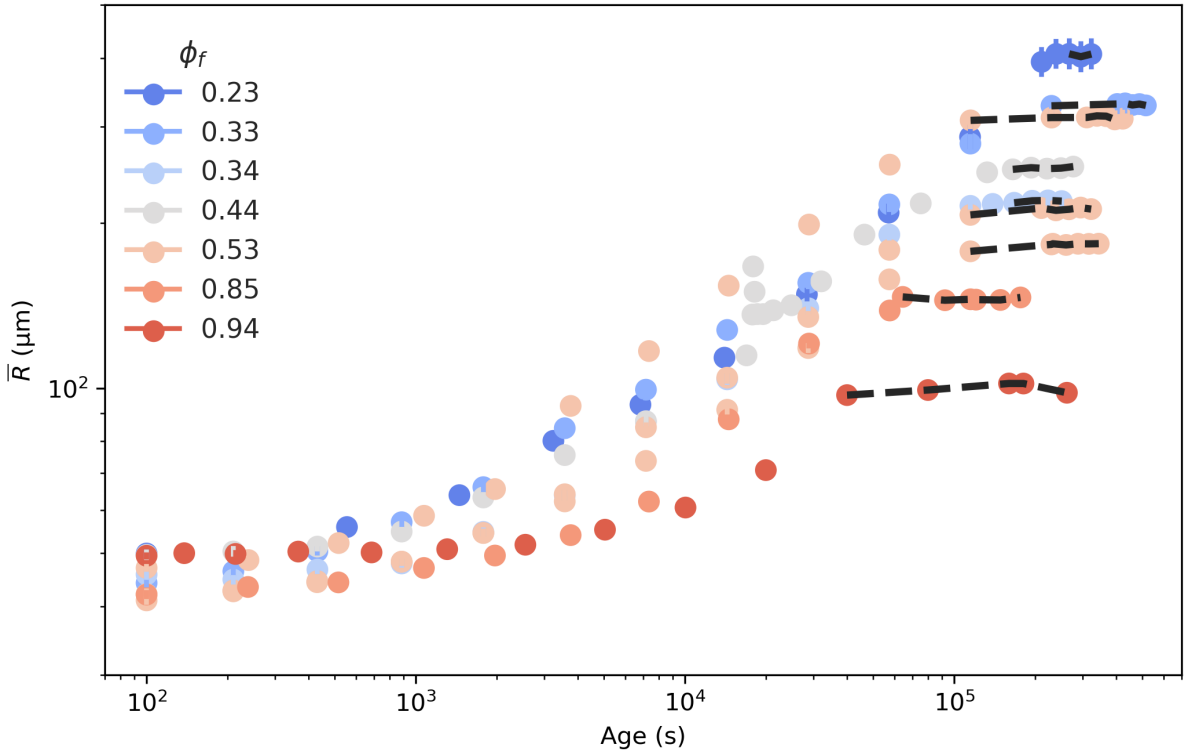

Figure 4.14: Mean radius $\overline{R}$ versus foam age for foamed emulsions ageing in the osmotic cell under a constant depression Π (cf. Table 4.2). The standard error of the mean is usually smaller than the dot size; when it is larger it is shown as an error bar. The legend identifies the final liquid fraction ϕ_f reached by each sample. Black dashed lines highlight the plateaus when coarsening is arrested.

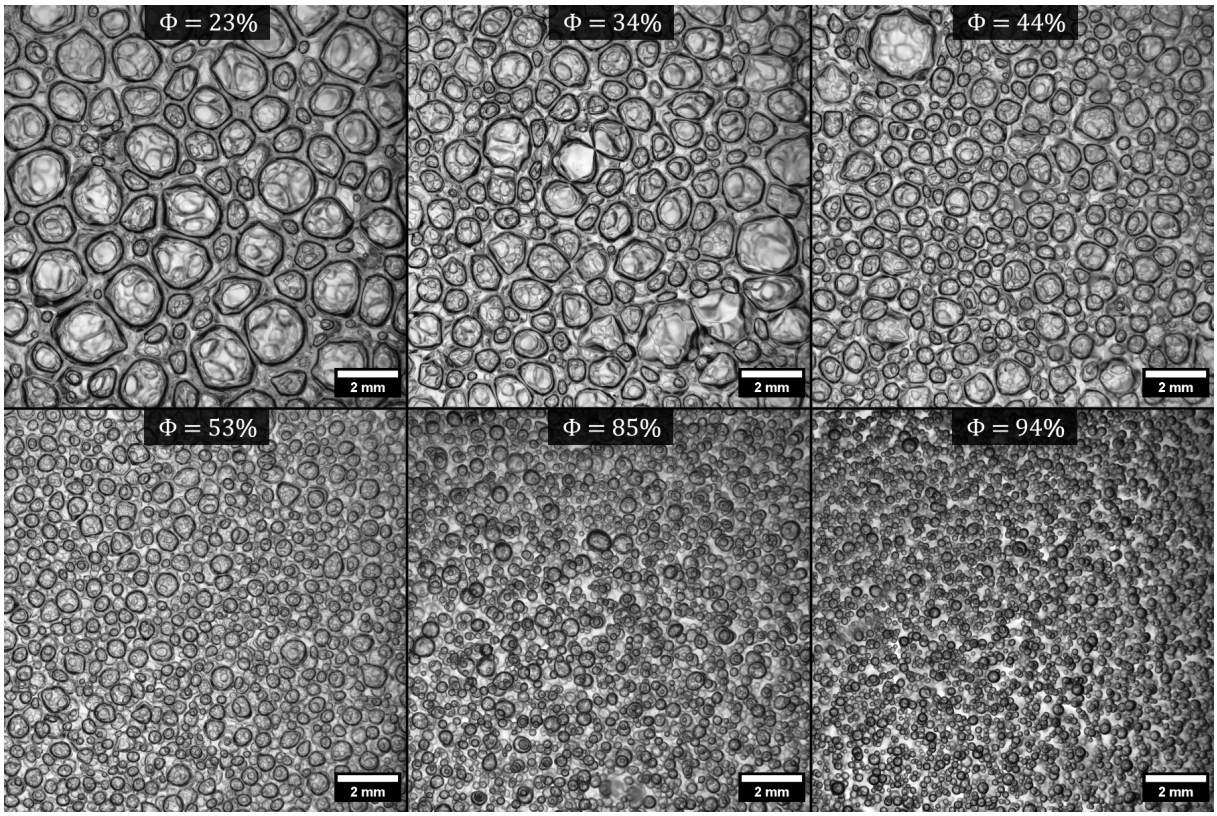

Figure 4.15: Pictures of foamed emulsions coarsened in the osmotic cell (cf. Table 4.2), in their arrested state (cf. Fig. 4.14). The final liquid fraction ϕ_f is indicated.

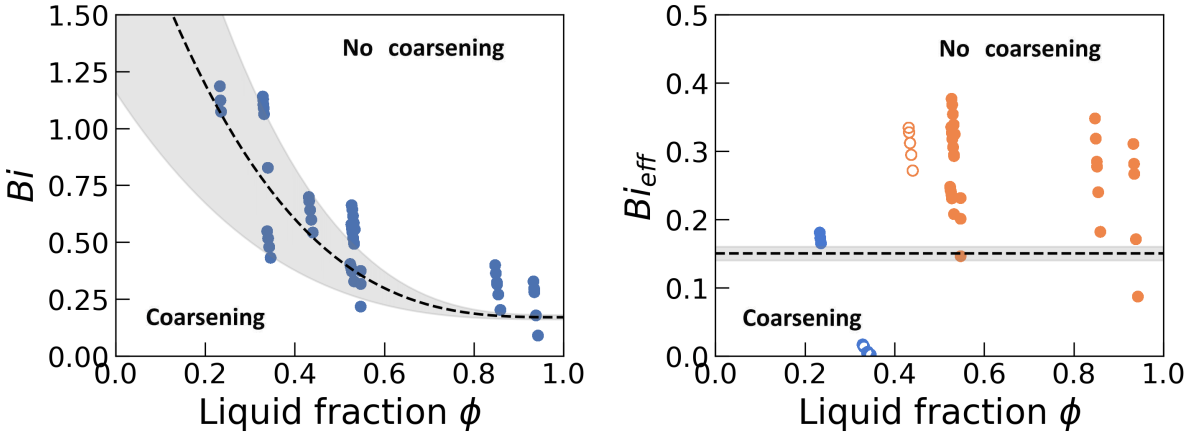

Figure 4.16: (left) Bingham number measured in the arrested state (cf. Fig. 4.14), as a function of the liquid fraction ϕ. The dashed line shows the predicted Bi^*, corresponding to Eq. 4.16 using the parameters $Bi^*_{dilute} \approx 0.17 \pm 0.01$, $A \approx 2 \pm 1$. The gray area shows 1 standard deviation (confidence interval 68%) around Bi^*_{dilute}, A. (b) Bingham number of the effective medium Bi_{eff}, determined as a function of the liquid fraction ϕ using: (blue) Eqs. 1.52 and 1.53; (orange) Eq. 4.19, with $\phi_{rcp} = 0.36$. Empty points identify the range of liquid fractions $0.3 \leq \phi \leq 0.5$, where the estimation of Bi_{eff} is less accurate. The black dashed line shows the critical effective Bingham for coarsening arrest $Bi^*_{eff} \approx 0.15 \pm 0.01$.

of the effective medium $Bi_{eff}(Bi, \phi)$ in the plateau, using Eqs. 1.52, 1.53 and 4.17 for the bubbly regime. In the foam regime we cannot apply the same physical framework, since the gas bubbles are jammed and exhibit a yield stress themselves. Instead, we determine the effective yield stress with Eq. 1.50, and combine it with Eqs. 1.48 and 4.17 to write an expression for the effective Bingham number in the foam regime:

$$Bi^{foam}_{eff}(Bi, \phi) \equiv Bi \frac{\tau_y^{eff}}{\tau_y^{emulsion}} = d(\phi - \phi_{rcp})^2 (1 + cBi^{2/3}\phi^{4/3}) \tag{4.19}$$

where $d = 0.51$ is the dimensionless prefactor for foam yield stress, and ϕ_{rcp} the random close packing fraction. In Chapter 2, we determined for coarsening wet foams $\phi_{rcp} = 0.31$, a value lower than the prediction valid for monodisperse systems, due to the high degree of polydispersity in the bubble size distribution. However, we will show that, in the arrested state, the bubble size distributions become narrower than the equivalent ones in the scaling state (cf. Fig. 4.18). Thus, we will prefer the classic random close packing fraction $\phi_{rcp} = 0.36$. For liquid fractions in the range $0.30 \leq \phi \leq 0.50$, the accuracy of Bi_{eff} is lower than in the other regimes. On the bubbly side, Eq. 1.52 is valid in the regime $\phi \gtrsim 0.50$; an accurate expression for more concentrated dispersions would require new micromechanical simulations. On the foam side, we are underestimating Bi_{eff} by not taking into account the adhesion between bubbles, which produces a yield stress even for $\phi \gtrsim \phi_{rcp}$ (cf. Section 3.1.1.3). We plot the effective Bingham numbers $Bi_{eff}(Bi, \phi)$ as a function of the liquid fraction ϕ in Fig. 4.16(b). We observe that the measured Bi_{eff} are in very good agreement with the criterion for coarsening arrest proposed in Eq. 4.18, with minimum values close to the prediction of Bi^*_{eff}. We deduce that the progressive damping of coarsening, discussed in Section 4.2.2, is indeed governed by the plasticity of the effective medium, with a critical Bingham Bi^*_{eff} which sets the arrest of coarsening.

For each sample, we gather all the relative bubble size $R/\overline{R}$ measured in the time range corresponding to the plateau, and determine their distribution in the arrested state. As shown in Fig. 4.17, relative bubble radii are asymmetrically distributed around the mean, with a positive skewness and a tail which extends up to $2 - 3$ times the average radius.

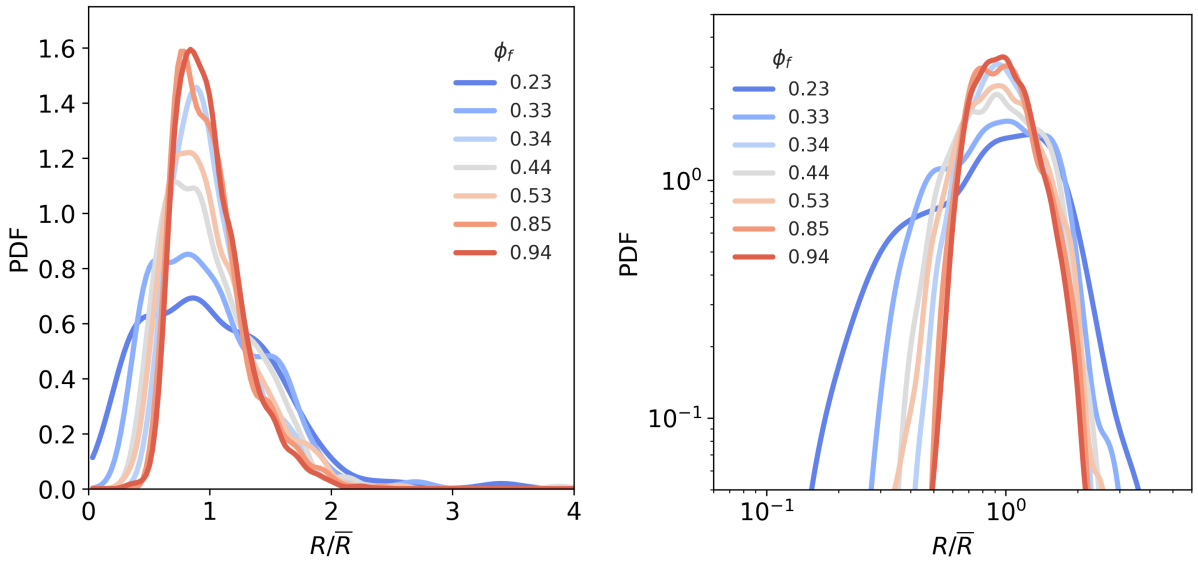

Figure 4.17: Bubble size distributions in the arrested state: (left) of the normalized radius $R/\overline{R}$, (right) of the logarithm of $R/\overline{R}$. The legend identifies the corresponding final liquid fraction ϕ_f.

The most diluted sample ($\phi_f = 0.93$) has the narrowest distribution, and the distributions broaden when decreasing the liquid volume fraction of the sample. In Fig. 4.17 we also plot the distributions of $\log R/\overline{R}$. In this representations, the distributions of diluted samples are symmetrical around the mean, as expected for a lognormal distribution. As ϕ decreases, the shape of the distributions evolve, toward a bimodal distribution. This is reminiscent of the bilognormal distributions observed in the scaling state of simple wet foams [19].

To delve into it, we compare the bubble size distributions measured for the same liquid fraction, either in the arrested state or in the scaling state, in Figure 4.18. For the foam regime ($\phi < \phi^*$), the scaling state distributions are measured for foams made of simple surfactant solutions [19] (cf. Chapter 2) Remarkably, the arrested state distributions are different from the scaling state ones. We recall that in the scaling state, the PDF of foams exhibits two peaks, corresponding to a large population (by number) of small roaming bubbles, and a small population of large jammed bubbles. The average size lays in the midpoint between the peaks. In contrast, as seen with $\phi = 0.25$, in the arrested state, the respective relevance of the peaks is inverted: the population of roaming bubbles is vanishing to the benefit of larger bubbles, which represent now the average size. This trend is also observed for $\phi = 0.35$. Finally, in the bubbly regime ($\phi = 0.93$), we observe a very narrow peak. We compare the distribution to that measured in bubbly emulsions in a scaling state (cf. Chapter 3). In this regime, where the scaling state distribution has only one peak, we cannot propose the same comparison. Nevertheless, the left tail of bubbles smaller than average has similarly disappeared.

In conclusion, for any liquid volume fraction ϕ, the arrested distributions has lost a relevant fraction of the smaller bubbles typical of the scaling state distribution. We propose a simple argument to explain this behaviour: the bigger bubbles of the distribution are the first to reach a Bingham number large enough to arrest their ripening. As a consequence, bubbles of medium size can only grow instead of alternatively grow or shrink. This kills the production of bubbles smaller than average (or roaming bubbles in foams), which will dissolve and disappear as long as there are still growing bubbles able to absorb their gas.

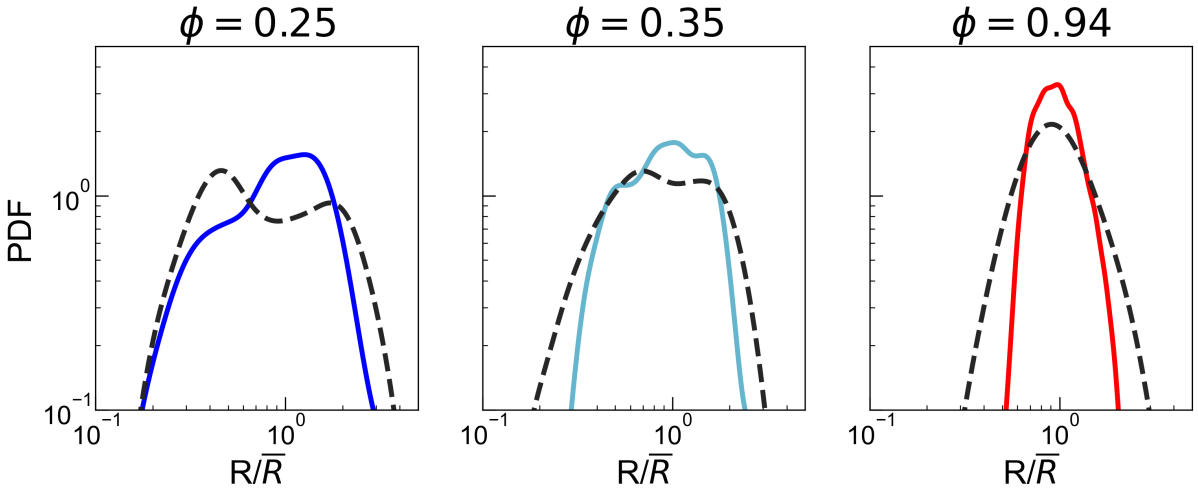

Figure 4.18: Bubble size distribution measured in: (colored line) the arrested state and (black dashed line) the scaling state distribution in: the foam regime ($\phi < \phi^* = 0.40$) and the bubbly regime ($\phi > \phi^*$). In the former, the reference scaling state distributions come from foams made from a simple surfactant solution, coarsening in microgravity [19] (cf. Chapter 2). In the latter, it comes from a bubbly emulsion coarsening in the clinostat (cf. Chapter 3).

4.2.4 Local gas exchange at the microscale

We continue the analysis started in the previous section: we recall that in these experiments the foamed emulsions undergo a combination of foam coarsening and emulsion drainage. We propose here an analysis of the instantaneous evolution of the individual bubble sizes, in a bubbly emulsion.

Thanks to the simulations (cf. Section 4.1.3) we retrieve the value of the yield stress of the emulsion at any time. Thanks to the bubble tracking implemented in our post-processing routine (cf. Section 4.1.4.2), we are able to link the bubbles in successive images, and determine their individual bubble radius variation dR/dt between two consecutive images, which we will consider as their instantaneous growth rate.

4.2.4.1 Modelization

For an isolated bubble, dR/dt depends on the gas pressure inside the bubble, $P(R)$, according to Eq. 1.16. If the bubble is surrounded by an elastoplastic medium, $P(R)$ is no more set by Laplace pressure only, but it is modified by the elastic stresses that build around. In the framework of Venerus model (cf. Section 1.4.4), the difference between the pressure in the bubble and at infinity $\Delta p = \bar{p}(R) - p_0$ is given by Eq. 1.75. Neglecting the viscous stress in view of the slow evolution of the bubbles, Eq. 1.75 writes:

$$\Delta p = \frac{2\gamma}{R} \pm 2\sqrt{3}\tau_y \ln\left(\frac{S}{R}\right) + \frac{G}{2}\left[5 - \left(1 - \frac{R^3 - R_0^3}{S^3}\right)^{1/3}\left(5 - \frac{R^3 - R_0^3}{S^3}\right)\right]. \qquad (4.20)$$

As a remainder, S is the radius of the frontier between the yielded ($r \leq S$) and unyielded ($r \geq S$) medium around the bubble. The second (resp. third) term on the right hand side represents the plastic (resp. elastic) stress around one bubble. In our foamed emulsions, we showed that $Y \equiv \frac{R^3 - R_0^3}{S^3} \approx \pm\frac{\sqrt{3}}{2}N_y$ (cf. Eq. 1.69 and Fig. 1.9), where the positive sign (resp. negative) corresponds to a growing (resp. shrinking) bubble. Within these

conditions, the pressure difference can be simplified to:

$$\Delta p = \frac{2\gamma}{R} \pm \frac{2}{\sqrt{3}}\tau_y \left[\ln\left(\left| 1 - \frac{R_0^3}{R^3} \right| \right) - \ln\left(\frac{\sqrt{3}}{2} N_Y \right) \right] \pm \frac{2}{\sqrt{3}}\tau_y + \mathcal{O}(N_Y^2). \tag{4.21}$$

The bubble size R_0 corresponds to the reference undeformed state, which we assume to be that right after the foaming. In our systems, where the average bubble size is continuously growing, we further assume that the continuous medium is never able to completely relax. If so, R_0 is constant. In our system, the bubbles size distributions are positively skewed, with $R_{min} \sim \overline{R}/3$ (cf. Fig. 4.18). Thus, after a transient time the majority of the bubbles, whether shrinking or growing, have become much larger than that, i.e. $R_0/R << 1$. It follows that, for any bubble, the medium around is under compression, and we keep only the positive sign in Eq. 4.21. We finally write the pressure difference as:

$$\Delta p = \frac{2\gamma}{R} + \frac{2}{\sqrt{3}}\tau_y \left[1 - \ln\left(\frac{\sqrt{3}}{2} N_Y \right) \right]. \tag{4.22}$$

In our system $0.004 \lesssim N_Y \lesssim 0.05$ (cf. Section 3.1.1.3), and so $-5.7 \lesssim \ln\left(\frac{\sqrt{3}}{2} N_Y\right) \lesssim -3.1$. So we expect that, for $Bi = \tau_y R/\gamma \gtrsim 0.3$, the plastic stresses should be dominant with respect to capillary stresses.

According to Eqs. 1.16 and 4.22, the ripening rate of an isolated bubble now writes:

$$\frac{dR}{dt} = \frac{DH_e v_m}{R} \left(sP_0 - \frac{2\gamma}{R} + \frac{2}{\sqrt{3}}\tau_y \left[1 - \ln\left(\frac{\sqrt{3}}{2} N_Y \right) \right] \right). \tag{4.23}$$

Using the critical saturation radius R_c (cf. Eq. 1.19), the Bingham, and defining $Bi_0 = \sqrt{3}/(1 - \ln\left(\frac{\sqrt{3}}{2} N_Y\right))$, we get:

$$\frac{dR}{dt} = \frac{2\gamma D H_e v_m}{R^2} \left(\frac{R}{R_c} - 1 + \frac{Bi}{Bi_0} \right). \tag{4.24}$$

For a bubble ripening in a dilute dispersion ($\phi \to 1$) that has reached the scaling state, as in LSW model, all the characteristic lengths of the system are governed by a unique independent lengthscale, which we can choose as the first moment of the distribution $\overline{R}$. We expect $\overline{R}/R_c$ to be a constant factor on the order of 1. Additionally, we empirically describe the plastic stress contribution as a term proportional to Bi, and generalize Eq. 4.23:

$$R^2 \frac{dR}{dt} = 2\gamma D H_e v_m \left(\frac{R}{\overline{R}} \left(\frac{\overline{R}}{R_c} + \frac{\overline{Bi}}{Bi^{**}} \right) - 1 \right). \tag{4.25}$$

where Bi^{**} is a characteristic Bingham number, potentially different from Bi_0. Note that the factor $(\frac{\overline{R}}{R_c} + \frac{\overline{Bi}}{Bi^{**}})$ is constant for a dispersion of bubbles with a given $(\overline{R}, \phi, \tau_y)$.

In a bubble dispersion with a finite liquid fraction ϕ, we expect the gas volume flux $J \equiv R^2 \frac{dR}{dt}$ to be modulated by the screening of the solute concentration (cf. Eq. 1.29). By consistency with our analysis of the macroscopic growth laws (cf. Sections 3.3 and 4.2.2), we use here the TM3 model [91], and write:

$$J = 2\gamma D H_e v_m \left(\frac{R}{\overline{R}} \left(\frac{\overline{R}}{R_c} + \frac{\overline{Bi}}{Bi^{**}} \right) - 1 \right) \left(1 + b\frac{R}{\overline{R}} \right) \tag{4.26}$$

where b is the function of the liquid fraction; in TM3 model, it writes:

$$b = \frac{\sqrt[3]{1-\phi}}{(1 - \sqrt[3]{1-\phi})}. \tag{4.27}$$

4.2.4.2 Results

We now compare this semi-empirical prediction (cf. Eq. 4.26) to our data. Since the emulsion yield stress τ_y increases from 4 Pa to 100 Pa in the course of each experiment, we construct 60 datasets where τ_y can be considered as constant, with a maximum relative variation $\pm 10\%$ for the following τ_y values (4, 10, 15, 20, 30, 40, 50, 60, 70, 80, 90, 100 Pa). Each dataset is composed of 30 images equally spaced in time, and we measure R and dR/dt for each bubble in the images.

Capillary regime

First, we consider the most dilute sample $\phi = 0.95$, for $\overline{Bi} \approx 0.01 \ll Bi^*$, where plastic effects are negligible compared to Laplace pressure (cf. Fig. 4.13). We plot J as a function of $R/\overline{R}$ in Fig. 4.19(a): the data constitute a sparse cloud, which reveals the amplitude of the local fluctuations in the microstructure. The cloud has a different shape than that predicted by simulations of coarsening grains [113] or that experimentally observed in coarsening alloys [114]. In our case, it accumulates densely in a limited range of $R/\overline{R}$, between 0.6 and 1.3, which reflects the narrowness of the bubble size distribution (cf. Fig. 4.18). We define a generic equation, of the same form as Eq. 4.26, in the limit where $\overline{Bi} \to 0$:

$$J = k\left(\alpha\frac{R}{\overline{R}} - 1\right)\left(1 + \beta\frac{R}{\overline{R}}\right) \tag{4.28}$$

where k, α, β are free parameters. By identifying Eqs. 1.24, 4.26 and 4.28, we expect $k = \frac{9}{4}K_0$. We expect also $\alpha \sim 1$, $\beta \sim b$. First, we fit Eq. 4.28 to the data, imposing $\beta = 0$, which corresponds to the LSW model. By comparing the result to the evolution of the average of J, we observe that Eq. 4.28 captures the increase of J for $0.75 \leq R/\overline{R} \leq 1.2$. We get $\alpha \approx 1.16$ and $k \approx 24(\mu m^3/s)$. Both are very close to the expected values for LSW model: $\alpha \approx 1$, $k \approx 26$, using $K_0 = 11.5\mu m^3/s$ as measured for the macroscopic growth laws of the same system (cf. Section 4.2.2).

Outside this range of $R/\overline{R}$, the discrepancy between the fit and the data could be due to the effect of the screened solute concentration. Since k is a common factor in Eq. 4.28, we determine it by linearly extrapolating the data at $R/\overline{R} = 0$, where $J(0) = -k$. We find $k \approx 11 \pm 1\mu m^3/s$, and then, we fit Eq. 4.28 to our data, with α and β as free parameters, which corresponds to the TM3 model. We get $\alpha \approx 1.19 \pm 0.01$ and $\beta \approx 0.65 \pm 0.01$. The value of α is very close to that determined with the LSW fit. The value of β is in agreement with the prediction arising from TM3 model Eq. 4.27: $b(0.95) = 0.58$. As seen in Fig. 4.19(a), the TM3 fit better captures the evolution for bubbles smaller than average. We conclude that the effect of screening is already present at $\phi = 0.95$, so we will keep the screening parameter in the following analysis, and we will keep the same value $k \approx 11\mu m^3/s$, since it should be independent from the liquid fraction.

We do a similar analysis for samples with lower liquid fractions, $\phi = 0.80, 0.60$, shown respectively in Fig. 4.19(b) and Fig. 4.19(c). We observe that, for decreasing liquid fractions, the evolution of J deviates more and more from a linear relation. The fitted parameters α and β are all shown in Fig. 4.19(d). We observe that $\alpha \approx 1.1$ is independent from the liquid fraction: this is consistent with the similarity observed between bubble size distributions in this range of liquid fractions (cf. Fig. 4.17). The variation of β with the liquid fraction is in good agreement with the TM3 prediction (cf. Eq. 4.27.

We conclude from this analysis of the capillary regime that the evolution of the average gas flux J is well described by TM3 model, with fitting parameters consistent with the expectations. Thus, for a general description of individual gas exchange, where the plasticity of the surrounding medium is considered, we will take into account the effect of screened solute concentration.

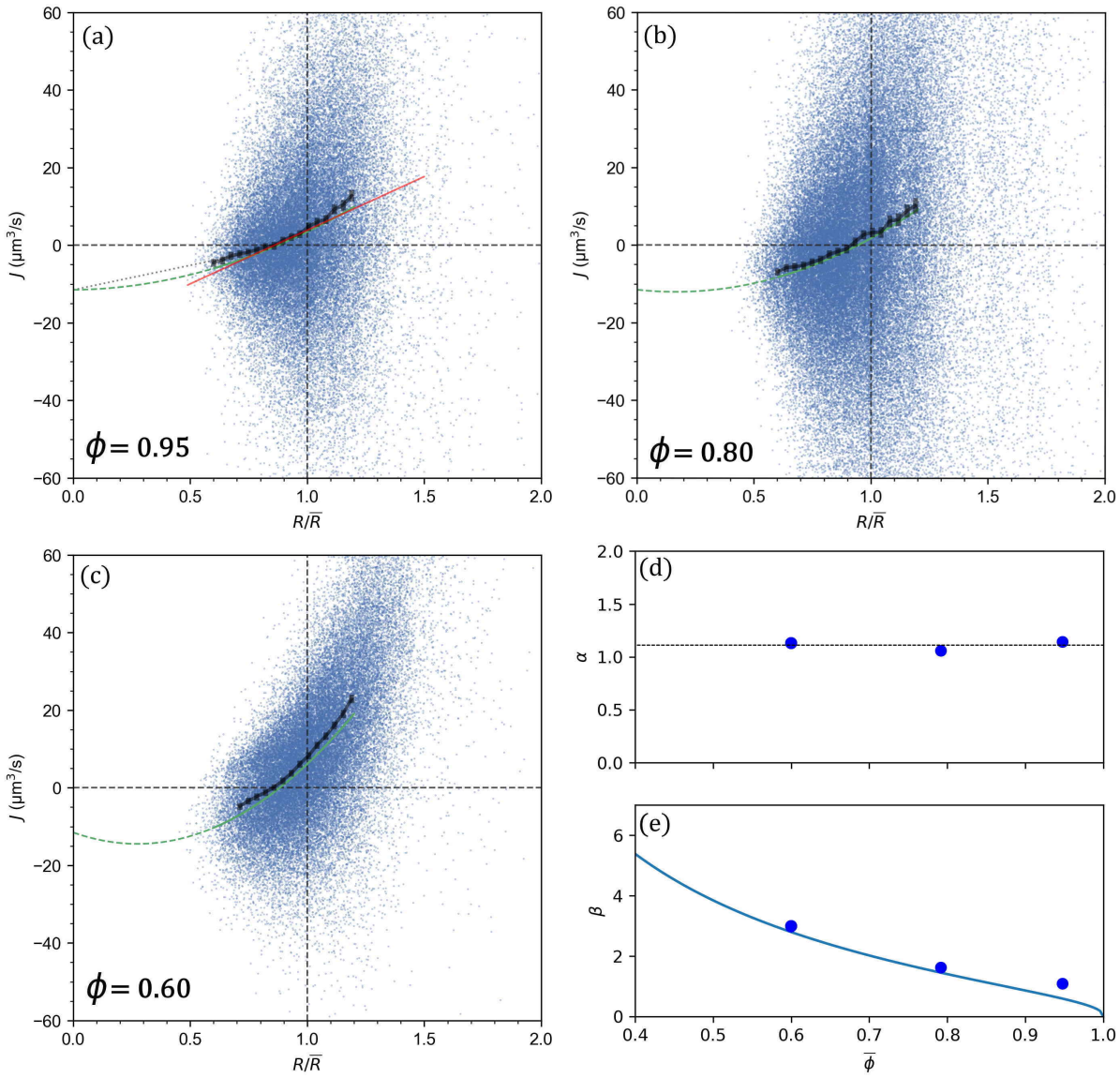

Figure 4.19: Capillary regime. Gas volume flux of individual bubbles $J = R^2 dR/dt$ as a function of the normalized radius $R/\overline{R}$, for bubbly emulsions with datasets corresponding to $\overline{Bi} \approx 0.01$ and three different liquid fractions, as indicated. The cloud of individual measurements is superimposed with a black line, obtained by binning the data in the range of $R/\overline{R}$ where the cloud is dense enough. Outside this domain the average J is too noisy. The size of the black points shows the standard deviation of the average. The red curve represents LSW model (Eq. 4.28 with $\beta = 0$) fitted to the data, while the green curve represents coarsening modified by screening in TM3 model (Eq. 4.28 with $k \approx 11 \mu m^3/s$). In (a), the gray dotted shows the linear extrapolation to $J = 0$. Fitted parameters as a function of the liquid fraction for Eq. 4.28: (d) α and (e) β. The black line shows $\alpha = 1.1$. The blue line shows the predicted β (Eq. 4.27).

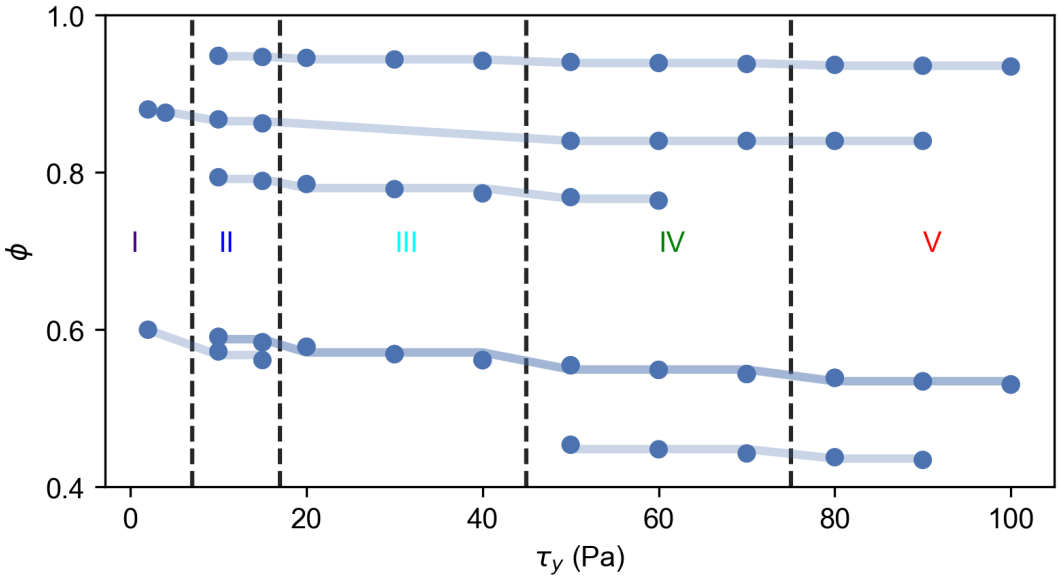

Figure 4.20: Variation of the liquid fraction ϕ as a function of the emulsion yield stress τ_y, along the coarsening of bubbly emulsions in the osmotic cell (cf. Section 4.1.2). The blue lines correspond to different experiments, with each point representing one dataset of individual gas exchange. As explained in the text, they are grouped into 19 super-dataset, according to 5 ranges of τ_y, with a liquid fraction ϕ which is the average of the points. Note that we identify ranges $I - II$ as the capillary regime.

General case: plasto-capillary regime

To study the scaling of J with $\overline{Bi}$, we need to disentangle the three main variables of the system: $R/\overline{R}$, τ_y and ϕ. In view of the wide data scattering, we consider for the analysis only those datasets of constant (τ_y, ϕ) with a large number of measured J ($N > 10'000$), with values well distributed over a wide range of $R/\overline{R}$. After this selection we construct 47 datasets of constant (τ_y, ϕ), as shown in Fig. 4.20.

Since J is expected to depend on two variables, $R/\overline{R}$ and $\overline{Bi}$ (cf. Eq. 4.26), to perform a surface fitting of J as a function of ($R/\overline{R}$, $\overline{Bi}$), we need to group datasets with the same ϕ and varying τ_y (varying $\overline{Bi}$) into 'super-datasets'. Since the liquid fraction slightly varies in each experiment (cf. Fig. 4.4), we make the super-datasets to have inside only small variations in the liquid fraction ($\Delta\phi \leq 0.01$). In this way, we get 19 super-datasets of constant ϕ, according to 5 ranges of τ_y (I-V), as shown in Fig. 4.20. Fig. 4.22(a-i) shows examples of J datasets, for three different liquid fractions ϕ, and three τ_y values.

As it was written in Eq. 4.26, the plasticity of the medium lowers the effective $R_c/\overline{R}$. Thus, for the bubbles smaller than average, the pressure difference driving their dissolution would be smaller than in an equivalent viscous fluid. On the contrary, the bubbles bigger than average would experience a stronger pressure difference, and grow faster. This is inconsistent with our experimental observations, where we see a systematic decrease of J as τ_y increases for a constant ϕ (cf. Fig. 4.22). Indeed, if we try fitting Eq. 4.26 to the 19 super-datasets, at large $\overline{Bi}$ the expected scaling proves incoherent with the data, failing to describe the damping and final arrest of coarsening shown by them. We conclude that the extension of Venerus model outside the case of isolated bubbles is definitely not valid.

Similarly to what we did for the damped growth laws in bubbly emulsions (cf. Section 4.2.2), we conjecture the existence of a critical Bingham $Bi^{**}(\phi)$, which sets the plastic limit ($\overline{Bi} \to Bi^{**}(\phi)$) where bubbles stop exchanging gas ($J \to 0$). Another requirement is to recover Eq. 4.28 in the capillary limit. This behaviour is captured by the

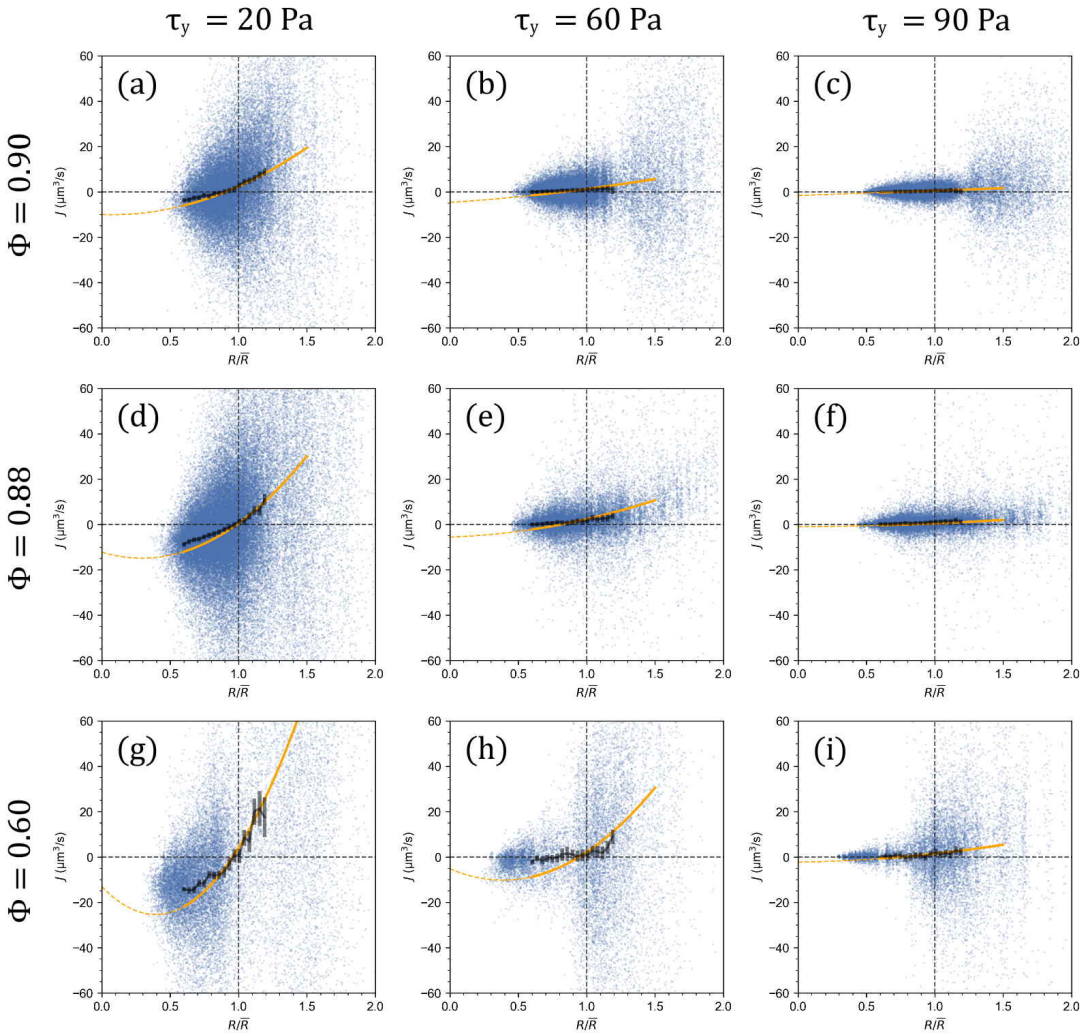

Figure 4.21: Ripening bubbly emulsions. Evolution of J as a function of the relative radius $R/\overline{R}$, for 9 datasets of specified τ_y, ϕ (cf. Fig. 4.20).

simple expression:

$$J = k' \left(\frac{R}{\overline{R}} \alpha - 1 \right) \left(1 + \beta \frac{R}{\overline{R}} \right) \left(1 - \frac{\overline{Bi}}{Bi^{**}} \right) \mathcal{H}(Bi^{**} - \overline{Bi}) \tag{4.29}$$

where $\mathcal{H}$ is the Heaviside step function, which ensures $J = 0$ for $\overline{Bi} \geq Bi^{**}$. By identification with Eqs. 4.27 and 4.28, we expect $\alpha = \overline{R}/R_c$, $\beta = b$. To ensure that Eq. 4.29 matches Eq. 4.28 in the capillary regime, we must have $k = k' \left(1 - \frac{\overline{Bi}}{Bi^{**}}\right)$. Thus, we fit Eq. 4.29 to the super-datasets: ($\phi = 0.95$, range II), ($\phi = 0.80$, range II), ($\phi = 0.60$, range I) (cf. Fig. 4.20), which include the data of Fig. 4.19. By fixing the values of α, β to their values previously found in the capillary regime (cf. Fig. 4.19(d,e)), we get $k' \approx 18 \mu m^3/s$. Next, we keep k' to this value, and fit Eq. 4.29 to each super-dataset with α, β, Bi^{**} as free parameters.

We show examples of the fitted J for 9 datasets, in Fig. 4.21(a-i); the complete ensemble of curves is given in Appendix C. We see that Eq. 4.29 describes well the evolution of J with $R/\overline{R}$, for the whole range of ϕ and τ_y. In Fig. 4.21(h) the agreement is not on par with the others, which we attribute to a sparser cloud of the data in the range $R/\overline{R}$. When deeply in the plastic regime ($\overline{Bi} \to Bi^{**}$), we expect the damping factor to dominate, and $J \sim \left(1 - \frac{\overline{Bi}}{Bi^{**}}\right) \to 0$. This is consistent with our observations in Fig. 4.21(c,f,i).

We plot the fitting parameters in Fig. 4.22. We observe that α is independent from the liquid fraction, as it was in the capillary regime, and get the same average $\alpha \approx 1.1$,

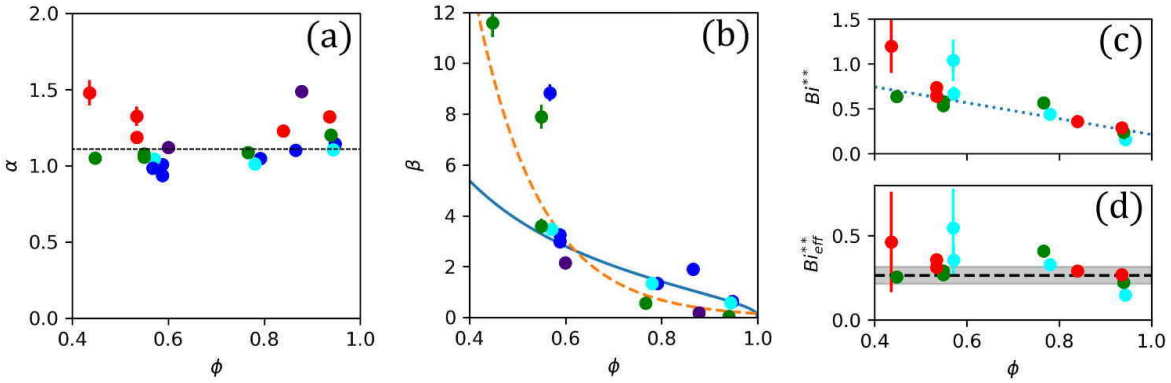

Figure 4.22: Fitted parameters of Eq. 4.29 as a function of the average liquid fraction ϕ in the super-datasets: (a) α, (b) β, (c) Bi^{**} (d) Bi^{**}_{eff}. The color of the points corresponds to the 5 ranges of τ_y defined in Fig. 4.20). In (a), the black line shows $\alpha = 1.1$. In (b), the fitted β for the range V of τ_y are not shown, in view of the scarce sensitivity of J to β in that regime. The blue solid line shows the β predicted from TM3 model (cf. Eq. 4.27). The orange dashed line is an exponential decay empirically fitted to β for ranges III-IV: $\beta \approx e^{(A-B\phi)}$, with $A = 5.6 \pm 0.7$ and $B = 8 \pm 1$. In (c), Bi^{**} values for the range $I - II$ of τ_y are not shown, in view of the scarce sensitivity of J to Bi^{**} in that regime. The green line is Eq. 4.30, with parameters $Bi^{**}_{dilute} = 0.16 \pm 0.06$, $m = 1.2 \pm 0.2$. (d) Effective critical Bingham of ripening arrest Bi^{**}_{eff} as a function of the liquid fraction ϕ. The black dashed line shows the average value $Bi^{**}_{eff} \approx 0.25 \pm 0.02$.

which is consistent. The values of β in the capillary regime are consistent with Eq. 4.27, predicted from TM3 model. However, for larger Bi, β follows a different evolution with ϕ. For smaller ϕ, we find larger values of β, as if the solute concentration was screened over shorter distances than in TM3 model. As the liquid fraction increases, β exhibits a faster decay. Empirically, we describe this evolution as an exponential decay $\beta = e^{(A-B\phi)}$, with coefficients $A = 5.6 \pm 0.7$, $B = 8 \pm 1$. We find that the critical Bingham for ripening arrest Bi^{**} scales linearly with the liquid fraction:

$$Bi^{**} \approx Bi^{**}_{dilute} + m(1 - \phi) \tag{4.30}$$

with coefficients $Bi^{**}_{dilute} \approx 0.20 \pm 0.02$ and $m = 0.92 \pm 0.09$. Similarly to the analysis we did for the growth laws, we conjecture that the yield stress of the effective medium is responsible for the observed evolution of Bi with ϕ. Thus, we determine the Bingham number of the effective medium $Bi_{eff}(Bi, \phi)$ using Eqs. 1.52, 1.53 and 4.17. On Fig. 4.22(d), we show the corresponding effective Bingham numbers $Bi_{eff}(Bi, \phi)$. We observe that it is independent from the liquid fraction, with an average value $Bi^{**}_{eff} \approx 0.25 \pm 0.02$. It is slightly larger than the critical effective Bingham for coarsening arrest $Bi^{*}_{eff} \approx 0.15$, that we determined from the growth laws (cf. Section 4.2.2). We expect that the average growth on the macroscopic scale should stop before the arrest of the gas exchange at the microscopic scale; which is consistent with our observations. We deduce that the yield stress of the effective medium governs the individual bubble ripening.

4.2.5 Conclusion

In Section 4.2, we study the coarsening of bubbly emulsions over long time ranges as a function of ϕ, at constant τ_y. In the capillary regime (for small $\overline{Bi}$), we observe that the average bubble radius grows according to a cubic law, as expected in the dilute regime and as discussed in Section 3.3. The coarsening rate Ω_c decreases with the liquid fraction ϕ as predicted by the TM3 mean-field coarsening model, where the solute concentration

around each bubble is screened over a distance which scales as $R/\overline{R}$, and monotonously increases with ϕ (cf. Fig. 4.13 (c)). In the plastic regime (for large $\overline{Bi}$), coarsening is still driven by the same coarsening rate Ω_c, but it is damped by the plastic response of the medium. We propose a semi-empirical law, Eq. 4.15, which accounts for the damped coarsening of a bubbly emulsion, encompassing both the capillary and the plastic regimes. We predict the coarsening arrest to be set by a critical Bingham number $Bi^*(\phi)$. The increase of $Bi^*(\phi)$ with decreasing liquid fraction arises from the presence of bubbles in the medium, which act as cavities and weaken its mechanical response. We show that this can be accounted by considering the Bingham number of the effective medium Bi_{eff} (cf. Eq. 4.17). We find a critical value $Bi^*_{eff} \approx 0.15$ above which coarsening is arrested (cf. Fig. 4.13 (b)).

Moreover, using an osmotic cell, we are able to observe the arrest of coarsening, for bubbly emulsions as well as emulsion foams ($0.23 \leq \phi \leq 0.94$) (Fig. 4.14). We analyse the bubble size distributions in the arrested state, and show that they differ from the 'frozen' scaling state distributions that we would have in a coarsening simple liquid (cf. Fig. 4.18). In contrast to the scaling state distributions in foams, the population of roaming bubbles vanishes, and the distributions narrow since bigger bubbles cannot grow anymore. The same trend is observed in bubbly liquids.

To get more insight on the underlying processes, we study in the ripening of individual bubbles in a bubbly emulsion, of average bubble radius $\overline{R}$, as a function of liquid fraction in the foam ϕ and the average Bingham number $\overline{Bi}$. We observe stochastic fluctuations in the distribution of the gas flux J as a function of $R/\overline{R}$, due to the variability of the local neighbourhood. We describe the average evolution of J as a function of $R/\overline{R}, \overline{Bi}$ and ϕ using a semi-empirical expression (cf. Eq. 4.29), which contains three factors related to: the individual capillary pressure, the screening of the solute concentration, and the plastic response of the medium. In the capillary regime (for small $\overline{Bi}$), our expression is consistent with the same mean-field ripening model TM3, which takes into account the screening of the solute concentration around bubbles (cf. Fig. 4.19(e)). In the plastic regime (for large $\overline{Bi}$), ripening is damped by the plastic response of the medium, similarly to the damping of the average growth law. The arrest of ripening is set by a critical Bingham number $Bi^{**}(\phi)$. We find a critical value $Bi^{**}_{eff} \approx 0.25$ above which ripening is arrested in the bubbly emulsion (cf. Fig. 4.22). We expect that the average growth on the macroscopic scale should stop before the arrest of the gas exchange at the microscopic scale; which is consistent with $Bi^*_{eff} < Bi^{**}_{eff}$.

In the next section, we will study coarsening of foamy emulsions, below the jamming transition ($\phi < \phi^*$).

4.3 Damped coarsening in foamy yield stress fluids

We present here coarsening experiments using the clinostat set-up, varying the oil fraction in the range $0.65 \leq \varphi \leq 0.775$, with liquid fractions in the *foam regime* ($\phi < \phi^* \approx 0.40$); the complete list of experimental parameters is detailed in Table 4.1.

4.3.1 Damped growth law

In the foam regime, we observe an evolution of the overall structure that is similar to that of simple foams. Exemplar pictures of these foamy emulsions are showed in Fig. 4.23. We characterize the structure by analyzing the bubble size distributions measured at the surface: after a transient time, the cumulative distributions of the normalized radius $R/\overline{R}$, shown in Figure 4.24, aggregate onto a unique curve at long times, which becomes invariant over time as expected in the Scaling State. This transition is observed to occur at a foam age of $T_{Scaling} \approx 3 \cdot 10^4$ s, without a dependency from ϕ, φ in the range under scrutiny. The scaling behavior is also captured by comparing two characteristic lengths of the distribution, the mean radius $\overline{R}$ and the Sauter radius R_{32}. Initially, they evolve at different rates, but for $t \geq T_{Scaling}$, the expected proportionality $R_{32} \propto \overline{R}$ is recovered, with a prefactor that is specific to the sample. Such a proportionality is expected in the Scaling State since any characteristic length scale should scale as the first moment of the size distribution.

We now aim to understand how the probability density functions (PDFs) evolve over time before reaching the Scaling State, and subsequently compare the Scaling State distributions across different samples. For a sample with $\phi = 0.35$ and $\varphi = 0.75$, shown in Fig. 4.25(a), the distribution initially exhibits a Gaussian-like shape, with the mode equal to the mean and a standard deviation of $\sigma \approx 0.5$. As time progresses, the skewness increases until the Scaling State is reached, at which point the distribution assumes a lognormal-like shape. In the Scaling State, its distribution closely resembles the Scaling State distribution of an equivalent simple foam studied in microgravity [19].

In Fig. 4.25(b)-(c), we plot the Scaling State distribution for samples with $\phi = 0.30$ and $\phi = 0.25$. For both liquid fractions, we observe that foams with a higher yield stress, $\tau_y \gtrapprox 3\ Pa$, behave similarly to their simple foam counterparts, whereas the samples with a lower yield stress exhibit a more symmetric distribution. We can better quantify the degree of similarity by fitting a bi-lognormal distribution to the data, as we did for simple foams (cf. Section 2.3):

$$\mathcal{F} = w \cdot \mathcal{L}(\rho; m_1, \sigma_1) + (1 - w) \cdot \mathcal{L}(\rho; m_2, \sigma_2) \tag{4.31}$$

where w is the proportion of roaming bubbles in the foam, and $\mathcal{L}$ is a lognormal distribution parameterized as:

$$\mathcal{L}(\rho; m, \sigma) = \frac{1}{\rho\sigma\sqrt{2\pi}} \exp\left[-\frac{\log^2(\rho/m)}{2\sigma^2}\right]. \tag{4.32}$$

Fig. 4.26 shows the resulting fitting parameters, where $m_2 = 1.66$ is fixed, as in the case of simple foams. At $\phi = 0.35$, the differences between the parameters for a simple foam and a foamed emulsion are negligible. As the liquid fraction decreases, at $\phi = 0.30$, we observe a steady increase in both m_1 and w with increasing yield stress, except in the range $1 - 3Pa$, where the parameters are more scattered. The standard deviation of the roaming bubbles remains stable at around $\sigma_1 \approx 0.5$, while the standard deviation of the jammed bubbles behaves similarly, except for two samples with $\tau_y = 5Pa$, where a small number of bubbles much larger than the average also affects R_{32}. Finally, at $\phi = 0.25$, we again observe data spreading for small yield stresses.

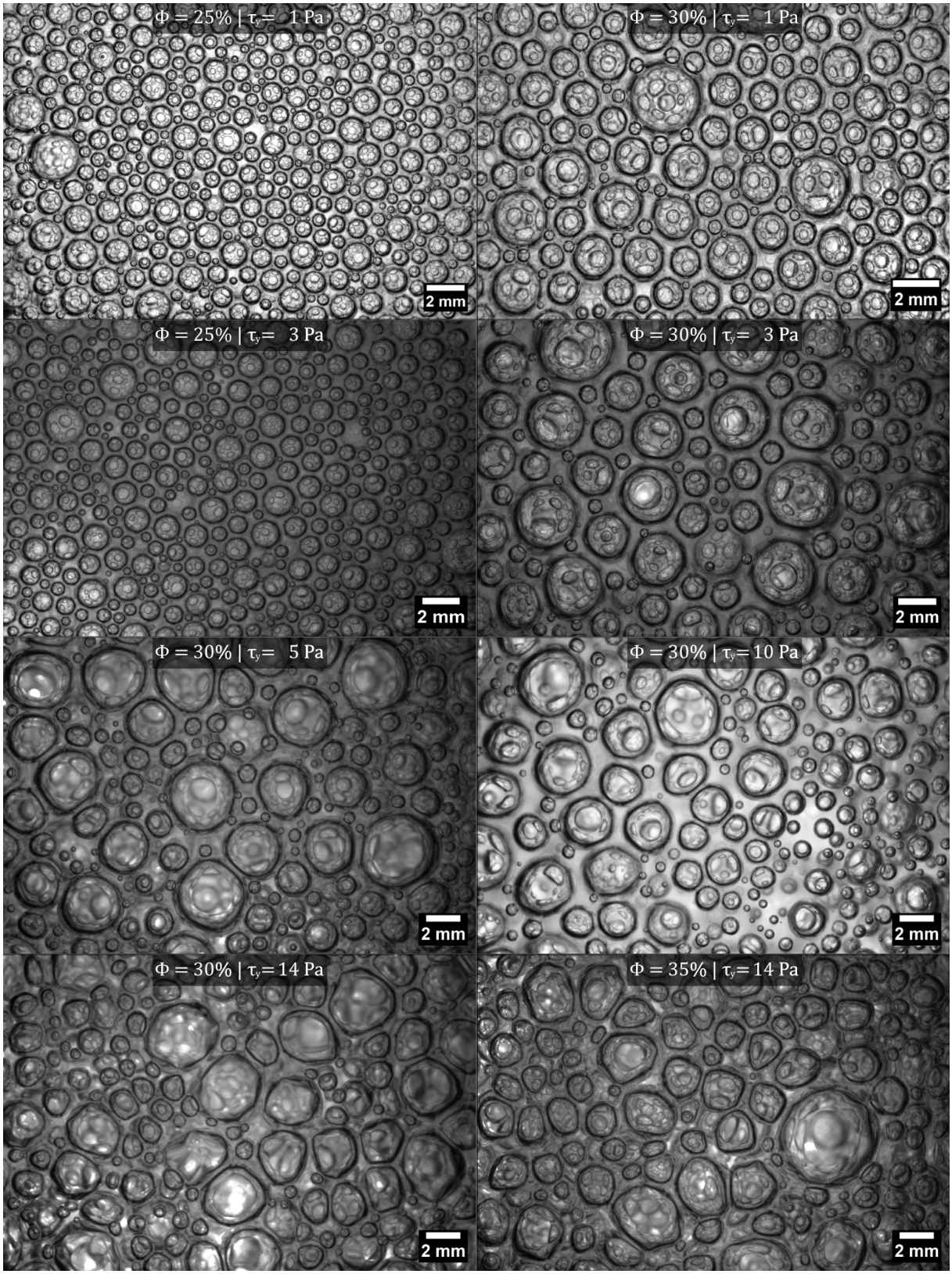

Figure 4.23: Pictures of foamy emulsions with varying yield stress τ_y and liquid fractions ϕ as indicated. The samples are dilutions of emulsion A coarsening in the clinostat (cf. Table 4.1). The pictures show the samples at the end of the corresponding experiment, at a time $2\ 10^5 \leq t < 1\ 10^6 s$ (cf. Fig. 4.27).

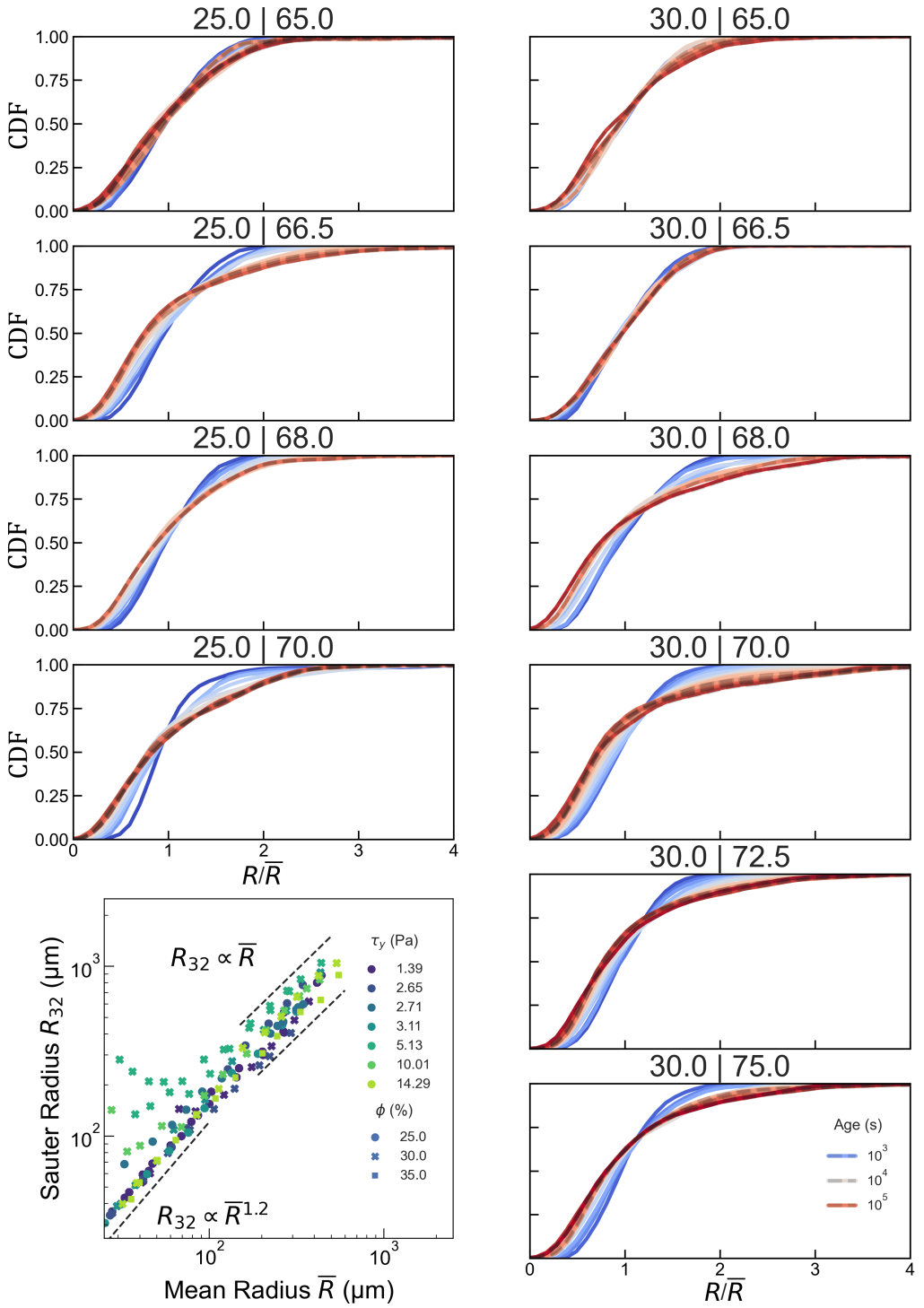

Figure 4.24: Temporal evolution of the cumulative distributions of normalized radius $R/\overline{R}$, for foamy emulsions with liquid fraction and oil fraction $\phi|\varphi$, as indicated. The corresponding yield stress values of the emulsions are given in Table 4.1. We recall that in the clinostat setup the yield stress is constant all along the coarsening. For each sample, the cumulative distributions in the scaling state ($t \geq T_{Scaling}$) are highlighted by transparent dashed black lines. (bottom left corner) mean Sauter radius R_{32} as a function of the mean radius $\overline{R}$, for the same samples. At early times (small $\overline{R}$) the Sauter radius grows at a different speed than the mean radius,while for $t \geq T_{Scaling}$ we observe the scaling $R_{32} \propto \overline{R}$, as expected for a statically self-similar growth. In three experiments at $\phi = 30\%$, a few bubbles much larger than the average are initially present, which affects R_{32} at early times. This difference fades away as time progresses.

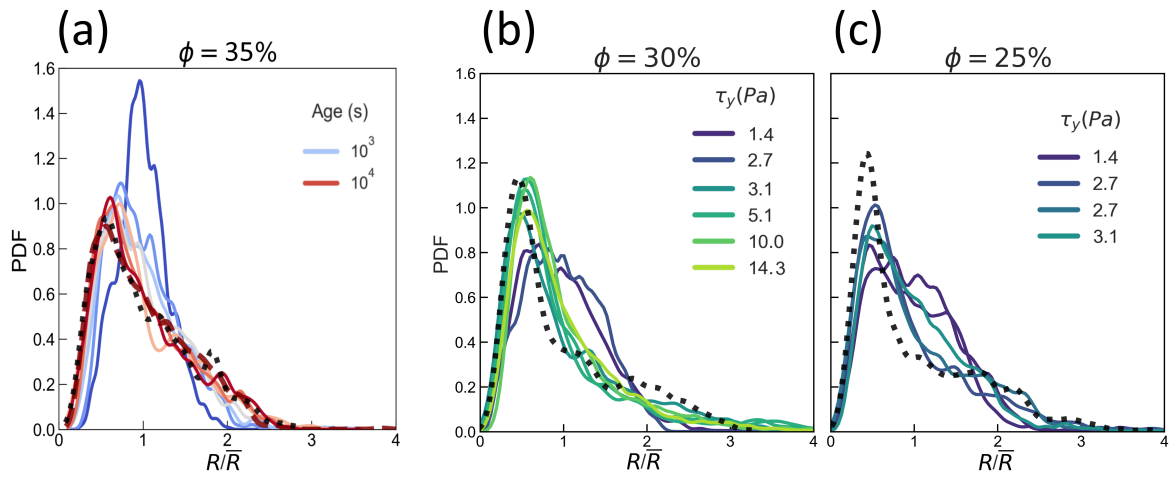

Figure 4.25: Bubble size distributions of coarsening foamy emulsions. (a) Evolution from $t = 180s$ to a final age $t = 9\ 10^5 s$ for a sample with $\phi = 0.35$, $\tau_y = 14.3Pa$. The dark red curve represents the scaling state distribution. (b-c) Scaling state distributions for samples with varying emulsion yield stress as indicated, for respectively $\phi = 0.30$, 0.25. In each plot, the dotted line represents the scaling state distribution of a simple foam of the corresponding liquid fraction [19].

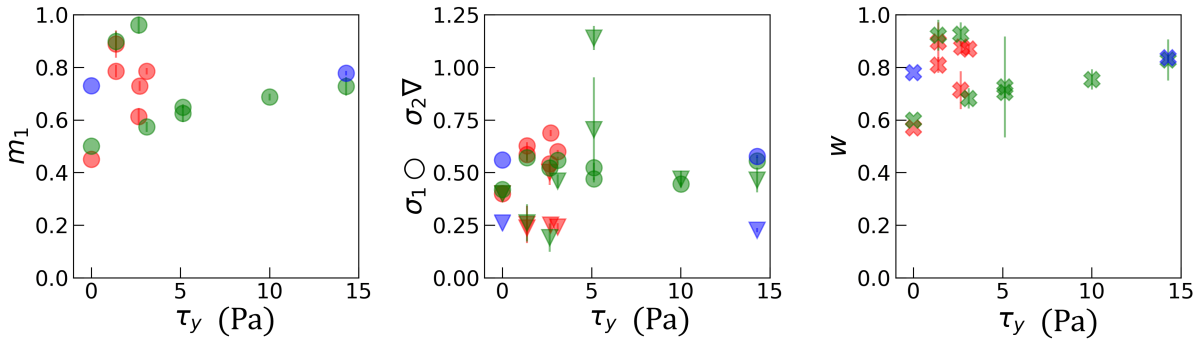

Figure 4.26: Variation of the fitted PDF parameters, as defined in Equation 4.31, with emulsion yield stress τ_y. Points at $\tau_y = 0$ correspond to simple foams [19]. The median of the jammed bubble population is fixed $m_2 = 1.66$. (a) Natural-scale median m_1 of the roaming bubbles. (b) Logarithmic-scale standard deviation : σ_1 for the roaming bubble PDF (disks), σ_2 for the jammed bubble PDF (triangles). (c) Relative weight w of the roaming bubble distribution. The color identifies the liquid fraction: (red) $\phi = 0.25$, (green) $\phi = 0.30$, (blue) $\phi = 0.35$.

Now that we have studied the bubble size distributions and identified the Scaling State we can pass to the growth laws. We show in Fig. 4.27(a) the evolution of the average bubble size for samples in the foam regime. We observe the Sauter radius R_{32} to scale with time similarly for all the samples, regardless of the sample composition. As a comparison, a variation of liquid fraction from 25% to 30% produced a decrease of the coarsening rate by a factor 2 in simple foams [13]. We notice that the average bubble size scales with time unlike simple foams, with an exponent which is in between 1/2 and 1/3. This is consistent with previous experiments in drier foamy emulsions ($0.09 \leq \phi \leq 0.11$) [55]; whose data are also shown in Fig. 4.27(a). The curves seem to share the same slope of our experiments, with a difference in the scaling prefactor coherent with the different liquid fraction and surfactant (sodium dodecyl sulphate $\mathcal{C} = 30g/L$). We fit Eq. 2.1 on each curve for R_{32} in the Scaling State, and we show in Fig. 4.27(b) the fitted exponents α_{R32}, as a function of the emulsion yield stress τ_y. One experiment with low yield stress

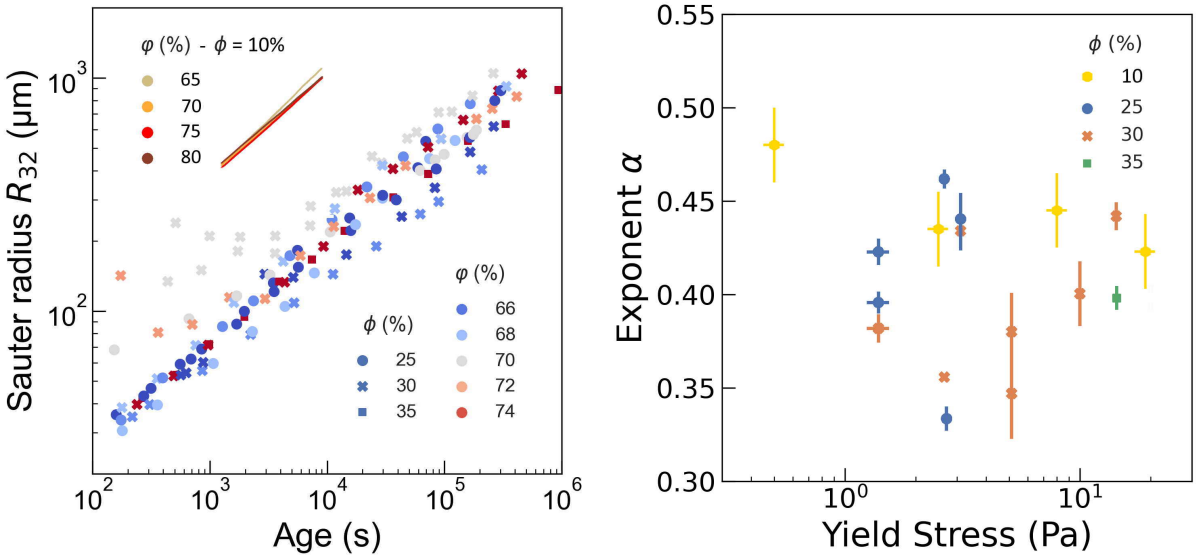

Figure 4.27: (a) Mean Sauter radius R_{32} as a function of foam age, for the same samples as in Fig. 4.24. The lines represent previous data for foamy emulsions with $\phi \approx 10\%$ and φ as indicated [55]. (b) Corresponding effective exponent α as a function of the emulsion yield stress τ_y.

$\tau_y = 0.5Pa$ has an exponent $\alpha \approx 0.475$ coherent with simple foams, otherwise we measure a large variability in $0.33 \leq \alpha \leq 0.46$, not scaling with either ϕ nor τ_y.

4.3.2 Discussion

In analogy to the discussion of coarsening in the bubbly regime in Section 4.2.2, we propose that the growth of the average bubble size is hindered by the plasticity of the continuous phase. We propose a semi-quantitative model, based on the assumption that the control parameter of the damping is the average Bingham capillary number $\overline{Bi} = \frac{\tau_y \overline{R}}{\gamma}$. In the capillary limit ($\overline{Bi} \to 0$), we expect the growth law of simple liquid foams (Eq. 1.38) to be valid. Beyond that, we conjecture the existence of a critical Bingham $Bi^*(\phi)$, such that coarsening arrests as $d\overline{R}/dt \to 0$ in the plastic limit ($\overline{Bi} \to Bi^*$). This behaviour is captured by the simple expression:

$$\overline{R}^2 - \overline{R_0}^2 = \Omega_p \left(1 - \frac{\overline{Bi}}{Bi^*}\right)(t - t_0) \tag{4.33}$$

where Ω_p is the coarsening rate of a simple foam of the same liquid fraction (Eq. 1.39). The factor $\left(1 - \frac{\overline{Bi}}{Bi^*}\right)$ describes the damping effect due to the plasticity of the continuous phase. In the investigated range of bubble size $\overline{R}$ and emulsion yield stress τ_y, we expect all of our samples to start coarsening in the capillary limit, and to undergo later a progressive damping as the bubble size increases. On a short timescale, that wold be indistinguishible from a power law with $\alpha < 0.50$. We fit Eq. 4.33 to each growth curve, using as free parameters the coarsening rate Ω_p and the critical Bingham $Bi^*(\phi)$. Fig. 4.28 shows the good agreement between the fit and the observed growth for each combination of ϕ and φ. The fitted parameters Ω_p and Bi^* are reported in Table 4.4.

The coarsening rate Ω_p does not exhibit a clear evolution with the emulsion yield stress, which is in agreement with our assumption that the plastic effect of the emulsion resides in the damping term. Moreover, we expect Ω_p to follow, at leading order, a dependency with liquid fraction similar to that measured for simple foams with the same surfactant

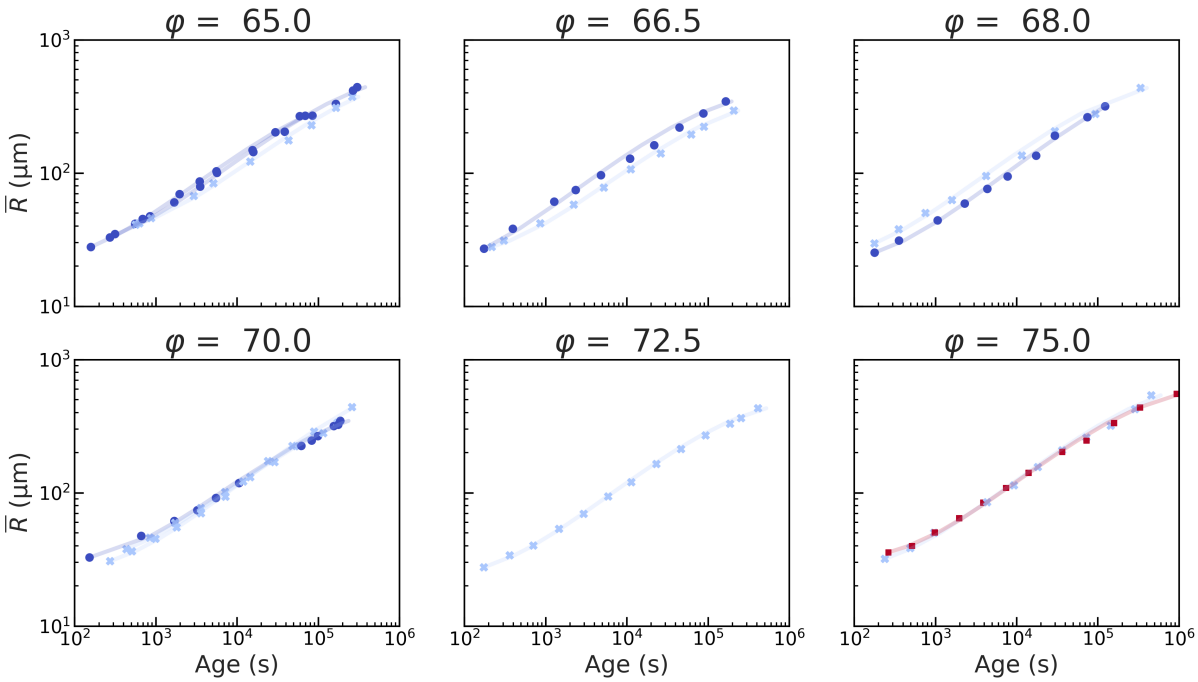

Figure 4.28: Mean radius $\overline{R}$ as a function of foam age, for foamy emulsions with different oil fraction φ as indicated. The liquid fractions ϕ are: (blue disks) 25%, (azure crosses) 30%, (red squares) 35%. The sample parameters are reported in Table 4.1. The lines show Eq. 4.33, with values of the fitted parameters Ω_p, Bi^* reported in Table 4.4.

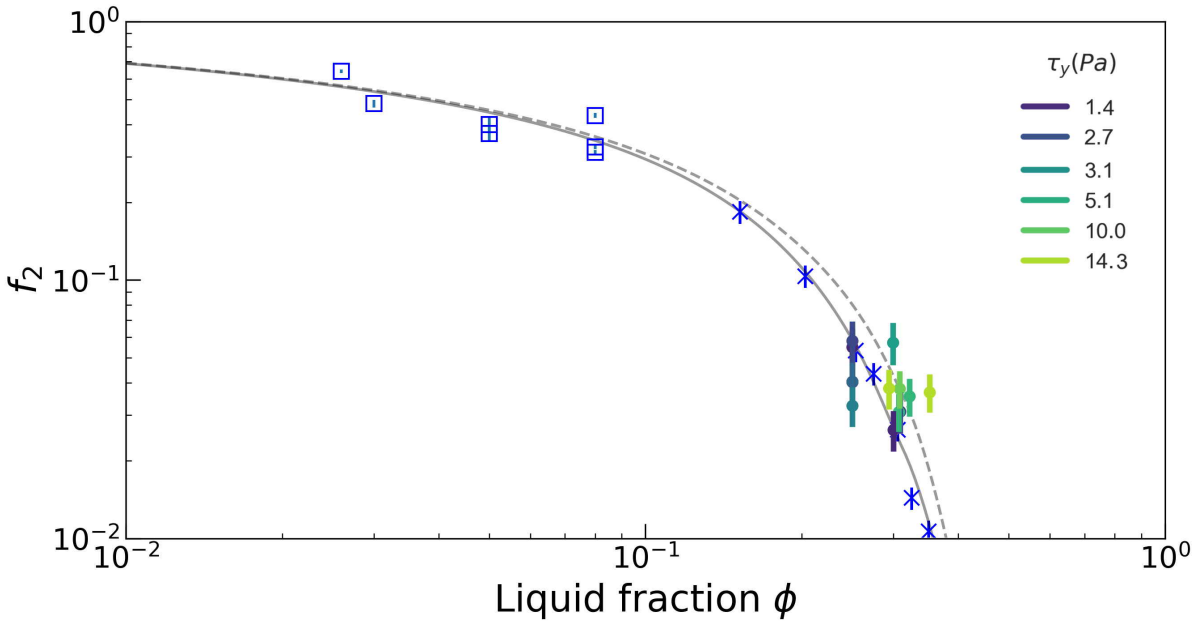

Figure 4.29: Fraction of the bubble area covered by film $f_2(\phi) = \Omega_p(\phi)/\Omega_0$ as a function of the liquid fraction ϕ, for: (disk) foamy emulsions with yield stress τ_y as indicated (from data of Fig. 4.28); (blue squares) simple foams in the dry regime (from data of Fig. 3.14); (blue asterisks) simple foams in the wet regime [13] (cf. Section 2.2). The lines represent $f_2(\phi)$ predicted by Eq. 3.30 for an adhesive foam, with $\phi_{rcp} = 0.31$, $a = 27$ and : (continuous line) $\theta = 3.6°$, (dashed line) $\theta = 4.6°$.

ϕ (%)	25	25	25	25	25	30	30	30	30	30	30	30	35
φ (%)	65	65	66.5	68	70	65	66.5	68	70	70	72.5	75	75
τ_y (Pa)	1.4	1.4	2.65	3.1	2.7	1.4	2.65	3.1	5.1	5.1	10	14	14
Emulsion	A	A	A	A	G	A	A	A	A	A	A	A	A
Ω_p ($\mu m^2/s$)	1.84	2.51	2.65	1.45	1.85	1.20	1.41	2.62	1.62	1.41	1.74	1.74	1.68
Bi^*	0.02	0.02	0.03	0.06	0.04	0.02	0.03	0.05	0.08	0.13	0.16	0.31	0.28

Table 4.4: Coarsening rate Ω_p and critical Bingham number for coarsening arrest Bi^*, for foamy emulsions with varying liquid fraction ϕ, oil fraction φ, emulsion yield stress τ_y, obtained by fitting Eq. 4.33. The emulsion characteristics are detailed in Table 3.1. The uncertainty on the fitted parameters is on the order of 6%.

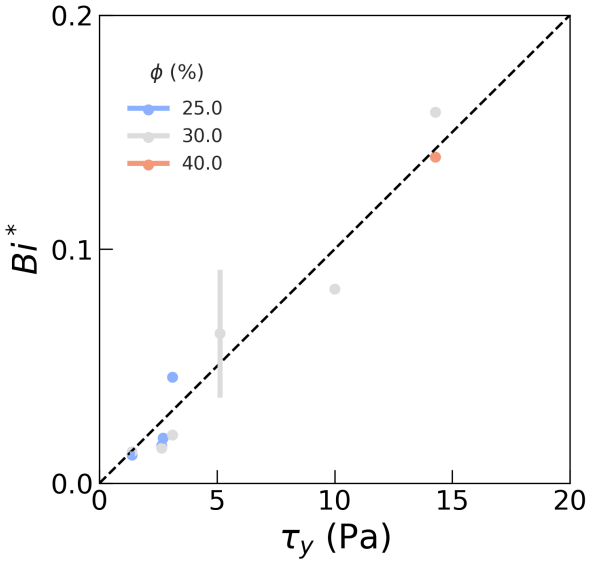

Figure 4.30: Critical Bingham Bi^*, determined by fitting Eq. 4.33 to the measured growth laws shown in Fig. 4.28, as a function of the emulsion yield stress τ_y. The black line is a guide for the eye.

(cf. Section 3.3.1.1). To test this hypothesis, we fit Eqs. 1.39, 3.30 and 3.31 to Ω_p as a function of the liquid fraction ϕ, with Ω_0 as a free parameter. The following parameters are kept fixed to their values corresponding to a simple foam with the same surfactant (cf. Fig. 3.14): the contact angle $\theta = 3.6°$, the random close packing fraction $\phi_{rcp} = 0.31$, the rate of decay of the number of contacts $a = 27$. We get: $\Omega_0 \approx 46 \pm 6 \mu m^2/s$, which is 6 times smaller than the value of Ω_0 determined for a simple foam. To compare these results, we plot the fraction of the bubble area covered by films, $f_2(\phi) = \Omega_p(\phi)/\Omega_0$, as a function of the liquid fraction ϕ for both foamy emulsions and simple foams, in Fig. 4.29. We notice that the dispersion of the data of foamy emulsions is similar to that of simple dry foams. In view of the surfactant concentration $\mathcal{C} = 15cmc$ in foamy emulsions which is larger than the concentration $\mathcal{C} = 4cmc$ in the compared simple foams, we cannot exclude to have a slightly larger film contact angle θ in foamy emulsions. It would increase f_2 in the studied range of $0.25 \leq \phi \leq 0.35$. Indeed, a contact angle $\theta = 4.6°$, within the range of uncertainty on $\theta_{4cmc} = 3.6° \pm 1$ (cf. Section 2.2), better represents the evolution of $f_2(\phi)$ in foamy emulsions.

The fitted critical Bingham numbers Bi^*, reported in Table 4.4, are much smaller than the values of Bi measured for foamy emulsions in the arrested state, where we find $Bi \sim 1$ (cf. Fig. 4.16). Here, in contrast to bubbly emulsions, for a fixed value of τ_y, Bi^* does not seem to evolve with the liquid fraction ϕ. Conversely, for a fixed liquid fraction ϕ, Bi^* increases linearly with τ_y, as shown in Fig. 4.30. This means that the damping factor

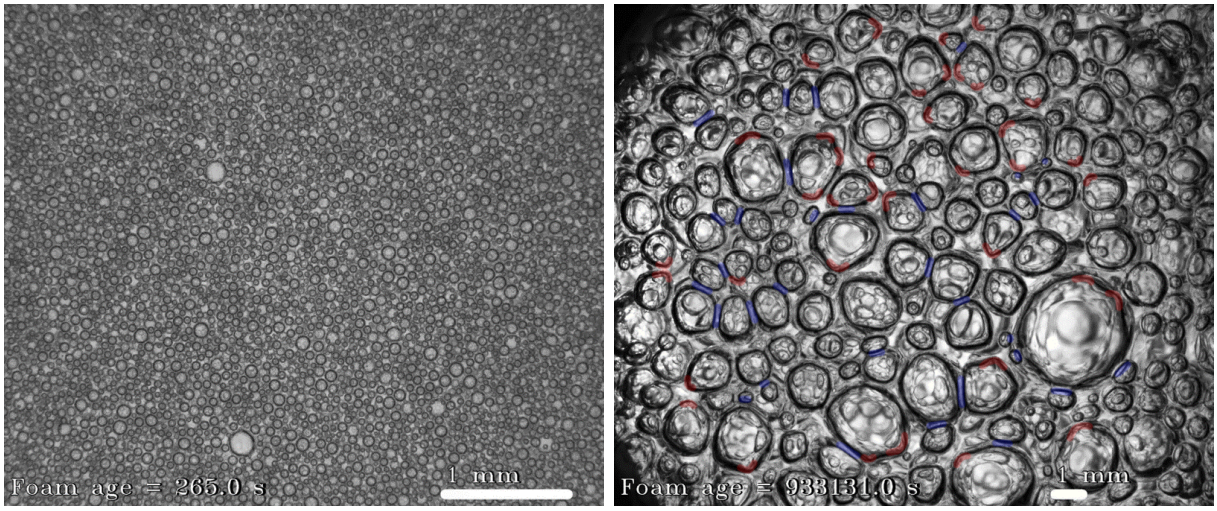

Figure 4.31: Pictures of a coarsening foam with oil volume fraction $\varphi = 0.75$, liquid fraction $\phi = 0.35$, yield stress $\tau_y = 14.3$ Pa, at two ageing times: (left) about 5 min after foaming; (right) about 11 hours later at the the end of coarsening. In the second picture, the bubbles do not minimize their surface, but present 2 unusual features, highlighted in the picture: (red) surface bumps, (blue) flattened surfaces.

in Eq. 4.33 must rather be interpreted as $(1 - \overline{R}/R^*)$, where R^* is some characteristic radius.

By visual inspection of the samples, we notice that the bubble morphology of coarsening foamy emulsions is very different from that of a coarsening simple foam with the same liquid fraction. Over time, the bubbles develop bumps on their contour; this must change the film contact areas between neighbours, which can no longer depend on the capillary-driven osmotic pressure of the foam (cf. Eqs. 1.6 and 1.41). The remanence of the bumps highlights the effect of the plasticity of the continuous phase, but the interplay between the plasticity and the capillarity on the foam microstructure remains challenging to disentangle. Finite elements numerical simulations would be helpful to gain more insight into this question. In the next section we investigate the conditions determining the appearance of bumps and their characteristic size.

4.3.3 Bubble morphology

We focus in this section on the evolution of the bubble morphology in a foamed emulsion undergoing coarsening. Fig. 4.31 shows two pictures of a foamed emulsion, recorded a short time after the foam production and after a prolonged coarsening. Initially, the foam structure looks alike that of a simple foam of the same liquid fraction ($\phi = 0.35$), with almost spherical bubbles and a disordered structure. In contrast, afterwards, coarsened bubbles exhibit a variety of shapes: small bubbles remain spherical or become elongated, whereas large bubbles present a series of *bumps* along their contour. We observe similar behaviour in a wide range of oil and liquid fractions, and search for a quantitative measurement of their presence, using the analysis detailed in Section 4.1.4.3.

4.3.3.1 Modelization

Let us consider an isolated bubble in equilibrium in an elastic medium. From Laplace law, we know that the capillary pressure must balance the pressure difference at the bubble/medium interface. It follows that, if the elastic stresses in the medium are not symmetrically distributed around the bubble, the curvature of the interface will vary

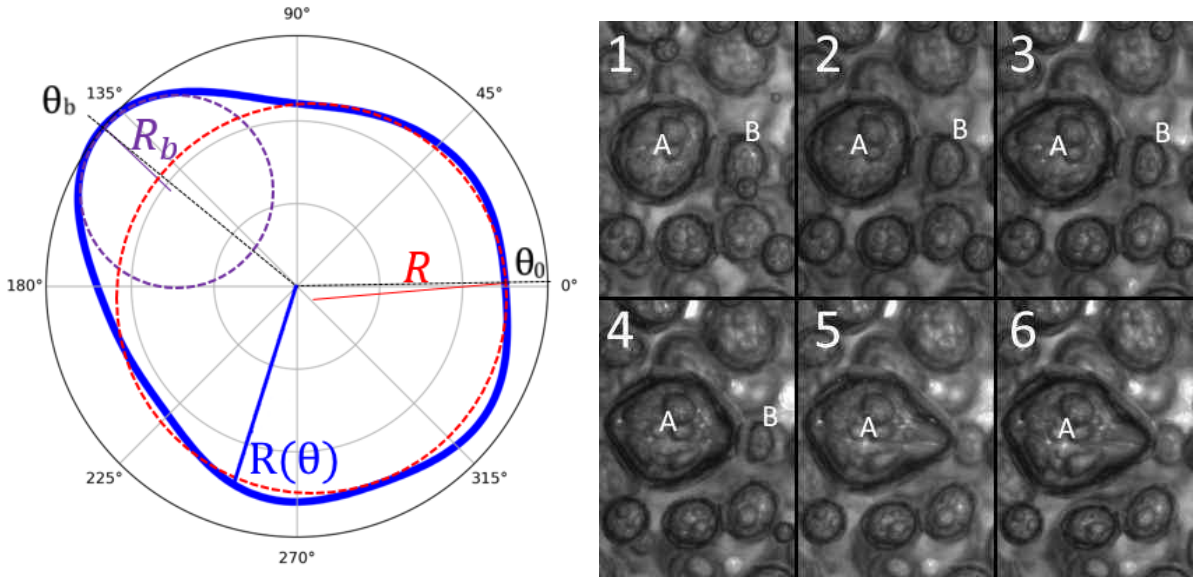

Figure 4.32: (left) Example of the contour profile $R(\theta)$ of a bumpy bubble, shown by the blue thick line, determined as explained in Section 4.1.4. The red dashed circle represents a bubble with the equivalent radius $R = \sqrt{A/\pi}$ where A is the bubble surface area. The radius R_b of the purple dashed circle shows the local interface radius of curvature at the angle θ_b. (right) Successive snapshots showing the evolution of a bump, in a foamed emulsion with liquid fraction $\phi = 0.50$ and oil fraction $\varphi = 0.75$. The pictures are taken with a time delay $\Delta t = 24$ h. From 1 to 3, the big bubble (A) grows slowly at the expense of the small one (B). In 4, the right side of the big bubble (A) starts developing a bump. In 5, the small bubble (B) has disappeared as it has dissolved. In 6, the bubble (A) keeps its shape, unable to relax and minimize its surface energy.

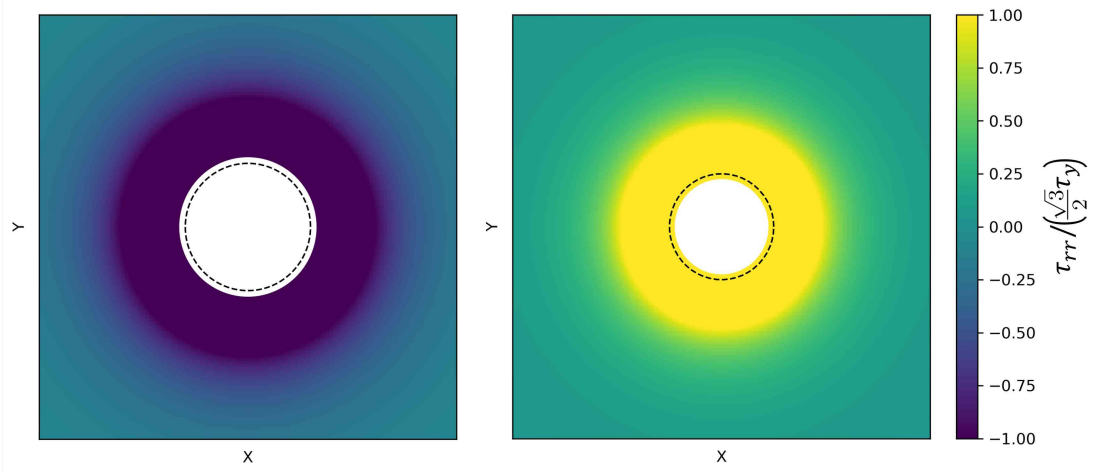

Figure 4.33: Normalized radial component of the deviatoric stress field τ_{rr}, around a ripening bubble, for: (left) bubble growth, the medium is under compression ($\tau_{rr} < 0$); (right) bubble shrinkage, the medium is under traction ($\tau_{rr} > 0$). In the yielded medium we have $\tau_{rr} = \mp\frac{2}{\sqrt{3}}\tau_y$, according to Eq. 1.65 neglecting the viscous effects; in the elastic domain τ_{rr} is evaluated with Eq. 1.66. In both cases, bubble radius has varied from the initial condition (black dashed line) to the final one (white contour) after a relative variation $\Delta R = 10\%$.

and the bubble will loose its sphericity. As discussed in Section 1.4.4, an isolated ripening bubble generates radial isotropic stresses in the surrounding medium, be them compressive stresses in case of growth or traction ones in case of shrinkage, as depicted in Fig. 4.33. In a coarsening foam, each bubble is surrounded by shrinking or growing neighboring bubbles that act as a constellation of elastic stress sources and generate an inhomogeneous stress field around the bubble. As a consequence, the morphology of the bubble changes: a bump appears as a shrinking neighbour pulls on its surface, while a flattened face appears as a growing neighbour pushes on it. In static conditions, such local variations of the stress around the bubble must be balanced by local variations of the interface curvature. The radius of curvature of the interface is expected to vary accordingly. Since the strain field in the vicinity of two evolving bubbles arises from the mutual influence of the pair, the stress field cannot be deduced by the simple superposition of the stresses induced by each bubble separately, we develop here a qualitative argument to relate the morphology of an isolated bubble deformed in an inhomogeneous stress field to the medium Bingham number, using the framework described in Section 1.4.4.

We note $R(\theta)$ the local radius of curvature of a bubble with polar coordinates in the plane of observation. The origin is taken at the center of mass of the bubble, with r the radial distance and θ the polar angle (cf. Fig. 4.32). The stress balance at the bubble interface Eq. 1.74 writes locally:

$$\bar{p} - p(R,\theta) = \frac{2\gamma}{R"(\theta)} - \tau_{rr}(R,\theta) \tag{4.34}$$

We recall that $\bar{p}$ is the gas pressure inside the bubble, $p(R,\theta)$ is the pressure in the (incompressible) medium at the bubble surface and τ_{rr} the radial component of the deviatoric stress tensor $\underline{\underline{\tau}}$. $R"(\theta) \equiv \frac{d^2R(\theta)}{d\theta^2}$ is the radius of curvature of the interface at an angle θ. The pressure $p(R,\theta)$ is given by the radial component of the equation of motion of the medium (Eq. 1.72):

$$p(R,\theta) = p_0 + 2\int_R^\infty \frac{\tau_{rr}(\theta) - \tau_{\theta\theta}(\theta)}{r} dr - \tau_{rr}(R,\theta) \tag{4.35}$$

where p_0 is the pressure at infinite distance from the bubble. By combining Eqs. 4.34 and 4.35, we get:

$$\bar{p} - p_0 = \frac{2\gamma}{R"(\theta)} + 2I(\theta) \tag{4.36}$$

where $I(\theta)$ is the integral shown in Eq. 4.35. Note that the left hand side of the equation is just the difference of pressure between the bubble and the medium at infinite distance Δp, and it must not depend on the angle θ. Thus, Eq. 4.36 sets the equilibrium condition for the local radius of curvature $R"(\theta)$.

Le us now consider a typical bumpy bubble, like in the example of Fig. 4.32(left), with a bump located at the angle θ_b and a radius of curvature $R_b = R"(\theta_b)$. For angles θ_0 far from θ_b, the bubble is almost spherical, with an average radius of curvature $R = R"(\theta_0)$. Since the gas pressure difference $\bar{p} - p_0$ is uniform, Eq. 4.36 must hold for both angles θ_0 and θ_b. Thus we can evaluate the ratio R/R_b as a function of the stress inhomogeneity:

$$\frac{R}{R_b} = 1 + Bi\frac{I(\theta_b) - I(\theta_0)}{\tau_y} \tag{4.37}$$

where the stresses have been normalized by the medium yield stress τ_y, and $Bi = R\tau_y/\gamma$ is the Bingham number of the bubble.

For a bubble with a small Bingham number, $Bi \to 0$ thus $R_b \to R$, we recover the capillary limit, and the bubble must be spherical. As Bi increases, the bubble is more

susceptible to the stresses in the medium, and it can develop bumps. This is consistent with our observation, of a progressive deviation from sphericity as the average bubble size increases, with a stronger effect on the largest bubbles of the foam. As illustrated in Fig. 4.32(right), bumps are observed on growing bubbles in the direction towards a shrinking close neighbour. Considering the stress field generated by an isolated bubble, we can guess the signs of the integrals $I(\theta_0)$ and $I(\theta_b)$. Since plastic effects are dominant (cf. Section 4.2.4.1), we approximate $\tau_{rr} - \tau_{\theta\theta} \approx \pm\frac{\sqrt{3}}{2}\tau_y$ (using Eq. 1.65) as illustrated in Fig. 4.33. Therefore, $I(\theta) < 0$ (resp. $I(\theta) > 0$) around an isolated growing (resp. shrinking) bubble. For a growing bubble with a shrinking neighbour in the direction θ_b, we expect $I(\theta_b)$ to be increased by the traction exerted by the shrinking bubble, while for angles θ_0 far from θ_b, $I(\theta_0) < 0$ is unchanged. As a consequence, we expect $I(\theta_b) - I(\theta_0) > 0$ and a bump to develops with $R_b < R$. On the contrary, for a pair of two growing bubbles, the medium in the contact region is under compression, and more so than in the directions far away from the contact. Thus, for both bubbles, we expect $I(\theta_b) - I(\theta_0) < 0$, and a flattened face at their contact. Note that, for the same reason, the shrinking bubble of the growing/shrinking pair must flatten in the direction towards the growing bubble. These expectations are in qualitative agreement with our observations of a pair of shrinking/growing bubbles (cf. Fig. 4.32(right)), as well as for pairs of growing bubbles (cf. Fig. 4.31(right)).

We expect the liquid fraction of the foamed emulsion to have an impact on the bumps. On one side, the presence of the bubbles weakens the elastic response of the effective medium [41]. Thus, we could expect to see sharper and more numerous bumps for higher liquid fractions ϕ. On the other hand, the bubble ripening is responsible for the elastic stresses in the medium, and for more dilute systems the average inter-bubble distance increases. This would reduce the reciprocal influence among the bubbles. It is not obvious which of the two effects will prevail, and we will try to determine it experimentally.

4.3.3.2 Results

We have studied the bubble morphology in foamed emulsions, either in the foam regime corresponding to liquid fraction $0.25 \leq \phi < \phi^* = 0.39$ or in bubbly dispersions ($\phi^* < \phi \leq 0.90$). The samples composition is provided in Table 4.5. Using Algorithm 4, described in section Section 4.1.4, we identified the appearance of the bumps along the coarsening (in the experiments described in sections Sections 4.2 and 4.3.1), analyzed their number statistics and then their characteristic radius of curvature.

To ensure statistically robust measurements, each coarsening experiment is segmented into sampling time intervals δt, whose duration is defined such that the relative variation of average bubble radius does not exceed 10%. In practice, each time interval encompasses between 2 to 260 analyzed images, with an average of 51 ± 17. The sampling time interval widens as the foam age increases, due to the slowing down of the coarsening rate.

Fig. 4.34 illustrates the temporal evolution of the histograms of bubble counts by radius R, and of bump counts by their radius of curvature R_b, for a foamed emulsion with a large number of counted bubbles and bumps, to get reliable statistical measurements. As time progresses, the average bubble size increases due to coarsening, and the histogram of bubbles shifts accordingly. The increase over time of the total number of counted bubbles arises from the increase of sampling time interval δt. After a transient regime, i.e. lasting about $9\ 10^3 s$, we observe that the bump histogram exhibits a shape similar to that of the bubbles, albeit rescaled for both counts (since there are less bumps than bubbles) and radii (since bump radii are smaller than bubble radii). The peak of the bump histogram systematically corresponds to a fraction of the radius at the bubble peak.

In the following, the objective is to characterize i) the onset of bump appearance by

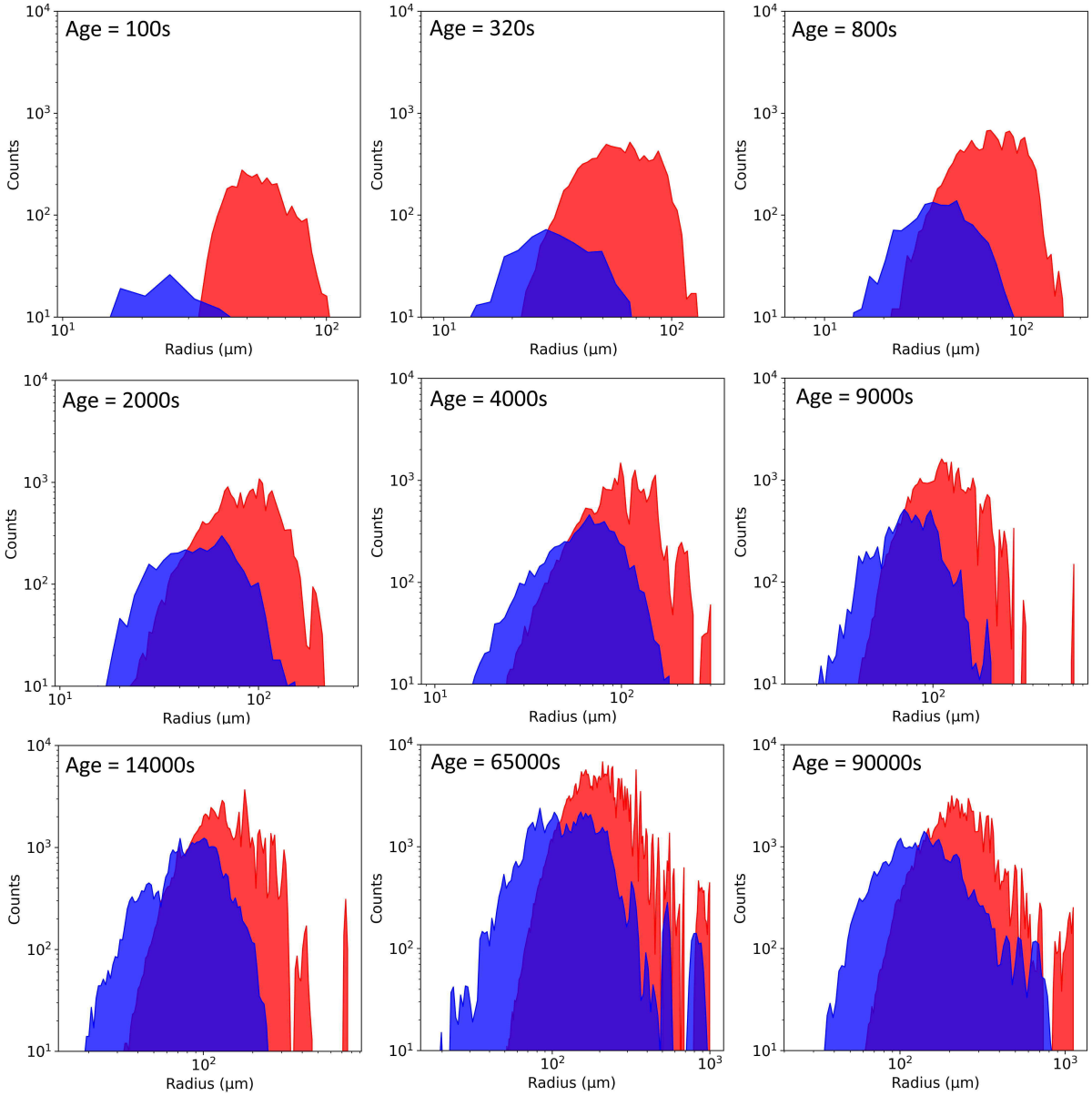

Figure 4.34: Histogram of: (red) bubble counts, (blue) bump counts, where radius refers to its radius of curvature R_b, for a coarsening foamed emulsion with $\phi = 0.50$, $\tau_y = 23$ Pa, at increasing foam ages as indicated. Each histogram represents data over a sampling time interval δt, as defined in the text.

ϕ	0.30	0.35	0.45	0.50	0.58	0.65	0.70	0.80	0.90
φ	0.75	0.75	0.75	0.775	0.725	0.725	0.725	0.725	0.725
τ_y (Pa)	14.3	14.3	14.3	23.0	16.5	16.5	16.5	16.5	16.5
Emulsion	A	A	A	G	B	B	B	B	B
$Bi_b(10^{-3})$	90 ± 5	110 ± 2	81 ± 4	32 ± 5	10 ± 10	10 ± 6	10 ± 10	10 ± 10	17 ± 6
ζ	3.7 ± 0.4	5.0 ± 0.1	4.2 ± 0.3	6.0 ± 0.5	9 ± 1	7.5 ± 0.8	7 ± 1	10 ± 1	10.4 ± 0.8

Table 4.5: Fitted parameters of Fig. 4.35. Critical Bingham for bump appearance Bi_b, rate of bump formation ζ, for foamed emulsions with varying liquid fraction ϕ, oil fraction φ, yield stress τ_y; prepared from different emulsions (cf. Table 3.1). The emulsion is made of silicone oil droplets (350 cP viscosity) in a TTAB (18 g/L) glycerol aqueous mixture (52wt% glycerol). The surface tension of the the TTAB/glycerol aqueous solution at the air-liquid interface is $\gamma = 34.3$ mN/m. See more details in sections 3.1.1 and 3.1.1.2.

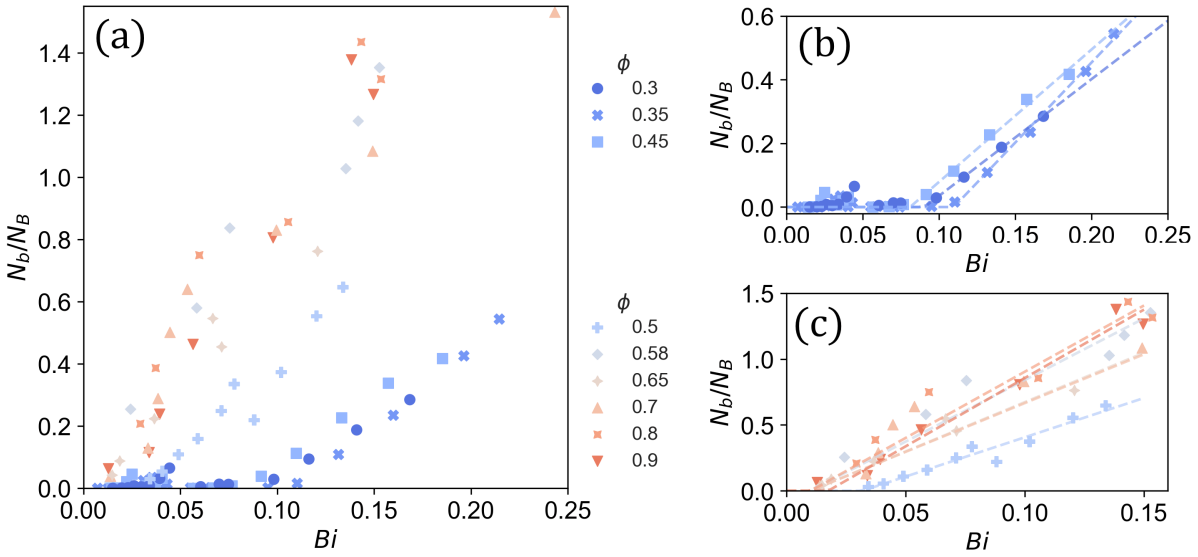

Figure 4.35: (a) Bump-to-bubble ratio N_b/N_B as a function of the average Bingham number Bi, for foamed emulsions with varying liquid fraction ϕ, as reported in the common legend, and emulsion yield stress τ_y (cf. Table 4.5). (b) data in or close to the foam regime; (c) data in the bubbly regime. The lines show Eq. 4.38, with fitted parameters Bi_b and ζ whose values are reported in Table 4.5 and shown in Fig. 4.36.

studying the relative number of bumps with respect to the counted number of bubbles N as a function of the average Bingham number, and ii) the relative size of the average bump radius $\overline{R_b}$ compared to the average bubble radius $\overline{R}$.

Onset of bump appearance

First, we focus on the conditions for the appearance of bumps. Calling N_b the number of bumps and N_B the number of bubbles at a given time, we measure for each sampling time interval δt the bumps-to-bubble ratio N_b/N_B, as a function of the average Bingham number $Bi = \langle R \rangle_{\delta t} \tau_y/\gamma$. As seen in Fig. 4.35(a), remarkably, the bump-to-bubble ratio increases with Bi for all of the liquid fractions. Moreover, N_b/N_B increases faster with Bi for higher values of ϕ. Samples with liquid fractions $0.30 \leq \phi \leq 0.45$, i.e. in or close to the foam regime, follow a similar evolution: $N_b/N_B \approx 0$ for $Bi \lesssim 0.1$, and then N_b/N_B linearly increases with Bi. For samples in the foam regime or with small emulsion yield stress ($\tau_y < 14$ Pa), we do not detect any bumps up to the end of the coarsening. This can be attributed to the fact that Bi remains smaller than $Bi \approx 0.1$. Additionally, for the driest samples with $\phi = 0.25$, bubbles have large contact facets, which make the detection of the bumps uncertain. For liquid fractions in the bubbly regime $\phi > 0.45$, we also observe a linear increase of N_b/N_B with Bi. The simplest equation which represents this behaviour is:

$$\frac{N_b}{N_B}(Bi, \phi) = \zeta(\phi)\ (Bi - Bi_b(\phi))\ \mathcal{H}(Bi - Bi_b(\phi)) \tag{4.38}$$

where $\mathcal{H}$ is the Heaviside step function, Bi_b the critical Bingham number for the appearance of bumps, and ζ the rate of bump formation.We fit Eq. 4.38 to the whole ensemble of data, with ζ and Bi_b as free parameters. Their values are reported in Table 4.5. The good agreement between the fit and the data is shown in Fig. 4.35(b-c).

In Fig. 4.36, we observe that Bi_b varies by one order of magnitude between foams $Bi_b \sim 0.1$ and dilute bubbly liquids $Bi_b \sim 0.01$, with intermediate values for $0.40 \leq \phi \leq$

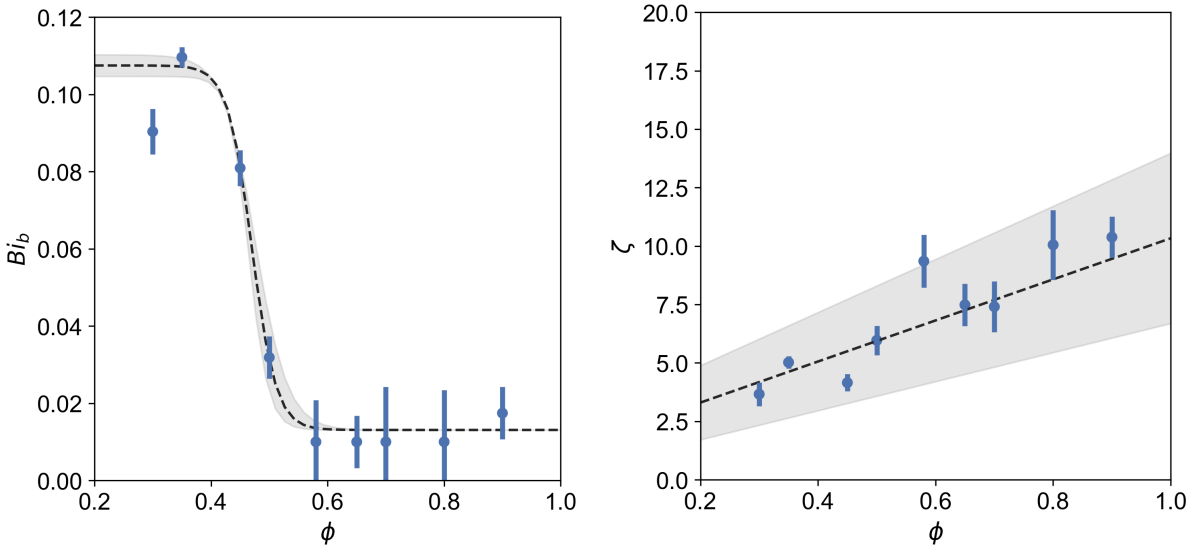

Figure 4.36: Fitted parameters of Eq. 4.38 as a function of the liquid fraction ϕ: (left) critical Bingham for bump appearance Bi_b; (right) rate of bump formation ζ. The lines show respectively: (left) Eq. 4.39, with fixed $Bi_b^{dilute} = (13 \pm 4)\ 10^{-3}$, and fitted parameters $Bi_b^{dry} = (107 \pm 3)\ 10^{-3}$, $\xi = 50 \pm 10$, $\phi_b = 0.470 \pm 0.006$; (right) linear relationship $\zeta(\phi) = \zeta_0 + \zeta_\phi \phi$, with fitted parameters $\zeta_0 = 2 \pm 1$, $\zeta_\phi = 9 \pm 3$. In each graph the colored area corresponds to a variation of $\pm 1\sigma$ in the fitting parameters.

0.50. We can approximate this evolution by a sigmoid function:

$$Bi_b(\phi) = Bi_b^{dilute} + \frac{Bi_b^{dry} - Bi_b^{dilute}}{1 + e^{\xi(\phi - \phi_b)}} \tag{4.39}$$

where $Bi_b^{dilute} = (13 \pm 4)\ 10^{-3}$ is fixed, from the weighted average of Bi_b in the range $\phi > 0.50$, while Bi_b^{dry}, ξ, ϕ_b are free parameters. By fitting Eq. 4.39 to the data, we get the values: $Bi_b^{dry} = (107 \pm 3)\ 10^{-3}$, $\xi = 50 \pm 10$, $\phi_b = 0.470 \pm 0.006$. We find it to describe well the data, as show in Fig. 4.36(left). Previously, we introduced the Bingham number of the effective medium $Bi_{eff}(Bi, \phi)$ (cf. Eq. 4.17), which takes into account the weakening of the effective surrounding medium, due to the presence of the other gas bubbles, which act as capillary inclusions. In the bubbly regime, for $\phi \gtrsim 0.50$, $Bi_{eff}(Bi, \phi)$ is given by the Mori-Tanaka scheme Eq. 1.52; in the foam regime, for $\phi \lesssim \phi_{rcp}$, it follows the semi-empirical relation Eq. 4.19. In the bubbly regime here, since we have small $Bi < 0.02$, the capillarity of the bubbles is strong enough to make them behave as solid inclusions, and the dependency of $Bi_{eff}(Bi, \phi)$ with ϕ is negligible: $Bi_{eff}(Bi, \phi) \approx Bi$. This is consistent with the plateau of $Bi_b(\phi) = Bi_b^{dilute}$ measured for $\phi \geq 0.58$. Thus, we identify Bi_b^{dilute} as the critical Bingham number of the effective medium for bumps appearance:

$$Bi_{eff}(Bi, \phi) \geq Bi_{eff}(Bi_b^{dilute}, \phi \to 1) \approx 0.011 \pm 0.005. \tag{4.40}$$

In drier systems, the threshold for bumps appearance is Bi_b^{dry}; we cannot make a similar comparison with Bi_{eff} in view of the small range of investigated ϕ.

Bump radius of curvature

The second characteristic feature of bumps is their radius of curvature R_b. To investigate it, we study the average values of the bubble radius $\overline{R}$ and the bump radius $\overline{R_b}$, in the range of Bingham numbers where the bump population is statistically relevant, *i.e.* $Bi > Bi_b$. We show the ratio $\overline{R}/\overline{R_b}$ as a function of Bi in Fig. 4.37(left). We focus on the

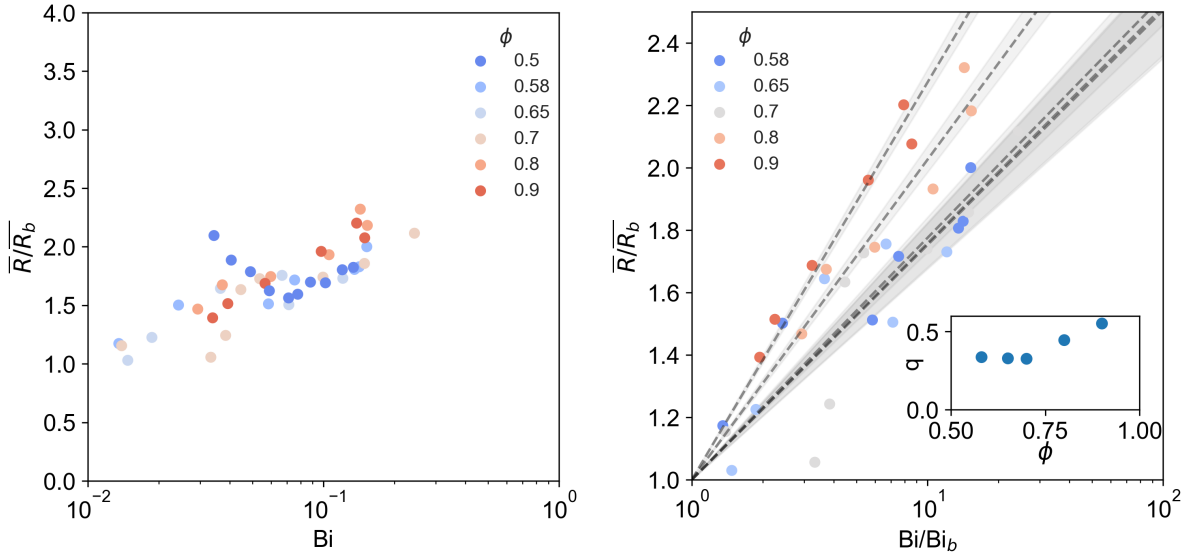

Figure 4.37: Ratio of the average bubble radius to the average bump radius $\overline{R}/\overline{R_b}$, as a function of: (left) the Bingham number Bi; (right) the rescaled Bingham number Bi/Bi_b. The lines show Eq. 4.41 fitted to the data, with $q(\phi)$ values as plotted in the inset. In both plots, only data in the bubbly regime with $Bi \geq Bi_b$ are considered.

bubbly regime $\phi \geq 0.50$, where we have data for large variations of Bi. Qualitatively, we observe that the average bubble radius is bigger than the average radius of curvature of bumps $\overline{R}/\overline{R_b} > 1$, and that this ratio is an increasing function of Bi. This is consistent with our qualitative modelization, captured by Eq. 4.37. In Fig. 4.37(right) we rescale the Bingham number by $Bi_b(\phi)$, and find a logarithmic dependency of $\overline{R}/\overline{R_b}$ with this quantity:

$$\frac{\overline{R}}{\overline{R_b}} = 1 + q(\phi) \ln\left(\frac{Bi}{Bi_b}\right) \tag{4.41}$$

where $q(\phi)$ is a fitting parameter, whose values are shown in the inset of the figure. We find this relation to describe well the data, and the slope q exhibit a tendency to increase with the liquid fraction.

We conclude that bubble dispersions in an emulsion (either dilute or foam regime) develop bumps over time. We propose a model for the bump formation (Eq. 4.37), based on the premise that when bubbles grow or shrink in a medium with inhomogeneous elastic stresses, local variations of the capillary pressure balance the stress variations at the bubble interfaces, which tunes the local bubble curvature. We determine that the presence of bumps in the medium, measured by the ratio N_b/N_B, increases with the average Bingham number Bi. We measure a critical Bingham for the onset of bubble appearance, Bi_b, below which the bubbles do not present bumps. We study the dependency of Bi_b with ϕ, and determine that the presence of bumps is favoured by an increase of the liquid fraction. Then, we analyze the ratio between the average bubble size $\overline{R}$ and the average bump radius of curvature $\overline{R_b}$. $\overline{R}/\overline{R_b}$ measures how strongly the bubbles deviate from sphericity, and we find it to correlate with both Bi and ϕ.

At this level, it would be interesting to identify the link between the damping of the coarsening and the presence of bumps. This would require a more quantitative modelization of the stress field that builds up around neighbouring pairs of shrinking/growing bubbles, beyond the Venerus prediction. To disentangle the large quantity of information emerging from the data and develop a complete model, the simpler case of two ripening bubbles could be studied, through experiments and micromechanical simulations.

4.3.4 Conclusion

In Section 4.3.1, we investigate the coarsening dynamics of foamy emulsions as a function of liquid fraction ϕ and emulsion yield stress τ_y. Similarly to simple liquid foams, we observe that the system reaches a Scaling State during coarsening (cf. Fig. 4.24), with bubble size distributions (cf. Fig. 4.25) well described by bi-lognormal functions (cf. Eq. 4.31). However, the growth laws of the average bubble radius deviate from those characteristics of simple foams: Instead of parabolic laws, we observe $\overline{R} \propto t^{\alpha}$ with an effective coarsening exponent $\alpha \approx 0.4$ independent of ϕ and τ_y.

In Section 4.3.2, we further attempt to extend our phenomenological approach developed for bubbly emulsions and propose to describe the slowing down of the growth by a simple damping factor leading to arrest for a characteristic Bingham number Bi^* (cf. Eq. 4.33). This equation can indeed be closely fitted to the data (cf. Fig. 4.28). It turns out that the coarsening rate Ω_0 decreases with liquid fraction as expected for capillary driven coarsening. But surprisingly, we find $Bi^* \propto \tau_y$, which means that this parameter does not catch the effect of the plasticity. In other words the damping must result from a more subtle interplay between capillary and plastic effects upon the foam microstructure. Indeed, we observe that the bubble morphology is altered along coarsening, and more so as the emulsion yield stress increases : the bubbles surface become deformed by bumps whose remanence can only be due to the emulsion plasticity.

We propose that the bumps observed on the bubble surfaces are shaped by the historical stresses within the medium. In Section 4.3.3, we model their formation as a result of stress field inhomogeneities surrounding the bubbles. First we predict the bump radius of curvature as a function of the Bingham number and the inhomogeneous stress field around an isolated bubble (cf. Eq. 4.37). Then by considering a pair of growing/shrinking bubble, we qualitatively predict bump development when a shrinking bubble is pulling on a bigger neighbour (which sets the emulsion in between under traction). In a pair of two growing bubbles, their contact faces must flatten as the emulsion in between is under compression. Furthermore, we provide a statistical analysis of the bump population as a function of their radius of curvature and show its correlation to the bubble population depending on the Bingham number. We show that the onset of bump appearance is governed by a critical Bingham number Bi_b which decreases as the liquid fraction increases: higher liquid fractions promote bump formation. In the dilute regime, we show that Bi_b is compatible with a single Bingham number of the effective medium $Bi_{b,eff} \approx 0.011$ (Eq. 4.17). Lastly, we investigate the ratio between the average bump curvature and the average bubble curvature, $\overline{R}/\overline{R_b}$. We find that it increases with the Bingham number Bi : liquid fraction promotes the sharpening of the bumps. These findings are consistent with our qualitative model based on stress inhomogeneities.

Further experiments and simulations are needed to complete our understanding of coarsening foamy emulsions. Nevertheless, we have produced an innovative description of this coarsening regime. We compare it with the other studied regimes in the next section, which summarises all of our knowledge of the coarsening behaviour of foamed emulsions.

4.4 Summary: a coarsening diagram

We have studied how the yield stress of the continuous phase impacts the coarsening growth law, the foam dynamics and the bubble morphology. The Bingham number Bi which is the ratio of yield stress to bubble Laplace pressure and the volume fraction of liquid in the foam ϕ are the control parameters of the coarsening. We establish the coarsening diagram (ϕ, Bi) that represents the domains where coarsening is driven by capillarity, or damped by the plasticity or even arrested (cf. Fig. 4.38).

In the region of small Bi, coarsening is driven by capillarity as plastic effects are negligible. We recover the well-known growth laws of the average bubble size, either a cubic law in the bubble regime (Eq. 1.23) or a parabolic law for foams (Eq. 1.38) above the jamming transition at ϕ^* (cf. Section 2.2)

As Bi increases above $Bi_b(\phi)$, the Laplace pressure acting on bubbles can no longer sustain the local plastic stresses. The bubble packing is no more of minimal surface. Instead the local bubble curvature accommodates the stress in the surrounding medium. Stress inhomogeneities induced by the structural disorder triggers the development of bumps at the bubbles surface, which we qualitatively predict (cf. Eq. 4.37). This is characteristic of domain I. We have studied the bumps-to-bubbles number ratio N_b/N_B, and determined that the percentage of bumpy bubbles increases linearly with Bi, with a prefactor ζ which is an increasing function of the liquid fraction ϕ (Eq. 4.38). The average sharpness of the bumps, measured by the ratio between the average bubble size and the average bump radius of curvature $\overline{R}/\overline{R_b}$, follows the same trend (Fig. 4.37). These findings are consistent with our interpretation. In domain I, the coarsening growth law is damped by the plasticity of the continuous phase. We propose a semi-empirical law which predicts coarsening arrest for a critical Bingham number $Bi^*(\phi)$, which encompasses both the capillary regime and domain I (cf. Eqs. 4.15 and 4.16, Fig. 4.12).

In the range $Bi^*(\phi) \leq Bi \leq Bi^{**}(\phi)$ (domain II), coarsening is arrested at the macroscopic scale: the average bubble size does not increase, but small individual bubbles still ripen (cf. Figs. 4.21 and 4.22). The biggest bubbles have an individual Bi large enough to stop their evolution, while middle size bubbles can only collect gas from the smaller ones, and grow until they reach the size of the biggest ones. This kills the bubble regression mechanism and depletes the population of small bubbles, which ripen as long as there are bubbles able to grow. However, this evolution is hardly noticeable at the macroscopic scale. This mechanism is compatible with the narrowing of the bubble size distributions that we observe in this domain (cf. Fig. 4.17). We propose a semi-empirical law, of the average gas volume flux flowing in a bubble with relative size $R/\overline{R}$, predicting the arrest of individual bubble ripening when the average Bingham number reaches a critical value $Bi^{**}(\phi)$ (cf. Eqs. 4.29 and 4.30). For $Bi \geq Bi^{**}(\phi)$, the plasticity of the continuous phase finally overcomes the capillarity, and it stops the evolution of the system.

The decrease of the critical Bingham numbers $Bi^*(\phi)$ and $Bi^{**}(\phi)$ with the liquid fraction observed in the bubbly regime is explained by taking into account the yield stress of the effective medium, which is weakened by the bubbles that act as soft elastic inclusions (cf. Eqs. 1.52 and 1.53). Thus, as their concentration decrease, the effective medium becomes stronger and more capable to resist to Laplace pressure. In the dilute regime ($\phi > 0.50$), intrinsic effective Bingham numbers drive the transitions between domain I and II, or domain II and the plastic domain: $Bi^*_{eff} \approx 0.15 \pm 0.01$, $Bi^{**}_{eff} \approx 0.25 \pm 0.02$. For small $Bi \sim 0.01$, bubbles become undeformable, they do not weaken the response of the effective medium, and $Bi_{eff}(\phi) \approx Bi$ is not dependent on the liquid fraction ϕ. Thus, a constant $Bi_{b,eff} \approx 0.011 \pm 0.005$ is consistent with the observed plateau between the capillary regime and domain I.

In domain III, all the studied foamy emulsions exhibit damped average growth laws,

but our experiments do not allow us to identify the border with the capillary regime. Nevertheless, the coarsening of foamy emulsions can be arrested in a range of Bi compatible with the extrapolation of Bi^* determined for bubbly emulsions. Remarkably, it corresponds to the same intrinsic effective Bingham number $Bi^*_{eff} = 0.15$ (cf. Fig. 4.16). We measure the onset of bump appearance at $Bi = Bi_b^{dry} \approx 0.107 \pm 0.003$, a value much larger than the Bi_b observed in the bubbly regime. As pointed out in a previous study on coarsening foamy emulsions for a given liquid fraction, the bubble dynamics slows down due to the elastoplastic response of the continuous phase [55]. With our wide corpus of data on foamy emulsions with varying liquid fraction ϕ, bubble radius R, and N_y, the maximum strain that the emulsion is able to sustain before yielding, we plan to perform dynamic analysis using our tracking algorithm to test the proposed hypothesis.

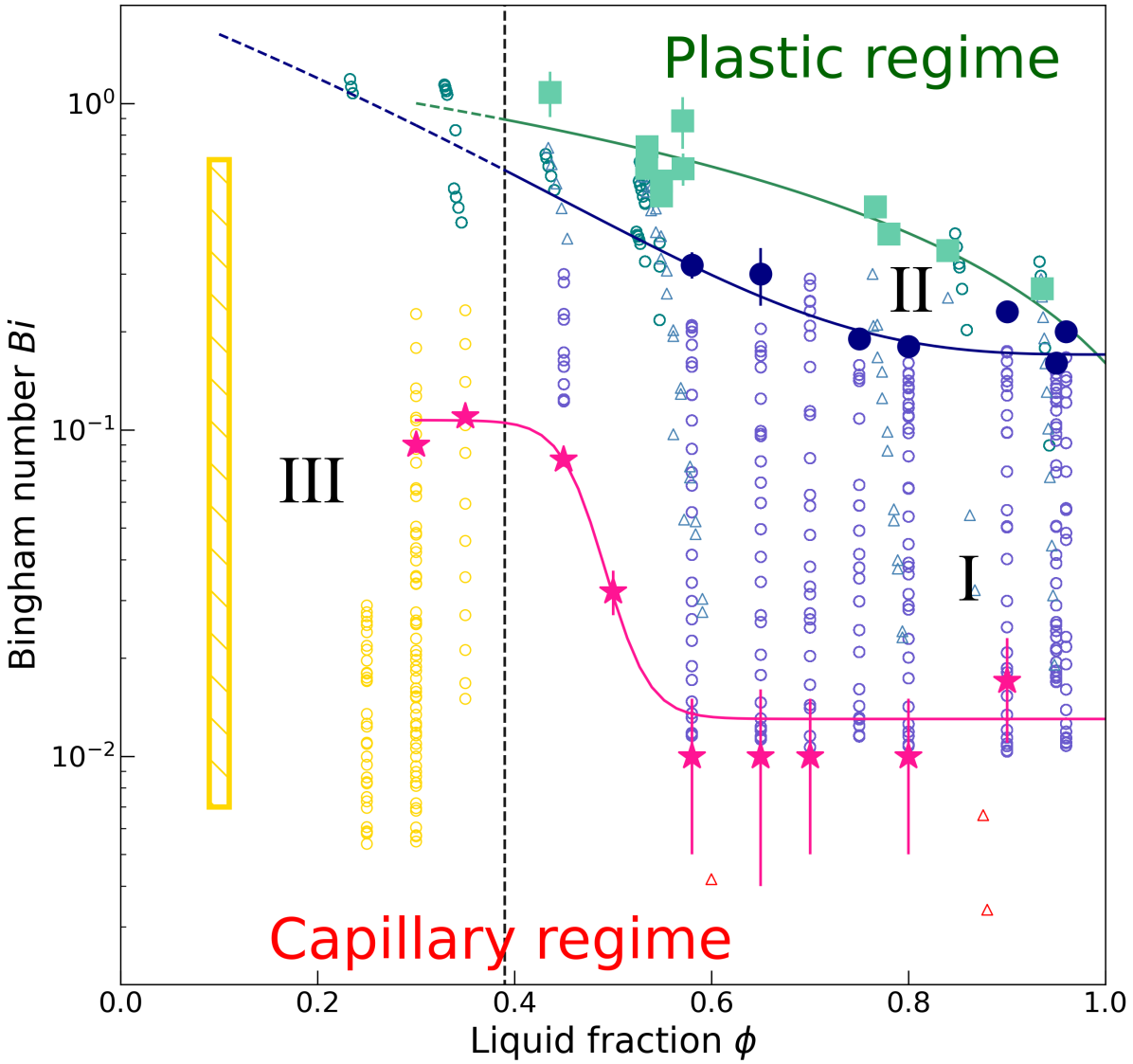

Figure 4.38: Diagram of the different coarsening regimes in the parameter space Bingham number $Bi = \overline{R}\tau_y/\gamma$ vs liquid fraction ϕ. The dashed vertical line identifies the jamming transition $\phi^* = 0.39$ between the foam and bubbly regimes (cf. Section 2.2). The filled symbols and the corresponding continuous lines represents the boundaries between the coarsening regimes: (★) Bi_b, for the appearance of bumps (cf. Fig. 4.36 and eq. 4.39); (●) Bi^*, for the coarsening arrest of the average bubble growth (cf. Fig. 4.13 and eq. 4.16); (■) Bi^{**}, for the ripening arrest of individual bubbles (cf. Fig. 4.22 and eq. 4.30). The dashed blue and green lines are extrapolations of the corresponding equations. In the capillary regime, foamed emulsions coarsen as simple foams or bubbly liquids. In the plastic regime, coarsening is arrested both on average and on the bubble scale. Between the capillary and plastic limits, we identify three regimes: (I) bumpy bubbly emulsions, with damped coarsening (cf. Fig. 4.12); (II) bumpy bubbly emulsions and bumpy foamy emulsions, where the average coarsening is arrested but individual bubbles still ripen (cf. Fig. 4.16); (III) foamy emulsions, with damped coarsening (cf. Fig. 4.28). Empty symbols are experimental observations of (circles) average growth and (triangles) individual ripening. The vertical golden rectangle corresponds to previous measurements [55].

Conclusion and Perspectives

Contributions

In this dissertation we have tackled issues related to bubble coarsening over the full range of bubble concentration, and, thanks to significant image and data processing, we have studied how the presence of a yield stress in the interstitial liquid alters the characteristics of coarsening, in terms of the rate at which this phenomenon occurs, the shape and size distribution of the resulting bubbles, and even the cessation of coarsening.

The major contributions of this thesis can be grouped into the following three points:

1. Growth Laws in simple bubble dispersions from the dry to the dilute regimes: the combination of experiments stabilised against gravity in different ways (microgravity, rotating setup, yield stress of the continuous phase) let us study coarsening across the full range of liquid fractions $0 < \phi < 1$. The study demonstrates that wet foams follow a parabolic coarsening growth law, similar to dry foams, up to the jamming transition $\phi^* = 39\%$, where a sharp transition to a cubic growth law occurs. This critical fraction is higher than the random close packing fraction ϕ_{rcp} of the system, highlighting the influence of weak attractive forces between bubbles at higher liquid fractions. Additionally, we propose a unified expression for the fraction of contact film areas, $f_2(\phi)$, that integrates the effects of both osmotic pressure and adhesion, effectively describing our data from the dry limit to the jamming transition. Beyond the jamming transition, our data allowed for a quantitative comparison of the various models that describe the evolution of the coarsening rate with increasing bubble concentration, and we highlighted that the TM3 model [91] is more suitable than the others for capturing this evolution through the coarsening enhancement factor $f_3(\phi)$.

2. Bubble size distributions: We studied the bubble size distributions of bubbly dispersions over the complete range of liquid fractions. We confirmed that in bubbly liquids the PDF presents a single-peak, resembling a lognormal distribution, and characterized its evolution from the jamming transition to very dilute systems. Below the jamming transition, we observe that wet foams exhibit a hierarchical bubble size distribution characterized by two distinct peaks: one representing the jammed bubbles commonly found in foams, and the other corresponding to the previously overlooked 'roaming bubbles,' which are trapped in the interstices formed by the jammed bubbles. We propose a model for the roaming bubbles, which correctly predicts the transition from jammed to roaming, and it explains the evolution of the roaming bubble peak with the liquid fraction.

3. Coarsening regimes in foamed emulsions: We focused on 3 features: the average growth law, the individual bubble ripening, and the bubble morphology. In the bubbly regime, we determine a unique growth law which predicts the evolution of the average bubble size for any $\phi > \phi^*$, and for any Bi up to coarsening arrest. We give a similar prediction for the individual gas exchange, which we find to continue,

on a small scale, even after the stop of the macroscopic coarsening. We explain the physical process behind the arrest of coarsening, compatibly with the variations observed in the bubble size distributions. We also observe the appearance of surface bumps, due to inhomogeneities in the stresses inside the surrounding medium. We characterize their appearance, their frequency in the bubble population and their characteristic size. This analysis has allowed us to propose, for the first time, a coarsening diagram for foamed yield stress fluids based on the Bingham number Bi (the ratio of yield stress to Laplace pressure) and the liquid fraction ϕ. In this diagram, we identify no fewer than five distinct regimes of coarsening, all identified during this study.

Perspectives

To extend this dissertation, some research works could be developed:

1. In microgravity, we performed experiments with other surfactants than TTAB, some of which involve a higher adhesion than what we studied during this thesis work, to understand the role of the physical-chemistry on the coarsening of wet foams and the jamming transition. The resulting study will be interesting to compare with our modeling for the evolution of the fraction of contact film areas with the foam osmotic pressure and the adhesion forces.

2. The analysis of the foamability of emulsions could be expanded to encompass the foamability of other complex fluids, allowing us to test whether the proposed mechanism applies to them and ultimately develop a comprehensive model capable of describing the foaming properties of various complex fluids.

3. Our analysis on bubble morphology could be enriched by micromecanichal simulations of a system of two or more bubbles ripening in a yield stress fluid. They would refine the simple model proposed and make it quantitative. Thus, it would be possible to characterize the bumps beyond the average behaviour, even at the individual scale.

4. The coarsening diagram could be enriched by considering also bubble dynamics as a feature. With our wide corpus of data on foamy emulsions with varying liquid fraction ϕ, bubble radius R, and N_y -the maximum strain that the emulsion is able to sustain before yielding-, we plan to perform dynamic analysis using our tracking algorithm, to test the hypothesis proposed in previous studies [55] This would allow us, in particular, to highlight in the diagram a boundary beyond which topological rearrangements, typically observed in the capillary regime, disappear past a certain value of the Bingham number.

5. The coarsening diagram is now established for foamed emulsions, or more generally, for yield stress fluids containing constitutive elements whose size is very small compared to the interstices between bubbles. What about foams prepared from different complex fluids that do not meet these assumptions, such as suspensions of non-Brownian particles? For such systems, a similar diagram exists for the drainage phenomenon [115]; could we construct one for coarsening? How different would it be from the one we have established?

Bibliography

1. Cantat, I. *et al. Foams: Structure and Dynamics* ISBN: 9780199662890. https://doi.org/10.1093/acprof:oso/9780199662890.001.0001 (Oxford University Press, July 2013).
2. Drenckhan, W. & Saint-Jalmes, A. The science of foaming. *Adv Colloid Interface Sci* **222.** Drenckhan, Wiebke Saint-Jalmes, Arnaud eng Review Netherlands 2015/06/10 Adv Colloid Interface Sci. 2015 Aug;222:228-59. doi: 10.1016/j.cis.2015.04.001. Epub 2015 Apr 18., 228–59. ISSN: 1873-3727 (Electronic) 0001-8686 (Linking). https://www.ncbi.nlm.nih.gov/pubmed/26056064 (2015).
3. Arzhavitina, A. & Steckel, H. Foams for pharmaceutical and cosmetic application. *Int J Pharm* **394,** 1–17. ISSN: 1873-3476 (Electronic)0378-5173 (Linking). https://www.ncbi.nlm.nih.gov/pubmed/20434532 (2010).
4. Tcholakova, S. & Petkova, B. Bubble size and foamability: Role of surfactants and hydrodynamic conditions. *Current Opinion in Colloid & Interface Science* **72.** ISSN: 13590294 (2024).
5. Saint-Jalmes, A., Vera, M. U. & Durian, D. J. Uniform foam production by turbulent mixing: new results on free drainage vs. liquid content. *The European Physical Journal B* **12,** 67–73. ISSN: 1434-6028. https://dx.doi.org/10.1007/s100510050978 (1999).
6. Politova, N., Tcholakova, S., Valkova, Z., Golemanov, K. & Denkov, N. D. Self-regulation of foam volume and bubble size during foaming via shear mixing. *Colloids and Surfaces A: Physicochemical and Engineering Aspects* **539,** 18–28. ISSN: 09277757 (2018).
7. Gaillard, T. *et al.* Controlled foam generation using cyclic diphasic flows through a constriction. *International Journal of Multiphase Flow* **96,** 173–187. ISSN: 03019322 (2017).
8. Kraynik, A. M., Reinelt, D. A. & van Swol, F. Structure of random foam. *Phys Rev Lett* **93,** 208301. ISSN: 0031-9007 (Print) 0031-9007 (Linking). https://www.ncbi.nlm.nih.gov/pubmed/15600978 (2004).
9. Drenckhan, W. & Hutzler, S. Structure and energy of liquid foams. *Advances in Colloid and Interface Science* **224,** 1–16. ISSN: 0001-8686. https://dx.doi.org/10.1016/j.cis.2015.05.004 (2015).
10. Farr, R. S. & Groot, R. D. Close packing density of polydisperse hard spheres. *The Journal of Chemical Physics* **131,** 244104. ISSN: 0021-9606. https://dx.doi.org/10.1063/1.3276799 (2009).
11. Hohler, R., Sang, Y. Y. C., Lorenceau, E. & Cohen-Addad, S. Osmotic Pressure and Structures of Monodisperse Ordered Foam. *Langmuir* **24** (2008).
12. Maestro, A., Drenckhan, W., Rio, E. & Höhler, R. Liquid dispersions under gravity: volume fraction profile and osmotic pressure. *Soft Matter* **9,** 2531–2540 (2013).

13. Pasquet, M. *et al.* Coarsening transitions of wet liquid foams under microgravity conditions. *Soft Matter* **19.** Pasquet, Marina Galvani, Nicolo Requier, Alice Cohen-Addad, Sylvie Hohler, Reinhard Pitois, Olivier Rio, Emmanuelle Salonen, Anniina Langevin, Dominique eng England 2023/08/08 Soft Matter. 2023 Aug 23;19(33):6267-6279. doi: 10.1039/d3sm00535f., 6267–6279. ISSN: 1744-6848 (Electronic) 1744-683X (Linking). https://www.ncbi.nlm.nih.gov/pubmed/37551883 (2023).

14. Höhler, R., Seknagi, J. & Kraynik, A. Capillary pressure, osmotic pressure and bubble contact areas in foams. *Soft Matter* **17,** 6995–7003 (2021).

15. Langevin, D. Recent Advances on Emulsion and Foam Stability. *Langmuir* **39.** PMID: 36880680, 3821–3828. eprint: https://doi.org/10.1021/acs.langmuir.2c03423. https://doi.org/10.1021/acs.langmuir.2c03423 (2023).

16. Bergeron, V. Disjoining Pressures and Film Stability of Alkyltrimethylammonium Bromide Foam Films. *Langmuir* **13.** doi: 10.1021/la970004q, 3474–3482. ISSN: 0743-7463. https://doi.org/10.1021/la970004q (1997).

17. Rouyer, F., Pitois, O., Lorenceau, E. & Louvet, N. Permeability of a bubble assembly: From the very dry to the wet limit. *PHYSICS OF FLUIDS* **22,** 043302. https://doi.org/10.1063/1.3364038 (2010).

18. Voorhees, P. W. Ostwald ripening of two-phase mixtures. *Annual Review of Materials Science* **22,** 197–215 (1992).

19. Galvani, N. *et al.* Hierarchical bubble size distributions in coarsening wet liquid foams. *Proc Natl Acad Sci U S A* **120,** e2306551120. ISSN: 1091-6490 (Electronic) 0027-8424 (Print) 0027-8424 (Linking). https://www.ncbi.nlm.nih.gov/pubmed/37708201 (2023).

20. Lifshitz, I. M. & Slyozov, V. V. The kinetics of precipitation from supersaturated solid solutions. *Journal of physics and chemistry of solids* **19,** 35–50 (1961).

21. Wagner, C. Theorie der alterung von niederschlägen durch umlösen (Ostwald-reifung). *Zeitschrift für Elektrochemie, Berichte der Bunsengesellschaft für physikalische Chemie* **65,** 581–591 (1961).

22. Pitois, O. in *Foam Engineering: Fundamentals and Applications* (ed Stevenson, P.) 59 (Wiley, Feb. 2012). https://hal.science/hal-00790460.

23. Michelin, S., Guérin, E. & Lauga, E. Collective dissolution of microbubbles. *Physical Review Fluids* **3.** ISSN: 2469-990X (2018).

24. Ardell, A. J. The effect of volume fraction on particle coarsening: theoretical considerations. *Acta Metallurgica* **20** (1972).

25. Baldan, A. Review Progress in Ostwald ripening theories and t. *JOURNAL OF MATERIALS SCIENCE* **37** (2002).

26. Mahalingam, K., Gu, B. P. & Liedl, G. J. Coarsening of δ'(Al, Li) precipitates binary Al-Li alloys. *Acta Metallurgica* **35,** 16 (1987).

27. Lemlich, R. Prediction of changes in bubble size distribution due to interbubble gas diffusion in foam. *Ind. Eng. Chem. Fundam.* **17** (1978).

28. Princen, H., Zia, I. & Mason, S. Measurement of interfacial tension from the shape of a rotating drop. *Journal of Colloid and Interface Science* **23,** 99–107. ISSN: 0021-9797. https://www.sciencedirect.com/science/article/pii/0021979767900902 (1967).

29. Cohen-Addad, S., Höhler, R. & Pitois, O. Flow in Foams and Flowing Foams. *Annual Review of Fluid Mechanics* **45,** 241–267. ISSN: 0066-4189 1545-4479 (2013).

30. Cohen-Addad, S. & Höhler, R. Rheology of foams and highly concentrated emulsions. *Current Opinion in Colloid & Interface Science* **19,** 536–548 (2014).

31. Pal, R. New Generalized Viscosity Model for Non Colloidal Suspensions and Emulsions. *Fluids* **5.** ISSN: 2311-5521 (2020).

32. Krieger, I. M. & Dougherty, T. J. A Mechanism for Non-Newtonian Flow in Suspensions of Rigid Spheres. *Transactions of The Society of Rheology* **3,** 137–152. ISSN: 0038-0032. eprint: https://pubs.aip.org/sor/jor/article-pdf/3/1/137/12574516/1_548848.pdf. https://doi.org/10.1122/1.548848 (Mar. 1959).

33. Pal, R. Novel viscosity equations for emulsions of two immiscible liquids. *Journal of Rheology* **45,** 509–520. ISSN: 0148-6055. eprint: https://pubs.aip.org/sor/jor/article-pdf/45/2/509/12674617/509_1_online.pdf. https://doi.org/10.1122/1.1339249 (Mar. 2001).

34. Ovarlez, G. *et al.* Wide-gap Couette flows of dense emulsions: Local concentration measurements, and comparison between macroscopic and local constitutive law measurements through magnetic resonance imaging. *Physical Review E* **78,** 036307 (2008).

35. Tcholakova, S., Denkov, N. D., Golemanov, K., Ananthapadmanabhan, K. P. & Lips, A. Theoretical model of viscous friction inside steadily sheared foams and concentrated emulsions. *Phys Rev E Stat Nonlin Soft Matter Phys* **78,** 011405. ISSN: 1539-3755 (Print) 1539-3755 (Linking). https://www.ncbi.nlm.nih.gov/pubmed/18763954 (2008).

36. Gorlier, F., Khidas, Y. & Pitois, O. Yielding of complex liquid foams. *Journal of Rheology* **61,** 919–930. ISSN: 0148-6055 1520-8516 (2017).

37. Salonen, A., Lhermerout, R., Rio, E., Langevin, D. & Saint-Jalmes, A. Dual gas and oil dispersions in water: production and stability of foamulsion. *Soft Matter* **8,** 699–706. ISSN: 1744-683X 1744-6848 (2012).

38. Guidolin, C., Jiang, N., Langevin, D. & Salonen, A. One-step generation and characterisation of aerated emulsions using laser diffraction. *Colloids and Surfaces A: Physicochemical and Engineering Aspects* (2022).

39. Ducloué, L., Pitois, O., Goyon, J., Chateau, X. & Ovarlez, G. Rheological behaviour of suspensions of bubbles in yield stress fluids. *Journal of Non-Newtonian Fluid Mechanics* **215,** 31–39. ISSN: 03770257 (2015).

40. Feneuil, B., Roussel, N. & Pitois, O. Yield stress of aerated cement paste. *Cement and Concrete Research* **127.** ISSN: 00088846 (2020).

41. Ducloue, L., Pitois, O., Goyon, J., Chateau, X. & Ovarlez, G. Coupling of elasticity to capillarity in soft aerated materials. *Soft Matter* **10.** Ducloue, Lucie Pitois, Olivier Goyon, Julie Chateau, Xavier Ovarlez, Guillaume eng Research Support, Non-U.S. Gov't England 2014/06/07 Soft Matter. 2014 Jul 28;10(28):5093-8. doi: 10.1039/c4sm00200h., 5093–8. ISSN: 1744-6848 (Electronic) 1744-683X (Linking). https://www.ncbi.nlm.nih.gov/pubmed/24905452 (2014).

42. Tsamopoulos, J., Dimakopoulos, Y., Chatzidai, N., Karapetsas, G. & Pavlidis, M. Steady bubble rise and deformation in Newtonian and viscoplastic fluids and conditions for bubble entrapment. *Journal of Fluid Mechanics* **601,** 123–164 (2008).

43. Deoclecio, L. H. P., Soares, E. J., Deka, H. & Pierson, J.-L. Bubble entrapment condition in Bingham materials. *Journal of Non-Newtonian Fluid Mechanics* **295.** ISSN: 03770257 (2021).

44. Goyon, J., Bertrand, F., Pitois, O. & Ovarlez, G. Shear induced drainage in foamy yield-stress fluids. *Phys Rev Lett* **104.** Goyon, J Bertrand, F Pitois, O Ovarlez, G eng 2010/04/07 Phys Rev Lett. 2010 Mar 26;104(12):128301. doi: 10.1103/PhysRevLett.104.128301. Epub 2010 Mar 22., 128301. ISSN: 1079-7114 (Electronic) 0031-9007 (Linking). https://www.ncbi.nlm.nih.gov/pubmed/20366567 (2010).

45. Feneuil, B. *et al.* Stability criterion for fresh cement foams. *Cement and Concrete Research* **125.** ISSN: 00088846 (2019).

46. Venerus, D. C. Diffusion-induced bubble growth and collapse in yield stress fluids. *Journal of Non-Newtonian Fluid Mechanics* **215,** 53–59. ISSN: 0377-0257. https://www.sciencedirect.com/science/article/pii/S037702571400202X (2015).

47. Saint-Michel, B. & Garbin, V. Bubble dynamics for broadband microrheology of complex fluids. *Current Opinion in Colloid & Interface Science* **50.** ISSN: 13590294 (2020).

48. W., M. C. *Rheology Principles* https://cir.nii.ac.jp/crid/1573387449190639744 (VCH Publishes, 1994).

49. Mullins, W. The statistical self-similarity hypothesis in grain growth and particle coarsening. *Journal of Applied Physics* **59,** 1341–1349 (1986).

50. Saint-Jalmes, A. Physical chemistry in foam drainage and coarsening. *Soft Matter* **2.** Saint-Jalmes, Arnaud eng Review England 2006/09/19 Soft Matter. 2006 Sep 19;2(10):836-849. doi: 10.1039/b606780h., 836–849. ISSN: 1744-6848 (Electronic) 1744-683X (Linking). https://www.ncbi.nlm.nih.gov/pubmed/32680275 (2006).

51. Briceno-Ahumada, Z. & Langevin, D. On the influence of surfactant on the coarsening of aqueous foams. *Adv Colloid Interface Sci* **244.** Briceno-Ahumada, Zenaida Langevin, Dominique eng Review Netherlands 2015/12/22 Adv Colloid Interface Sci. 2017 Jun;244:124-131. doi: 10.1016/j.cis.2015.11.005. Epub 2015 Nov 26., 124–131. ISSN: 1873-3727 (Electronic) 0001-8686 (Linking). https://www.ncbi.nlm.nih.gov/pubmed/26687804 (2017).

52. Isert, N., Maret, G. & Aegerter, C. M. Coarsening dynamics of three-dimensional levitated foams: From wet to dry. *Eur Phys J E Soft Matter* **36.** Isert, N Maret, G Aegerter, C M eng Research Support, Non-U.S. Gov't France 2013/10/19 Eur Phys J E Soft Matter. 2013 Oct;36(10):116. doi: 10.1140/epje/i2013-13116-x. Epub 2013 Oct 17., 116. ISSN: 1292-895X (Electronic) 1292-8941 (Linking). https://www.ncbi.nlm.nih.gov/pubmed/24136181 (2013).

53. Bibette, J., Calderon, F. L. & Poulin, P. Emulsions: basic principles. *Reports on Progress in Physics* **62,** 969–1033. ISSN: 0034-4885. https://dx.doi.org/10.1088/0034-4885/62/6/203 (1999).

54. Fuhrmann, P. L. *et al.* Rheological behaviour of attractive emulsions differing in droplet-droplet interaction strength. *Journal of colloid and interface science* **607,** 389–400. ISSN: 0021-9797 (2022).

55. Guidolin, C., Rio, E., Cerbino, R., Giavazzi, F. & Salonen, A. Matrix Viscoelasticity Decouples Bubble Growth and Mobility in Coarsening Foams. *Physical Review Letters* **133.** ISSN: 0031-9007 1079-7114 (2024).

56. Deleurence, R., Freymond, C., Saison, T., Lequeux, F. & Monteux, C. Foamability and stability of foams obtained with silica/PEI gels. *Colloids and Surfaces A: Physicochemical and Engineering Aspects* **534.** A Collection of Papers Presented at the 11th Eufoam Conference, Dublin, Ireland, 3-6 July, 2016, 2–7. ISSN: 0927-7757. https://www.sciencedirect.com/science/article/pii/S0927775717305551 (2017).

57. Hilgenfeldt, S., Koehler, S. A. & Stone, H. A. Dynamics of Coarsening Foams: Accelerated and Self-Limiting Drainage. *Physical Review Letters* **86,** 4704–4707. ISSN: 0031-9007 (2001).

58. Born, P. *et al.* Soft matter dynamics: A versatile microgravity platform to study dynamics in soft matter. *Rev Sci Instrum* **92,** 124503 (2021).

59. Pasquet, M. *et al.* Aqueous foams in microgravity, measuring bubble sizes. en. *Comptes Rendus. Mécanique* **351,** 139–161 (2023).

60. Cohen-Addad, S., Hohler, R. & Khidas, Y. Origin of the slow linear viscoelastic response of aqueous foams. *Phys Rev Lett* **93.** Cohen-Addad, Sylvie Hohler, Reinhard Khidas, Yacine eng 2004/08/25 Phys Rev Lett. 2004 Jul 9;93(2):028302. doi: 10.1103/PhysRevLett.93.028302. Epub 2004 Jul 8., 028302. ISSN: 0031-9007 (Print) 0031-9007 (Linking). https://www.ncbi.nlm.nih.gov/pubmed/15323957 (2004).

61. Van der Net, A., Blondel, L., Saugey, A. & Drenckhan, W. Simulating and interpretating images of foams with computational ray-tracing techniques. *Colloids and Surfaces A: Physicochemical and Engineering Aspects* **309,** 159–176. ISSN: 09277757 (2007).

62. Hoballah, H., Höhler, R. & Cohen-Addad, S. Time evolution of the elastic properties of aqueous foam. *Journal de Physique II* **7,** 1215–1224 (1997).

63. Ariyaprakai, S. & Dungan, S. R. Influence of surfactant structure on the contribution of micelles to Ostwald ripening in oil-in-water emulsions. *Journal of colloid and interface science* **343,** 102–108 (2010).

64. Ferrell, R. T. & Himmelblau, D. M. Diffusion coefficients of nitrogen and oxygen in water. *Journal of chemical and engineering data* **12,** 111–115 (1967).

65. Sander, R. Compilation of Henry's law constants (version 5.0.0) for water as solvent. *Atmospheric Chemistry and Physics* **23,** 10901–12440. https://acp.copernicus.org/articles/23/10901/2023/ (2023).

66. Brailsford, A. & Wynblatt, P. The dependence of ostwald ripening kinetics on particle volume fraction. *Acta Metallurgica* **27,** 489–497. ISSN: 0001-6160. https://www.sciencedirect.com/science/article/pii/0001616079900415 (1979).

67. Davies, C. K. L., Nash, P. & Stevens, R. N. The effect of volume fraction of precipitate on ostwald ripening. *Acta Metallurgica* **28,** 10 (1980).

68. Voorhees, P. & Glicksman, M. Solution to the multi-particle diffusion problem with applications to ostwald ripening—II. Computer simulations. *Acta Metallurgica* **32,** 2013–2030. ISSN: 0001-6160 (1984).

69. Forel, E. *et al.* The surface tells it all: relationship between volume and surface fraction of liquid dispersions. *Soft Matter* **12,** 8025–8029. ISSN: 1744-683X. http://www.tara.tcd.ie/bitstream/2262/78687/1/proofs.pdf (2016).

70. Seknagi, J. *Structure et perméabilité des mousses liquides en présence d'une interaction attractive entre les bulles* Theses (Sorbonne Universite, Dec. 2022). https://theses.hal.science/tel-03988854.

71. Leal-Calderon F. Schmitt V., B. J. *Emulsion Science* second. ISBN: 0-387-39682-9 (Springer, 2007).

72. Bibette, J. & Mason, T. French Patent 96 04736. *PCT SR97/00690* **5** (1996).

73. Denkov, N. D., Subramanian, V., Gurovich, D. & Lips, A. Wall slip and viscous dissipation in sheared foams: Effect of surface mobility. *Colloids and Surfaces A: Physicochemical and Engineering Aspects* **263,** 129–145. ISSN: 09277757 (2005).

74. Rouyer, F., Cohen-Addad, S., Höhler, R., Sollich, P. & Fielding, S. M. The large amplitude oscillatory strain response of aqueous foam: Strain localization and full stress Fourier spectrum. *Eur. Phys. J. E* **27,** 309–321. http://www.springerlink.com/content/1u03736526k13733/ (2008).

75. Rouyer, F., Cohen-Addad, S. & Höhler, R. Is the yield stress of aqueous foam a well-defined quantity? *Colloids and Surfaces A: Physicochemical and Engineering Aspects* **263,** 111–116. ISSN: 09277757 (2005).

76. Datta, S. S., Gerrard, D. D., Rhodes, T. S., Mason, T. G. & Weitz, D. A. Rheology of attractive emulsions. *Physical Review E* **84.** ISSN: 1539-3755. https://dx.doi.org/10.1103/physreve.84.041404 (2011).

77. Feneuil, B. *Cement foam stability : link with cement paste rheological properties* Theses (Université Paris-Est, Oct. 2018). https://pastel.hal.science/tel-02084040.

78. Denkov, N. D., Tcholakova, S., Golemanov, K., Ananthpadmanabhan, K. P. & Lips, A. The role of surfactant type and bubble surface mobility in foam rheology. *Soft Matter* **5,** 3389. ISSN: 1744-683X. https://dx.doi.org/10.1039/b903586a (2009).

79. Baker, O. Simultaneous flow of oil and gas. *Oil Gas Journal* **53,** 185–195 (1954).

80. Moreno Quibén, J. *Experimental and analytical study of two-phase pressure drops during evaporation in horizontal tubes* en. PhD thesis (EPFL, Lausanne, 2005). https://infoscience.epfl.ch/handle/20.500.14299/215783.

81. Bauer, D. *et al.* Experimental and numerical determination of Darcy's law for yield stress fluids in porous media. *Physical Review Fluids* **4.** ISSN: 2469-990X. https://dx.doi.org/10.1103/physrevfluids.4.063301 (2019).

82. Hohler, R., Seknagi, J. & Kraynik, A. Capillary pressure, osmotic pressure and bubble contact areas in foams. *Soft Matter* **17,** 6995–7003. ISSN: 1744-6848 (Electronic) 1744-683X (Linking). https://www.ncbi.nlm.nih.gov/pubmed/34240084 (2021).

83. Yuen, H., Illingworth, J. & Kittler, J. Detecting partially occluded ellipses using the Hough transform. *Image and Vision Computing* **7,** 31–37. ISSN: 0262-8856. https://www.sciencedirect.com/science/article/pii/0262885689900176 (1989).

84. Tcholakova, S., Denkov, N. D. & Lips, A. Comparison of solid particles, globular proteins and surfactants as emulsifiers. *Physical Chemistry Chemical Physics* **10** (2008).

85. Petkova, B., Tcholakova, S. & Denkov, N. Foamability of surfactant solutions: Interplay between adsorption and hydrodynamic conditions. *Colloids and Surfaces A: Physicochemical and Engineering Aspects* **626.** ISSN: 09277757 (2021).

86. Grace†, H. P. Dispersion phenomena in high viscosity immiscible fluid systems and application of static mixers as dispersion devices in such systems. *Chemical Engineering Communications* **14,** 225–277. ISSN: 0098-6445. https://dx.doi.org/10.1080/00986448208911047 (1982).

87. Golemanov, K., Tcholakova, S., Denkov, N. D., Ananthapadmanabhan, K. P. & Lips, A. Breakup of bubbles and drops in steadily sheared foams and concentrated emulsions. *Physical Review E* **78.** ISSN: 1539-3755. https://dx.doi.org/10.1103/physreve.78.051405 (2008).

88. Huisman, F. & Mysels, K. J. Contact angle and the depth of the free-energy minimum in thin liquid films. Their measurement and interpretation. *The Journal of Physical Chemistry* **73.** Publisher: American Chemical Society, 489–497. ISSN: 0022-3654 (Mar. 1969).

89. Princen, H., Aronson, M. & Moser, J. Highly concentrated emulsions. II. Real systems. The effect of film thickness and contact angle on the volume fraction in creamed emulsions. *Journal of Colloid and Interface Science* **75,** 246–270. ISSN: 0021-9797 (1980).

90. Van Hecke, M. Topical review: Jamming of soft particles: geometry, mechanics, scaling and isostaticity. *J. Phys.: Condens. Matter* **22,** 033101 (2010).

91. Tsumuraya, K. & Miyata, Y. Coarsening models incorporating both diffusion geometry and volume fraction of particles. *Acta Metallurgica* **31,** 16 (1982).

92. Streitenberger, P. Analytical description of phase coarsening at high volume fractions. *Acta Materialia* **61,** 5026–5035. ISSN: 13596454 (2013).

93. Cheng, N.-S. Formula for the Viscosity of a Glycerol-Water Mixture. *Industrial & Engineering Chemistry Research* **47,** 3285–3288. ISSN: 0888-5885. https://dx.doi.org/10.1021/ie071349z (2008).

94. Battino, R. & Clever, H. L. The Solubility of Gases in Liquids. *Chemical Reviews* **66.** doi: 10.1021/cr60242a003, 395–463. ISSN: 0009-2665. https://doi.org/10.1021/cr60242a003 (1966).

95. Association, G. P. *et al. Physical properties of glycerine and its solutions* (Glycerine Producers' Association, 1963).

96. Zander, R. The Distribution Space of Physically Dissolved Oxygen in Aqueous Solutions of Organic Substances. *Zeitschrift für Naturforschung C* **31,** 339–352 (1976).

97. Silicones, B. *Rhodorsil Oils 47* Generic.

98. Zhang, Y. & Liu, L. On Diffusion in Heterogeneous Media. *American Journal of Science* **312,** 1028–1047. ISSN: 0002-9599 (2013).

99. Sircar, S. & Rao, M. B. Estimation of surface diffusion through porous media. *AIChE Journal* **36,** 1249–1254. ISSN: 0001-1541 (1990).

100. Feitosa, K., Marze, S., Saint-Jalmes, A. & Durian, D. J. Electrical conductivity of dispersions: from dry foams to dilute suspensions. *Journal of Physics: Condensed Matter* **17,** 6301 (2005).

101. Turner, J. C. R. Two phase conductivity: the electrical conductance of liquid-fluidized beds of spheres. *Chemical Engineering Science* **31,** 487–492 (1976).

102. Zabulis, X., Papara, M., Chatziargyriou, A. & Karapantsios, T. D. Detection of densely dispersed spherical bubbles in digital images based on a template matching technique. *Colloids and Surfaces A: Physicochemical and Engineering Aspects* **309,** 96–106. ISSN: 09277757 (2007).

103. Strokina, N., Matas, J., Eerola, T., Lensu, L. & Kälviäinen, H. Detection of bubbles as concentric circular arrangements. *Machine Vision and Applications* **27,** 387–396. ISSN: 0932-8092 1432-1769 (2016).

104. Haas, T., Schubert, C., Eickhoff, M. & Pfeifer, H. BubCNN: Bubble detection using Faster RCNN and shape regression network. *Chemical Engineering Science* **216,** 115467. ISSN: 0009-2509 (2020).

105. Jocher, G., Chaurasia, A. & Qiu, J. *Ultralytics YOLOv8* version 8.0.0. 2023. https://github.com/ultralytics/ultralytics.

106. Vijayakumar, A. & Vairavasundaram, S. YOLO-based Object Detection Models: A Review and its Applications. *Multimedia Tools and Applications.* ISSN: 1573-7721 (2024).

107. Zhao, X. *et al. Fast Segment Anything* 2023. arXiv: 2306.12156 [cs.CV].

108. Bradski, G. The OpenCV Library. *Dr. Dobb's Journal of Software Tools* (2000).

109. Buades, A., Coll, B. & Morel, J. Non-Local Means Denoising. *Image Processing On Line* **1,** 208–212. ISSN: 2105-1232 (2011).

110. Zuiderveld, K. J. *Contrast Limited Adaptive Histogram Equalization* in *Graphics gems* (1994). https://api.semanticscholar.org/CorpusID:62707267.

111. Akyon, F. C., Altinuc, S. O. & Temizel, A. Slicing Aided Hyper Inference and Fine-tuning for Small Object Detection. *2022 IEEE International Conference on Image Processing (ICIP),* 966–970 (2022).

112. Allan, D. B., Caswell, T., Keim, N. C., van der Wel, C. M. & Verweij, R. W. *soft-matter/trackpy: v0.6.3* version v0.6.3. June 2024. https://doi.org/10.5281/zenodo.11522100.

113. Wang, K. G. & Glicksman, M. E. Noise of microstructural environments in late-stage phase coarsening. *Phys Rev E Stat Nonlin Soft Matter Phys* **68.** Wang, K G Glicksman, M E eng 2003/12/20 Phys Rev E Stat Nonlin Soft Matter Phys. 2003 Nov;68(5 Pt 1):051501. doi: 10.1103/PhysRevE.68.051501. Epub 2003 Nov 3., 051501. ISSN: 1539-3755 (Print) 1539-3755 (Linking). https://www.ncbi.nlm.nih.gov/pubmed/14682799 (2003).

114. Werz, T., Baumann, M., Wolfram, U. & Krill, C. E. Particle tracking during Ostwald ripening using time-resolved laboratory X-ray microtomography. *Materials Characterization* **90,** 185–195. ISSN: 10445803 (2014).

115. Haffner, B., Khidas, Y. & Pitois, O. The drainage of foamy granular suspensions. *Journal of Colloid and Interface Science* **458,** 200–208. ISSN: 0021-9797. https://www.sciencedirect.com/science/article/pii/S0021979715300709 (2015).

116. Forel, E., Langevin, D. & Rio, E. Measurement of film permeability in 2D foams. *The European Physical Journal E* **42,** 1–7 (2019).

Appendix A

Dependency of the coarsening constant from physical-chemistry

The coarsening constant in the dry limit Ω_0 (cf. Eq. 1.40) depends on the physical-chemistry of the gas/surfactant/liquid system. The main problem in its determination resides in the film thickness h_{eff}, which is dynamically set by the equilibrium between the disjoining pressure Π_d and the foam osmotic pressure Π (cf.Section 1.1.2). Moreover, the effective film thickness h_{eff} determining the coarsening constant can be enhanced by the resistance of the surfactant monolayer to the gas permeability [1].

To provide additional information to the study conducted in the ISS, the Orsay group conducted quasi-2D coarsening experiments. The evolution of the bubble areas was measured following the method described in [116]. The rate of evolution of 2D bubbles, according to Aboav law for fully dry foams, follows:

$$\frac{dA}{dt} = (n-6)\frac{2\pi\Omega_0}{3}. \tag{A.1}$$

where n is the number of sides of the bubbles. These experiments were performed on 9 kind of surfactant solutions, shown in Fig. A.1, chosen to represent a variety in the physical-chemistry: presence of micelles, bulk viscosity, surface rheology, film thickness, and adhesion. Wet foams prepared from these surfactant solutions have also been studied in microgravity experiments. At a liquid fraction $\phi = 0.30$, all of them present a parabolic growth law, from which we determined their coarsening rate Ω_{32}. In Figure A.1, we compare the coarsening rate Ω_{32} with Ω_0. The linearity between the two means that the coarsening rate measured in bulk foams is mainly controlled by the film permeability, which can be determined from measurements of quasi-2D foam evolution. Thus, as discussed in Section 3.3, we consider reliable the update value of $\Omega_0 = 240\mu\text{m}^2/\text{s}$ for TTAB surfactant foams with $\mathcal{C} = 5\text{g/L}$.

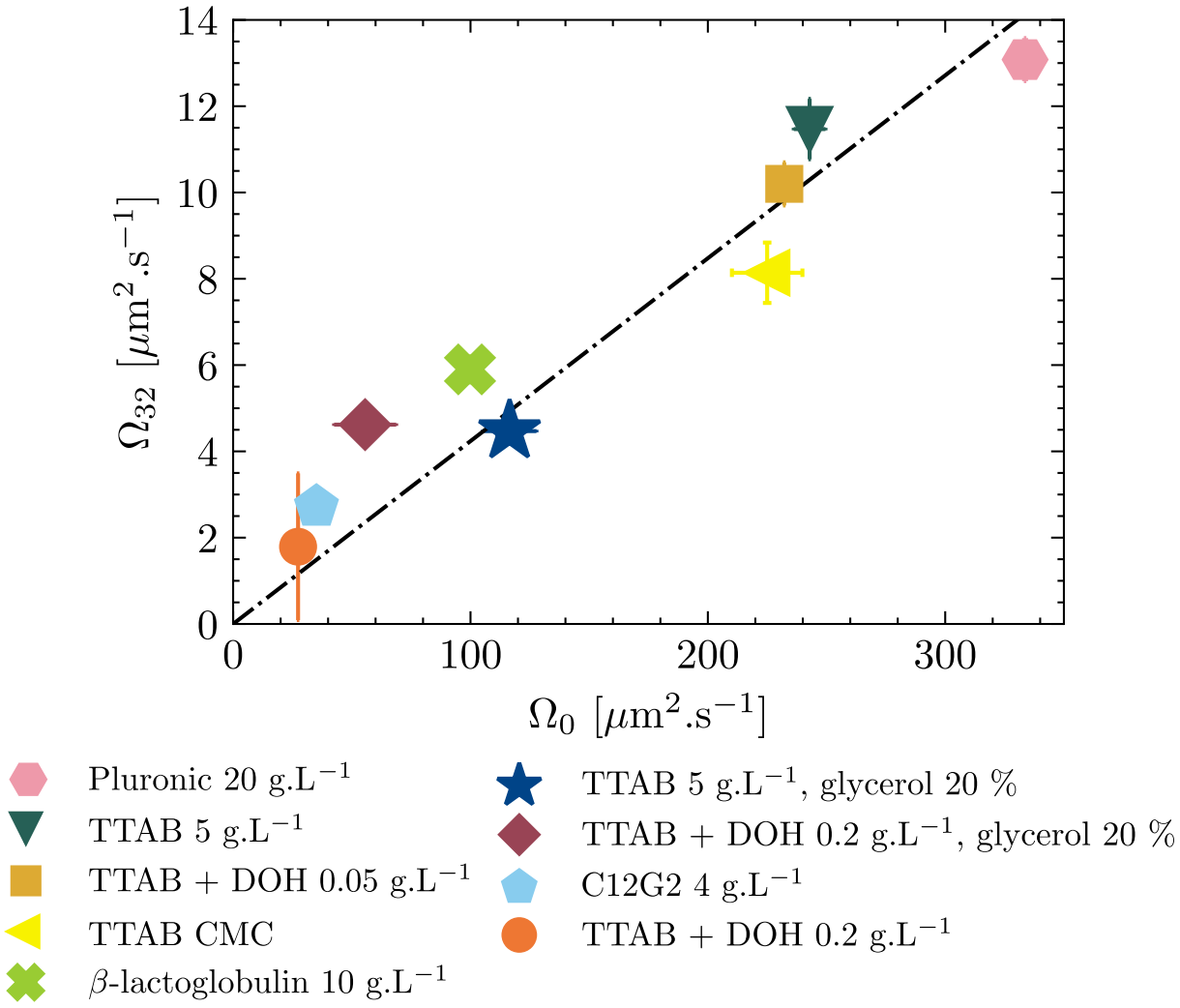

Figure A.1: Coarsening rate Ω_{32} as a function of the coarsening constant Ω_0, for foams with constant liquid fraction $\phi = 0.30$, and varying viscosity, surfactant composition, interface rigidity, and contact angle.

Appendix B

Bubble size distributions of dispersions with liquid fractions from the dry to the dilute limit

As explained in Section 3.3, we performed coarsening experiments on bubbly emulsions at a constant yield stress $\tau_y = 16.5$ Pa. For the considered range of coarsening time $t \lesssim 10^5$s, the plasticity of the emulsion counteracts gravitational drainage without affecting the coarsening growth laws. We present in Fig. B.1 the bubble size distributions of these samples for all the ages shown in Fig. 3.17. For all the liquid fractions, we observe a scaling state for coarsening times $t \gtrsim 10^4$s. We show in Fig. B.2 the corresponding scaling state distributions. We observe that the shape of the distribution evolves with the liquid fraction, narrowing and reducing its maximum radius as $\phi \to 1$.

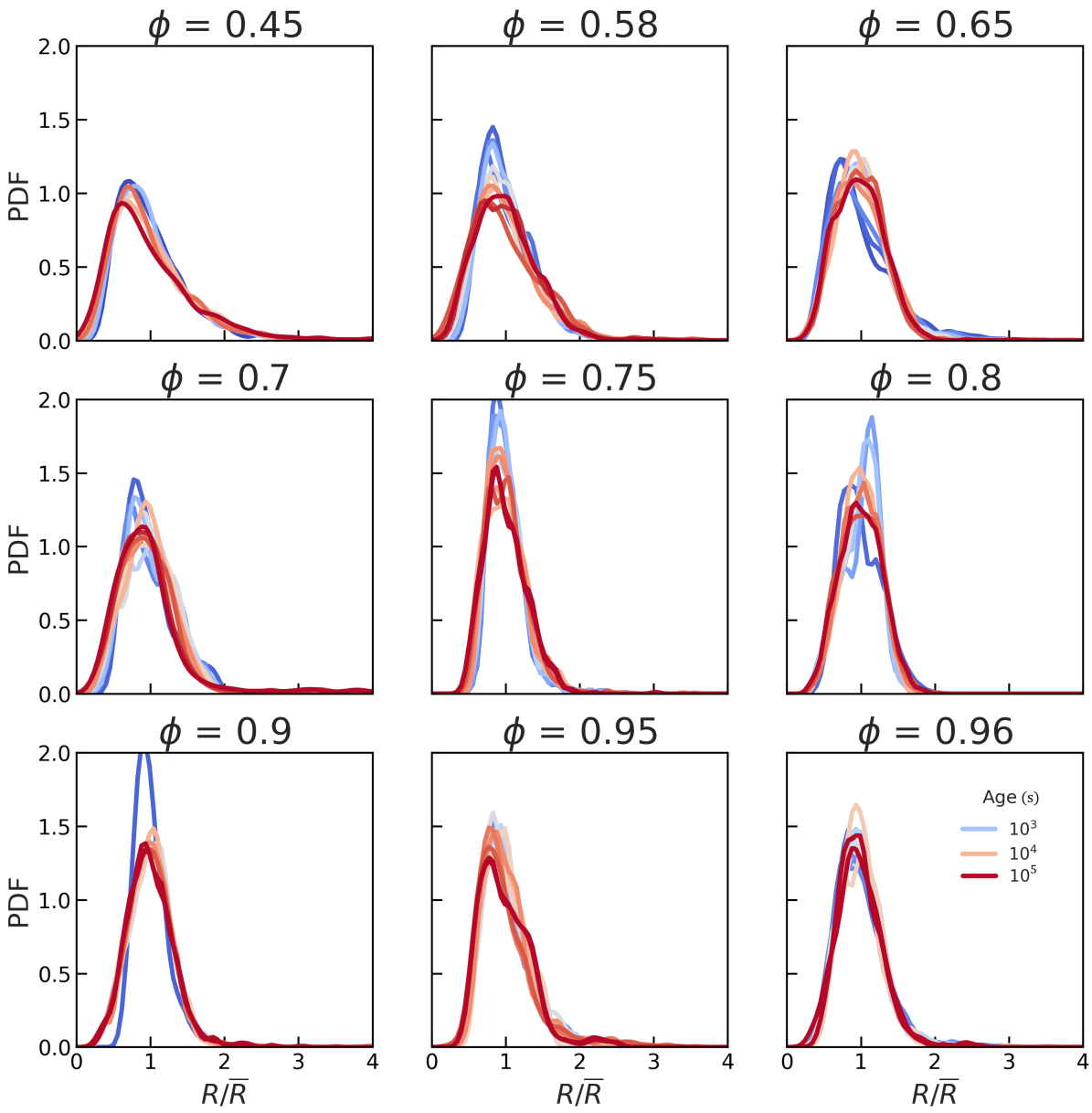

Figure B.1: Bubble size distributions of coarsening bubbly emulsions, with a constant yield stress $\tau_y = 16.5$ Pa, evolving toward the scaling state. The liquid fraction varies between $\phi = 0.45$ and $\phi = 0.96$, as indicated. For all the presented duration, the Bingham capillary number is small enough not to observe any dampening in the growth law $Bi \leq 0.02$.

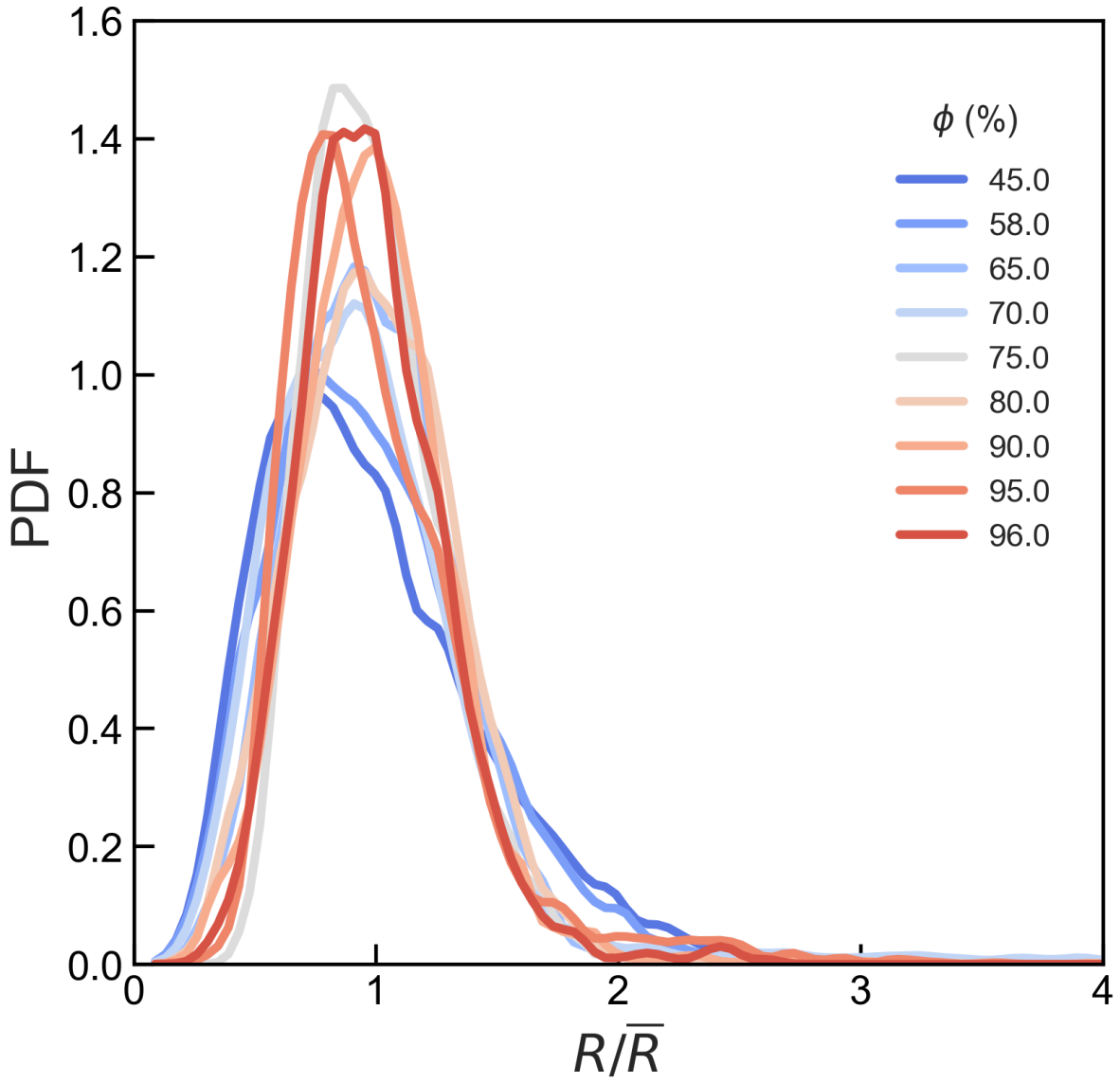

Figure B.2: Bubble size distributions corresponding to the Scaling state for coarsening bubbly emulsions, with a constant yield stress $\tau_y = 16.5$ Pa. The liquid fraction vary between $\phi = 0.45$ and $\phi = 0.96$, as indicated. For all the presented duration, the Bingham capillary number is small enough not to observe any dampening in the growth law $Bi \leq 0.02$.

Appendix C

Individual gas exchange in bubbly emulsions

Following the discussion of Section 4.2.4, we present here the complete series of plots of the individual gas volume flux J, as a function of the relative radius $R/\overline{R}$, for bubbly emulsions studied in the osmotic cell. Each panel corresponds to an experiment, with varying initial liquid fraction ϕ_0, and each plot corresponds to data corresponding to a given yield stress τ_y for the emulsion. The evolution of the liquid fraction ϕ with time is shown in Fig. 4.20. In Figs. C.1 to C.3, we show the data for samples closer to the dilute regime. In Figs. C.4 to C.6, we show three repetitions of a coarsening bubbly liquid with initial liquid fraction $\phi_0 = 0.60$. Finally, in Fig. C.7, we show the sample with the highest gas concentration.

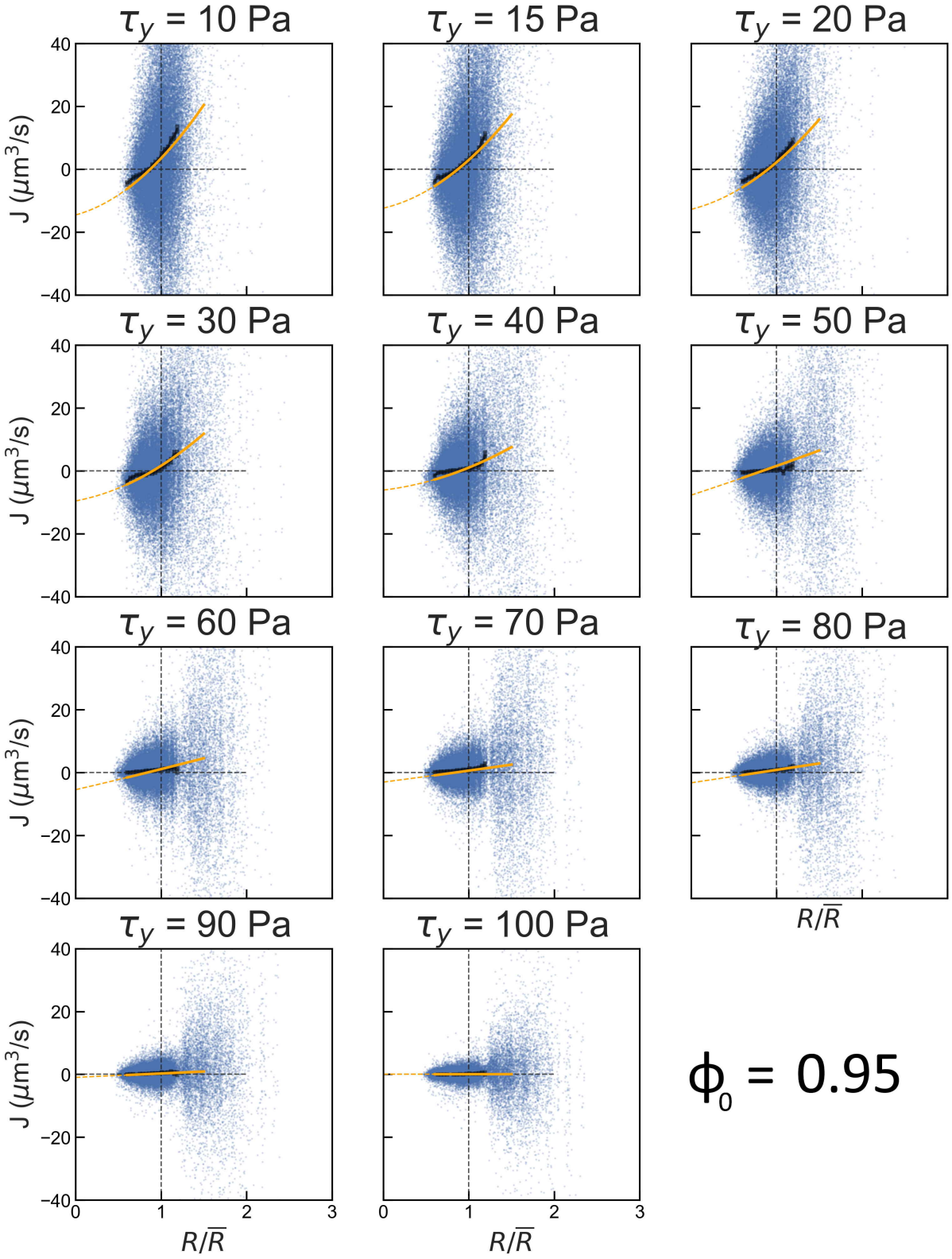

Figure C.1: Individual inward gas volume flux $J = R^2 dR/dt$ as a function of the relative radius $R/\overline{R}$, in a bubbly emulsion with initial liquid fraction $\phi = 0.95$ and varying emulsion yield stress τ_y, as indicated.

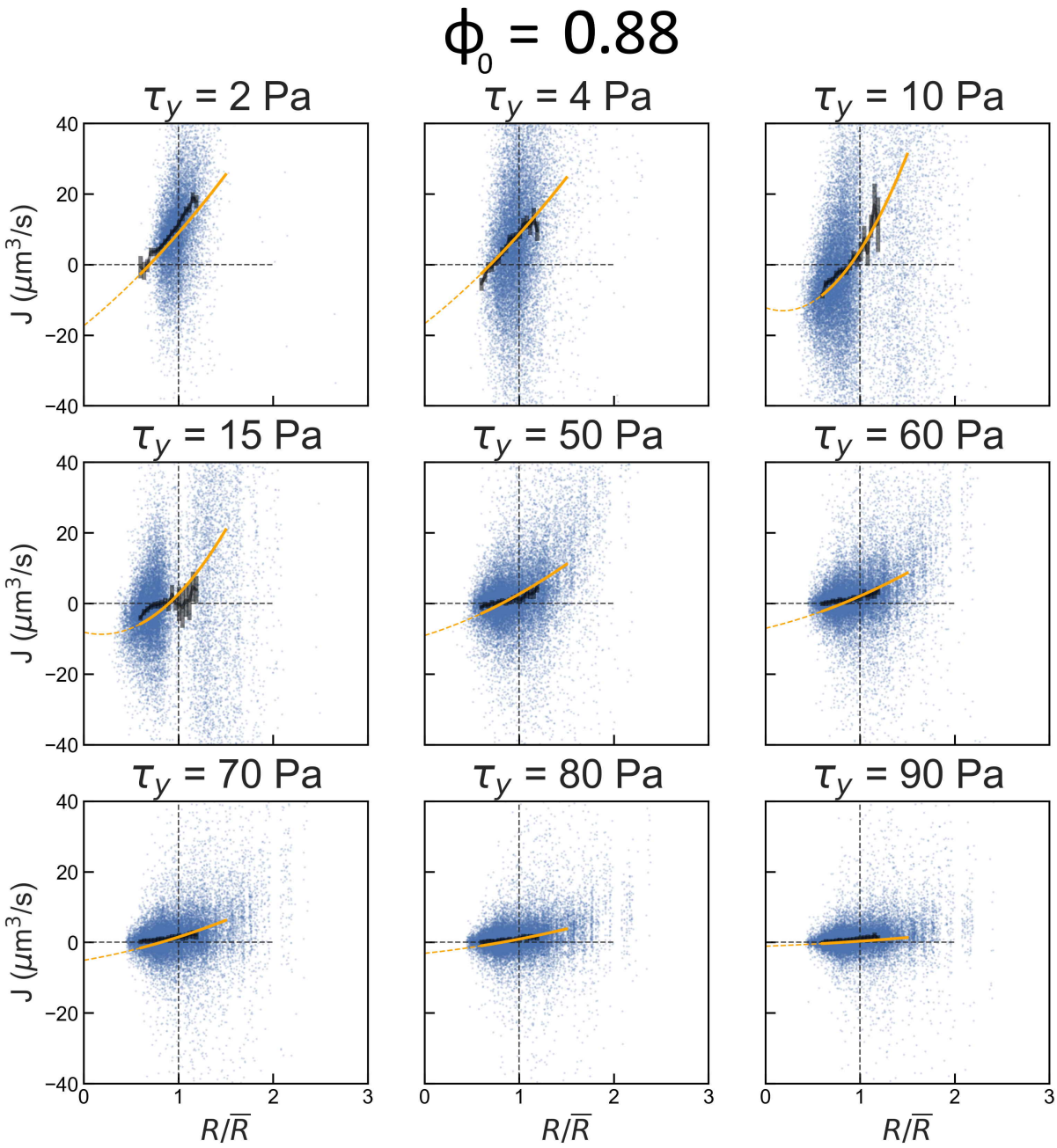

Figure C.2: Individual inward gas volume flux $J = R^2 dR/dt$ as a function of the relative radius $R/\overline{R}$, in a bubbly emulsion with initial liquid fraction $\phi = 0.88$ and varying emulsion yield stress τ_y, as indicated.

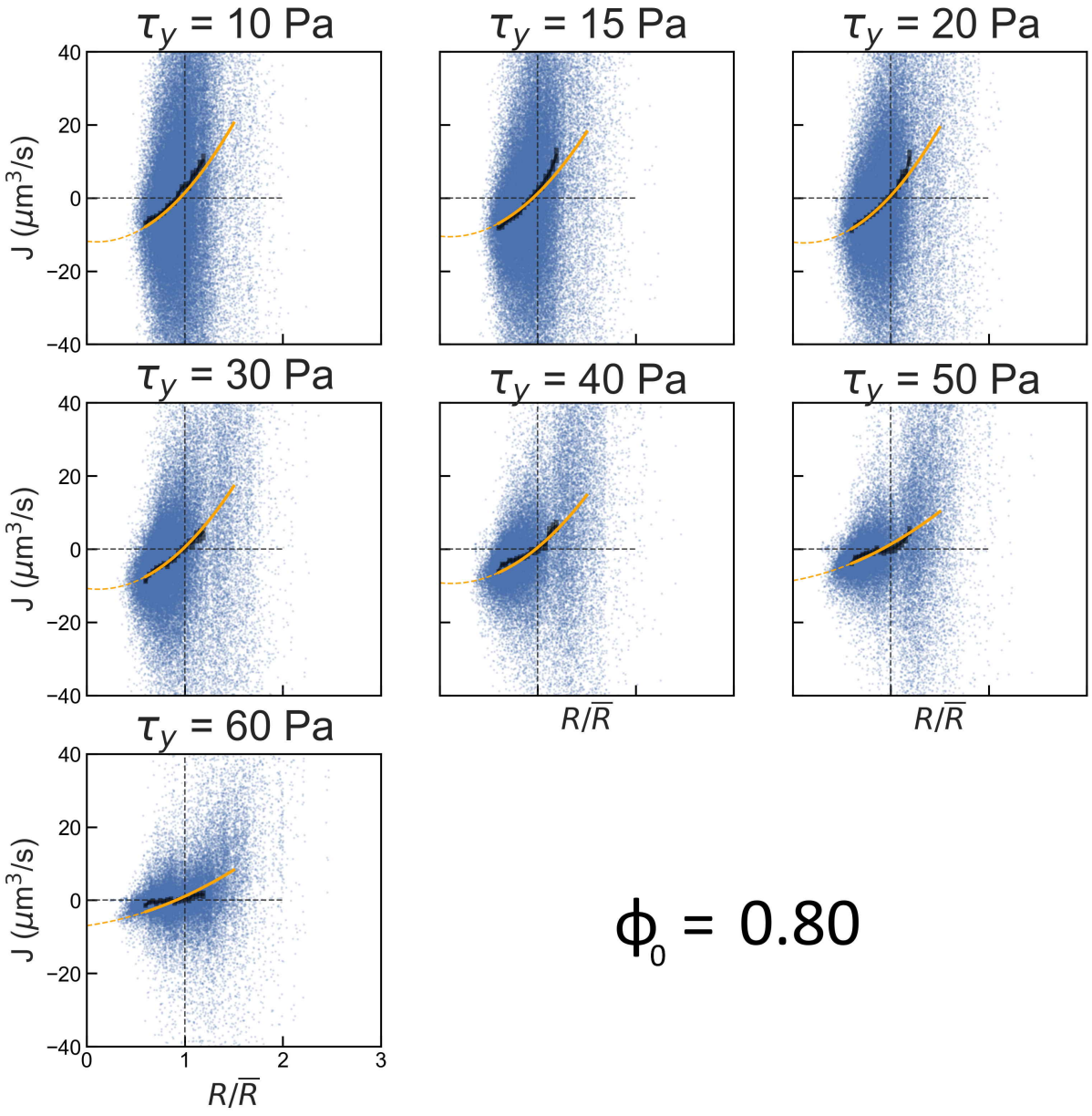

Figure C.3: Individual inward gas volume flux $J = R^2 dR/dt$ as a function of the relative radius $R/\overline{R}$, in a bubbly emulsion with initial liquid fraction $\phi = 0.80$ and varying emulsion yield stress τ_y, as indicated.

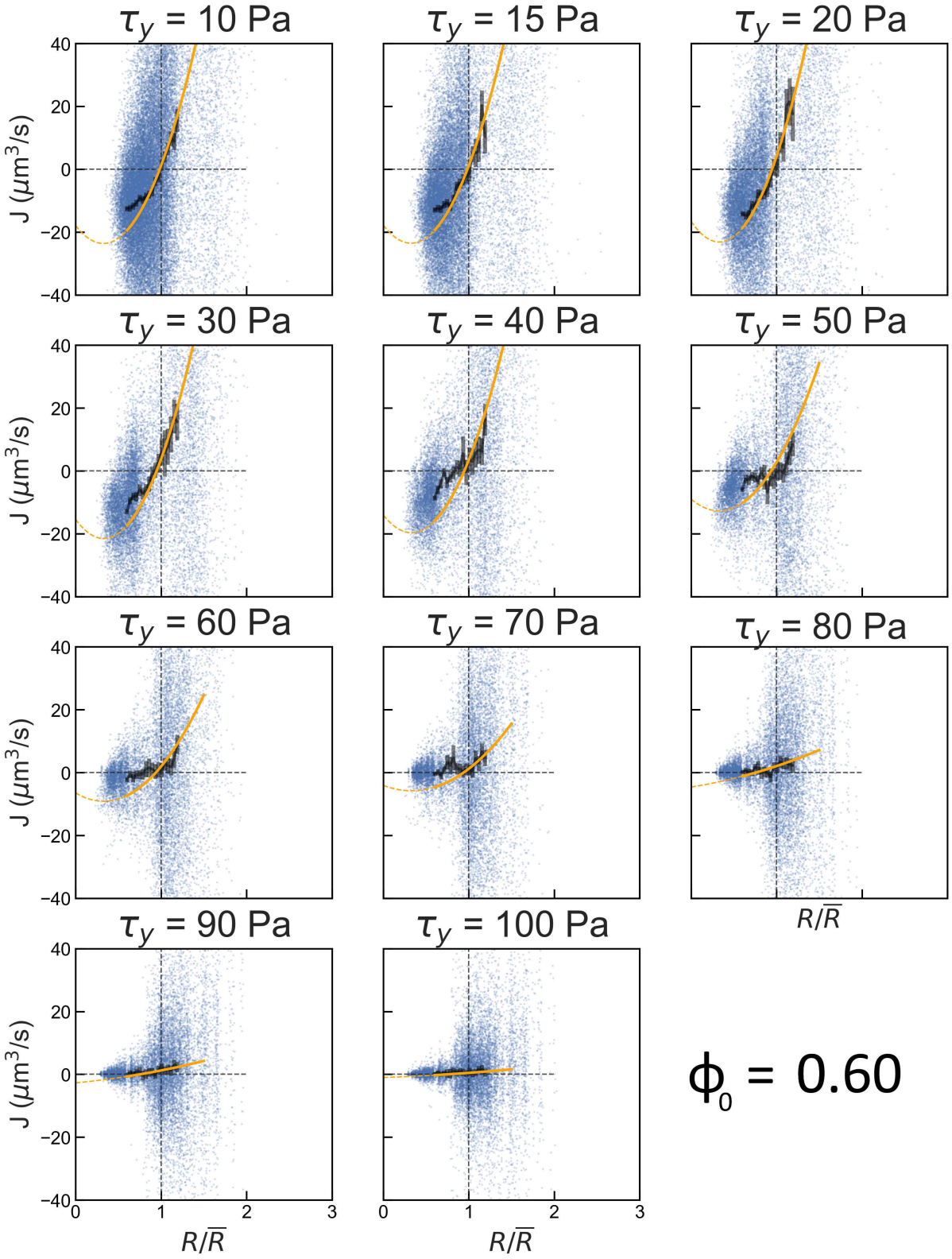

Figure C.4: Individual inward gas volume flux $J = R^2 dR/dt$ as a function of the relative radius $R/\overline{R}$, in a bubbly emulsion with initial liquid fraction $\phi = 0.60$ and varying emulsion yield stress τ_y, as indicated.

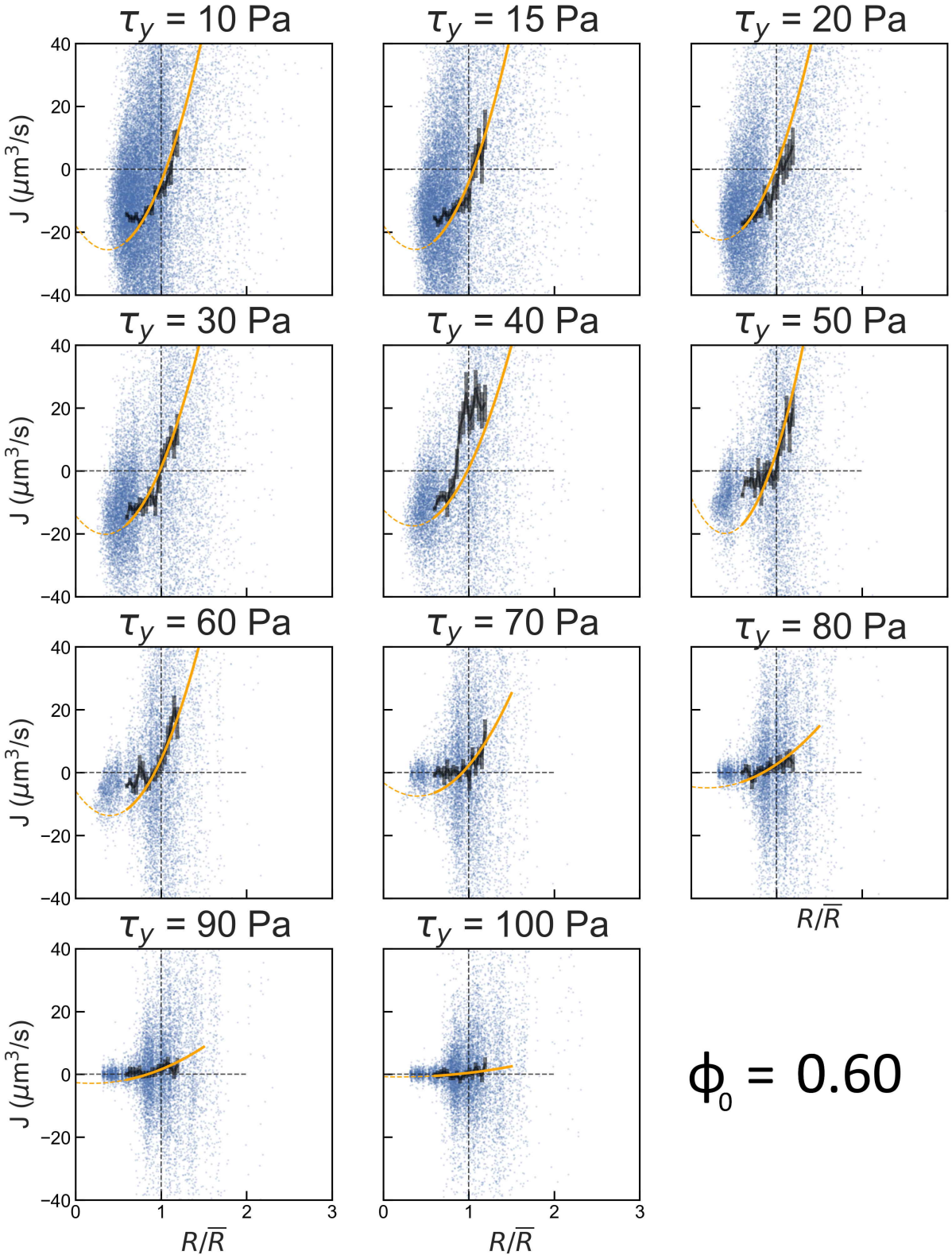

Figure C.5: Individual inward gas volume flux $J = R^2 dR/dt$ as a function of the relative radius $R/\overline{R}$, in a bubbly emulsion with initial liquid fraction $\phi = 0.60$ and varying emulsion yield stress τ_y, as indicated.

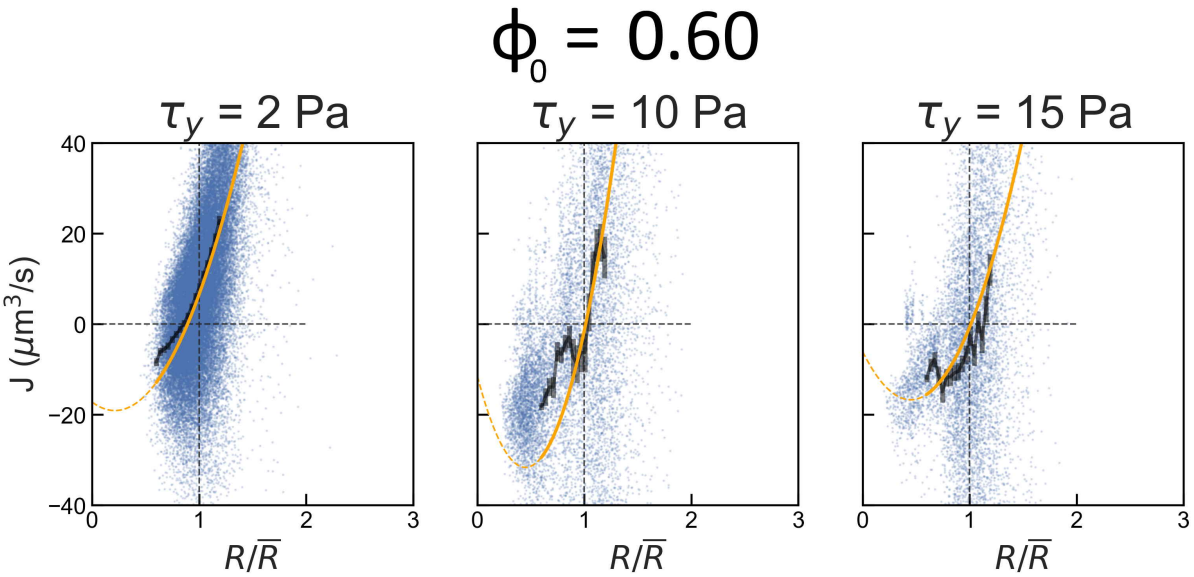

Figure C.6: Individual inward gas volume flux $J = R^2 dR/dt$ as a function of the relative radius $R/\overline{R}$, in a bubbly emulsion with initial liquid fraction $\phi = 0.60$ and varying emulsion yield stress τ_y, as indicated.

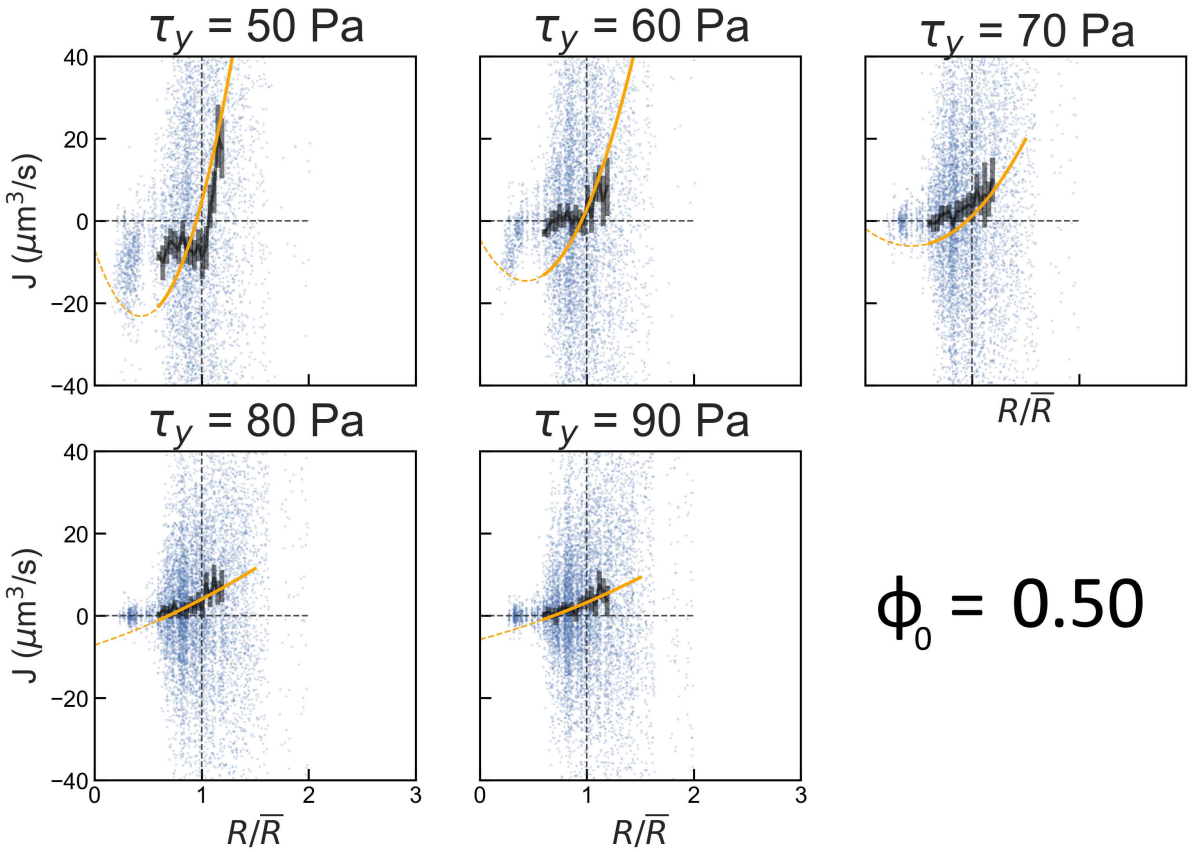

Figure C.7: Individual inward gas volume flux $J = R^2 dR/dt$ as a function of the relative radius $R/\overline{R}$, in a bubbly emulsion with initial liquid fraction $\phi = 0.50$ and varying emulsion yield stress τ_y, as indicated.